Myosin 1b – Membrane mechanics and cellular dynamics Myosine

Thibaut J Lagny

THÈSE DE DOCTORAT

de l'Université de recherche Paris Sciences et Lettres
PSL Research University

Préparée à l'Institut Curie

Myosin 1b – Membrane mechanics and cellular dynamics

Myosine 1b – Mécanique membranaire et dynamique cellulaire

Ecole doctorale n°564

Physique en Île de France

Spécialité PHYSIQUE

Soutenue par Thibaut Jean **LAGNY**

le 13 Juillet 2018

Dirigée par
Patricia BASSEREAU
& Evelyne COUDRIER

COMPOSITION DU JURY :

M. MARGUET Didier
Université de Marseille, Président du jury

Mme. MATTILA Pieta
University of Turku, Rapporteur

M. DERGANC Jure
University of Ljubljana, Rapporteur

Mme. DIZ-MUÑOZ Alba
EMBL Heidelberg, Membre du jury

M. WEDLICH-SÖLDNER Roland
University of Münster, Membre du jury

institutCurie

PSL RESEARCH UNIVERSITY PARIS

Thèse de Doctorat

de l'Université de recherche

Paris Sciences et Lettres

PSL Research University

Préparée à l'Institut Curie

Myosin 1b – Membrane mechanics and cellular dynamics

Myosine 1b – Mécanique membranaire et dynamique cellulaire

Ecole doctorale N° 564 - Physique en Île de France

Spécialité: Physique

dirigée par

Patricia BASSEREAU & Evelyne COUDRIER

soutenue le 13 Juillet 2018 par

Thibaut Jean LAGNY

devant le jury composé de:

Président:	Didier MARGUET
Rapporteurs:	Pieta MATTILA
	Jure DERGANC
Examinateurs:	Alba DIZ-MUÑOZ
	Roland WEDLICH-SÖLDNER

Acknowledgements

The last years that I spent at Curie have been both challenging and incredibly rewarding and I am happy to look back on this time while writing my acknowledgements, just before leaving Curie for good.

I would like to start thanking my two thesis directors Evelyne and Patricia, who, ever since I joined the lab, have supported, pushed, comforted and inspired me. It has been a tremendous pleasure to work with you, spending numerous hours discussing science, being confused by the data, and often times realizing that maybe it is the questions and not the answers that I enjoy most in life. I have always appreciated working with you, the freedom you gave me to explore science and the guidance you offered when I got lost. I am extremely grateful for the opportunities you gave me, notably to explore science outside the lab.

Thank you very much to my jury members Didier Marguet, Alba Diz-Muñoz, Roland Wedlich-Söldner, and a layer of even more gratitude to my 'rapporteurs' Pieta Mattila and Jure Derganc who were willing to read my manuscript, came to Paris in summer and made the experience of defending my PhD very stimulating and enjoyable.

I would like to thank Guy Tran van Nhieu for being my external thesis advisor, delving into my little bubble of desperation once a year and offering plenty of good advice throughout this PhD.

Thank you to the BMBC platform for continuous support: John, Fanny, Fahima, Aude, and Anna.

Team Coudrier, thank you! Olga and Priscilla for a biological perspective; and Maïté for a thousand 'petits conseils' and a lot of blotting magic.

Team Bassereau Superstar, thank you so much! It has been a great privilege to work with you during all these years. I have always appreciated the spirit in our team and everybody's willingness to help! A special shout-out to the Bassriers/Coudereaus: Feng and Julian, for at least three group meetings a week!

Thank you to all the theoreticians I have had the pleasure to interact and discuss my experiments with: Pierre Sens, Madan Rao, and Françoise Brochard-Wyart.

Thank you to Bruno Goud and his team for many Tuesday morning Rab-ventures and some ERC-worthy dinners.

Thank you to the UMR168 support team along these years, Brigitte, Karen, Agnès, Christelle, Laurence, Naïma, Remy and Eric. Without you, nothing would work.

Thank you to Jitu Mayor for inviting me to spend some weeks in his lab. Beyond the great results that we obtained I have enjoyed this stay beyond any expectation and I am deeply grateful for the opportunity you offered. Thomas, Parijat and Amit, thank you so much for all your help and thank you to the entire team at NCBS for such a great spirit.

Thank you to all those amazing people met during the summer schools at Woods Hole, Cargèse, and Albuquerque.

Thank you to Josef Kaes and Jürgen Lippoldt for our small collaboration on cancer cells.

As there are way too many people to thank within the UMR/ at Curie I will go for keywords here. While this might be less enjoyable for an outside reader (Yes, you!) it serves as a good enigmatic conclusion of these years.

Free food / _ave / snoring roomies / rice in the elevator / Urgent! / Vélib /

Wroclaw / Goat? / Trampoline / Chinois / Cocophobia / Tak! /

Bratislava / Montagne / Bar trials / Communism / Disney / LabView

To all the babtous from CDI, thank you for some poun!

Thank you to la Sirène, the CRf family and my fellow students at the IMA for invigorating distractions from work.

Thank you to Rick Astley for never giving up.

Thank you to my family who throughout these years has been a source of support and has always been there for me.

Leonie, thank you for everything. If I started to make a list, I wouldn't be able to stop.

Table of Contents

List of Figures

List of Tables

List of abbreviations

AFM	Atomic Force Microscopy
BS	S-Nitro-Blebbistatin
CHO	chinese hamster ovary
DOPC	1,2-dioleoyl-sn-glycero-3-phosphocholine
Eph	erythropoietin-producing human hepatocellular receptor
EphHEK	EphB2-YFP HEK 293T
Ephrin	Eph family receptor interacting proteins
ERM	Ezrin Radixin Moesin
F-actin	filamentous actin
FCS	Fluorescence correlation spectroscopy
FRAP	Fluorescence recovery after photobleaching
G-actin	globular actin
GPI	glycosyl-phosphatidyl-inositol
GPL	glycerophospholipids
GSL	glycosphingolipids
HEK293T	Human Embryonic Kidney 293 large T
LatA	LatrunculinA
MLCK	Myosin Light Chain Kinase
Myo1b	Myosin 1b
OT	Optical Tweezer
PClP	Penta-Chloro-Pseudilin
PI(3,4,5)P3	Phosphatidyl-Inositol-(3,4,5)-Tris-Phosphate
PI(4,5)P2	Phosphatidyl-Inositol-(4,5)-Bis-Phosphate
PIV	Particle Image Velocimetry
PM	plasma membrane
SIM	Structural illumination microscopy
SM	Sphingomyelin
SPT	single particle tracking
STORM	Stochastic optical reconstruction microscopy
TIRF	Total internal reflection fluorescence
TM	transmembrane
WT	wildtype

Preface

Previous work in the lab of Evelyne Coudrier has established a role of Myosin 1b in regulating membrane shape at the Golgi apparatus[1] and endosomes[2]. It is also involved at the plasma membrane, where it is required for efficient EphB2-driven cell segregation through cell retraction[3]. Work performed by Ayako Yamada showed that Myosin 1b can elongate membranes along actin bundles *in vitro*[4] in a way reminiscent of membrane tube elongation at the Golgi apparatus. Subsequently, work performed on neurons by Olga Iuliano showed effects on axon formation by Myosin 1b, linked to changes in actin wave dynamics[5].

In an effort to consolidate these observations into a coherent mechanistic model, and taking into account that Myosin 1b can interact with membrane receptors[3] and has been reported to change the mechanical properties of the plasma membrane[6,7] we thus hypothesized that the mechanism of action of Myosin 1b at the plasma membrane has a mechanical origin. By such a general effect, we thought to be able to explain the variety of biological phenotypes, linking them to one fundamental change when Myosin 1b is absent, i.e. altered deformability of the membrane and/or inefficient coupling between the underlying actin cytoskeleton and the plasma membrane.

Using optical tweezers we characterized the effect of Myosin 1b and ERM proteins, as a benchmark for plasma membrane-cortex linkers, on effective membrane tension, membrane-cortex friction and membrane-cortex adhesion. Yet, to our surprise, we did not observe any striking difference in the assessed parameters. The results are presented and discussed in part A of this thesis.

This prompted us to pursue a secondary hypothesis during the last year of this thesis. Inspired by the many demonstrations showing a functional dependence of receptor signaling on actin dynamics, we hypothesized that for EphB2, and potentially other receptors, Myosin 1b might alter the diffusive and thus functional landscape within the membrane, or the actin flows that happen downstream of EphB2 activation. We thus characterized the effect of Myosin 1b on diffusivity, clustering behavior and immobilization of EphB2. Furthermore, we studied the effect of Myosin 1b on actin cytoskeleton dynamics. We studied the dynamics of EphB2 by employing FRAP, FCS, and fluorescence anisotropy. Using TIRF-SIM imaging and subsequent PIV analysis, we studied the dynamics of actin. The obtained results are described and discussed in part B of this thesis.

Introduction

The cell boundary is a defining feature of all living organisms, as it separates the cell from its surrounding environment. It serves as an integration hub for cell signaling, allows exchange with the surroundings, and is fundamental to both cell migration and morphology. In a simplified view, this interface can be reduced to 3 main functional layers[8] (Figure 1). The plasma membrane, which separates inside from outside by a thin lipid bilayer, is highly enriched in proteins that can interact with either side of the leaflet or span the bilayer. Secondly, the underlying actin cytoskeleton often referred to as the cellular cortex, which is a highly dynamic network of semi-flexible polymers, conferring rigidity to the cell that allows it to withstand mechanical stresses from the inside and outside. The interplay and intricate balance between rigidity and constant turnover defines cellular morphology, while allowing for dynamic deformations required for, e.g. cell migration. Thirdly, the interface between the plasma membrane and the actin cytoskeleton is populated by a variety of proteins that link both.

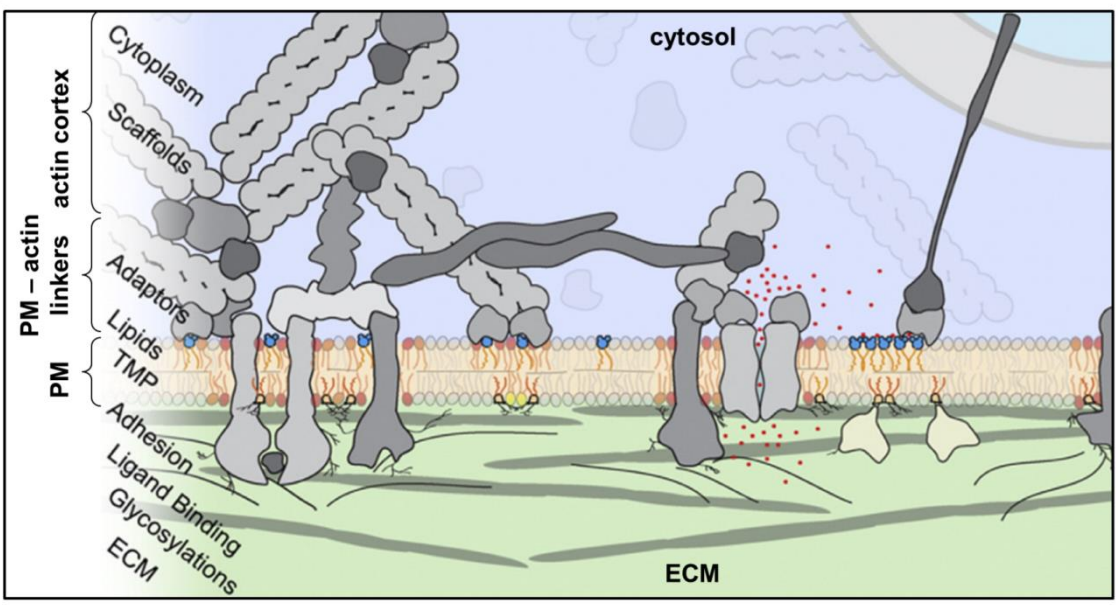

Figure 1 The cell boundary.
Schematic representation of the cell boundary, the extracellular space is represented in green and the intracellular space in blue. The three functional layers as mentioned in the manuscript are highlighted on the left side from top to bottom: actin cortex, PM-actin linkers, and the PM. Modified from reference 8.

In this thesis, we have focused on two fundamental processes happening at the cell boundary:

1. The contribution of membrane-cortex linkers to the cell membrane's mechanical properties.
2. The contribution of membrane-cortex linkers to the dynamics of trans-membrane receptors and the underlying actin cortex.

A detailed introduction regarding both processes precedes the two chapters that describe and discuss our results. This general introduction aims at giving an overview of the current state-of-the-art on the different components involved in these processes.

1. The plasma membrane

The conceptual view of the plasma membrane has been predicted to an impressive degree by Singer and Nicolson in their 'fluid-mosaic model' in the early 70s[9]. Nowadays we know much more about the heterogeneity and asymmetry of involved lipids[10], their spatial segregation in short-lived nanodomains[11], and the abundance of proteins within the lipid bilayer[12]. Yet, conceptually, one may still think about the plasma membrane as a composite material consisting of amphiphilic lipids that assemble into a bilayer, bilayer-spanning transmembrane proteins (integral), and proteins interacting with either side of the leaflet (peripheral)[13] (Figure 2). Functionally, the majority of proteins serve the purpose of extracellular signal integration and ion exchange through the membrane, nutrient uptake, and the control of actin cytoskeletal dynamics. For the lipids, one might differentiate between majority species that establish the biophysical properties of the plasma membrane and maintain an efficient boundary from those that are closely linked to protein function and regulation, e.g. $PI(4,5)P_2$.

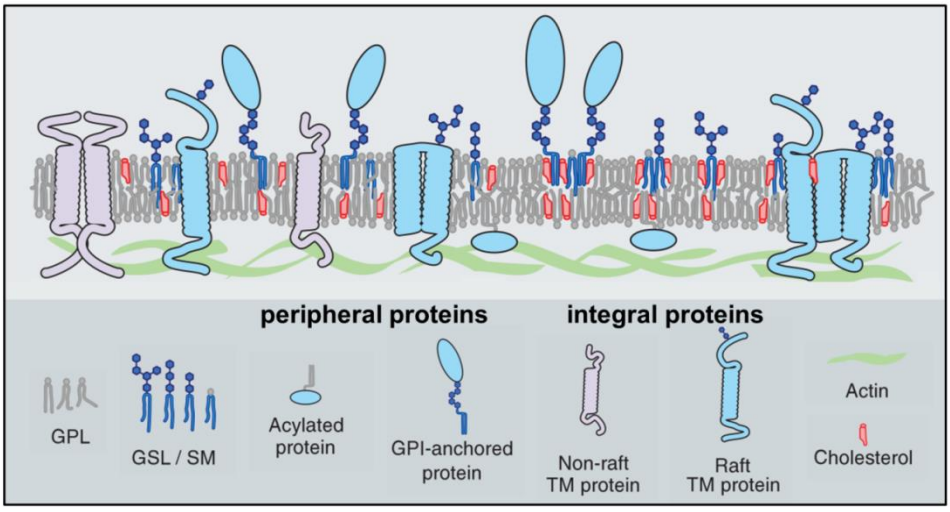

Figure 2 Schematic view of plasma membrane organization.
This schematic view of the PM underlined by actin (green). Glycerophospholipids (GPL) form the majority of the PM lipid content. In addition one finds sphingomyelin (SM) and glycosphingolipids (GSL) that can form nano-domains (lipid rafts) together with cholesterol (red). Integral, bilayer-spanning transmembrane (TM) proteins can have affinities for 'raft' and 'non-raft' phases. Peripheral proteins can be attached to the leaflets of the plasma membrane through lipid anchors, e.g. acylation or glycosylphosphatidylinositol (GPI). Proteins binding to actin and the plasma membrane can serve as pickets, to form the membrane skeleton, as posited in the picket-fence model. Modified from reference 11.

1.1 Lipid composition of the PM

The PM's lipids are generally synthesized at the ER and subsequently trafficked to the PM in a controlled way, with sorting mechanisms that allow maintaining a specific lipid composition[14–16]. The main constituents of the eukaryotic plasma membrane are glycerophospholipids, cholesterol, and sphingomyelin. The family of glycerophospholipids, i.e. phosphatidyl-choline, phosphatidyl-serine, phosphatidyl-ethanolamine, phosphatidyl-inositol, and phosphatidic acid all share a common hydrophobic di-acyl-glycerol backbone; yet they have a different polar headgroup. Sphingolipids, with a ceramide backbone, preferentially interact with cholesterol[10]. Variability in the hydrophobic acyl chains regarding both length and the degree of unsaturation fundamentally impacts the biophysical properties of the individual lipids and in consequence the plasma membrane[17]. This adaptability is important for an organism's adaptability towards, e.g. changes in temperature[18,19].

Furthermore, the PM is asymmetrically organized and lipids are differentially distributed between the inner and outer leaflet. This asymmetry is important for a variety of cellular processes, e.g. during apoptosis[20], and is maintained by the action of transmembrane proteins that catalyze transitions from one bilayer to the other[21].

1.2 Lipid-protein interactions

Lipids can affect protein function in two fundamental ways, either by changing local biophysical properties, or as a messenger and interaction hub. In the former case, the distribution of lipids in the lipid bilayer determines the lateral pressure profile and can, e.g. affect a transmembrane protein's opening probabilities[22,23]. In the latter example, lipids, e.g. phosphoinositides, can locally recruit proteins or act as messengers over large distances[24,25].

1.3 Lateral organization of the PM

The spatial organization of the plasma membrane has remained a controversial topic, especially considering the biological relevance of observations made under non-physiological conditions. Yet two main concepts that are now widely been accepted involve the formation of short-lived, small lipid domains, termed 'lipid rafts'[26,27], and spatial organization of the membrane via the underlying cytoskeletal network and connecting proteins, the 'picket-fence model'[28].

2. The actin cytoskeleton

The eukaryotic cytoskeleton consists of different proteins able to form higher order, linear polymers. The current canonical members include microtubules, intermediate filaments, septins, and actin[29] (Figure 3A, septin not displayed). Other proteins being able to form linear structures *in vivo* have been proposed to be included, e.g. cytidine triphosphate synthase filaments and Pil1[30] (Figure 3B). In this thesis we have worked only on actin and shall focus exclusively on actin from now on.

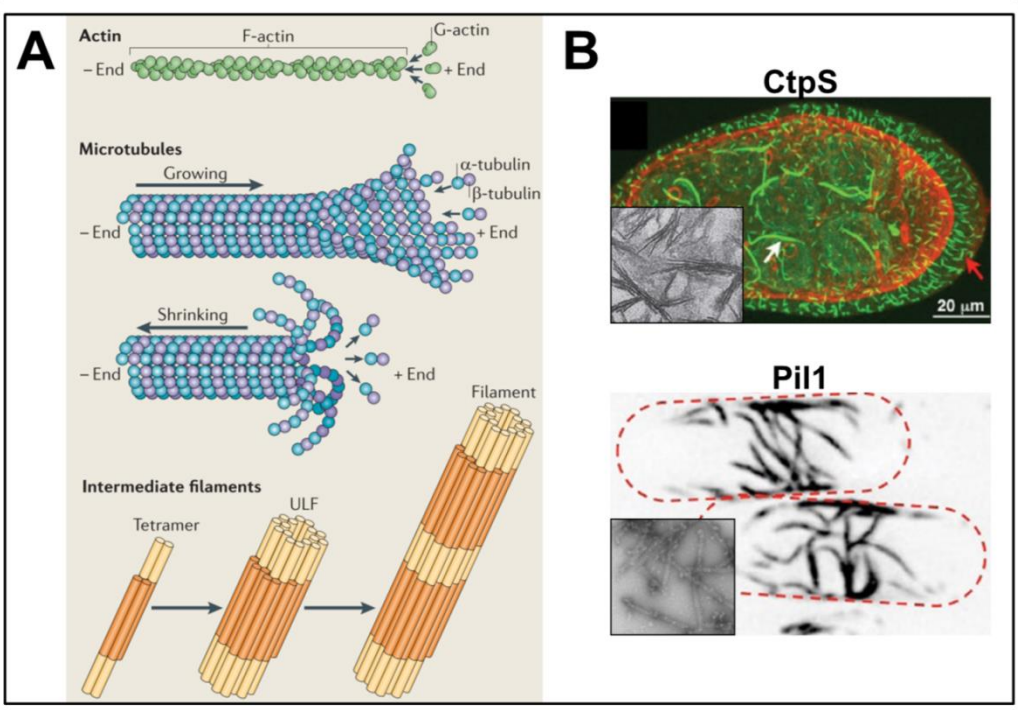

Figure 3 Cytoskeletal elements
(A) Schematic representation of the three canonical cytoskeletal elements actin (top), microtubules (middle), and intermediate filaments (bottom). (reference 29) | **(B)** Proposed cytoskeleton-like structures as found *in vivo* by fluorescence microscopy, and their respective *in vitro* structures imaged by electron microscopy (inset). (modified from reference 30) Cytidine triphosphate synthase (CtpS) from *Drosophila* egg chambers and Phosphorylation inhibited by long chain bases (Pil1) from fission yeast.

2.1 Nucleation and growth dynamics

Actin filaments are present in all eukaryotes and their structure is highly conserved throughout evolution[31]. The molecular building block is G-actin (globular actin), a protein of 42 kDa, consisting of four subdomains[32], with a size of about 6 nm (Figure 4A). In humans, one can distinguish between highly specialized and stable actin fibers associated with Myosin II (actomyosin) optimized for contraction as present in muscle cells[33–37], and more diverse networks in non-muscle cells[38,39]. Non-muscle cells exhibit spatially segregated populations of different actin isoforms, with γ-actin being predominantly found in stress-fibers and actin arcs, while β-actin is preferentially incorporated into dynamic lamellipodial networks[40], introduced hereafter.

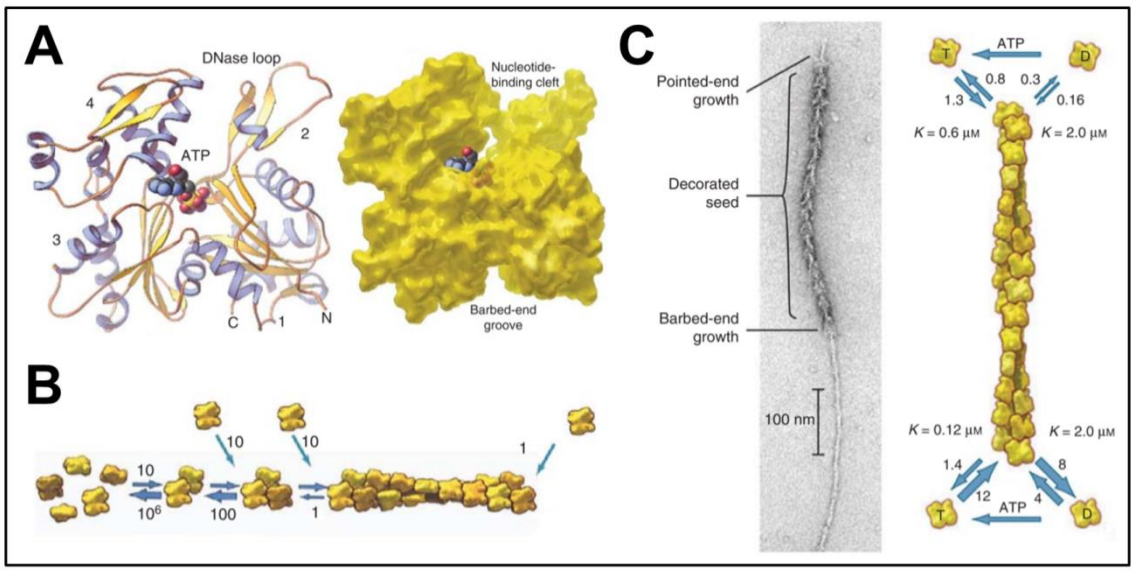

Figure 4 Actin biochemistry
(A) Structure of the actin subunit [PDB: 1ATN]. Ribbon diagram (left) and space-filling representation (right), each with ATP bound. N (amino terminus), C (carboxyl terminus), 1-4 label the four domains. The ribbon diagram shows the DNase-I binding loop, whereas the space-filled subunit shows both the nucleotide binding cleft and the barbed end groove. | **(B)** Nucleation rates from monomers, to dimers, trimers and polymers. | **(C)** Polarized actin filament elongation. The left-hand side shows an electron micrograph from a negatively stained actin filament decorated with Myosin head fragments, giving rise to a pointed end (top) and a barbed end (bottom). Elongation is clearly favored at the barbed end. The right-hand side shows the respective rate constants for elongation and disassembly at both ends. | Association rates in units of $\mu M^{-1}.sec^{-1}$; dissociation rates in units sec^{-1}. Modified from reference 31.

G-actin spontaneously forms polar filaments by polymerizing into a single-stranded, left-handed helix (Figure 4C). Growth is favored at the barbed end, a terminology dating back to the decoration of actin filaments with Myosin II subunits, yielding a pointed (-) and barbed (+) end[31] when observed by electron microscopy (Figure 4C). At physiological concentrations, the difference in elongation kinetics at both extremities leads to a filament that is growing at the barbed and shrinking at the pointed end (Figure 4C). A steady-state filament of given length is thus constantly changing its microscopic constituents, and this flow of subunits along the filament is called 'treadmilling'. The total cellular concentration of actin has been estimated to be on the order of 100 µM, with roughly 70% being filamentous[41].

Actin polymerization and different actin networks are controlled by multiple accessory proteins in cells (Figure 5). G-actin binding proteins, i.e. Thymosin-β-4 and profilin, control the available pool of free monomers[31] and differentially favor incorporation in either linear filaments or branched networks[42–44]. These two distinct morphologies, linear vs. branched, are generated by different proteins. Formins and other related proteins, e.g. Ena-VASP, bind to the barbed end and prevent capping of filaments, while still allowing elongation by addition of actin subunits. This 'leaky capping' leads to linear elongation of filaments[45], whereas the Arp2/3 complex, binds laterally to filaments and induces branching at 35 ° or 70 °, depending on the

mechanical load[46]. Arp2/3 is itself regulated by nucleation promoting factors, e.g. members of the WAVE complex[47].

Individual filaments can be assembled into higher order, parallel arrays by bundling proteins, e.g. fascin, leading to increased stiffness. Bundled actin filaments are found in a variety of cellular structures, e.g. membrane protrusions, stress fibers, and cell-cell junctions[48].

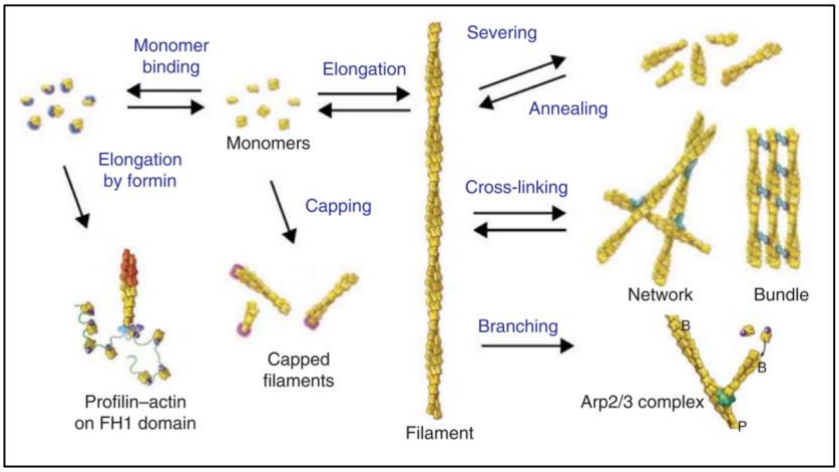

Figure 5 Actin modifications by actin-binding proteins.
Overview of different actin modifications that are mediated by actin-binding proteins in cells. Reference 31.

In order to maintain a dynamic equilibrium with free actin monomers, some proteins induce depolymerization of actin structures. These actin depolymerizing factors, e.g. cofilin and gelsolin, disassemble actin structures by severing and de-branching. The increased availability of barbed ends generates new nucleation points and maintains a stable pool of G-actin[49].

Over the last decades *in vitro* approaches have been instrumental to identify and functionally characterize the numerous regulatory interaction partners of the actin cytoskeleton and have led to a good understanding of its basic biochemistry and biophysical properties. In cells, all the described networks and regulatory proteins coexist in a tightly regulated ecosystem of interactions. It is noteworthy that a lot of the described actin dynamics happen in proximity of cell membranes, on the one hand because key regulators are specifically localized to membranes, e.g. the plasma membrane through interactions with $PI(4,5)P_2$, and on the other hand because signaling cascades lead to changes in actin dynamics in immediate vicinity to the plasma membrane (Figure 6).

2.2 Control of actin dynamics and network crosstalk.

Within cells all the described proteins regulating the dynamics of different actin networks coexist and require a system-wide control[50–52]. The control of these different

functional actin networks is achieved through Rho GTPases[53,54], e.g. Rho, Rac and Cdc42, which serve different functions yet share a common biochemical cycle of activation (Figure 6). Their recruitment to membranes in response to activation restricts their activity and induces actin dynamics generally close to membranes.

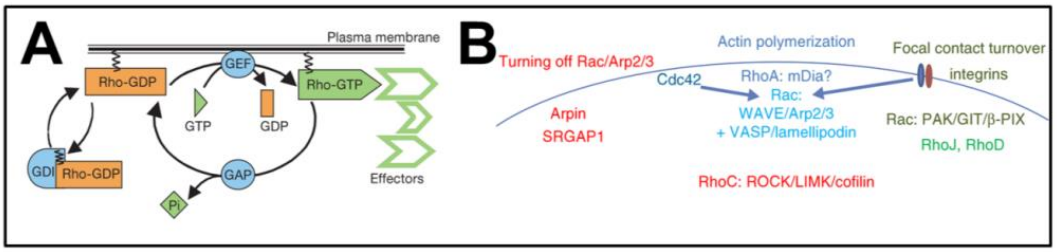

Figure 6 Control of actin dynamics by Rho GTPases.
(A) Schematic representation of the Rho GTPase cycle: Activation of Rho GTPases involves a nucleotide exchange (GDP → GTP) that is catalyzed by a guanine nucleotide exchange factor (GEF). GTPase-activating proteins (GAP) trigger hydrolysis of GTP, returning the GTPase to its inactive GDP-bound state. Membrane localization is controlled by a lipid anchor that can be masked by the guanine nucleotide exchange inhibitior (GDI). Reference 53 | **(B)** Overview of the different Rho GTPases (Cdc42, RhoA, Rac) that control cellular actin dynamics in the lamellipodium. Rac is involved in recruiting Arp2/3 and its activator WAVE to generated branched networks at the leading edge (center). Furthermore RhoA can drive actin polymerization through formin activation (mDia). Both Cdc42 and focal adhesion signaling control the activation of Rac, which is limited by negative feedbacks through Arpin (an Arp2/3 inhibitor) and SRGAP (a GAP for Rac). Towards the cell center, RhoC controls actin filament severing through LIMK/cofilin, and contractility through ROCK. Reference 54.

All of the different actin networks and their regulatory factor, together with signaling inputs create an intricate network of feedback loops which governs the balance between, e.g. branched and linear actin filaments, as shown in Figure 7[42–44].

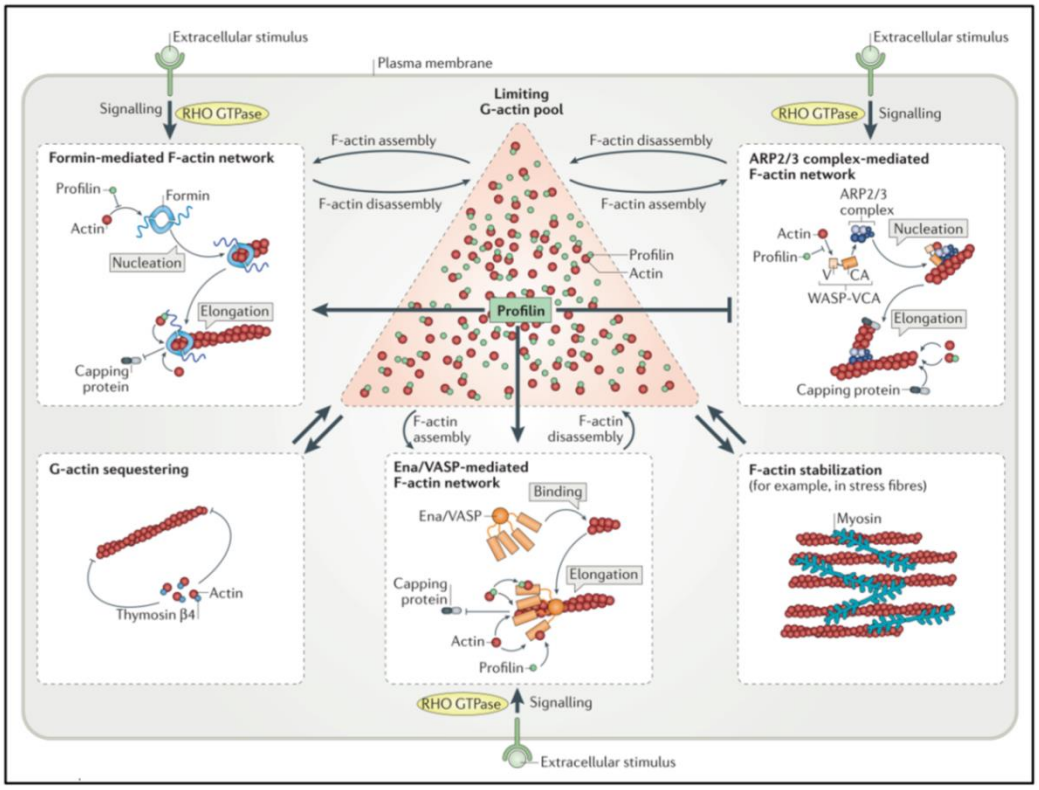

Figure 7 F-actin homeostasis through inter-network crosstalk.
F-actin networks are controlled by signaling and are dynamically interconnected by a limited pool of G-actin subunits. E.g., disassembly of stress fibers can drive polymerization of branched networks by increasing the available amount of G-actin. Reference 42

2.3 Actin structures at the ventral surface

The actin cytoskeleton shows a remarkable morphological and functional complexity in cells[55].

The ventral side of adherent cells is characterized by a complex actomyosin network with the presence of long bundles spanning multiple µm in length (Figure 8, Figure 9A). One can distinguish dorsal fibers, that originate at focal adhesions and are generated in a formin-dependent manner, and transverse arcs which originate from annealing of actomyosin bundles in the lamella and are not linked to focal adhesions. Both structures can become stress fibers when the respective free end(s) is/are bound to focal adhesions[56]. Ventral stress fibers can connect and bridge adhesion sites[57,58]. They have been shown to be distinct in composition from cortical and lamellipodial networks by preferential incorporation of different actin isoforms[59].

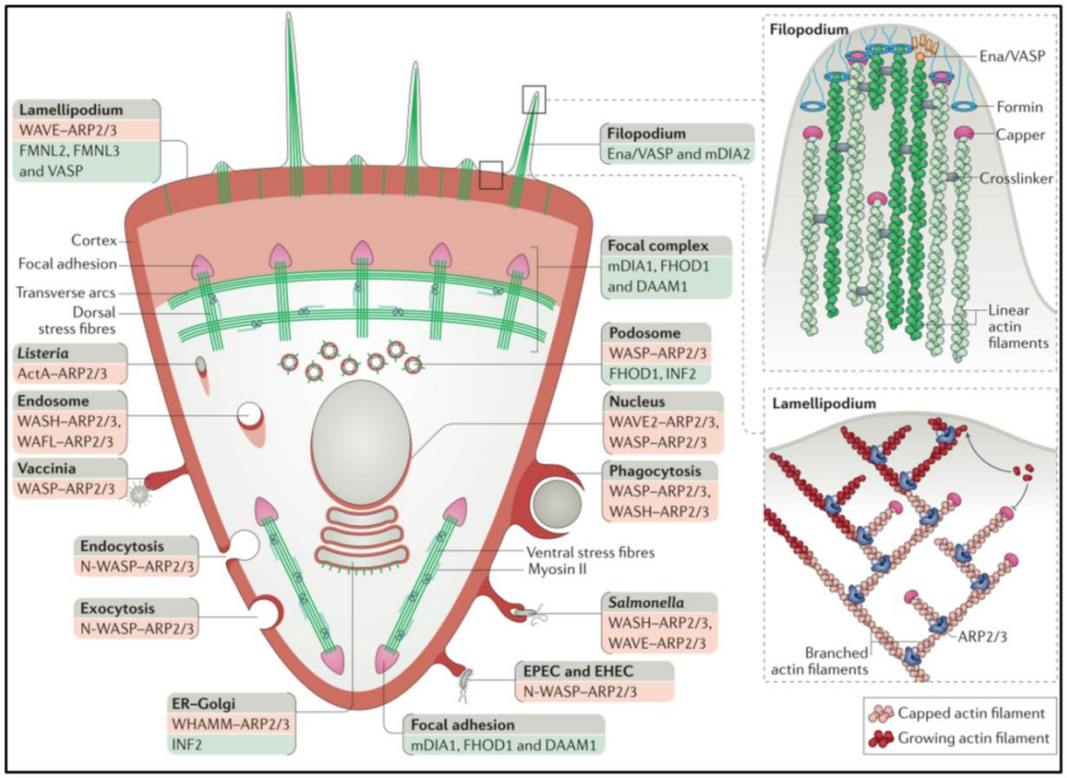

Figure 8 Cellular actin structures and their machineries.
Branched actin filaments (red) are generated from Arp2/3 and its regulatory interaction partners, e.g. WASP and WASH, at different locations in the cell. The leading edge of the cell is characterized by and broad actin network that decreases in density towards the cell center. Linear actin filament bundles (green) are found in thin membrane protrusions at the front, as well as in stress fibers. The stress fibers containing Myosin II link focal adhesions at the ventral surface yet are also found in the dorsal parts of the cell. The right-hand side shows the architecture of filopodia (top) and lamellipodia (bottom) in more detail. Reference 55

Adherent cells generate inward facing traction stresses on their substrate[60] which are predominantly localized to the cell periphery[61]. The generation of these stresses depends on Myosin II contractility[62] and limits cell spreading[61]. Roughly two-thirds of contractile stresses originate from Myosin II isoform A, whereas isoform B accounts for one third[61]. Efficient force transmission along the cell is necessary to achieve force balance on the cell scale and led to the concept of cytoskeletal coherence, which defines coherence as the ability of the highly dynamic actin network to establish force transmission that can span the entire cell body[63]. By using the spreading process of adherent cells as a model for coherence, in which isotropic spreading occurs with remarkable symmetry, Myosin II was shown to establish and maintain such cell wide coherence of the ventral cytoskeletal network in adherent cells[64].

2.4 Actin structures at the cell edge

2.4.1 Filopodia

At the cell edge, linear actin bundles can generate finger-like protrusions, e.g. filopodia and microvilli[65]. Filopodia are dynamic, finger-like protrusions (Figure 8, Figure 9B) that serve a variety of cellular functions, e.g. establishment of focal adhesion points during migration or sensing of the environment[66]. They consist of parallel actin filaments which are bundled by fascin, or related proteins, e.g. villin[65]. The origin of these parallel filaments remains debated as there is evidence supporting two main theories: The 'convergent elongation' model posits that actin filaments originating from Arp2/3 are bundled at the membrane and the elongation of that bundle, possibly through Ena-VASP, drives the formation of a filopodium[67]. The 'filament nucleation' model proposes the local, formin-based generation of new actin filaments at the nascent filopodial tip. It was notably based on the observation that filopodia form in absence of Arp2/3[68] and the involvement of formins in the generation of filopodia[69]. The motor proteins Myosin X is important for functional filopodia, probably due to its ability to control actin dynamics at the cell edge[70], and is involved in transport along the filopodial core towards the tip[71]. Finally the 'inversed Bin/amphiphysin/Rvs' (I-BAR) domain containing proteins IRSp53 and MIM drive filopodia formation[72]. A mechanism has been proposed, based on the ability of I-BAR domains to sense negative membrane curvature, which could in turn locally stabilize membrane deformations followed by recruitment of actin nucleators to the nascent protrusion[73].

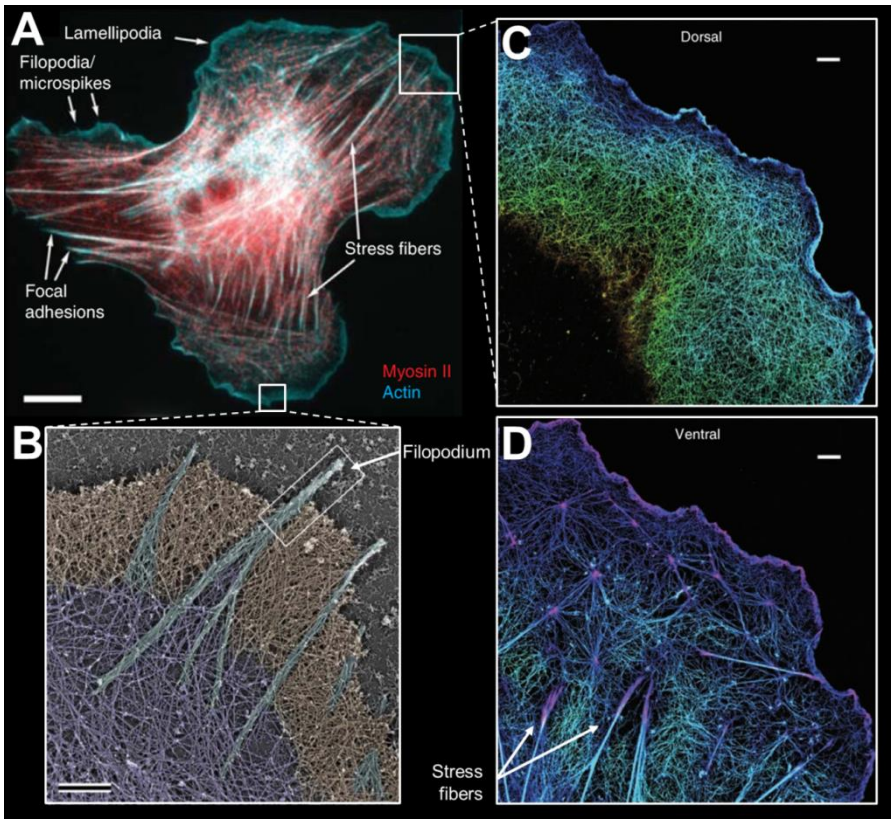

Figure 9 Actin structures at the leading edge
(A) Confocal fluorescen micrograph showing the presence of lamellipodia, filopodia, focal adhesions and ventral stress fibers in a cell. Myosin II is represented in red, Actin in turquoise. Modified from reference 62|**(B)** Electron micrograph showing the ultrastructure of actin at the leading edge in false colors, highlighting long bundled filaments (turquoise) that are rooted in an actin meshwork (lamella, violet) which is separated from the leading edge through a high-density mesh of actin (lamellipodium, orange). Modified from reference 77|**(C&D)** Super-resolved dorsal and ventral side of a lamellipodium through dual-objective STORM imaging. Whereas the dorsal side (C) shows a homogeneous mesh, the ventral side (D) shows prominent stress fibers. Modified from reference 79.

2.4.2 Lamellipodia

Cells migrating in 2D often have a thin plasma membrane sheet (Figure 8, Figure 9C&D), called lamellipodium, which is, after decade spanning debate[74–76], apparently characterized by a highly branched Arp2/3 driven network[77,78]. Super-resolution imaging has been able to resolve two separate functional layers of actin within the lamellipodium, one that closely resembles the ventral surface of cells, and another one which is more dorsal and more homogenous[79]. The lamellipodial actin network is characterized by cycles of extension and contraction[80] and is separated kinetically from an underlying, less dynamic yet more persistent 'lamella', as established by analysis of actin flow profiles[81]. The transition between these zones is characterized by assembly of actin arcs, which are created from retrograde actin originating in the lamellipodium by Myosin II driven bundling[82].

2.5 Cell migration

Much of our understanding considering how cells move is based on work performed on adhesive 2-dimensional substrates with keratocytes which are both stereotypic in shape and highly motile. In these cells, both cell shape and movement can be predicted at astonishingly high accuracy by taking into account only the interaction between dynamic actin growth towards the cell edge and deformation of the excess plasma membrane[83]. Plasma membrane-localized actin regulators, e.g. Ena-VASP, are important under these conditions, and their mislocalization leads to reduced motional persistence and altered leading edge shape[84]. Furthermore, Myosin II is important for symmetry breaking of actin to engage in motion[85] and drives the depolymerization of actin at the cell rear leading to a cell spanning actin flow[86]. In keratocyte-derived lamellipodial fragments, decreasing actin density towards the rear has been hypothesized to be sufficient by itself to reach a threshold mechanical sensitivity where membrane tension alone can induce network collapse at the rear, thus theoretically allowing for a motion that only involves actin dynamics and a membrane[87,88]. Retrograde flow is defined as the property of actin structures to move 'backwards' from the barbed end. Beyond the effect of the previously described tread milling that is inherent for actin, Myosin II can have an additional effect on this retrograde flow. Blocking Myosin II activity with Blebbistatin can decrease retrograde flow by around 50 % in neuronal growth cones and is responsible for severing of actin bundles in the lamella[89]. The retrograde flow is slowed down by counteracting Arp2/3 activity[90]. In line with these results, siRNA depletion of both Myosin II isoforms A & B in CHO cells leads to altered protrusion and retraction behavior of the lamellipodium, while each isoform has additional, specific effects[91]. In fibroblasts, only Myosin II A affects retrograde flow significantly[61].

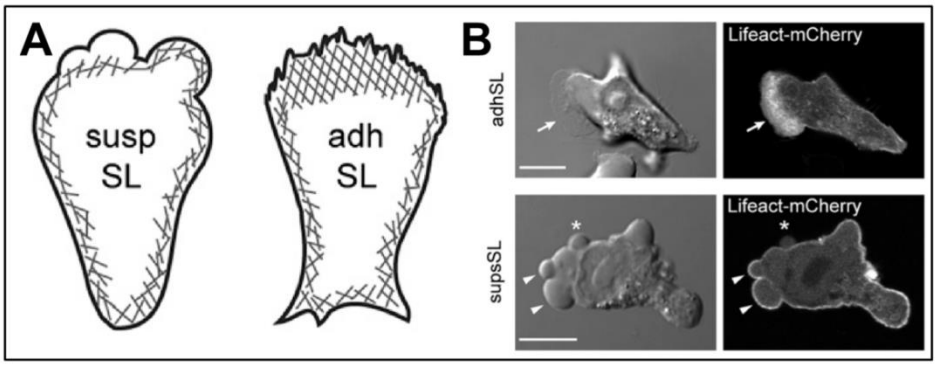

Figure 10 Amoeboid vs. lamellipodial motion
(A) Schematic depiction of the differences between amoeboid (left) and lamellipodial (right) motion. Amoeboid motion is characterized by generation of blebs at the leading edge of cells with a homogeneous cortex. Blebs are subsequently lined by a newly assembling cortex. Lamellipodial motion is characterized by a large actin dense structure at the leading edge, i.e. a lamellipodium. | **(B)** Representative images of cells migrating in lamellipodial (top) and amoeboid mode (bottom) derived from common precursor cells through adhesion-based selection (suspSL suspension subline; adhSL adhesion subline). The left-hand panel shows a DIC micrograph, the arrow highlights the lamellipodium, arrow heads indicate matured blebs, and the asterisk shows a nascent/young bleb. The right-hand panel show the respective fluorescence micrographs through staining with Lifeact-mCherry, in which one can clearly observe the lack of cortex in the newly assembling bleb, and the high density of actin in the lamellipodium. Reference 95

Yet, some cells can also move without extensive generation of traction forces on the underlying substrate through actin at the leading edge in an adhesion independent way. Such motion is generally referred to as 'amoeboid' (Figure 10), yet it is found in a variety of cells from vegetative *Dictyostelium discoideum*[92] cells to leukocytes[93], and in 3-dimensional environments. While the term amoeboid covers a variety of motion mechanisms, it generally critically depends on Myosin II contractility located at the back of the cell and creates blebbing at the cell front[94]. By changing the balance between actin polymerization and contractility, cells can switch between both types of motion in a dynamic way[95].

2.6 Actomyosin contractility

2.6.1 *In vitro*

In vitro assemblies of Myosin II and actin tend to self-organize, first by creating local foci of high Myosin II densities, followed by generation of an actin shells through coalescence of the foci[96] (Figure 11D). Myosin II activity depends on local actin geometry, notably the orientation of the polar actin filaments relative to each other, i.e. parallel vs antiparallel, where contractile efficiency scales with the relative abundance of antiparallel filaments[97]. The generation of contractility and its dominance over extension has been explained considering different geometries and dimensionalities by filament buckling (Figure 11 A-C) [98,99], high Young's moduli[96], or independently of these two phenomena, because random networks with contractile stresses have lower energy than those with expansive stresses[100]. *In vitro* experiments confirmed that Myosin II induces actin buckling, buckling-dependent severing, and describe an increased severing rate of phalloidin-stabilized F-actin due to local attachment to the membrane[101].

2.6.2 *In vivo*

In the cellular context, both extensile and contractile actomyosin filaments might be expected due to different filament polarities, yet predominantly contraction has been observed[102], corresponding to highly polarized inward-facing traction forces on the substrate (Figure 11E). Recent theoretical work suggests that nevertheless efficient extensile fibers might exist *in vivo*[103]. It has been suggested that formin-enriched nodes account for optimized contractile network properties *in vivo* because they could create high densities of anti-parallel branch encounters[104]. Indeed such actin asters concentrated around local nodes have been visualized at the ventral surface of cells using advanced imaging[79]. In order to create contractile stresses, Myosin II gets

activated by phosphorylation of its regulatory light chain in cells. This phosphorylation is catalyzed either by the myosin light chain kinase (MLCK), or downstream of Rho through Rho-associated kinase[105].

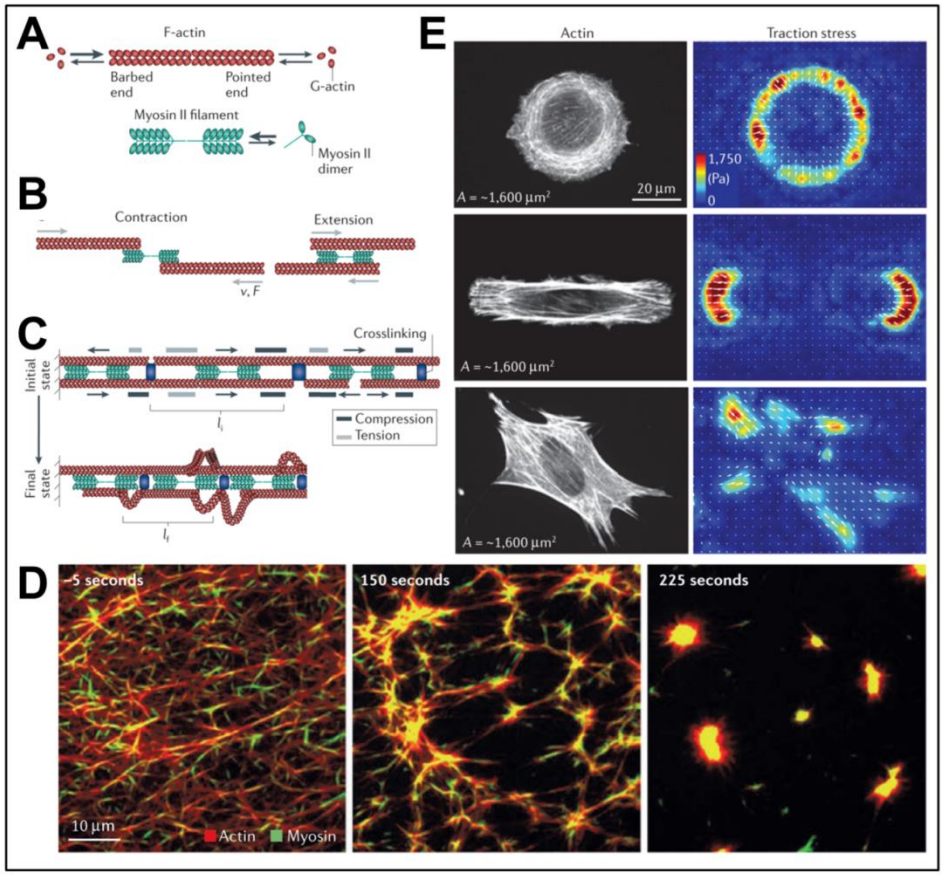

Figure 11 Actomyosin contractility.
(A) Schematic depiction of Myosin II and actin, the key players in actomyosin contractility. |**(B)** The basic outcome of Myosin II activity on actin can lead to both contraction or extension depending on the filament orientation (parallel vs. anti-parallel). |**(C)** Cross-linked actin bundles can lead to contraction by Myosin II assemblies through creation of tensile and contractile stresses on the filament, eventually leading to filament buckling. |**(D)** Reconstitution of actomyosin contractility *in vitro* by addition of Myosin II filaments to a pre-assembled, homogeneous actin network. |**(E)** Cells create highly polarized, inward facing traction forces that show symmetry over cellular length scales. Modified from reference 102

2.7 The cellular cortex governs cellular mechanics

Seminal work by Warren H. Lewis in 1939 proposed the presence of a superficial contractile 'plasmagel' layer, which would be under tension and play a fundamental role in cell movement and shape[106,107]. Actin was identified as the key protein in this functional layer[108,109], called the 'cortex'. Part of the cortex is the membrane skeleton, a composite of actin and accessory proteins that forms a corralling network at immediate apposition to the plasma membrane, only few nanometers apart[110]. It consists of a branched actin network and highly dynamic small actin filaments[111].

As the actin network is much stiffer than the plasma membrane[112], it is the cortex that defines cell shape[113] and confers a mechanical stability to cells towards external

stresses, e.g. osmotic pressure[114]. Tension within the cortex arises from the action of Myosin II and plays a major role in cellular processes such as cell division[115]. During cell division, the dynamics of the cortex and its thickness are controlled by α–actinin, an actin filament crosslinker. Successful cytokinesis requires the right balance between cortex stability and the possibility of disassembly[116]. Beyond generation of tension, Myosin II changes the network's viscoelastic properties[117]. After first approaches based on deformable plates[115], micropipette aspiration of cells, initially applied to study the mechanical properties of spectrin network in red blood cells[118] has been instrumental to quantitatively characterize the apparent viscosity and cortical tension in detail[119]. In endothelial cells, stiffness and viscoelasticity strongly depend on actin[120–123] (up to 50% reduction in stiffness upon Cytochalasin D treatment which blocks actin filament polymerization[124]). In line with these observations, AFM mapping and correlative fluorescence microscopy show correlation between elastic moduli and relative density of actin and intermediate filaments[125]. This has been corroborated by the effects of drug treatments specifically disturbing actin organization[126]. When measured in suspended fibroblasts to avoid the contribution of stress fibers and adhesions sites the cortex shear modulus is on the order of 200 Pa[127]. The importance of adhesion in determining the cellular mechanical properties is highlighted by comparison of identical cells in different conditions, showing that spread cells are stiffer than rounded cells[128].

Laser ablation experiments in *Caenorhabditis elegans* embryos have shown that the mechanical properties of the cortex are isotropic, yet significant anisotropies are created during development by cortical flows, that are driven by Myosin II contractility[129]. Recent evidence suggests that feedback regulation by Rho can explain how the creation of localized Myosin II foci does not lead to large scale aggregation of these foci and ensures efficient morphogenesis in the *Caenorhabditis elegans* embryo[130]. Along these lines but at much larger length scales, Myosin II distribution is sufficient to predict the flow profile of cells in the developing *Drosophila melanogaster* embryo[131].

3. Plasma membrane-actin linkers

Many receptors residing in the plasma membrane have cytosolic domains that directly or indirectly lead to attachment to this actin cortex, and both layers are in close proximity and mechanically interconnected[132]. Furthermore, specific peripheral proteins link the plasma membrane and the actin cytoskeleton (Figure 12). The importance of connections between the membrane and actin is highlighted by the fact that embryo cell shape changes during early development both in *Caenorhabditis elegans* and *Drosophila melanogaster* are not induced by *ad hoc* generation of

actomyosin contractility. Rather, pre-existing contractility is exploited during apical constriction, probably through increased linkage of the membrane to the underlying cortex[133].

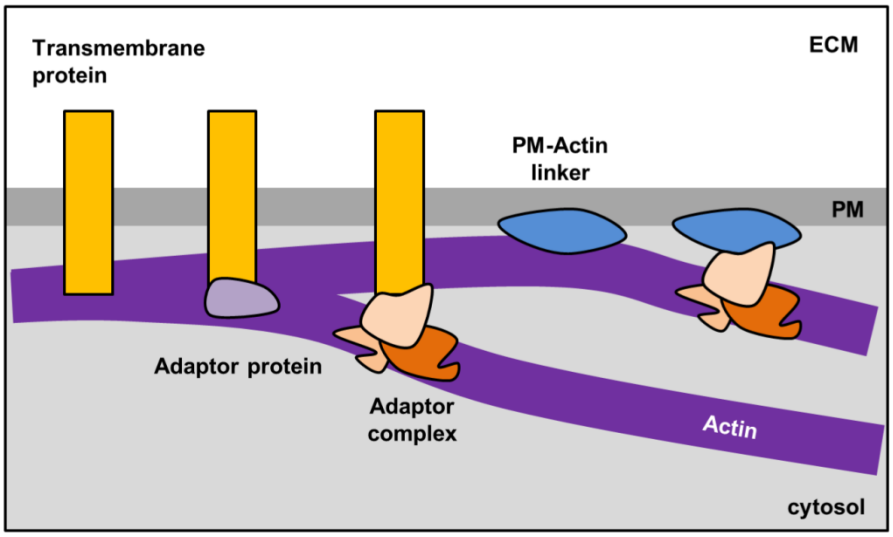

Figure 12 PM-actin linkers
Schematic depiciton of the fundamental ways that proteins couple the actin cortex to the plasma membrane. From left to right : Direct interaction between a transmembrane protein and actin, coupling via an adaptor / adaptor complex, direct binding of a peripheral protein to both actin and the plasma membrane, or via an adaptor complex. Adapted from reference 135

In general all these proteins share a domain architecture which enables them to bind both the plasma membrane and actin filaments[134,135]. Within this group one can emphasize three particular groups:

- BAR domain proteins sense membrane curvature through their peculiar shape and bridge actin dynamics to membranes with specific curvature.
- Class 1 myosins are monomeric motor proteins that act in conjunction with bound light chains, fulfil a wide range of cellular functions and, for certain subtypes, show sensitivity to external forces.
- Ezrin-Radixin-Moesin (ERM) proteins bridge the cortex and are involved in bleb behavior and the formation and maintenance of the immunological synapse.

Many of these proteins are recruited specifically via binding domains for $PI(4,5)P_2$ which is highly enriched at the plasma membrane[10], yet other ways of plasma membrane recruitment exist, e.g. via electrostatic interactions with phosphatidylserine. The importance of $PI(4,5)P_2$ for cortex integrity is illustrated by the effects of competitively masking $PI(4,5)P_2$ by overexpression of PH domains[136,137], or neomycin treatment[138]. Furthermore, the interaction with the plasma membrane can be mediated indirectly by, e.g. interaction between an actin binding protein and the cytosolic domain

of a trans-membrane receptor in response to biochemical cues, thus locally increasing connectivity to the underlying actin.

In this thesis we have focused on two of the above mentioned protein families: Class 1 Myosins and ERM.

3.1 Class 1 Myosins

Early work on the microvilli-covered surface of enterocytes identified proteinaceous cross-bridges connecting the plasma membrane to underlying actin structures[139,140]. Addition of a 110 kDa protein to actin bundles *in vitro* reconstituted the regular pattern of cross bridges along the actin core[141] and was the first vertebrate myosin 1 to be identified[142,143]. The Myosin 1 family consists of, to this date, 8 (subtypes a – h) single-headed, monomeric motor proteins that bind calmodulin or related calmodulin-like light chains[144]. All class 1 myosins comprise a motor domain at the N-terminus that is linked to a tail domain by a regulatory neck domain, which serves as a lever arm for force transmission[145] (Figure 13A). Class 1 myosins bind to negative membrane lipids and interact with actin in an ATP-dependent way[146–148]. Based on their tail structure, members of the myosin 1 family can be sub-grouped into short- and long-tailed myosin 1s[149]. The length of the tail domain correlates with their ATP turnover rates. Long-tailed isoforms, i.e. e and f, have short actin binding lifetimes, while short-tailed myosin 1, i.e. a-d, g, and h, have long actin-bound lifetimes[150].

While many class 1 myosins show cell-type specific expression profiles, both myosin 1b and myosin 1c are found in virtually all cells. The following introduction thus primarily focuses on these two myosin 1s.

3.1.1 Conserved motor and variable regulatory neck domain.

The motor domain of myosin 1 is highly conserved and shares structural homology with myosin II[151]. Its ATPase activity is regulated by calcium ions and binding of calmodulin to the regulatory neck[142,152–158]. Calmodulin binding is mediated by IQ domains, a common domain that shares a pattern in amino acid composition[159]. The identification of mammalian myosin 1b revealed the existence of splice isoforms that differ in the number of calmodulin-binding sites[160].

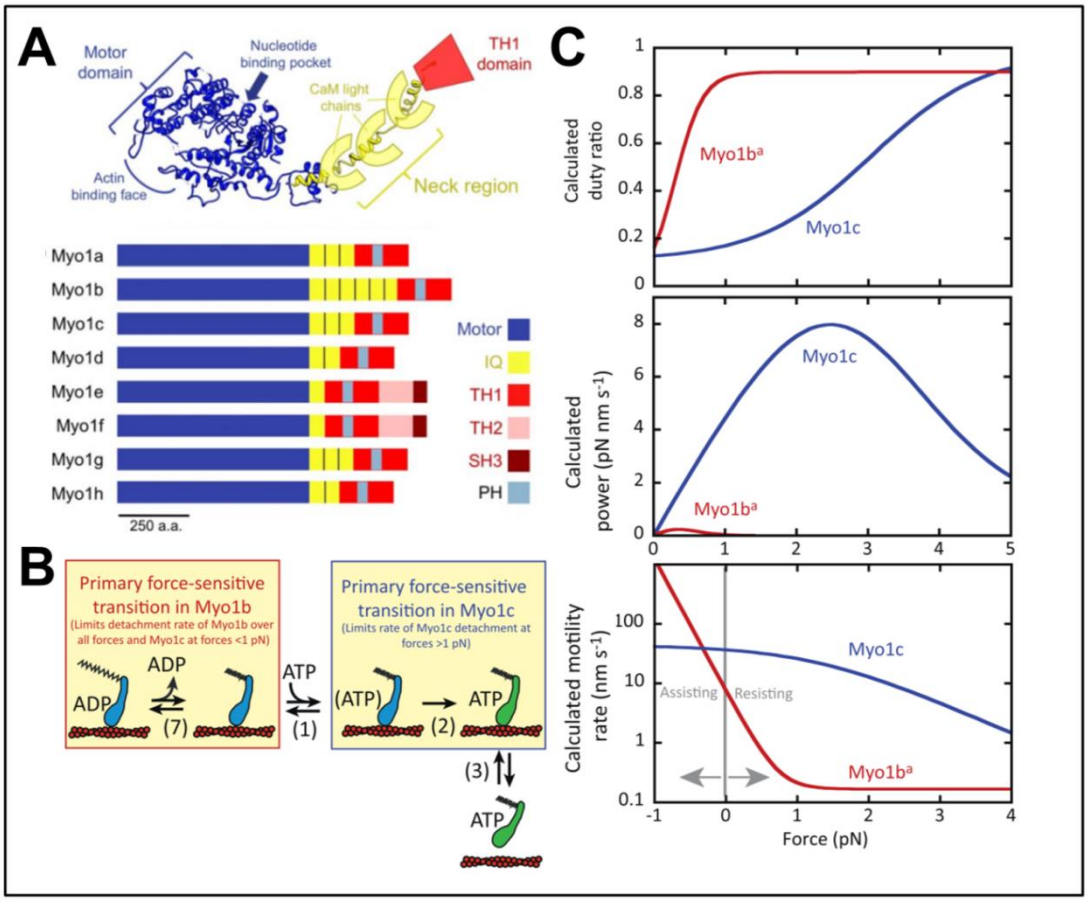

Figure 13 Class 1 myosins
(A) Domains of class 1 myosins, with the N-terminal motor domain (blue), the neck / lever arm bound to calmodulin light chains (yellow), and the C-terminal tail domain. The shown structure is not a crystal structure but a predicted Myosin 1a structure from homology inference. Reference 144 | **(B)** Schematic representation of the molecular origin of different force-sensitivities between myosin 1b and myosin 1c based on different rate-limiting steps during their ATPase cycle. | **(C)** Characterization of different sensitivities to force of myosin 1b and myosin 1c: Effect of force on the duty ratio (top), the generated power (middle), and the motility rate (bottom). Modified from reference 172

3.1.2 Catch-bond behavior of myosin 1.

Kinetic analysis of short-tailed myosin 1s showed that they have prolonged actin attachment times in comparison to other myosin classes. This suggested that they might be involved in tension maintenance and sensing[161,162]. The length of the lever arm and its large 30° rotation required for ADP release suggested force dependent behavior for myosin 1s. An opposing force to this large rotation could hinder the release of ADP, thus prolonging the actin bound state, as a function of lever arm length[163,164]. This was confirmed by single molecule studies *in vitro* showing that Myosin 1b detachment from actin decreased by almost two orders of magnitude when experiencing loads of around 2 pN[165] and that force sensing is controlled both by the lever arm length[166] and the binding of calcium to calmodulin[167] (Figure 14). Alternative splice isoforms of myosin 1b have different numbers of IQ motifs with different binding

affinities for calmodulin. Calmodulin binding stabilizes the lever arm and is important for the *in vitro* motility of myosin 1b[168].

A bond with prolonged lifetime with increasing force, up to a critical point, is called 'catch bond', in contrast to 'slip bonds' whose detachment increases with increasing force. Recent crystallographic evidence confirms the role of lever arm rotation in controlling the release of ADP and thus mechanistically explains myosin 1b's high sensitivity to external force[169]. Myosin 1c, although qualitatively similar, is less sensitive to calmodulin, calcium[170] and much less strain-sensitive[171,172] (Figure 13B&C). In comparison to unloaded conditions, Myosin 1b detaches 100 times slower from actin[165], whereas Myosin 1c only slows down by a factor of 5[171]. Myosin 1c's mechanism of tension sensing is different from Myosin 1b and depends on the isomerization upon binding of ATP[171], rather than ADP release (Figure 13B). This difference is partly controlled by the N-terminal region of Myosin 1c and Myosin 1b as evidenced by biochemical studies swapping domains[173] and crystallography[174]. Due to its catch bond behavior, Myosin 1b can form and elongate membrane tubes from GUVs along bundled actin i*n vitro*[4].

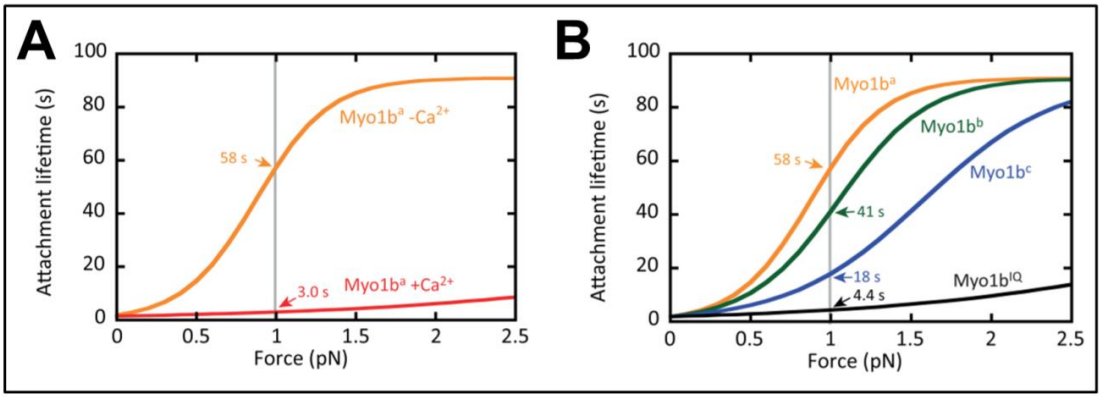

Figure 14 Regulation of myosin 1b's catch-bond.
(A) The negative effect of calcium on catch-bond behavior. Upon addition of calcium, the increase in actin attachment lifetime is lost. | **(B)** Catch-bond behavior is regulated by the length of the lever arm. Myosin 1b isoforms with different length due to alternative splicing in the IQ domains (^{a}: 6, ^{b}: 5, ^{c}: 4 IQ domains) show decreased attachment lifetimes with decreasing lever arm length. The IQ mutant which has only one IQ domain shows similar behavior as upon calcium treatment. Reference 172

3.1.3 Tail domains drive lipid interactions and govern function.

Myosin 1s share a 'tail-homology' domain, characterized by high density of positive charges[175,176], yet tail length varies between isoforms. Myosin 1b binds specifically to phosphoinositides, i.e. PI(4,5)P_2 and PI(3,4,5)P_3, through a non-canonical pleckstrin homology domain[177], while Myosin 1c preferentially binds to the PI(4,5)P_2 headgroup. Pleckstrin homology domains allow specific binding to phosphoinositides[178] via a β1-loop-β2 structure[179,180]. Myosin 1c binds phosphatidylserine only at un-physiologically high concentrations[181,182], yet Myosin 1e binds anionic phospholipids, including

phosphatidylserine, at physiological concentrations and in a pleckstrin homology independent way[183].

The binding strength between Myosin 1c and PI(4,5)P_2 is in the range of 6 to 16 pN and thus below the force required for lipid extraction that is around 27 pN at equivalent force loading rates[184,185].

3.1.4 Myosin 1's cellular functions converge towards actin.

When looking at the scientific literature involving myosin 1, it is striking to see an impressive plethora of different cellular functions that are affected by class 1 myosins. While little mechanistic insight exists so far, all the different observed phenotypes converge towards a role regarding the control/interaction with dynamic actin.

As mentioned above, we focus mainly on the ubiquitously expressed myosin 1b and myosin 1c. They should *a priori* be expected to have a more general function as they are found in virtually all cell types.

Myosin 1b

Myosin 1b concentrates to membranes ruffles at the leading edge of cells, yet it is excluded from stable actin bundles and stress fibers due to negative regulation by tropomyosin[186]. The recruitment towards actin-rich protrusions depends on its binding to PI(4,5)P_2[177]. Furthermore it is enriched in the mitotic cleavage furrow[187]. Myosin 1b regulates endosomal traffic and morphology[2], lysosome positioning[188], and is involved in trans-Golgi-network membrane remodeling through interaction with actin filaments[1]. Furthermore, it is found in the developing brain and required for axon formation, likely by changing the dynamics of actin waves and the actin network in the growth cone[5]. Myosin 1b also functions as an effector of EphB2 and controls the efficiency of cell repulsion and dynamic actin structures[3] after EphB2 activation. Myosin 1b is involved in secretory granule biogenesis[189] and together with myosin 1c in surfactant exocytosis[190]. Its deregulation has been implied in cancer progression[191,192]

Myosin 1c

Myosin 1c is found in membrane protrusions in B cells and recruited to the immunological synapse[193]. It can bind to G-actin and promotes G-actin accumulation and membrane ruffling at the leading edge of endothelial cells[194]. It is involved in the translocation of the glucose transporter GLUT4 to the plasma membrane downstream of insulin signaling[195].

Other short-tail class 1 myosins

In the brush border both myosin 1a and myosin 1d are expressed, yet they show distinct localization profiles, which seem to be governed by competitive binding along the actin core of the microvillus[196]. Myosin 1a regulates vesicle shedding at microvillar tips in isolated brush borders after ATP addition[197]. It furthermore affects the characteristic tether length upon elongation from microvilli and changes the propensity to form multiple tubes and their coalescence dynamics[7].

Myosin 1g is recruited to the plasma membrane of lymphocytes through its PH domain[198]. It controls meandering motility with higher average speeds and polarization dynamics[199]. CD44 surface levels and recycling depend on myosin 1g[200].

Finally, myosin 1d is found in the developing brain[201] and is involved in laterality determination[202].

Long-tail class 1 myosins

Myosin 1e is localized to the lamellipodial tip and affects actin dynamics and the formation of adhesions[203]. Myosin 1e is involved in *Xenopus laevis* cortical granule exocytosis, possibly controlling actin distribution around the coat[204,205]. Furthermore, via its SH3 domain, it interacts with synaptojanin-1 and dynamin and is involved in receptor endocytosis[206].

Myosin 1f regulates adhesion in neutrophils and slightly affects cortex thickness, i.e. KO cells are more adhesive and have a thinner cortex[207]. During the early steps of yeast endocytosis the long-tailed class 1 myosin Myo5 is localized at both the tip and base of buds with actin[208,209].

Reported mechanical effects of class 1 myosins

Several studies have identified effects of class 1 myosins on cellular mechanics, notably effective membrane tension and cell stiffness.

In prechordal plate progenitor cells from *Danio rerio*, myosin 1b depletion reduces effective membrane tension, increases blebbing propensity and respective bleb sizes[6]. Myosin 1c ensembles are able to generate pN forces parallel to lipid bilayers[210]. Myosin 1a influences effective membrane tension in enterocytes[7], and within this report the authors provide data that is represented in a way that suggests an effect on the coalescence behavior of multiple tubes for all myosin 1 subtypes[7]. Myosin 1g depletion leads to a decrease in cell elasticity in Jurkat cells[211], furthermore it is involved in B-lymphocyte stiffness[212] and regulates effective membrane tension in lymphocytes[199]. In a similar fashion, cortical tension in *Dictyostelium discoideum* is reduced upon

depletion of myosin 1, but only when depleting two isoforms at the same time, while single overexpression does lead to significant effects[213].

In conclusion, myosin 1b bridges the actin cortex to the plasma membrane and is a likely candidate to dynamically respond to force due to its catch bond property. In contrast to myosin 1c its biochemical properties suggest that it is best suited to serve as an anchor between the plasma membrane and actin. Its described cellular roles point to two main directions: On the one hand it might change the plasma membrane's mechanical properties, e.g. effective membrane tension. On the other hand many observations suggest an effect on actin dynamics.

3.2 Ezrin-Radixin-Moesin

In contrast to class 1 myosins, Ezrin-Radixin-Moesin (ERM) do not have a motor domain, yet they are also consistently involved in cellular processes that depend on actin dynamics and the linkage between the plasma membrane and actin, notably in the spatial organization of the immunological synapse, i.e. the interaction interface between a lymphocyte and a target or antigen presenting cell.

3.2.1 ERM link actin to the plasma membrane.

The ERM family[214] has initially been described in the context of epithelial membrane protrusions[215,216], controlling their morphogenesis during development[217–219] and in cell culture[220,221]. Based on a common ancestral protein[218,219], mammals have three genes encoding for Ezrin, Radixin, and Moesin respectively[214], sharing high sequence homology[222]. Ezrin knock-out mice show defects in gut develoment[217], yet Radixin and Moesin knock-outs show only minor developmental defects[223,224], without compensatory upregulation in the case of Moesin. Based on these observations, a general redundancy of these proteins with limited specificity, either by actual function or location, has been suggested in the literature[225].

The ERM family is characterized by a general architecture in three domains [222] (Figure 15A). Their C-terminus has an actin-binding domain[226], yet it is auto-inhibited by interaction with its own N-terminus[227–231]. Unmasking of the actin-binding domain depends on threonine phosphorylation at the C-terminus[232–234] and PI(4,5)P_2 binding[235] (Figure 15B). These two events act sequentially[236] and in synergy[237]. This sequential activation permits binding of the N-terminal FERM domain to PI(4,5)P_2 and binding of its C-terminus to actin.

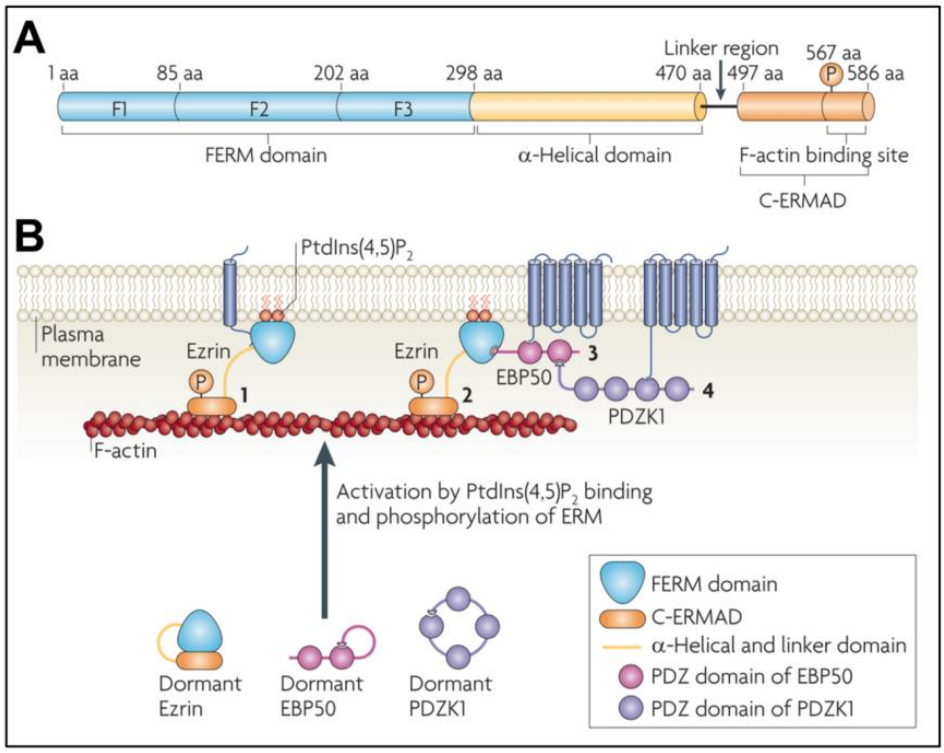

Figure 15 ERM structure & Ezrin activation
(A) Domains of ERM proteins: The N-terminal part contains a FERM domain that binds to phosphoinositides, and the C-terminus contains the actin binding site, connected via an α–helical domain. | **(B)** Ezrin is activated through sequential phosphorylation and unmasking of its binding domains. Ezrin has an autoinhibited conformation which masks both its binding sites for $PI(4,5)P_2$ and actin. Upon phosphorylation at its C-terminus and $PI(4,5)P_2$ binding Ezrin can efficiently couple actin to the plasma membrane and interact with other adaptor proteins, e.g. EBP50. Reference 225

3.2.2 ERM influence cellular mechanics.

Moesin has been implicated in the mechanical rigidity and organization of the cell cortex during mitosis[238–240], potentially by aligning the plasma membrane and actin filaments[239]. Furthermore, in the developing zebrafish mesendoderm, ezrin depletion reduces effective membrane tension and friction between the plasma membrane and the cortex, while increasing membrane bleb frequency[6]. In cultured mammalian cells, ezrin and moesin are found in stabilized blebs, and ezrin precedes actin cortex formation before bleb retraction[241]. In epithelial kidney cells, ezrin changes cell height and stiffness[242]. Phosphomimetic ezrin (T567E) increases effective membrane tension in lymphocytes and slows migratory speed[243].

3.2.3 ERM controls spatial organization of receptors.

Beyond their mechanical role at the cortex, ERM proteins have been implicated in cellular signaling[244]. ERM proteins interact with the polybasic cytoplasmic domain of CD44[245,246], CD43, ICAM-2, which has been proposed as a general mode of interaction between receptors and ERM proteins[247]. In subsequent studies, this interaction was linked to microvillar growth in response to epidermal growth factor stimulation[248]. Interaction of ERM with both actin and CD44 was shown to be required for Ras

activation downstream of hepatocyte growth factor, proposing an active role of actin in signal transduction[249].

In lymphocytes, ERM influence cell morphology[250], polarity establishment[251] and are phosphorylation targets[252]. Furthermore, they have been shown to be important in the establishment of the immunological synapse. Both Ezrin and Moesin were shown to co-localize with CD43 and drive its spatial segregation, i.e. the exclusion from the central zone of the immunological synapse between antigen presenting cells and T cells, and towards the distal pole[253–255]. Subsequent work described a functional link between early ERM dephosphorylation at the synapse site and increased deformability, supposedly driven by decreased actin membrane linkage, thus facilitation the synapse formation[256]. Direct comparison of Ezrin and Moesin in T cell activation, showed that both proteins have complementary functions with differences in cellular localization[257,258]. In B cells, a role of Ezrin has been established in tuning humoral activity, by means of changed B cell receptor diffusion and altered clustering behavior[259–261], as well as functional differences between Ezrin and Moesin, based on a non-conserved tyrosine residue relevant for JNK signaling[262]

On a side note, from an evolutionary perspective, ERM proteins are intriguing, as the FERM domain arose in conjunction with cadherin and receptor tyrosine kinases, thus suggesting a potential co-evolution between adhesion, signaling, and FERM domains[244].

3.3 Plasma membrane blebbing

While general membrane deformation is generally driven by actin-generated pushing forces, one notable exception is membrane blebbing. A bleb is defined as a plasma membrane protrusion that is detached from the underlying actin cortex and assumes a roughly spherical shape due to hydrostatic pressure (Figure 16). First descriptions of blebs can be found associated to osmotic shocks on fibroblasts[263]. While being a hallmark of apoptotic/necrotic processes[264], blebbing can occur under physiological conditions as well[265–268]. It can account for motion in the amoeboid mode, e.g. in *Dictyostelium discoideum*[269]. Bleb formation is driven by increases in cell contractility. It can be induced by injection of the catalytic subunit of MLCK[270]. It critically depends on cortex tension, and can be experimentally induced by laser ablation[271]. The importance of cortical integrity in the control of blebbing propensity is highlighted by observation of impaired cell movement and increased membrane blebbing in cells with disturbed cortices[272].

While lamellipodial protrusion based motion depends on Rac signaling, amoeboid motion is independent of Rac, yet depends on Rho/ROCK[273] and requires Ezrin[274]. In

line with these findings, Ezrin is recruited soon after bleb expansion ceases, and precedes the assembly of a new cortex within the bleb. The proposed importance of Ezrin in establishing a new cortex inside the bleb is to link the newly forming cortex to the membrane bleb. In agreement with this hypothesis, overexpression of the phosphomimetic EzrinT567D that couples actin to the plasma membrane independently of activation, accelerates bleb retraction, and dominant negative Ezrin T567A increases blebbing[241]. Different formins are implied in bleb generation, e.g. DIAPH3[275] and FHOD2, which does not itself induce blebbing, but exacerbates ROCK1-induced blebbing[276]. Dip, the **D**ia-**i**nteracting **p**rotein (sic), has been reported to control blebbing propensity by specifically inhibiting the mDia2 formin in cells, yet this phenotype depends on concomitant overexpression of activated Cdc42[277]. In line with the importance of amoeboid motion for cancer cell invasion, other formins, i.e. Dia1[278], FMNL2[279], have been shown to affect invasion efficiency, although the presence of blebs was not studied in detail.

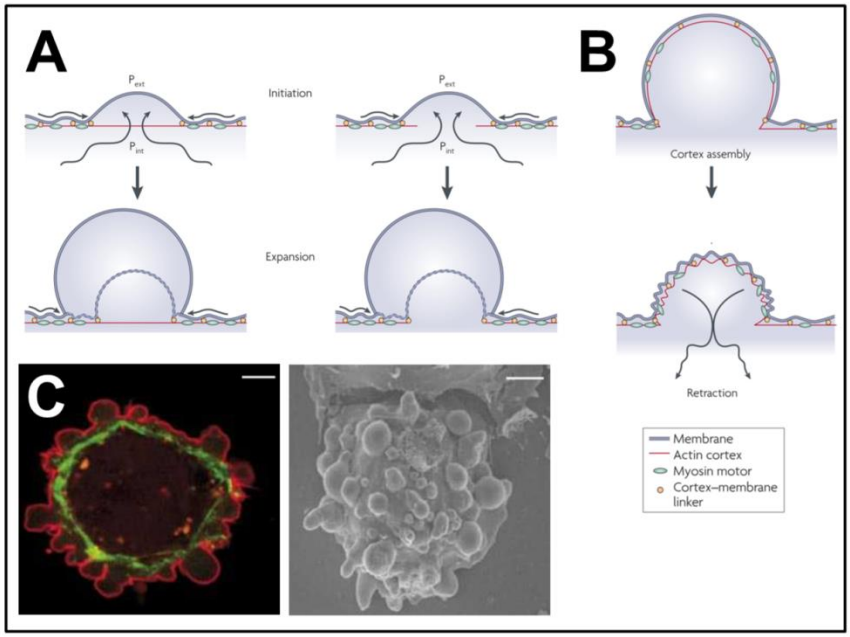

Figure 16 Bleb dynamics in cells.
(A) Hydrostatic generation of blebs can be triggered by either a loss in membrane-cortex attachment (left) or cortex disassembly (right) leading to bleb expansion. | **(B)** Assembly of a contractile cortex along the bleb surface allows the bleb to retract. | **(C)** Fluorescence end electron micrograph of blebs in a cell. Fluorescence signals : plasma membrane (red) and actin (green). Reference 267

Bleb dynamics have been studied and can be divided into roughly two phases. The initial expansion of a bleb on the scale of 30 seconds (Figure 16A) is followed by progressive retraction over the time scale of few minutes[280]. Initially devoid of an actin cortex, the bleb can be retracted by a newly formed actin cortex within the bleb[281] (Figure 16B). In agreement with the establishment of a new cortex, the retracting bleb is more rigid than the expanding one[280]. The fact that an initially free plasma

membrane is decorated with a functional cortex has established blebs as a model system to study the composition of the cell cortex using proteomic approaches, showing enrichment in actin and actin-regulating proteins, as well as plasma membrane-actin linkers[282]. The finding that both the formin mDia1 and the Arp2/3 complex contribute to cortical actin in M2 melanoma cells suggests the co-existence of two, probably interacting, actin networks which control blebbing propensity and dynamics[283].

4. Eph receptors

4.1 Introduction

The Eph receptors, overexpressed in an **e**rythropoietin-**p**roducing human **h**epatocellular carcinoma (hence its name), were first identified as a putative new class of receptor tyrosine kinase by inference from homologies with different growth factor receptors. They are overexpressed in a variety of cancers, i.e. colon carcinoma, lung adenocarcinoma; and mammary carcinoma[284]. For reasons of clarity, a coherent nomenclature has been agreed on: Ligands are named ephrins (**Eph** family **r**eceptor **in**teracting protein**s**), and receptors are named Eph receptors[285] (Figure 17A). Different screening methods led to identification of two subclasses, represented by Elk (EphB1) and Eck (EphA2) respectively, that show tissue-specific expression profiles[286,287]. EphB receptors are evolutionary conserved structures found in *Hydra* where they show opposing gradients along tissue boundaries[288].

The ephrins can be divided into two main subclasses, i.e. GPI-anchored proteins (ephrin-As), and transmembrane proteins (ephrin-Bs)[285] (Figure 17B). The different Eph receptors are separated into groups according to their relative affinity for these two ligand classes: Generally EphA receptors preferentially bind ephrin-As, and EphB receptors bind ephrin-Bs due to differences in their structure[289–292], yet there are notable exceptions to this, e.g. ephrin-A5 can bind to EphB2 receptors[293].

A first subclass of ephrins showed only weak activation of the receptor, i.e. large quantities of soluble ligand were needed to achieve efficient phosphorylation. This finding was explained by a potential requirement for membrane binding of the ligand via a GPI-anchor for full activation [294]. In line with this finding, efficient activation requires membrane-bound or artificially clustered ligands. The requirement of ligands to be pre-clustered or membrane-bound suggests that ligand dimerization and/or aggregation at a membrane is of critical importance for efficient stimulation of Eph receptors and thus establishes a role of Eph receptor signaling in cell-to-cell communication (Figure 17C). The different ligands were shown to be specific yet overlapping in their receptor binding behavior[295].

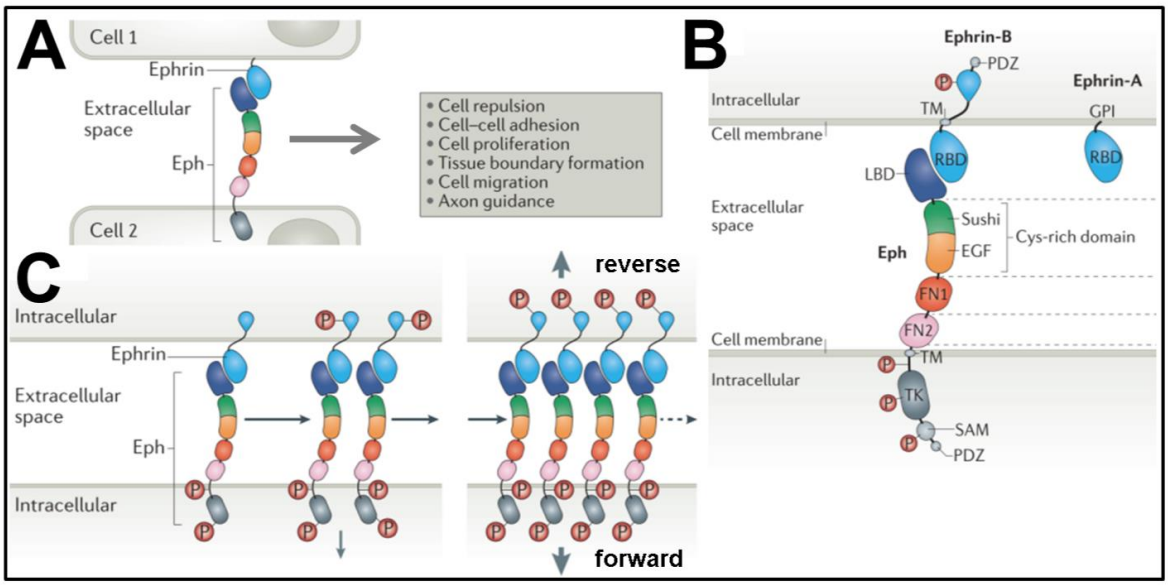

Figure 17 Eph-ephrin signaling
(A) Both Eph receptors and corresponding ephrins are associated to the cell membrane, drive cell-cell communication and are involved in a variety of cellular properties. | **(B)** Domain architecture of Eph and ephrins. Both Ephs and ephrin-Bs can be directly phosphorylated and recruit accessory proteins, whereas the GPI-linked ephrin-As do not have an intracellular domain that can itself serve as a hub for proteins. | **(C)** Clustering. Upon ligand-binding, the receptor-ligand complexes get phosphorylated and clustering leads to signal amplification. Both Eph receptors and their ephrin ligands engage in signaling, i.e. Eph-ephrin interaction can drive bidirectional signaling. Modified from reference 316.

4.2 Bidirectional signaling in the Eph/ephrin system

The ligand itself is phosphorylated in response to Eph receptor binding, and can act as a signaling molecule itself, thus Eph receptor and ligand contact can induce bidirectional signaling [296–299] (Figure 18A). By convention, signaling that happens downstream of the Eph receptor is called 'forward signaling', while signaling downstream of ephrins is called 'reverse signalling'[300].

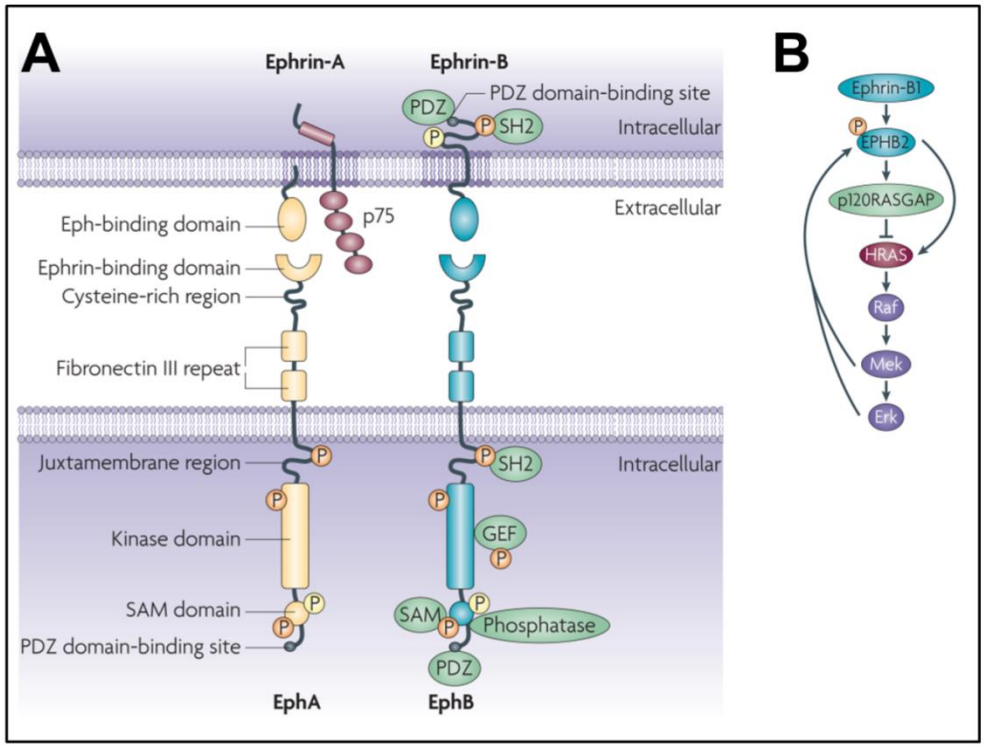

Figure 18 Eph/ephrin as a signaling hub
(A) Phosphorylation of intracellular residues (serine/threonine yellow, tyrosine orange) can recruit proteins through, e.g. SAM, PDZ, and SH2 domains. Domain names are depicted on EphA and recruitment is shown on EphB for reasons of readability, but apply to both subtypes. Whereas ephrin-B can recruit accessory proteins to its intracellular domain, ephrin-A needs interaction partners to bridge the plasma membrane, e.g. the nerve growth factor receptor p75 in neurons.|**(B)** Schematic representation of the EphB2 signaling cascade after stimulation with ephrin-B1. Reference 299

4.3 Eph receptors can discriminate ligand quantities.

As most detail is known about the B subclass of receptors, and we have worked on the functional interaction between Myosin 1b and EphB2, the following paragraphs are mainly focusing on the EphB receptor subtype.

Evidence from crystal structures indicates that clustering of receptors is indeed an inherent property, driven by initial hetero-dimerization between ligand and receptor (EphB2 and ephrin-B2), with subsequent formation of tetramers and higher-order structures, in which each ligand can be bound by two receptors[301]. Cellular response to stimulation with ephrin-B1 is sensitive to differences in ligand oligomerization state[302,303] and density[304]. Notably, phospho-tyrosine phosphatase is recruited only upon stimulation with multimeric/tetrameric ligands, but not with dimers[302]. Comparative studies have shown that accordingly only clustered ephrin-B1 induces growth cone collapse. In inversed signaling conditions, i.e. EphB2 being the ligand for ephrin-B, only unclustered EphB2 led to similar phenotypes[305].

The recruitment of receptors into an existing cluster, i.e. condensation or cluster propagation, does not depend on direct ligand binding, i.e. 'free' receptors can be recruited into an existing cluster without the need to interact with a ligand themselves[306]. Interaction sites that allow these homotypic receptor interactions have been identified by crystallography[307,308]. Furthermore, different receptors tend to form clusters of different sizes[309]. Artificial clustering of EphB2 shows that receptor dimers are weakly phosphorylated, yet trimers and higher order oligomers show comparably high phosphorylation levels. This led to a proposed critical threshold of receptor trimers required for efficient activation, in which the relative amount of multimers determines signaling output[310]. Analysis of EphB2 cluster size distributions after stimulation with immobile, nano-clustered ephrin-B1[311] for 60 minutes revealed a switch from a trimer dominated population, to a broad distribution with 28-mers as average clusters. Kinase-deficient receptor strikingly only assembled into a well-peaked distribution around 12-mers. This cluster distribution was changed fundamentally when stimulating with soluble, pre-clustered ligands, yielding a switch from heptamers

(unstimulated) towards 11-mers and 22-mers, for the case of kinase-deficient and wildtype EphB2 respectively[312].

4.4 Trafficking and phosphatase activity control the effective receptor surface concentration

Just like other receptor tyrosine kinases, Eph receptors can phosphorylate each other at a low basal level without ligand binding. It has been shown for EphA that such receptors are recycled through vesicular trafficking, dephosphorylated in the perinuclear region by the phosphatase PTP1B, and then recycled to the plasma membrane. This cycle was suggested to maintain a ligand-sensitive pool at the plasma membrane. Ubiquitination of EphA after ligand binding switches the transport towards the lysosome[313]. In the case of EphA3, dephosphorylation by PTP1B can happen directly at the membrane[314]. In a similar way, negative regulation of the epidermal growth factor receptor (EGFR) membrane recycling by Eph has been described, which modulates EGFR signaling outcome[315].

4.5 Tissue patterning and homeostasis

Different Eph receptors are involved in patterning and maintenance of homeostasis in a variety of tissues[316]. During development, Eph-signaling is involved in embryonic tissue separation[317,318]. EphB2 and EphB3 in conjunction with their ligand ephrin-B1 maintain separation of stem cells from differentiated cell types in the colon by directing cell migration[319,320], and controlling proliferation rates[320–322] (Figure 19). In agreement with these findings they can act as tumor supressors[323,324] and potential therapeutic target[320,325,326]. In contrast, ephrin-B2 activation of EphB3 and EphB4 abolishes contact inhibition of locomotion in prostate cancer cells[327]

Retinal development depends on multiple Eph receptors[328]. Experiments in the mouse retina evidenced the generation of gradients for different receptors[329–331]. Yet, even at uniform distribution prior to any gradient generation, axon pathfinding is impaired, independently of EphB2's kinase activity[332] Opposing gradients could be observed for corresponding ligands, and subclasses A and B distributed separately along perpendicular axes. This suggested that Eph receptors and their ligands could specify tissue organization and guide cell fate decisions along gradients[333]. Taken together, these results suggest that the Eph system can not only drive cellular behavior along gradients, but can establish these gradients *de novo* from homogeneous cell populations. During wound healing ephrin-B1 allows for re-epithelialization by reducing cortical tension and cell-cell adhesion[334]

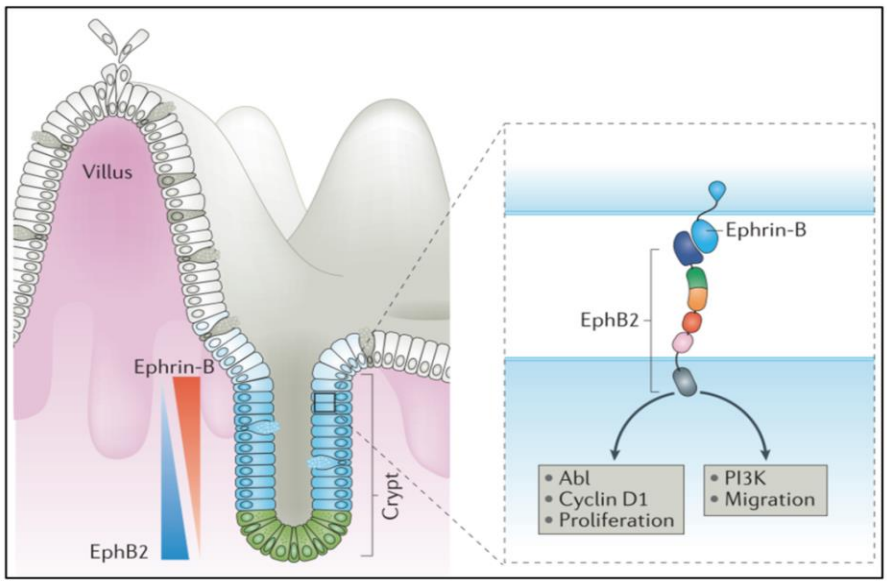

Figure 19 Cell sorting by EphB2/ephrin-B in intestinal crypts.
EphB2/ephrin-B signalling maintains the stem cell niche at the bottom of intestinal crypts. Stem cells (green) are maintained in the crypt through a repulsive opposing gradient between EphB2 (stem cells) and ephrin-B (differentiated cells that move out of the crypt). The right inset shows the dual function of this gradient, controlling both proliferation and migration. Reference 316

4.6 Functional divergence in the Eph family

Eph receptor activation by identical ligands can induce different reactions depending on cell types and expressed receptors[309], e.g. influencing adhesion[335] and cortical actin[336]. It is important during synapse formation and maintenance as it controls filopodial motility during synapse formation[337], and depletion of EphB2 results in reduced synaptic plasticity in mouse models[338]. Dendritic filopodia formation is induced by EphB2 independently of Rac and Cdc42[339].

By exploiting different splice isoforms, repulsive signals by Eph–ephrin interaction can be shifted to adhesion, notably through the loss/removal of Eph's kinase domain[340]. Similarly, synaptogenesis and synaptic plasticity do strongly depend on EphB2, yet are independent of its kinase activity[341,342]

Activation of Eph receptors can induce repulsive signals, inducing neuronal growth cone collapse and axon guidance both *in vitro*[343,344] and *in vivo*[342,344], and positioning of cells in the brain[345]. Similarly, reverse signaling through ephrin-B1 is involved in axon guidance in mice[346]. *In vivo* it is required for patterning of the somite[347,348] and the skeleton[349]. It induces cell sorting in zebrafish embryos[350], after bidirectional signaling[351]. In the developing brain cell segregation is independent of reverse signaling[336]. Modeling and experiments suggest that heterotypic repulsion is necessary and sufficient to achieve cell segregation and border sharpening[352,353], even independently of EphB2 kinase activity[353]. The establishment of tissue boundaries

involves supra-cellular, long-range force generation and leads to propagation of mechanical waves, independently of specific signals[354].

4.7 Switching from strong adhesion to repulsion.

Cell repulsion mediated by Eph/ephrin follows the fundamental stages of contact inhibition of locomotion[355] (Figure 20). In cell culture contact between two cells expressing the ligand and receptor respectively, increases membrane ruffling and an increase in tyrosine phosphorylation at the interface is followed by cellular retraction. Separation of engaged receptor – ligand complexes is achieved through full length clathrin-mediated[356] trans-endocytosis of either receptor or ligand in the case of the B subclass. The directionality of this endocytic activity depends on the cell type[357–359]. Receptor clusters can preferentially localize to filopodia[358], and increase actin dynamics by activating Rac[357,359]. In subclass A, metalloproteases, e.g. ADAM10, cleave the ligand in trans conformation (i.e. the metalloprotease is located on the outer leaflet of the receptor expressing cell and cleaves the ligand)[360,361]. Metalloprotease-based cleavage of EphB2 in response to stimulation with ephrin-B2 has also been reported[362]. ADAM10 has furthermore been involved in cleavage of E-cadherin thus further facilitating separation of cell-cell contacts downstream of EphB activation[363].

4.8 Eph signaling drives actin dynamics.

Activation of Eph receptors feeds into Rac and RhoA signaling[317] (Figure 18B). Thereby, stimulation induces cytoskeletal rearrangements that lead to cell retraction, characterized by reversible lamellipodial collapse dependent on Cdc42[303] and Myosin II contractility. Optogenetic activation has allowed the local activation under controlled conditions. In cell culture, stimulation of EphB2 induces cell rounding and de-adhesion[339]. The deadhesion can be explained by altered FAK signaling[364,365]. Ligand-bound EphA receptors experience radial flow originating from actomyosin contractility, and tend to be assembled into large scale aggregates if not hindered by mechanical resistance[366–368]. CD44 was shown to be excluded from EphA clusters[366]. In order to allow re-spreading after stimulation-induced deadhesion, the internalization of receptor-ligand complexes is important, probably because engaged signaling hubs need to be deactivated as described before[369].

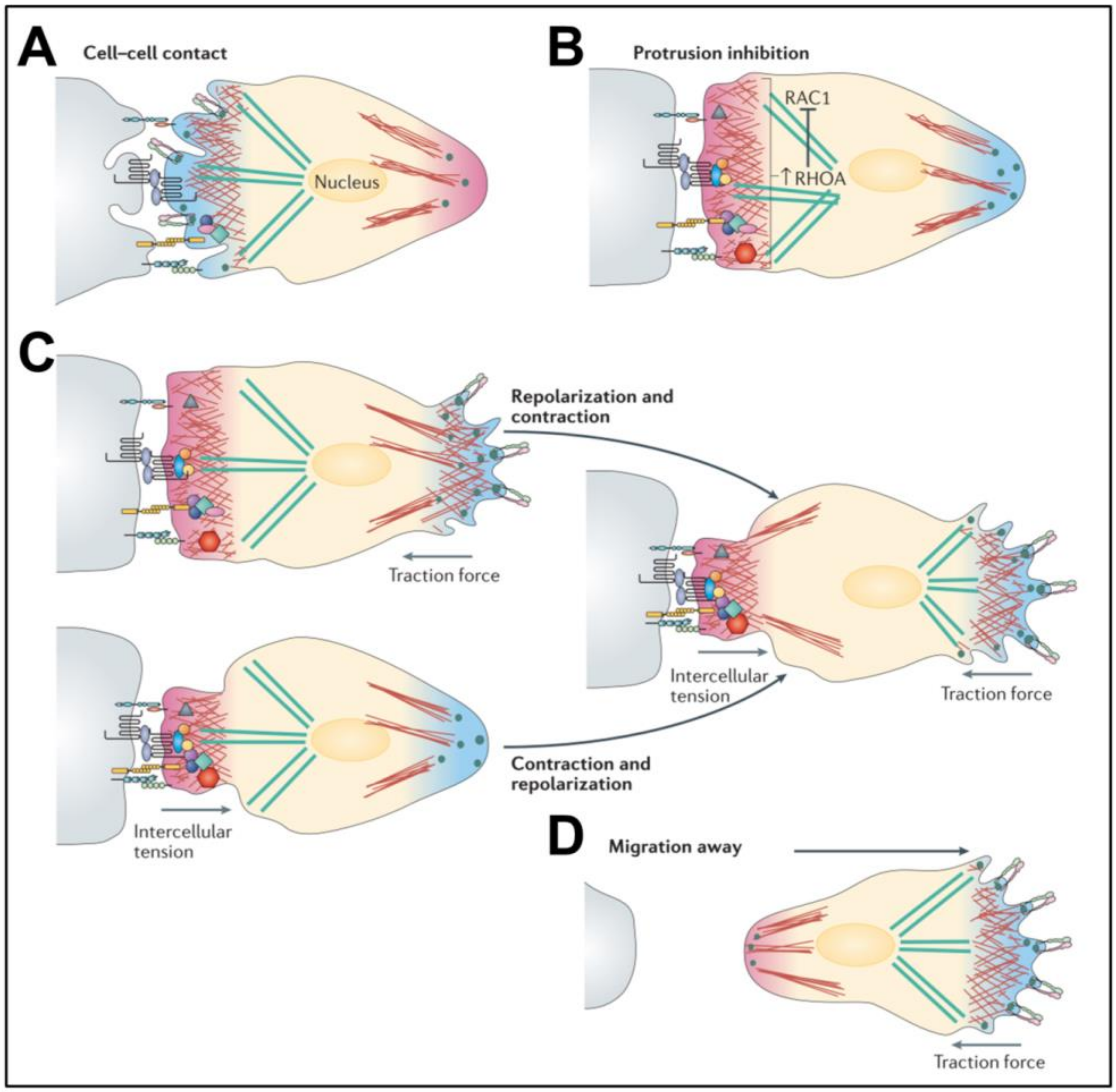

Figure 20 Cell repulsion through contact inhibition of locomotion.
(A) Cellular contact at the leading edge activates receptors that elicit a CIL response. | **(B)** In a first step, protrusion formation is inhibited at the leading edge through changes in Rho GTPase activity, i.e. activation of RhoA and inhibition of Rac. | **(C)** This initial phase is followed by the sequential steps of contraction and repolarization, which can happen in different order depending on the cell type and involved receptors. | **(D)** The inversion of cell polarity and detachment of the cell-cell contact leads to migration away from the contact site. Reference 355

Materials & Methods

1. Cell culture

HEK 293T

As previously described[3], stably YFP-EphB2 expressing HEK293T cells were cultured at 37 °C and 5% CO_2 in DMEM GlutaMAX medium (gibco 61965-026), supplemented with 10% fetal bovine serum (gibco 10270106, heat-inactivated at 56°C for 30 minutes) and 0.7mg/mL Geneticin (gibco 10131-019) (full medium).

NIH 3T3

NIH 3T3 cells were cultured at 37 °C and 5% CO_2 in DMEM GlutaMAX medium (gibco 61965-026), supplemented with 10% Fetal Bovine Serum (gibco 10270106, heat-inactivated at 56 °C for 30 minutes) and 1% Penicillin Streptomycin (gibco 15070063).

2. Transfection

Plasmids

Part A

Transfection of cells with protein-encoding plasmids was performed using Lipofectamine™ 2000 (Invitrogen 11668-019). 250000 cells per well were seeded in a 6 well plate (TPP 92006) 24 hours prior transfection with 0.5 µg (for mCherry and mCherry-CAAX) or 1 µg of DNA per well. The transfection mix was prepared as follows: 5 µL of Lipofectamine™ 2000 and the respective amount of DNA were added to 250 µL of OptiMEM (gibco 31985-062) each in a separate 2 mL microtube (Sarstedt 72.695.500). After 5 minutes of incubation at room temperature, both solutions were mixed by pipetting up and down several times and incubated at room temperature for 15 minutes. The resulting 500 µL of transfection mix was added to the corresponding well, containing 1.5 mL freshly added, pre-warmed full medium. The medium was exchanged for full medium 6-8 hours after transfection and cells for assessed after ~24 hours of transfection.

Part B

Transfection of cells with protein-encoding plasmids was performed using FuGene®6 (Promega E2691). 250000 cells per well were seeded in a 6 well plate (TPP 92006) 24 hours prior transfection with 1 µg of DNA per well. The transfection mix was prepared as follows: 3 µL of FuGENE®6 was added to 100 µL of OptiMEM (gibco 31985-062) medium in a 2 mL microtube (Sarstedt 72.695.500). After 5 minutes of incubation at room temperature, DNA was added and mixed by carefully pipetting up and down and incubated at room temperature for 15 minutes. The resulting ~100 µL of transfection mix were added to the corresponding well, containing 1.5 mL freshly added, pre-warmed full medium.

siRNA

Cells were transfected with siRNA using Lipofectamine™ RNAiMAX (Invitrogen 13778-030). The transfection mix was prepared as follows: 5 µL of Lipofectamine™ RNAiMAX and the respective amount of siRNA were added to 250 µL of OptiMEM (gibco 31985-062) each in a separate 2 mL microtube (Sarstedt 72.695.500). After 5 minutes of incubation at room temperature, both solutions were united and mixed by pipetting up and down several times and left to incubate at room temperature for 30 minutes. The resulting 500 µL of transfection mix was added to the corresponding well, containing 1.5 mL freshly added, pre-warmed full medium.

For depletion of Myo1b and the respective control, 125000 cells were seeded per well in a 6 well plate (TPP 92006) 24 hours prior transfection. A final concentration of 15 nM siRNA was used. Cells were assessed ~48 hours after transfection. For depletion of Ezrin, ERM, and respective controls, 80000 cells were seeded out 24h prior treatment and transfected twice, the secondary transfection following 48 hours after the first. Cells were assessed after a total of ~96 hours. The respective concentrations of siRNA were 20 nM for Ezrin, and 10 nM for each siRNA of Ezrin, Radixin, and Moesin, thus yielding a total of 30 nM for ERM depletion.

3. Drug treatments

Part A

LatrunculinA (LatA) (Sigma L5163) was used at 100 nM for 20 minutes, and S-nitro-Blebbistatin (BS) (Cayman Chemical 13891) at 20 µM for 15 minutes at 37 °C before the respective measurements. In both cases, DMSO concentration within the cell medium was at 0.1%, as in the corresponding DMSO control.

Part B

In the FRAP experiments, all drugs were used at a final dilution of 1:1000 (corresponding to 0.1 vol. % DMSO), with the following concentrations and treatment times at 37 °C:

LatA	100 nM	10 minutes
CK-666	50 µM	15 minutes
SMIFH2	25 µM	15 minutes

Penta-chloro-pseudilin (PClP) treatment for TIRF-SIM datasets was done at 1 µM for 30 minutes before imaging and stimulation.

4. Optical Tweezer

The custom-built optical tweezer (OT) set-up consisted of a 1064 nm Ytterbium fiber laser (IPG Photonics) and a Nikon C1 Plus confocal microscope. We employed a Nikon CFI Plan Fluor 100x, NA 1.3 oil immersion objective which was surrounded by a resistive collar to allow heating of the objective to maintain a stable temperature of 37°C within the experimental chamber. The sample chamber was fixed on a voltage-controlled piezo-drive (MadCityLabs Nano-LP100). Bright field images of the bead were acquired using an EM-CCD camera at a frame rate of ~ 180 frames per second (iXon DU-897, Andor), and analyzed by a custom MATLAB script. Forces were calculated from bead positions following the equation $= k(x - x_0)$, where k is the trap stiffness, x the position of the bead, and x_0 the reference position at equilibrium. Trap stiffness calibration was obtained using the viscous drag method, including Faxen's correction for calibration close to surfaces [370], with a trap stiffness adjusted to 44 pN/µm at 3W input power (400mW at the back focal plane of the objective).

Experimental chamber

Cells were grown on 25 mm circular glass cover slips (VWR ECN 631-1584) prepared in the following way: 1) Cleaning with Isopropanol, Ethanol, water, Ethanol and then dried under a cell culture hood. 2) Coating with a 20 µg/mL solution of Laminin (Sigma L2020) for ~2 hours at 37 °C. Cells were analyzed 16-20 hours after seeding out 250000 cells per glass coverslip. The medium was exchanged for CO_2 independent DMEM medium (gibco 21063-029), supplemented with 1.5 mg/mL β-Casein (Sigma C6905) to passivate the surface (experiment medium), 1 hour before a measurement. The glass cover slips were fixed on a custom-made experimental chamber using vacuum grease (Sigma Z273554). The cells were maintained in experimental medium throughout the experiment supplemented with carboxylated polystyrene beads (Spherotech CP-30-10, 3.07 µm nominal diameter, 0.001 % suspension) used for tether

pulling. The temperature was maintained at ~37 °C throughout the experiment using a custom-built objective-heater based on a resistive collar.

Bead tracking

Image sequences of the bead were used to track its position over time using a simple MATLAB script, by fitting a circle to the bead. See Annex for the used code.

5. Tube pulling from cells

Using a custom LabVIEW program to control the piezo stage, tubes were pulled, by trapping an isolated floating bead, bringing it into contact with the cell for a short period (~3 seconds), and then moving the cell away from the trap center in x direction using the piezo. For measuring the static tether force, the tube was about 10 µm long and held steady for at least 10 seconds. For the dynamical force measurements, the initial tether had a length of about 10 µm. While the initial force overshoot for tether formation varied widely, a relaxation of the force to a stable plateau could generally be observed within the first 10 seconds after tube formation.

Tether step elongations

Once the tether holding force was stabilized, step elongation of the tube was performed by imposing a step-displacement of the piezo stage away from the trap center of 5 µm at a speed of 75 µm/s. The force relaxation was then recorded.

The change in force is monitored by imaging the bead holding the tube at high temporal resolution (175 fps). This allows following the peak in force upon step elongation and the subsequent relaxation.

Exclusion of data sets for tube elongation

Tube elongations, in which bead displacements perpendicular to the pulling direction larger than 1 pixel were detected, were not assessed.

Constant elongation

Once the tether holding force was stabilized, constant speed elongation of the tube was performed by imposing a continuous displacement of the piezo stage away from the trap center at a speed ranging between 0.1 and 15 µm/s and adjusting the displacement to allow detection of the plateau (between 2 µm at 0.1 µm/s and 40 µm at 15 µm/s). The force was continuously monitored by imaging the bead holding the tube at 95 frames per second.

6. Micropipette aspiration

Cells were grown to confluency on Laminin-coated glass coverslips in order to yield cells of sufficient height to allow approaching a micropipette roughly parallel to their side. 45 minutes before the experiment the coverslip was scratched manually with a fine forceps to create cell free areas. Pipets with a diameter of roughly 5 μm were used. By controlling the basin height and initial establishment of the null position at which no net flow was observable, a quantifiable suction pressure was created and the cell was brought in contact with the micropipette, using the micropipette micromanipulators. Bleb formation was considered to happen if a clear protrusion formed inside the pipet within 2 seconds of cell contact to the micropipette.

7. Stimulation of EphB2 with ephrin-B1

Global

Ephrin-B1 (200 μg/mL in PBS, R&D systems 7654-EB) was pre-clustered with goat anti-human IgG Fc (molar ratio 2:1, i.e. 9 μg ephrin-B1:6.75 μg anti-IgG; Jackson ImmunoResearch 109-005-098) for 1h on ice; pre-diluted in 500 μL serum-free DMEM and used at 1 μg/mL final ephrin-B1 concentration.

Local

In this case, we used beads coated with Ephrin-B1tethered to a lipid bilayer. The bead coating was achieved as follows: SUVs were formed from a 200 μg lipid mixture containing EggPC 97.9%, DOGS Ni-NTA 2%, BodipyTexasRed Ceramide 0.1%, w/w. The lipid mixture was dried under nitrogen until all solvent had evaporated, and subsequently left in a vacuum for 30 minutes to ensure full evaporation. 100 μL SLB buffer (10 mM HEPES, 150 mM NaCl, pH 7.4) was added to the dried lipids and left at room temperature for 30 minutes for rehydration. Vortexing of the solution gave an opaque liquid that was sonicated in a sonicator bath for 5 minutes, which was sufficient to yield a translucent SUV solution. The SUV solution was stored at -20 °C for up to 2 months in aliquots of 10 μL. A 10 μL SUV aliquot was diluted with 140 μL SLB buffer and sonicated for 3 minutes in a sonicator bath. 1 μL of silica beads (Kisker Biotech PSI-1.5, 1.5 μm, plain surface, 50 mg/mL) was added to the solution and 0.75 μL of a 1 M $CaCl_2$ solution to induce SUV fusion with the silica particles. The mixture was incubated at 37 °C for 30 to 45 minutes in a shaker at 550 rpm and subsequently washed 3 times with 1 mL of SLB buffer supplemented with 5% BSA (SLB/BSA). The beads were pelleted at RT and 500 g in a benchtop centrifuge. After the final wash, the beads were resuspended in 200 μL SLB/BSA, half of which was used for

ephrin-B1 coupling. 5 µL of recombinant biotinylated ephrin-B1 stock solution (200 µg/mL in PBS, stored at -80 °C) was added and incubated in a turning wheel at 8 °C in the cold room for 2 hours. Washing with cold SLB/BSA buffer was performed in a pre-cooled centrifuge as previously described. The resulting solution (~100 µL) was kept on ice and used for two consecutive days. The final concentration of beads varied widely depending on the loss during washing steps and was calibrated for each batch to give reasonable amounts of beads per chamber. To locally stimulate a cell expressing EphB2_YFP (checked by fluorescence), a lipid-coated bead (again checked by fluorescence) was deposited on the lamellipodial protrusions using the optical tweezer, either at the edge, or in most cases due to poor visibility close to the edge in order to mimic physiological activation geometry.

8. FRAP

In this work, we employed an inverted Nikon EclipseTi Spinning Disk microscope located at the Nikon imaging platform of the Institut Curie, equipped with an iLAS2 FRAP module, a sCMOS Prime95B camera from Photometrics and a temperature controlled heating device. All experiments were performed at ~36°C. Imaging conditions were chosen to give reasonable signal to noise ratio while minimizing photobleaching during imaging and allowing a frame rate of 2 frames per second, for EphB2_YFP 45 % laser power, at 450 ms exposure time with an internal gain function set to 200 MHz.

Ventral FRAP

Ventral FRAP was performed using a 100x CFI Plan Apo oil immersion objective (NA 1.4) with circular bleaching spots of a nominal diameter of 30 pixels, a 100% laser power, and 50 bleach repetitions per area (Figure 21A). In theory this should correspond to a bleach radius of 1.65 µm with a physical pixel value of 11 µm, yet the actual bleach radius was observed to be considerably larger, on the order of 2.6 µm at half-width.

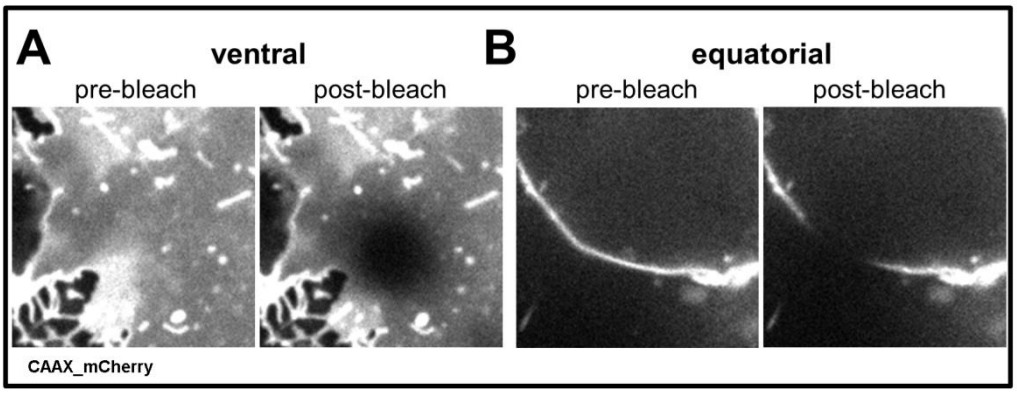

Figure 21 Ventral vs. equatorial FRAP
Representative images of overexpressed CAAX_mCherry before and after a bleach pulse in **(A)** ventral and **(B)** equatorial position.

Equatorial FRAP

A 60x CFI Plan Apo oil immersion objective (NA 1.4) was used and bleaching was performed on the edge of the cell using a squared region. Detection after the bleach was manually chosen to be at a focal plane which showed little sensitivity of the cell edge position to variations in z, i.e. the position of the cell edge did not change much when changing the focus. As the set-up's camera was changed during the time all experiments were performed bleaching sizes were different for some experimental conditions (same input in bleach area in pixels resulted in different effective bleach sizes). We also found that the region was not controlled in z (control bleaching of a fixed cell showed that 'local' bleaching in one focal plane in fact bleached the entire cell in z). This precluded estimation of D_{eff} from the equatorial FRAP data (within the time of this thesis). Thus we decided to represent these FRAP results based on the recovery halftimes which were reasonably robust within experimental sets, and to normalize them to the respective control condition that had identical bleaching areas (i.e. LatA normalized to DMSO, siMyo1b normalized to sicontrol).

Analysis of recovery data

Using ImageJ we measured the average intensity in the bleach area over time and doubly normalized it by background subtraction and correction for bleaching during recovery (Figure 22A), where

$$f_{norm}(t) = (f(t) - f_{BG}(t))/(f_{ref}(t)/f_{ref}(0)).$$

with f_{norm} being the normalized fluorescence intensity, f_{BG} the background intensity, and $(f_{ref}(t)/f_{ref}(0)$ the bleaching factor due to imaging obtained from a reference cell.

From there, we calculated the halftime of recovery with:

$$F(t) = (f_{norm}(t) - f_{bleach})/(f_{plateau} - f_{bleach})$$

where f_{bleach} is the normalized intensity after bleaching, and $f_{plateau}$ is the normalized fluorescence intensity after full recovery. This gives the halftime of recovery τ at $F(\tau) = 0.5$ (Figure 22B).

The mobile fraction (MF) was similarly calculated with:

$$MF = F(\infty) = (f_{norm}(t) - f_{bleach})/(f_{prebleach} - f_{bleach})$$

where $f_{prebleach}$ is the normalized intensity before the bleach and $F(\infty)$ is the value of the stable plateau after full recovery (Figure 22B).

In the case of ventral FRAP we calculated the effective diffusion coefficient from the obtained halftime τ and the effective bleach radius r_{eff} with[371]: $D_{eff} = 0.224\, r_{eff}^2/\tau$

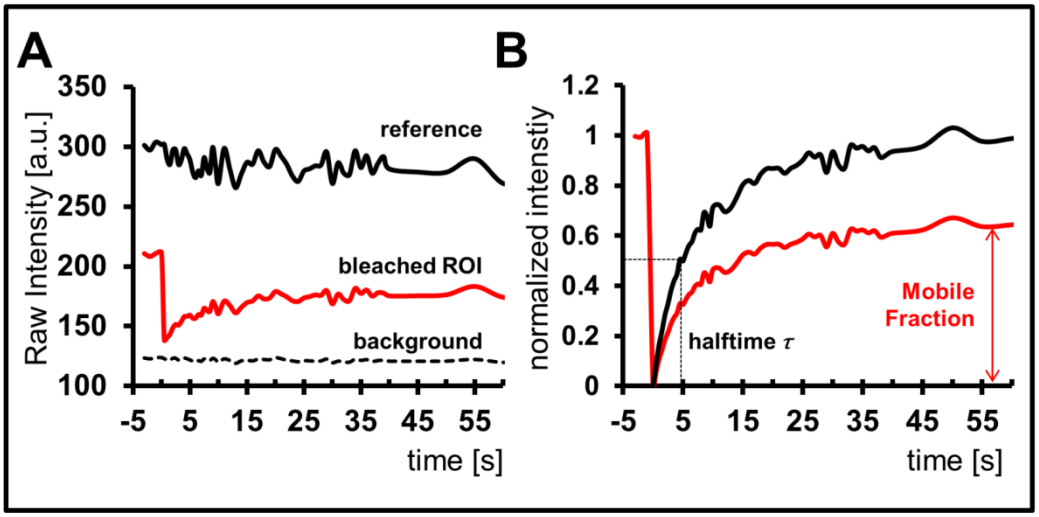

Figure 22 FRAP data analysis
(A) Representative example of fluorescence recovery after photobleaching of EphB2_YFP in a sicontrol-treated EphHEK cell. The red curve shows the average intensity within the bleached region of interest, the dashed black line the background intensity, and the solid black line the bleaching due to imaging of a non-bleached reference cell. | **(B)** Normalization of fluorescence recovery over time: Red line shows the normalization as described in the main text, allowing to identify the mobile fraction, whereas the black line shows the normalization that allow determining the halftime of recovery.

The obtained bleach profiles from the set-up were not perfectly uniform and exhibited effective radii that were bigger than the nominal values. We thus measured the half width of the bleach profile and considered this as the effective radius to estimate the effective diffusion coefficients (Figure 23).

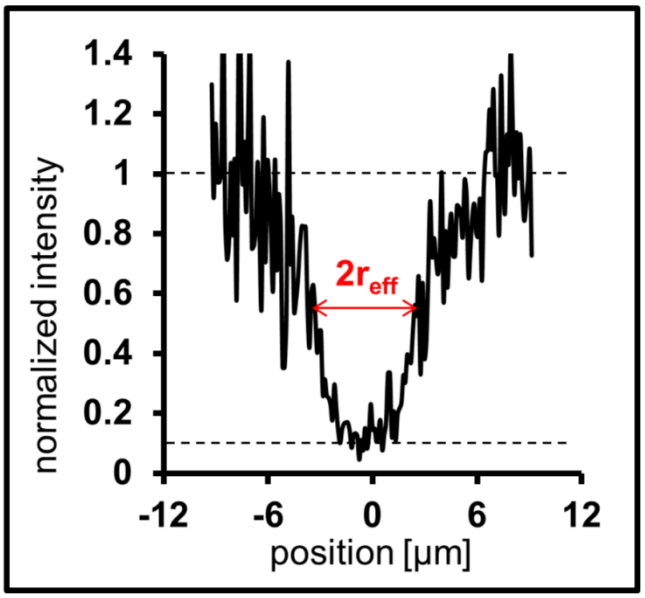

Figure 23 Lateral bleach profile in ventral FRAP.
Lateral intensity profile through the bleached area immediately after the bleach in a cell at 37 °C. The red arrow shows the bleach diameter at 50 % bleach efficiency.

9. Fluorescence correlation spectroscopy

Dishes containing cells were placed on a point scanning confocal Zeiss LSM 780 Confocor 3 System. The temperature was maintained at 37 °C by a Tokai Hit temperature stage and objective heating collar. Each cell measurement included at least six 10 seconds fluorescent traces that were obtained at the ventral membrane surface using a 40X 1.2 NA UV-VIS-IR C Achromat water-immersion objective. The back-focal plane of the objective was overfilled with the excitation beam in order to create a diffraction-limited confocal volume that was calibrated on each day before the experiment using the known diffusion coefficient of rhodamine 6G (426 $\mu m^2.s^{-1}$ at RT and 611.8 $\mu m^2.s^{-1}$ at 37°C[372]). The confocal spot was immobilized in the center of the field and each individual cell was moved there by moving the stage. The correct focal distance was determined from and defined each time as the *z*-focus where the initial estimate of counts per molecule was highest. Next, the emission photon stream was recorded with the same objective, descanned through an aligned pinhole (34 um), wavelength selected (491-553 nm for mYFP) and detected on a gallium arsenide detector array.

Each 10 second trace (I(t)) was autocorrelated into an autocorrelation curve G(τ) using the Zeiss onboard autocorrelator which calculates the self-similarity through:

$$G(\tau) = \frac{\langle \delta I(t) \delta I(t+\tau) \rangle}{\langle I(t) \rangle^2}$$

Here $\langle\rangle$ denotes the time-average, $\delta I(t) = I(t) - \langle I(t) \rangle$ and τ is the time lag. Traces that showed effects of drift or sporadic high intense bursts were discarded from further analysis. We find 3 timescales as described in[373]. The first timescale of about 20-120 µs corresponds to the triplet state, a second timescale (0.3-3 ms) arising from free/unbound fluorophore in the cytosol very close to the plasma membrane and a third timescale of around 10-200 ms corresponding to membrane bound EphB2-YFP diffusing through the confocal spot.

For all the data reported in this manuscript we fitted each raw 10 s autocorrelation (G(τ)) versus time lag (τ; 5.10^{-6} s) to:

$$G(\tau) = \frac{1}{N} G_T(\tau) G_D(\tau)$$

where N reflects the number of moving particles in the confocal volume and $G_T(\tau)$ is the correlation function associated to blinking/triplet kinetics:

$$G_T(\tau) = 1 + \frac{T}{1-T} e^{(-\tau/\tau_T)}$$

Where T is the fraction of molecules in the dark state and τ_T corresponds to the lifetime of the dark state.

$G_D(\tau)$ is the correlation function associated to diffusion which in this case contains two diffusional timescales τ_{D1} and τ_{D2}:

$$G_D(\tau) = f * G_{D1}(\tau) + (1-f) * G_{D2}(\tau) = \frac{f}{\left(1 + {\tau}/{\tau_{D1}}\right) * \sqrt{1 + {\tau}/{S^2\tau_{D1}}}} + \frac{1-f}{1 + {\tau}/{\tau_{D2}}}$$

The fraction f corresponds to the intracellular diffusing pool of unbound fluorophores that has a timescale of τ_{D1}. S is the structure factor that accounts for timescales arising from the fact that the intracellular fluorophores diffuse in a volume rather than a plane. Free fitting of S converged to a value of about 0.2, consistent with earlier reports. In order to limit the number of free parameters, S was thus fixed to 0.2. The diffusion time of interest is finally calculated with τ_{D2}. The diffusion coefficient was calculated by:

$$D_{FCS} = {w_{xy}^2}\Big/{4\tau_{D2}}$$

where w_{xy} is the width of the point spread function which is calibrated using a Rhodamin 6G solution. For 488 nm excitation wavelength w_{xy} was 223±30 nm.

10. Fluorescence anisotropy measurements

HomoFRET measurements were performed in the lab of Satyajit Mayor at the NCBS in Bangalore, India, with Thomas van Zanten. HomoFRET allows studying the local organization of proteins, e.g. their relative packing in the membrane, by analyzing the anisotropy of emission after polarized excitation, i.e. the relative loss in excitation polarization during the time of fluorescence emission[374]. The following paragraph details the actual experimental procedure, details on the interpretation are found in the respective results.

Homo-FRET between like-fluorophores was measured as steady state emission anisotropy in a total internal reflection fluorescence microscopy mode. The

measurements were carried out on a Nikon Eclipse Ti-E microscope with polarized laser excitation equipped with an 100x 1.45 NA TIRF objective with a dual camera imaging arrangement as described in[373]. The emission was split into I_{pa} (parallel) and I_{pe} (perpendicular) components by means of a high-performance wire grid polarizer (Moxtek) and then collected onto two separate EMCCD cameras (Photometrics Evolve 512 EMCCDs).

Anisotropy r is calculated as: $r = \frac{(I_{pa} - I_{pe})}{(I_{pa} + 2I_{pe})}$

where I_{pa} is the intensity measured in the parallel direction and I_{pe} the intensity in the perpendicular direction with respect to the plane of polarization of the excitation beam. For analysis, the images were background subtracted (buffer image taken with identical imaging conditions) and the I_{pa} and I_{pe} images were aligned (Registration) using the affine transformation function in Matlab (Mathworks, USA). An image of fluorescein in water was used to compute the G-factor image (I_{pa}/I_{pe}) which was then corrected onto the I_{pe} image. This G factor allows normalizing the data according to different detection sensitivities regarding polarization in the optical set-up. Roughly 1.6x1.6 µm regions on the membrane with no apparent endosomal presence were selected and the extracted intensities in the I_{pa} and G-factor corrected I_{pe} channels were used to compute the emission anisotropies for each ROI. The anisotropy values were binned based on total intensity values ($I_{pa}+2I_{pe}$) and the binned data was plotted using GraphPad Prism software.

11. TIRF-SIM

TIRF-SIM (total internal reflection fluorescence – structured illumination microscopy) datasets were obtained on a commercial Nikon N-STORM set-up in the imaging facility of NCBS in Bangalore, India. Actin was labelled by expression of mCherry-tractin, and excited at 561 nm. The set-up was aligned in a rough way on a daily basis ensuring centered fiber entry into the microscope, and accurate base-voltage in the piezo system controlling the TIRF-SIM grating.

The method is based on a grating that leads to a patterned excitation of the sample by using the first order beams, hence structured illumination[375,376]. Using the grating and a polarizer, the set-up creates an illumination pattern with different angles and phases (here: 3 angles and 3 phases) and allows subsequent reconstruction of an image with higher resolution due to improved gathering of high-frequency information from the sample (Figure 24). While this allows improving the lateral resolution considerably, total internal reflection illumination restricts the excitation to a thin sheet in z, thus

further reducing out-of-focus contributions in a high background conditions as in the cell.

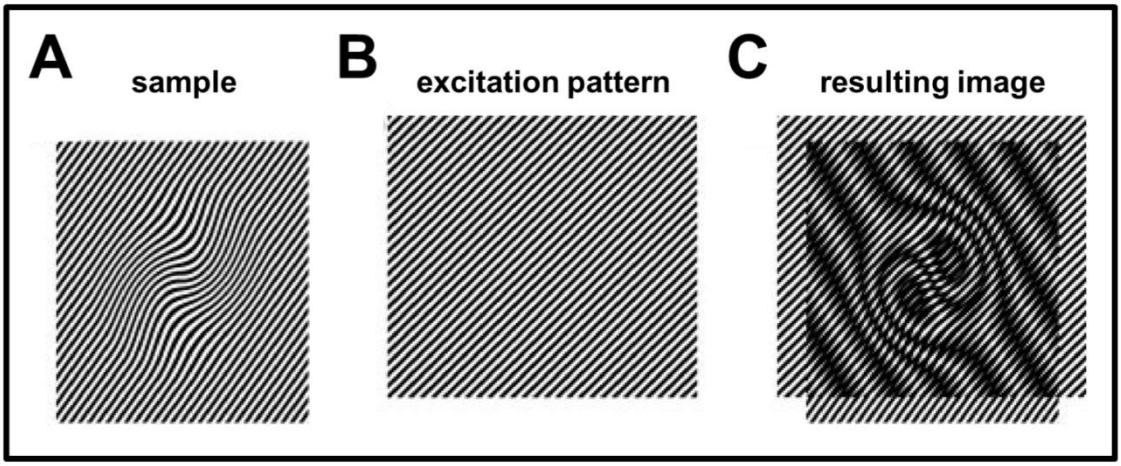

Figure 24 Working principle of SIM
Representation of resolution improvement through patterned excitation: A sample **(A)** is illuminated with a pattern **(B)**, creating Moiré fringes that reveal otherwise unresolved details **(C)**. From reference 376.

12. Reconstruction of SIM data

Reconstruction of TIRF-SIM datasets was performed with the Fiji plugin FairSIM[377] (Figure 25). This required transformation of the 3x3 image montages (3 angles at 3 polarizations each) into single image stacks, done with Fiji using the stack manipulation functions. Stacks were then imported into FairSIM with background subtraction using the graphical user interface (Figure 25A). This resulted to be a critical step as both high levels of background and "over-subtraction" of intensities resulted in unsuccessful reconstructions.

Taking into consideration the origin of images, i.e. TIRF-SIM data, following parameters were chosen in agreement with the manual's suggestion:

The optical transfer function (OTF) was estimated with an NA of 1.49, an emission wavelength of 610 nm and an OTF compensation of 0.25, allowing for deviations due to system aberrations (Figure 25B). No attenuation was chosen as TIRF illumination is already restricted to an almost 2-dimensional excitation sheet. Reconstruction parameters were obtained from fitting the peak in the high frequency domain (small yellow circle, top right) excluding 70% of the lower frequency intensity (large yellow circle) (Figure 25C). These allow to define which information remains and which gets rejected during reconstruction. Subsequent reconstruction was performed with a Wiener filter set to 0.099 and an APO cutoff of 0.2 (Figure 25D).

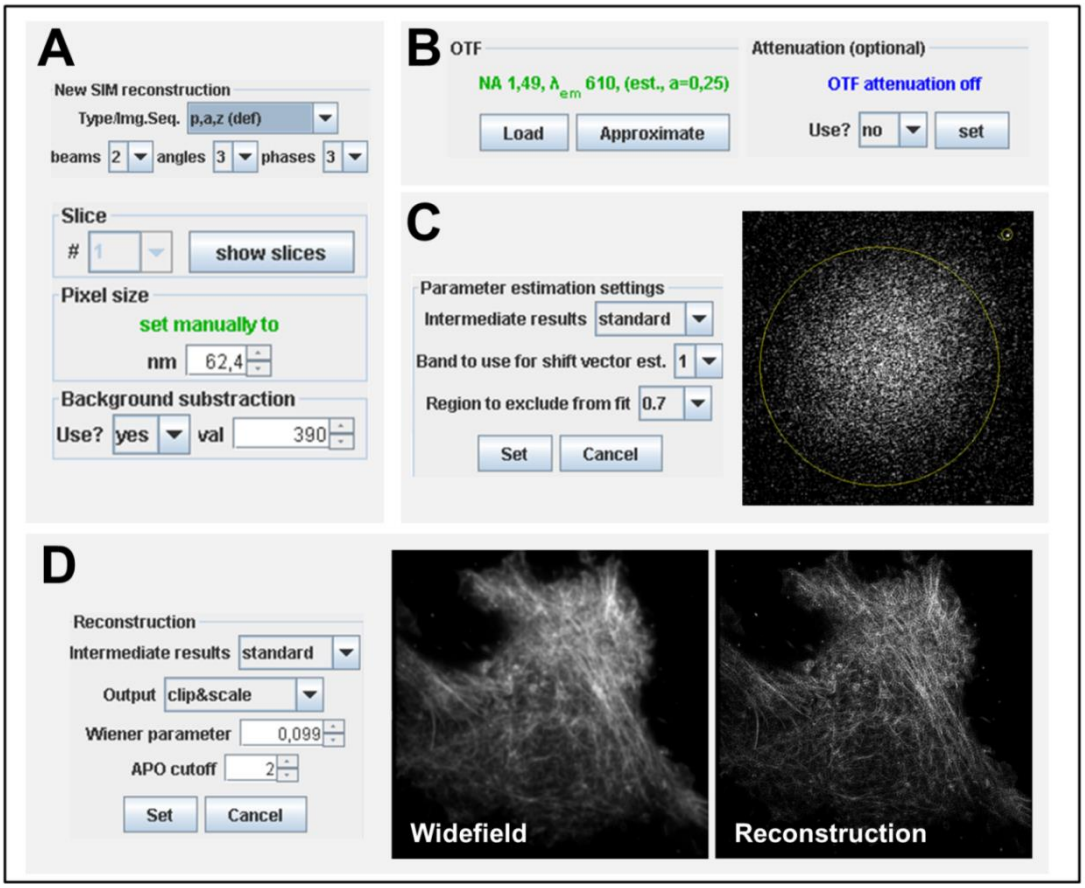

Figure 25 TIRF-SIM reconstruction using fairSIM
(A) Import of TIRF-SIM datasets defining the acquisition details, pixel size, and background correction. | **(B)** Optical transfer function (OTF) approximation by providing the numerical aperture of the system, the fluorophores emission wavelength, and attenuation to account for deviations from a 'perfect' OTF. | **(C)** Reconstruction parameter estimation through fitting. For TIRF datasets, the recommended exclusion to fit the correlation peaks(small yellow circle on the upper right) is 0.7 (representing the large yellow circle on the right. | **(D)** Reconstruction was performed with the Wiener filter set to 0.099, and the standard APO cutoff of 2. (See main text for details)

13. Particle image velocimetry

Data treatment prior PIV analysis

The reconstructed TIRF-SIM datasets were treated to allow robust estimation of actin flow profiles as follows (Figure 26): Reconstructed images were subjected to a band-pass filter with the limits of 3 to 15 pixels, thus enhancing the filamentous structures over background, and reducing reconstruction artifacts, e.g. honeycomb patterns.

In order to follow the actin filaments over time, we employed a ridge detection using the Fiji plugin developed by Steger e*t al.*[378], with following parameters: line width 2 pixels, high contrast limit 200, low contrast limit 75. The resulting binary image sequences were averaged stepwise over three frames and the resulting frames subjected to a 1 pixel Gaussian blur. The resulting data was used for flow profile analysis using particle image velocimetry (PIV) (Figure 26).

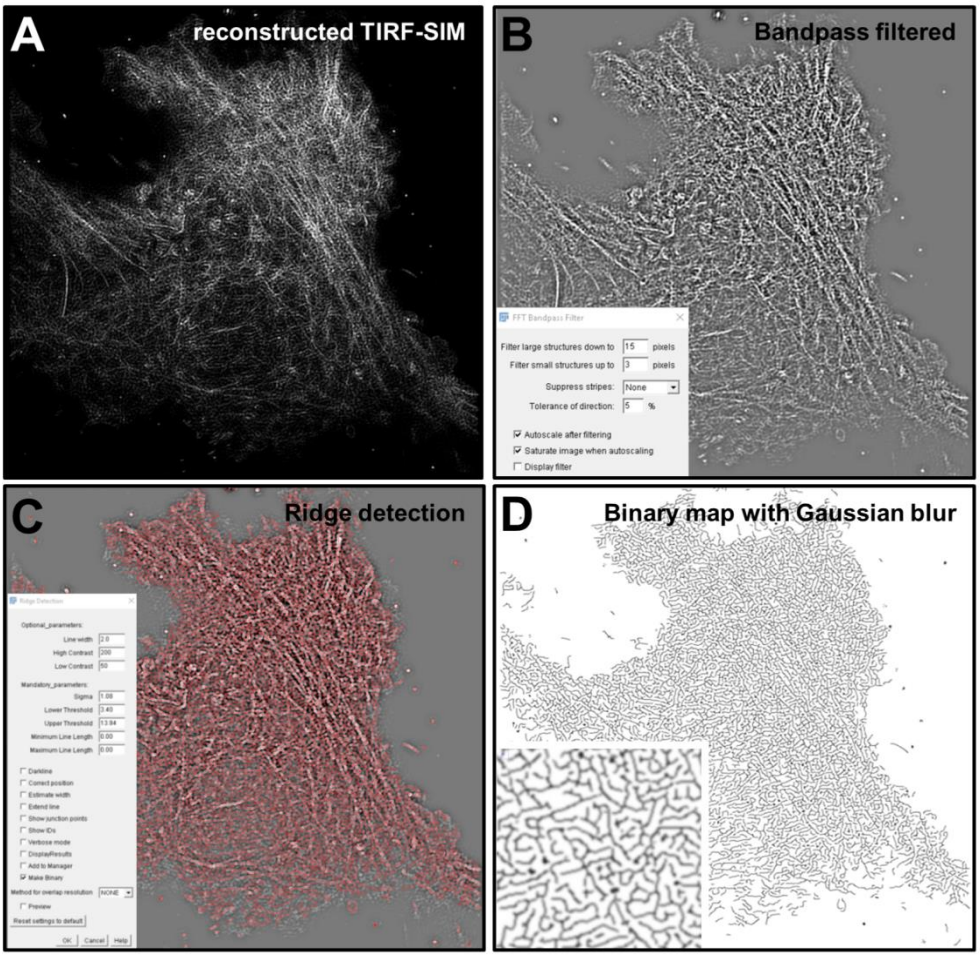

Figure 26 Binary ridge map creation from TIRF-SIM data
(A) Input data after reconstruction. | **(B)** Result after applying a bandpass filter (3-15 px) that biases the image towards larger actin structures and reduces small-scale reconstruction artifacts. | **(C)** Results from the ridge detection performed with the indicated parameters. | **(D)** Resulting binary map from ridge detection with a 1 pixel Gaussian blur.

PIV analysis

PIV analysis was performed using PIVlab, a freely available Matlab App[379,380]. We used the FFT window deforming algorithm for PIV, with an iterative interrogation area size of 64, 32 and 16 pixels respectively and shifting the interrogation area by half its width to find the best correlation between subsequent frames (Figure 27A). This allowed sampling of a wide variety of flow velocities, with high vector resolution and reproducible results. Sub-pixel localization was estimated using a linear deformation and 2x3 pixel Gaussian fit. In order to reduce noise, recover spatially coherent flows and fill the flow map, individual frame-to-frame flows were averaged over 10 frames, yielding a final effective time resolution of roughly 1 flow profile per 60 to 90 seconds (depending on the initial time resolution) (Figure 27B). Vector validation was performed excluding spurious vectors larger than 40 nm/s.

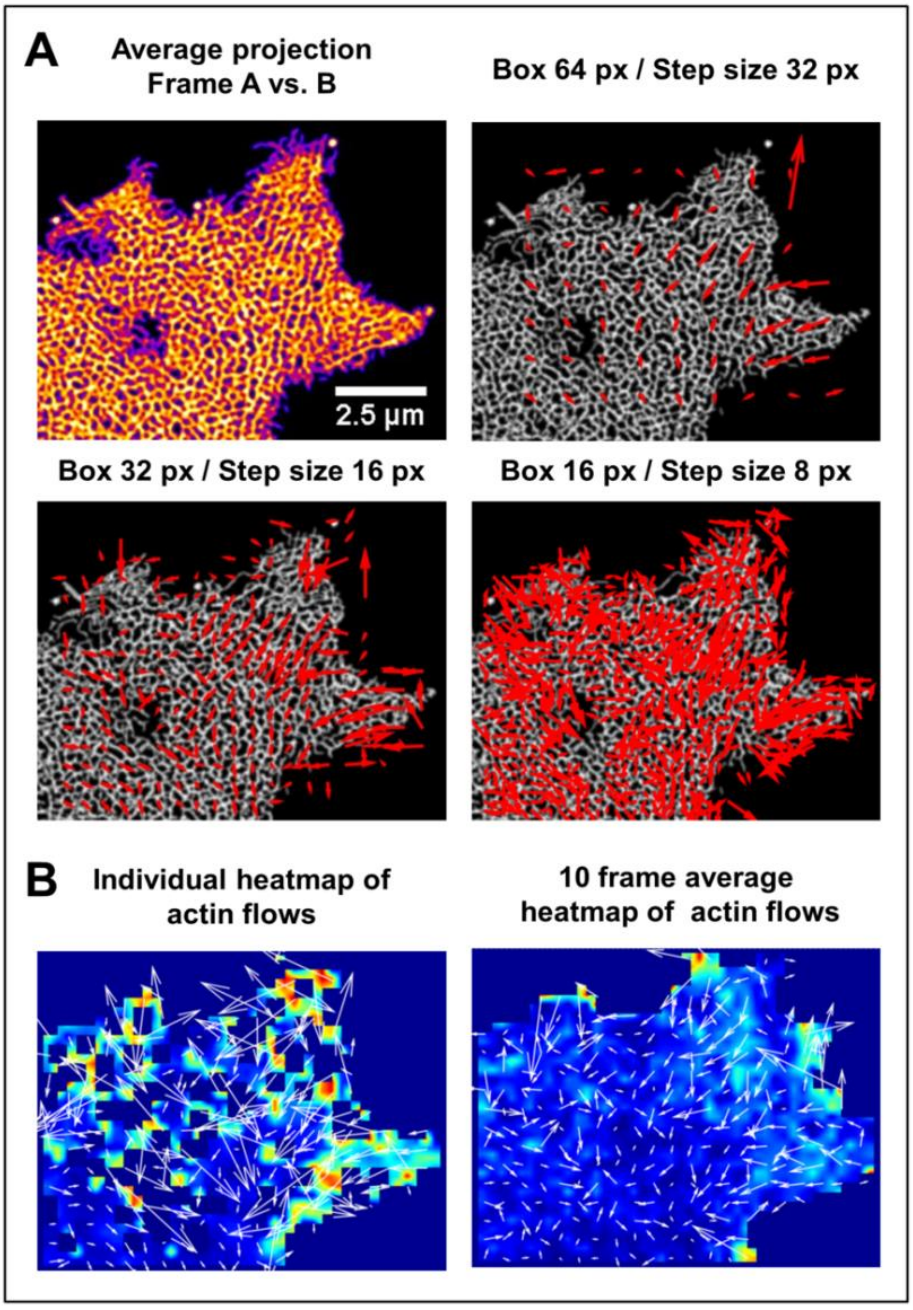

Figure 27 PIV analysis
(A) Upper left window showing the average projection of two consecutive time frames in which the cell visibly retracted towards the lower left. Flow vectors obtained from applying the PIV algorithm at reducing interrogation window size, with 50 % shifts, as indicated on top of each image. The amount of vectors inversely scales with the size in interrogation area, at the cost of increasing false correlations. | **(B)** Heatmap of flows for an individual frame after iterative PIV analysis (left), recovering the general flow direction. Single frame sampling is insufficient to generate flow maps that cover the cell surface. The right shows the average of ten individual PIV heatmaps that allows full sampling of the cells surface and favors flows of coherent directionality during the time of averaging.

14. Statistics

Data sets for were analyzed for statistical significance using the statistical toolbox of Excel. One-way ANOVA was employed to check for the presence of statistically

significant deviations within experimental data populations. If the null hypothesis was successfully rejected, F-tests were conducted on a paired basis to compare variances and, depending on the outcome, two-tailed t-tests assuming equal or unequal variances were employed. Only p-values smaller than 0.05 were considered statistically significant and displayed in the figures.

15. Assessment of protein expression

Western Blot

After washing with PBS, cells were lysed in 1.5x SDS-loading buffer supplemented with β-mercapto-ethanol pre-heated to 95°C. After treatment with benzonase, cell lysates were analyzed by SDS-PAGE and transferred to nitrocellulose membranes. Myo1b, Ezrin and ERM were detected with antibodies as indicated on the respective figures.

Fluorescence microscopy

Transfected cells were imaged using a conventional confocal microscope at the equatorial plane to assess expression and localization of fluorescently tagged proteins prior to tube pulling.

Part A -The effect of Myosin 1b & ERM proteins on membrane mechanics

1. Mechanical properties of lipid membranes

Early interest in cell membranes, and particularly the peculiar shapes of the erythrocyte membrane, led to efforts to understand the membrane's elastic properties that govern membrane shape and deformations. Fundamental theoretical models of membrane elasticity were generated for lipid bilayers, which offered the advantage of homogeneity. The membrane could thus be treated as a continuous, two-dimensional layer without need to include molecular details[381,382]. Three main elastic deformations were described: Stretching, bending and shearing[382–384] (Figure 28).

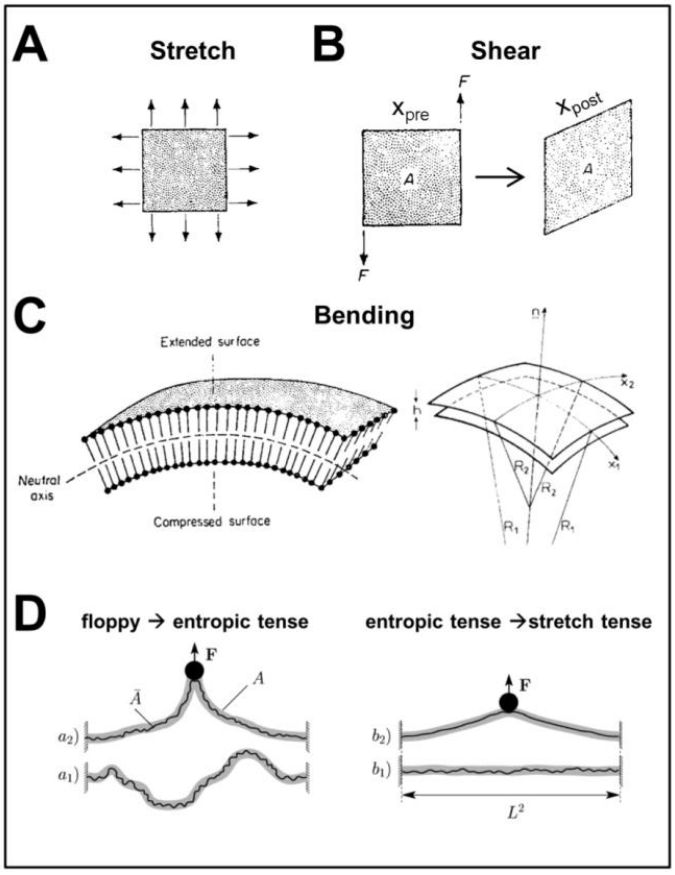

Figure 28 Lipid membrane deformations
(A-C) The three principal membrane deformations: **(A)** Stretching of a membrane sheet to increase its area. |**(B)** Shearing a membrane along an axis while maintaining a constant area. Reference 382|**(C)** Bending a membrane leading to a compressed and an extended surface (left) (reference 382). Curvature can be characterized by two principal curvatures that are the inversed respective radii R_1 and R_2.(Reference 369) |**(D)** Regime changes in membrane tension through application of external forces. The left-hand side shows the transition from a floppy membrane (a_1) to the entropic tense regime (a_2), whereas the right-hand side shows the transition from the macroscopically flat entropic tense regime (b_1) to the stretch tense regime (b_2). Reference 383

1.1 Membrane stretching

Stretching of a membrane is defined as the in plane change in area, i.e. application of a tangential stress. In this case, the elastic stretching energy W_s per unit area is a quadratic function of the relative area change $\Delta A/A$, with

$$W_s = \frac{1}{2}\kappa_S \left(\frac{\Delta A}{A}\right)^2, \quad (1)$$

where κ_s is the elastic stretching modulus, with dimensions of an energy per unit area. For pure lipid vesicles of phosphatidylcholine this value is around 250 $mJ.m^{-2}$, with little variation depending on chain length and unsaturation[385]. It must be noted that changes in membrane thickness were not considered in the model[381].

1.2 Membrane shear

Shear is the in-plane deformation of a membrane at constant area. The shear energy W_{shear} per unit area is proportional to a quadratic function of the extension ratio of the membrane, with:

$$W_{shear} = \frac{1}{2}\kappa_{shear}(\lambda^2 + \lambda^{-2}), \quad (2)$$

where λ is the extension ratio x_{post}/x_{pre} with x being the edge length before and after shearing, and κ_{shear} is the shear modulus of the membrane with dimensions of an energy per unit area[384]. In pure lipid membranes, the fluidity of the bilayer results in a shear modulus of 0 as lipids can move around freely. This is fundamentally different in the case of biological membranes, a fact that is discussed hereafter.

1.3 Membrane bending

Membrane bending accounts for out of plane deformations of the membrane. In a first instance one can define the bending energy per unit area g which is a function of the two principal curvatures c_1 and c_2, as well as a spontaneous curvature c_0 which can arise from lipid asymmetry, with:

$$g = \frac{1}{2}\kappa_b(c_1 + c_2 - c_0)^2 + \frac{1}{2}\overline{\kappa_c}c_1c_2, \quad (3)$$

where κ_b and $\overline{\kappa_c}$ are elastic bending moduli relative to the mean and Gaussian curvature respectively.

As the second term of equation 3, which is related to the Gaussian curvature c_1c_2, is shape-independent for closed surfaces, the energy of the membrane can be described by the Canham-Helfrich Hamiltonian, as:

$$\mathcal{H}_{C-H} = \frac{1}{2}\kappa_b \oint(c_1 + c_2 - c_0)^2 dS\,, \tag{4}$$

with κ_b being the bending elastic modulus of the membrane with dimensions of an energy[386] and S the surface. In contrast to the stretching modulus, bending moduli vary strongly depending on acyl chain length and degree of unsaturation. For a DOPC lipid bilayer, κ_b is on the order of $0.85.10^{-19}$ J[385].

1.4 In-plane membrane tension

The in-plane membrane tension σ_m with the dimensions of a force per unit length can be defined as the change in free energy F over a change in surface S with:

$$\sigma_m = \frac{\partial F}{\partial S}\,, \tag{5}$$

One can describe three distinct regimes for this tension (Figure 28D): A floppy regime where the membrane is not 'tense' and $\sigma_m = 0$, and a tense regime, which can itself be separated into two distinct regimes.

By application of external stresses, the entropic-tense regime is found at macroscopically flat surface area, which microscopically is characterized by thermal membrane undulations, which are controlled in their amplitude by the bending modulus of the membrane. The apparent area can be further expanded to match the microscopic area and undulations are increasingly suppressed, leading to the stretch-tense regime[383,387].

For a plane membrane in the stretch-tense regime one readily gets:

$$\sigma_m = \kappa_S\left(\frac{\Delta A}{A}\right) \tag{6}$$

At lower tensions, i.e. in the entropic-tense regime below 10^{-5} N/m, the description of tension becomes more complex, and scales exponentially with the relative area change.

2. Studying cellular membranes

While some methods have been conceptually proposed to directly assess membrane tension without any perturbation to the system, e.g. exploiting mechanosensitive ion channels[388], most experimental approaches have focused on generating membrane tethers from cells. In general, tethers can be generated from hydrodynamic flows[389,390], pulling with an AFM cantilever or by pulling with a bead that is either held by a micropipette[391] or an optical tweezer[392–394] (Figure 29A).

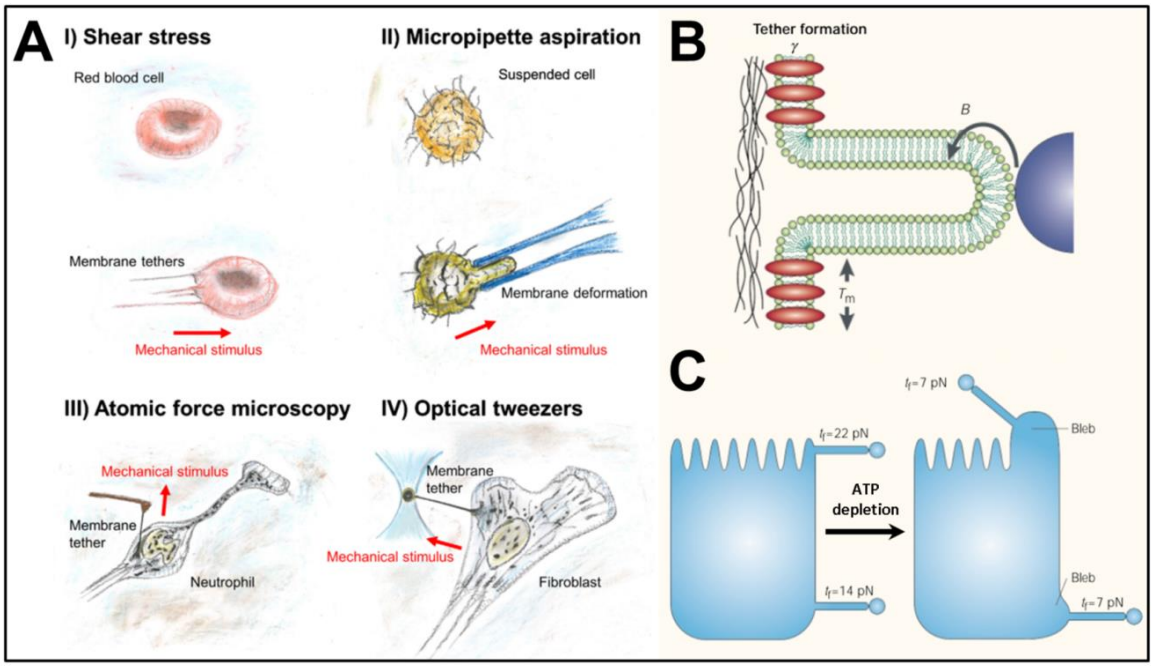

Figure 29 Studying membrane mechanics in cells.
(A) Schematic representation of the four main methods to study membrane mechanics in cells : (I) Shear by hydrodynalic flows, (II) Micropipet aspiration, (III&IV) Membrane tether formation : dorsal tethers through AFM (III) and lateral tether pulling by optical tweezers. Reference 393 | **(B)** Schematic representation of the principal contributions to tether holding force, i.e. in plane membrane tension T_m and membrane-cortex adhesion energy γ. | **(C)** Energy-dependent polarization of tether forces in epithelial cells. The basolateral membrane (bottom) has a lower tether holding force than the apical side, yet after ATP depletion and blebbing, both show equal tether holding force. Reference 394

2.1 Cortex contribution to effective membrane tension

In the cellular context, the membrane is underlined by a cytoskeletal network (cortex) and generally presents large excess areas[395,396] as compared to the cortex. Early on it became clear that this cytoskeleton affects the mechanics of membrane tethers although the actual tether is devoid of actin, leading to the conceptual parameter of 'effective membrane-tension' (σ_{eff}): it convolutes the contributions from in-plane membrane tension (σ_m) and the additional effects originating from membrane interactions with the underlying actin cortex which are generally represented by an adhesion energy (W)[392,397–401] (Figure 29B). This adhesion energy can be directly measured on a larger scale, by micropipette aspiration[402,403] (Figure 29A), and notably

depends on PI(4,5)P_2 levels[136] and of course on the presence of the actin cortex[398] (Figure 29C). W is on the order of 10^{-5} J.m^{-2} in cells[136,404]. In summary, because of the large excess of membrane area the contribution of W dominates the effective membrane tension, thus cell membrane mechanics is generally assumed to be dominated by adhesion of the plasma membrane to the actin cortex.

2.2 Tether pulling from cells

In a large vesicle, i.e. pure lipid environment of flat nanoscale geometry, tube generation is characterized by a critical energy barrier which when overcome leads to formation of a tube of length-independent radius[405]. The initial energy barrier for tube formation is critically dependent on the initial patch size, i.e. the interaction area of membrane with pulling probe[406]. In order to form a membrane tether in cells this force barrier is considerably higher as a patch of membrane has to be separated from the underlying actin cortex[407,408]. Upon formation of a membrane tether two opposing processes govern the tether's equilibrium radius and the force required to hold it. While the surface tension σ_{eff} drives the system towards smaller radii, i.e. minimizing the tether surface, it eventually reaches a point where further reduction in radius is unfavorable due to the membrane's bending rigidity κ_b[405]. When the distance between two tethers is below a threshold value, coalescence of tethers can be observed[405,409].

The equilibrium radius r_{eq} and tether force f_{tether} are related to effective membrane tension and bending rigidity by[410]:

$$r_{eq} = \sqrt{\frac{\kappa_b}{2\sigma_{eff}}} \qquad f_{tether} = 2\pi\sqrt{2\sigma_{eff}\kappa_b} \tag{7}$$

with $\sigma_{eff} = \sigma_m + W$.

Combining both equations, one finds:

$$\kappa_b = \frac{f_{tether}\, r_{eq}}{2\pi} \qquad \sigma_{eff} = \frac{f_{tether}}{4\pi r_{eq}} \tag{8}$$

Thus, in theory, one can readily deduce both the effective membrane tension and bending rigidity from tether forces, yet it is difficult to precisely measure the tube radius as it is below the optical resolution, of the order of 100 nm and below. As the bending rigidity is generally assumed to be reasonably stable in between experimental

samples, one can compare tether forces to observe changes in effective membrane tension.

Following table shows a selection of published tether forces for different cell lines:

Table 1 Selection of published tether forces for different cell lines, as summarized in[393].

Cell type	Cell line	Tether Force [pN]
Neurons	Chick dorsal root ganglion	7
	mouse cortical neurons	15
	rat dorsal root ganglia neurons	32
Endothelial cells	EA hy926	30
Chinese hamster ovary		30
Melanoma	M2 & A7	30
Neutrophil	L-60	8
		40
Macrophage	RAW 264.7	30
	(mouse peritoneum)	70
Fibroblast	NIH3T3/WTCL3	30
	MEFs	15
Astrocyte/glioblastoma		30
Microglia		60
Keratocyte		55
		40

2.2.1 Dynamic tether pulling

Holding a tether, or elongation at very low speeds (0.1 $\mu m.s^{-1}$), gives a tether of constant radius over wide ranges of length in most cases[395,396], and thus a constant force. Yet for example in outer hair cells a different behavior was observed, leading to length-dependent tether forces[411].

During elongation at constant speed three main dissipation mechanisms come into play: flow of lipids into the tether, slippage within the bilayer, and membrane slippage along the cortex[410]. The tether radius decreases with increasing pulling velocity, due to inherent tether elasticity and membrane viscosity[412]. At the neck, slippage between the inner and outer monolayer is expected, although in pure lipid bilayers such effects emerge only upon very fast tether elongation, i.e. around 100 $\mu m.s^{-1}$ elongation rates[413]. Furthermore, in cells compressive resistance of the proteinaceous core at the cytosolic membrane leaflet leads to high effective viscosities during flow into the tube[391,412].

Elongation at constant speed is an experimental way to assess the friction between the actin cortex and the plasma membrane. As a membrane tether is elongated, lipids have to flow from the cell body into the tube in order to equilibrate the difference in tension that is created by the pulling (Figure 30B). This imbalance is reflected by an increase in the force required to hold the tether (Figure 30A). It is a function of the cortex - plasma membrane linker density and of a phenomenological surface viscosity.

This surface viscosity can be understood in terms of an effective friction between the plasma membrane and the cortex. Its measurement should *a priori* allow probing the properties of the linkers and should be dependent on the linker density. In this scenario, three dynamic ranges can be distinguished: At very slow pulling, the membrane, including proteins that might bind actin, flow as a viscous sheet, because individual detachment happens faster than the elongation. At intermediate speeds, bonds between actin and linkers persist and are 'felt' by the lipids that have to flow around them in order to equilibrate the rising tension in the tube. Finally, at very high speeds, the friction force is higher than the interaction energy between actin and the linkers, thus rupturing these bonds and leading to generalized slippage along the actin[390]. In the intermediate range, which is commonly assessed, the increase in force f scales non-linearly with pulling speed $\dot{L}$[390] :

$$f(\dot{L}) \cong 2\pi(2\kappa_b^2 \nu \eta_e \dot{L} \ln(R/r_t))^{1/3} \quad (9)$$

where: $\dot{L}$is the speed of tether elongation, $\kappa_b$is the bending rigidity of the membrane, ν is the density of cortex-membrane linkers, η_e is the surface viscosity, $R$is the cell's 'radius', and $r_t$is the tether radius.

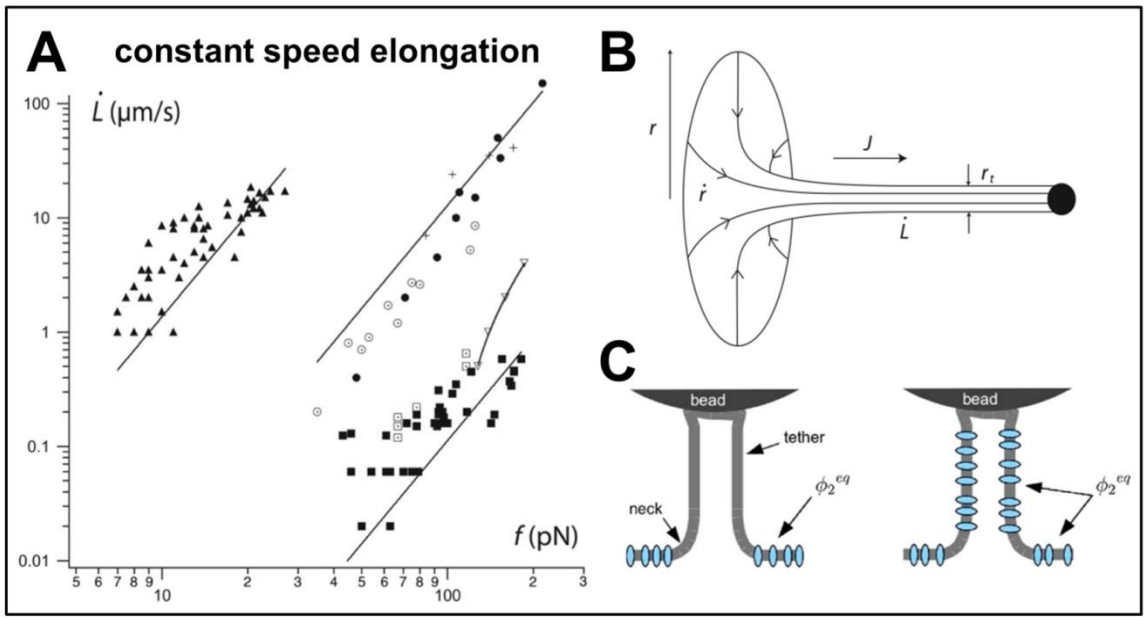

Figure 30 Dynamic tether pulling.
(A) Non-linear scaling law of tether holding force f with elongation velocity $\dot{L}$ for different cell types (corresponding to different symbols)as described and theoretically explained in reference 390|**(B)** Schematic depiction of lipid flows from the cell into the tether. Reference 390 |**(C)** Schematic depiction of the initially homogeneous tether immediately after step elongation with the minority component ϕ_2 being retained at the tether neck (left) and after full equilibration (right). Reference 414

A more recent approach consists in imposing step-displacements at high speed and monitoring the subsequent relaxation dynamics. Phenomenologically this has been interpreted as the build-up of a diffusive barrier at the tube neck for a non-specified minority component, thus leading to non-exponential relaxation kinetics (Figure 30C).

The relaxation of the force $f$over time can then be understood as the initial creation of a concentration gradient of the slower component, relative to the majority component, that relaxes over time t, with[414]:

$$f(t) = \sqrt{f_{peak}^2 - \left(f_{peak}^2 - f_0^2\right)\left(1 - e^{t/\tau_{cross}}\left(erfc\sqrt{t/\tau_{cross}}\right)\right)} \qquad (10)$$

where: $f_{peak}$is the peak force immediately after tether elongation, $f_0$is the force after full relaxation of the tether, and $\tau_{cross}$is the characteristic time of relaxation.

An effect of membrane cortex interaction was proposed to affect the relaxation time if actin-binding proteins were significantly contributing to the postulated concentration gradient[414].

2.2.2 Tension regulation

Different results considering the effect of protein expression and activation on effective membrane tension in various cell lines might be explained by different availability of buffering mechanisms, e.g. the presence of membrane invaginations that disassemble upon stresses[415–419], or compensatory endocytosis and exocytosis[417,420–422]. In line with this, changes in tension reciprocally influence endocytosis and exocytosis events[423,424], and phagocytosis increases the effective membrane tension[425]. Blebs are supposed to maintain/ buffer effective tension during spreading and retraction[426]. Cells can buffer tension changes by disassembling caveolae[415], or potentially other buds[416]. A cellular way of tension sensing might lie in the mechanosensitive channel Piezo1 which is activated by membrane stretching[427–430]. Indeed, local increases in tension can lead to local activation of Piezo1[431].

2.2.3 Experimental observations

Effective membrane tension in keratocytes is polarized, i.e. the leading-edge lamellipodium during migration has a higher tension than the cell body[432]. Large surface area changes are buffered within 10 minutes with no persistent effect on tether force after this time, yet cytoskeletal drugs change effective membrane tension persistently[433]. Cholesterol depletion increases effective membrane tension in various cell lines[401,434–436].

The gradient in effective membrane tension in migrating cells might be explained by the role of local actin polymerization towards the leading edge which locally increases tension[437,438]. Accordingly, lamellipodial extension rates and effective membrane tension are coupled[439,440]. Effective membrane tension is dynamically adapted during cell spreading through a feedback loop which couples the induction of actomyosin contraction and exocytosis events to increases in effective membrane tension[421]. Depletion of MLCK, an activator of Myosin II contractility, has been shown to reduce effective membrane in some cells[441], whereas this effect was absent in another cell line[442]. Effective membrane tension has furthermore been reported to play a role during polarity establishment[443,444] and increases during mitosis[445].

Evidence generated *in silico, in cellulo* and from theoretical arguments suggests that a feedback loop between membrane tension and the recruitment and spatial organization of membrane curvature sensing proteins exists[446–448].

Taken together, the literature regarding the role of effective membrane tension in cells suggests that it plays a role in many cellular functions. Cells have developed a variety of dynamic processes that set the effective membrane tension, and regulate and adapt it, either locally or globally, to fulfil specific functions through, e.g. changes in contractility, membrane trafficking, and actin dynamics. Yet, we are still at a descriptive stage in which the various experimental results do not obviously paint a coherent picture of how cells respond to changes in effective membrane tension, how effective membrane tension is regulated within cells, and how changes in effective membrane tension propagate in space and time.

Working hypotheses

The overarching goal of this part of the thesis was to characterize the effect of two types of plasma membrane - actin linkers on membrane mechanics.

This was motivated by the initial observation that cell contraction after activation of EphB2 was less efficient in absence of Myosin 1b (this work). As the EphB2 receptor was still activated in cells (tyrosine phosphorylation), and Myosin II activity was still induced after depletion of Myosin 1b[3] (MLCK phosphorylation), we hypothesized that Myosin 1b could play a mechanical role in this process by coupling the Myosin II-generated contractile forces to the membrane. In line with this hypothesis, former literature evidenced a role of Myosin 1b in the control of membrane tension[6,7], while showing the exclusion of Myosin 1b from tropomyosin-decorated actin structures[186]. Taken together this suggested a position of Myosin 1b at the plasma membrane rather than at the contractile apparatus, and accordingly biochemical evidence showed that Myosin 1b interacts, either directly or indirectly, with the EphB2 receptor[3]. We thus hypothesized, that reduced contractility in absence of Myosin 1b was due to a decreased coupling between the cortex and the plasma membrane, and figured that such a decrease in linkage should translate into a **change in the membrane's mechanical properties**, routinely assessed by tube pulling from cells.

We thus sought to characterize the effect of Myosin 1b depletion and overexpression in the cellular system in which we had seen reduced contractility.

As we surprisingly did not observe an effect on effective membrane tension in HEK293T cells, we expanded the initial study and assessed the role of Myosin 1b in a more general way, thus performing experiments on NIH3T3 cells, experimentally assessing cortex-plasma membrane interaction in a broader way by performing dynamic tether pulling experiments, and including the ERM protein family as a benchmark in our study.

Most of the work of this chapter has been submitted to the journal 'Molecular Biology of the Cell' and is presented in the format adapted to the requirements of the journal (i.e. Results and Discussion together). Initial results and additional experiments that were undertaken in this project are presented following the general organization of this thesis with separate Results and Discussion.

Unpublished Results

Unless specifically stated all experiments were performed on a HEK293T cell line stably expressing YFP-tagged EphB2 receptor[3], referred to as EphHEK cells.

Local activation of EphB2 with bead-coupled ligands induces cellular contraction.

Previous studies on the interaction between EphB2 and Myosin 1b used two main sets of experiments: growth of two cell lines expressing EphB2 and ephrin-B1 respectively, with subsequent description of random cell – cell encounters and 'global' stimulation of EphB2 by adding soluble, pre-clustered ephrin-B1 into the medium[3]. While the first method allowed for 'physiological' activation of EphB2 at membrane contact sites, it did not offer any spatiotemporal control of receptor activation, whereas global stimulation did not allow studying local activation events.

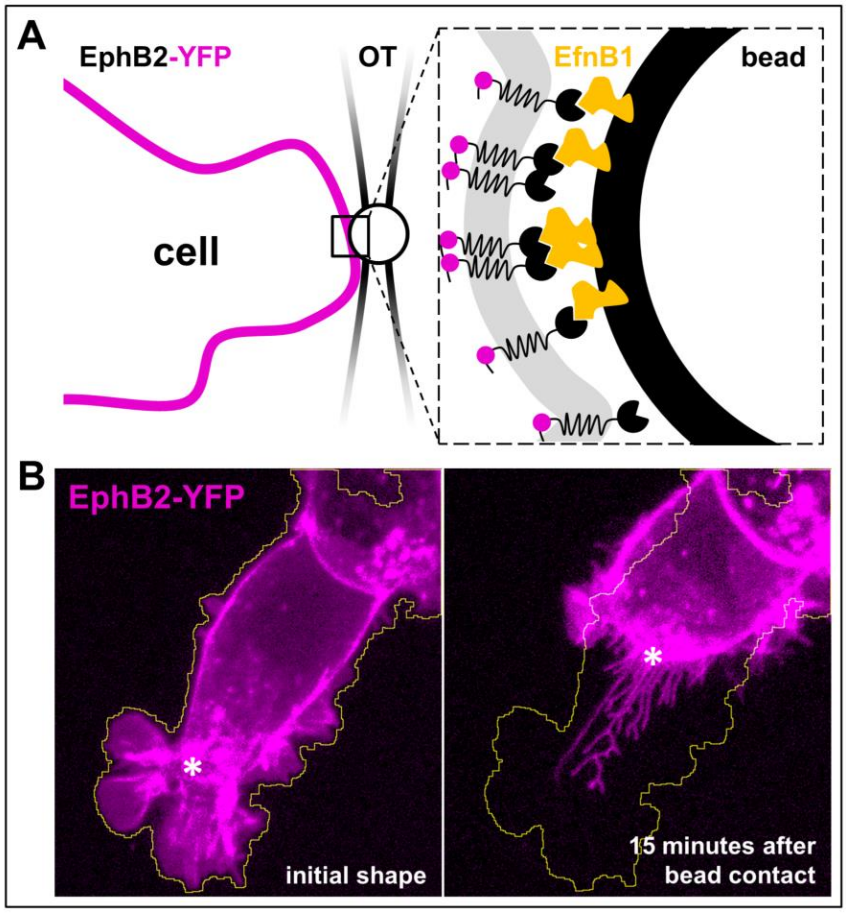

Figure 31 Local stimulation of EphB2 with ephrin-B1 coated beads.
(A) Schematic depiction of the contact between a ligand-coated bead and the cell (left). Diffusible ephrin-B1 is able to locally induce EphB2 clustering and activate the cell (right). | **(B)** Experimental data showing a cell's ventral surface before (left) and 15 minutes after bead contact. The position of the bead is indicated with an asterisk in both frames. The yellow outline is the cell shape before activation.

We thus developed an optical tweezer-based approach to locally stimulate the EphB2 receptor with its ligand ephrin-B1. It is based on coupling the ligand to a lipid bilayer covered bead, allowing the diffusion of ephrin-B1 along the bead surface and thus clustering, that we control with an optical tweezer and bring in contact with cells (Figure 31, detailed protocol in Methods section).

We observed a clear recruitment of the EphB2 receptor to the bead contact site (Figure 32). To check the increase in phospho-tyrosines, a hallmark of receptor tyrosine kinase activity and thus of EphB2 activation, we used a previously characterized mCherry-labelled dimeric SH2 domain (dSH2_mCherry)[313,449]. We showed that local increases in EphB2 receptors around the beads coincided with increases in the dSH2 marker in cells depleted for Myosin 1b, thereby qualitatively confirming previous biochemical evidence of functional receptor phosphorylation in absence of Myosin 1b[3] (Figure 32).

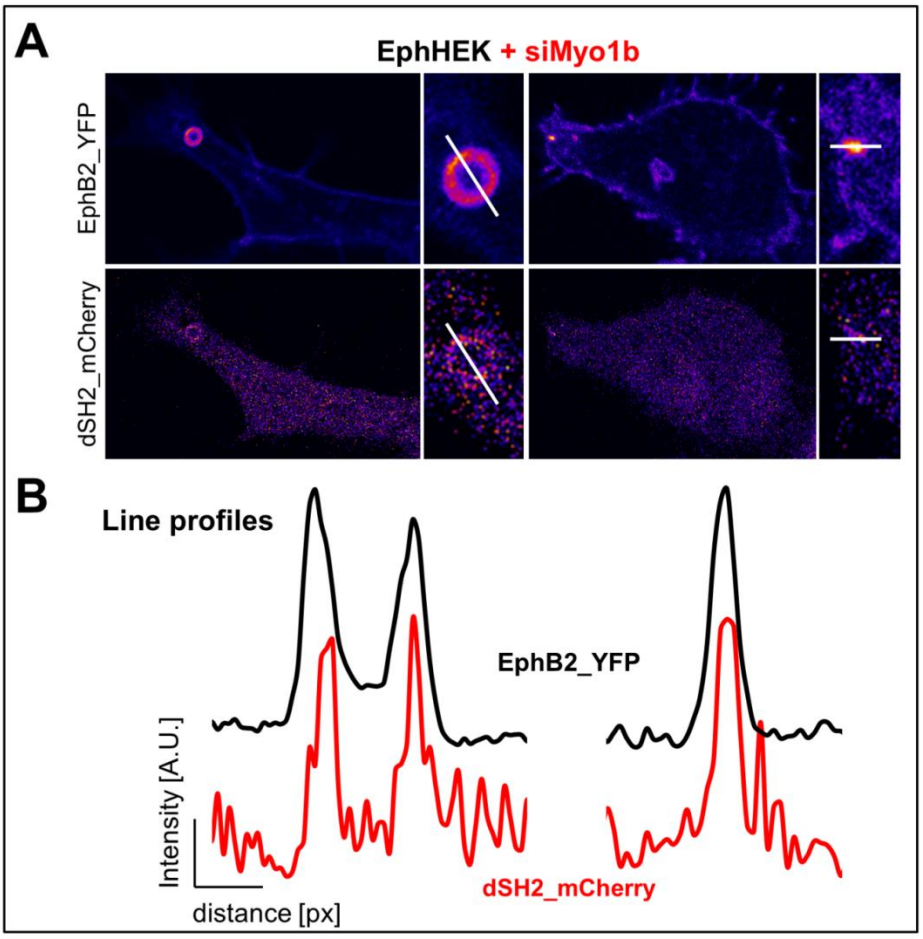

Figure 32 Beads induce receptor recruitment and tyrosine phosphorylation.
(A) Intensity-scaled fluorescence micrographs of EphHEK cells depleted of Myosin 1b by siRNA (siMyo1b) and expressing dSH2_mCherry after 1 minute of bead contact. The left cell was contacted from above, whereas the right one is in contact with a bead at its extremity. The upper panels show the fluorescence signal from EphB2_YFP and the lower ones from dSH2_mCherry, a dual SH2 domain probe that detects phospho-tyrosines. On the right of each micrograph a zoom of the bead-contact site is depicted. | **(B)** Line profiles of the intensity along the white line in (A). One can see a clear correlation in intensity peaks between EphB2-YFP (top black lines) and dSH2-mCherry (bottom red lines).

To quantify the contraction we measured the apparent surface area from the ventral EphB2 signal before activation and after 15 minutes. We chose 15 minutes as the 'end-point' as most of the contraction happens within this time frame. The results obtained with this approach are summarized in Figure 33, showing that local receptor activation induced by the bead is sufficient to specifically induce a contractile response from cells, as expected from previous reports on EphB-driven contractility[4,50].

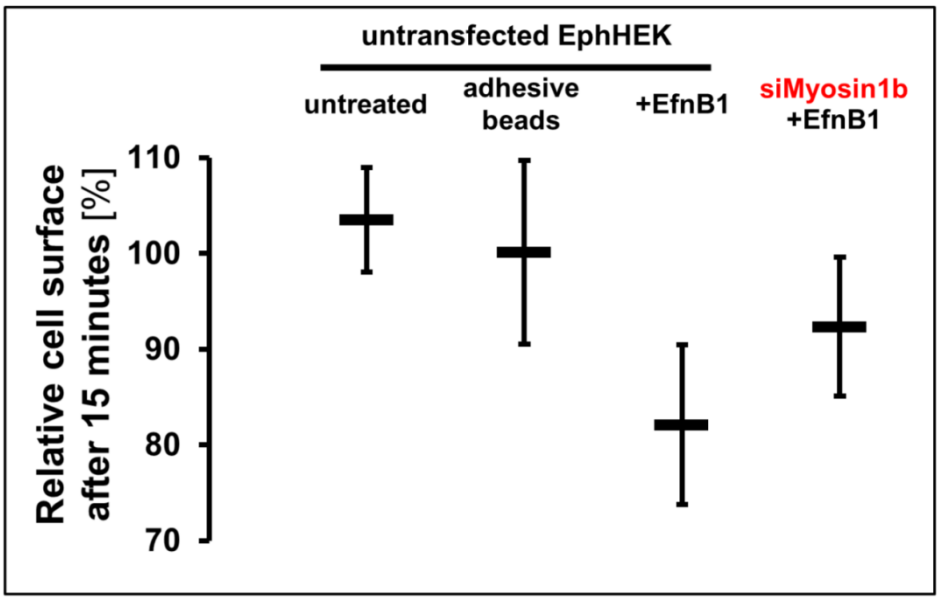

Figure 33 Cell contraction after local stimulation with ephrin-B1 beads.
The plot shows the cell surface after 15 minutes relative to its initial area. A value above 100% means the cell expanded during the 15 minute time frame, whereas a value under 100% means that it contracted. | Untreated (n=24): Cells were imaged at time point 0 and after 15 minutes without any perturbation besides imaging; Adhesive beads (n=20): A carboxylated bead that sticks to the cell surface is deposited on the cell; +Efnb1: An ephrin-B1 coated bead was deposited close to the cell edge of a lamellipodial protrusion, either on control cells that were not treated with siRNA (n=21) or cells depleted of Myosin 1b using siRNA(siMyosin1b) (n=14).

While cells show considerable activity, i.e. protrusion dynamics, at steady state, untreated cells maintained their area over 15 minutes, with a slight tendency of area increases within our data. Addition of non-coated carboxylated beads as a negative control regarding any potential effect of adhesion, again showed no change in apparent surface area, yet an increased spread. The contractility after activation with ephrin-B1 coated beads (mean of relative area 82 %) was reduced after depletion of Myosin 1b using siRNA (92 %) consistent with previously observed effects of global stimulation[3]. Based on our results, the observation that EphB2-driven cell sorting loses efficiency in absence of Myosin 1b[3], and on the generally accepted role of Myosin 1b in the control of effective membrane tension[6,7], we hypothesized that Myosin 1b depletion could affect the coupling between cortical actin and the plasma membrane, and in consequence the transmission of Myosin II-driven cytoskeletal contraction to the plasma membrane. We have thus used different mechanical methods for measuring the effective membrane

tension and the friction at the interface with the cortex (submitted paper), or the adhesion energy between cortex and membrane (see below).

Micropipette aspiration on HEK293T cells does not reveal any mesoscale difference in membrane to cortex adhesion.

Micropipette aspiration has been employed to characterize the adhesion energy between the plasma membrane and the actin cortex[403,407,408,451]. In practice, such measurements allow identifying the critical pressure P_{bleb} at which a membrane bleb forms inside the micropipette, equivalent to the detachment of the plasma membrane from its underlying cortex. Ignoring the contribution of membrane tension as it is negligible quantitatively (see previous Introduction), the relationship between critical blebbing pressure and membrane-cortex adhesion is described through[402]:

$$P_{bleb} = \rho_l \alpha^* \frac{k_B T}{L_l} - 2\frac{\sigma_c}{R} \quad (11)$$

where ρ_l is the linker density, L_l is the characteristic linker length, σ_c is the cortex tension, R is the cell's radius (assumed to be spherical) and α^* is a dimensionless ratio proportional to the critical force of detachment per link:

$$\alpha^* \equiv \frac{\sigma_n^* L_l}{\rho_l k_B T} \quad (12)$$

Where σ_n^* is the critical normal stress exerted on the membrane and is obtained from taking the kinetics of binding/unbinding of the linkers under stress into account. The first term of equation 9 represents the contribution of the detachment of a certain amount of linkers to the critical pressure through detachment, while the second term is the contribution of cortex contractility which creates a stress on the linkers and thus reduces critical blebbing pressure[402].

The critical blebbing pressure was previously shown to change in response to Myosin II inhibition in *Dictyostelium discoideum*[403] and related experiments have revealed a role for membrane cytoskeleton attachment in bleb behavior in *Paramecium* (unpublished C. Campillo, C. Sykes' lab).

As we studied adherent cells with complex morphology we only report comparative measurements of the critical pressure between control and Myosin 1b depleted cells, without inferring the actual adhesion energy between the cortex and the plasma membrane. We employed a micropipette connected to a height-controlled water reservoir to measure the critical blebbing pressure in Myosin 1b-depleted and control

conditions (Figure 34A). As shown in Figure 34B, we measured a critical blebbing pressure (defined as the pressure at 50% bleb formation probability[403]) of the order of 750 Pa with no clear difference between control cells and cells after Myosin 1b depletion. Critical blebbing pressure thus does not seem to depend on Myosin 1b in EphHEK cells. As we could not detect a difference at large scales as probed by micropipette aspiration we thus resorted to more local measurements, employing optical tweezer based tube pulling.

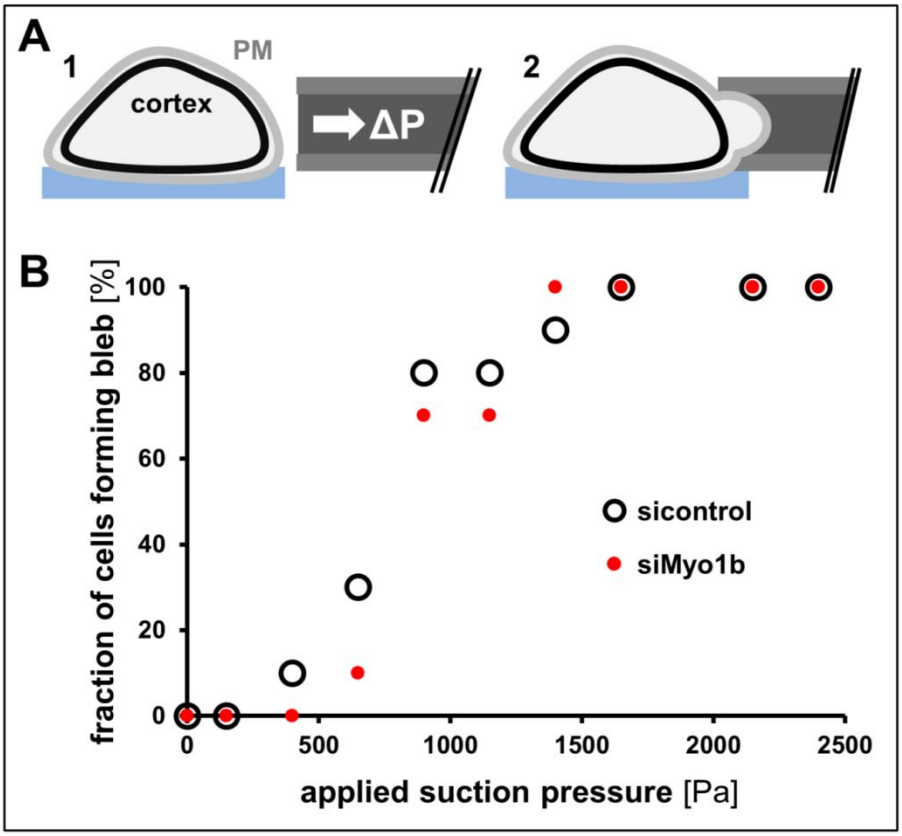

Figure 34 Micropipet aspiration
(A) Schematic depiction of the experimental procedure: A micropipet with a suction pressure ΔP is brought into contact with a cell. If the critical pressure is overcome, the plasma membrane detaches from the cortex and forms a bleb in the micropipette that is observable by brightfield microscopy. | **(B)** Fraction of cells forming a bleb in the micropipette as a function of applied suction pressure in [Pa]. Data for sicontrol cells is shown as black circles, data for Myosin 1b depleted cells as red dots. For each suction pressure 10 cells were probed.

Submitted MBoC manuscript

Abstract

In eukaryotic cells, different linkers connect the plasma membrane (PM) to cortical actin. Several methods have been designed to determine the contribution of these linkers to PM mechanics. Tether pulling with optical tweezers (OT) has been commonly used to measure the effective membrane tension from static tether force. Using this approach, we show that the effective membrane tension in HEK293T cells is independent of the expression of the linkers Myosin 1b (Myo1b) and Ezrin-Radixin-Moesin (ERM). Since linkers are expected to contribute to the friction between the PM and actin, we measured their contribution upon dynamic tether elongation in two ways. No difference in the effective friction was measured for the different linkers when elongating tethers at constant speed. In contrast, the force relaxation following fast tether elongation revealed a change after expression of a Myo1b rigor mutant permanently linked to actin and after depleting ERM. Our results indicate that these measurements, for a given PM-actin linker, depend on its relative fraction among the total number of linkers and the turnover rate of actin-membrane association. Thus, they might strongly vary from one cell type to another, which could explain the differences with previous reports.

Introduction

The different linker types that connect the PM to the cortical actin network in eukaryotic cells contribute to a variety of key processes. ERM proteins and the Myosin 1 family represent two important classes of cortical linkers that attach the actin cortex to the PM via interaction with PIP2 and membrane partners[177,452]. Myo1b is a motor protein able to deform membranes[4]. It has been implicated in a variety of cellular functions, e.g. cell segregation[3], cell motility[191,192], control of organelle shape[1,2] and filopodia formation[3]. It shows catch-bond behavior, i.e. it is sensitive to mechanical loads of a few pN which increase its actin attachment lifetime by two orders of magnitude[165]. Ezrin is required for the formation of protrusions, e.g. microvilli, and its actin interaction is regulated by phosphorylation[227,236].

Sheetz and colleagues have emphasized the role of PM-actin linkers in cell membrane tension[394,398,453]. In general, membrane tension is defined as the variation of mechanical energy upon area change. Since PM and actin cortex are mechanically coupled in cells, membrane tension encompasses two contributions: the in-plane PM

tension σ_m[398] and the interaction between the actin cortex and the PM, represented by an adhesion energy W_0. Both contributions are difficult to distinguish experimentally. Practically, an effective (membrane) tension $\sigma_{eff} = \sigma_m + W_0$ [398] is generally measured using two main methods: micropipette aspiration and tether pulling[454,455]. The most prominent technique is pulling membrane tethers from cells, using either OT or AFM[393,456]. The static force ftether – required to hold the tether when pulling is stopped and equilibrium is reached – depends directly on the effective tension[398] (Equation 7):

$$f_{tether} = 2\pi\sqrt{2\kappa_b\sigma_{eff}}$$

where κ_b is the bending rigidity of the membrane. κ_b is generally assumed to remain stable over different experimental conditions and can in principle be deduced from measurements of the tube radius[433]. Equation 7 supposes that no actin polymerizes in the tether, which is true at short times, i.e. less than a few minutes[414].

Myosin 1s and Ezrin have been reported to influence tether force in cells. Using AFM, Diz-Muñoz and colleagues showed that Myo1b or Ezrin depletion decrease membrane tether force in zebrafish progenitor cells[6]. A similar result was obtained with Myosin 1g in lymphocytes[199]. Overexpression of Myosin 1s has also been reported to change the coalescence of multiple tubes[7]. OT-based tether pulling showed that Ezrin phosphorylation increases the tether force in lymphoblasts[243]. Globally, this data has been interpreted as evidence that Myosin 1s and Ezrin contribute to effective membrane tension in general.

Our data on adhesive HEK293T cells expressing YFP EphB2 (EphHEK) revealed that Myo1b depletion perturbs acto-myosin stress fiber distribution after EphB2 stimulation[3]. This suggested a role of Myo1b in cell contraction independent of the activation of Myosin II. A loss in coupling between the PM and the actin cortex in the absence of Myo1b would a priori support a contribution of Myo1b to effective membrane tension. We used OT-based tether pulling on EphHEK cells to measure the effect of Myo1b and rigor mutant expression on membrane mechanics and compared it to the expression of Ezrin and ERM. We performed three kinds of experiments to probe these effects. We measured static tether force and performed dynamic tube pulling assays since PM-actin linkers are also expected to affect membrane friction on the cytoskeleton upon tube pulling[453]. We deduced friction from the force vs. pulling speed scaling and measured the force relaxation time that is related to this friction.

Effective membrane tension in EphHEK cells is dominated by actin.

In order to measure the effective membrane tension, tethers were pulled from adherent cells as depicted in Figure 35A with a typical length of 10 µm. As previously shown, the initial force overshoot depends on the interaction area between the bead and the PM[406] and is not well controlled under experimental conditions (Figure 35A – step 3 and Figure 36A). Upon tube formation the force next decreases and rapidly reaches a plateau. To measure the static tether force, we waited 10 seconds to let the force equilibrate (Figure 35A – step 4). As a previous report showed the presence of multiple tethers and different coalescence depending on Myo1b expression[7], special care was taken to ensure the measurement of forces for single tethers. In agreement with previous reports[395], we confirmed that the tether force doesn't depend on tether length over a broad range in EphHEK cells (Figure 36B).

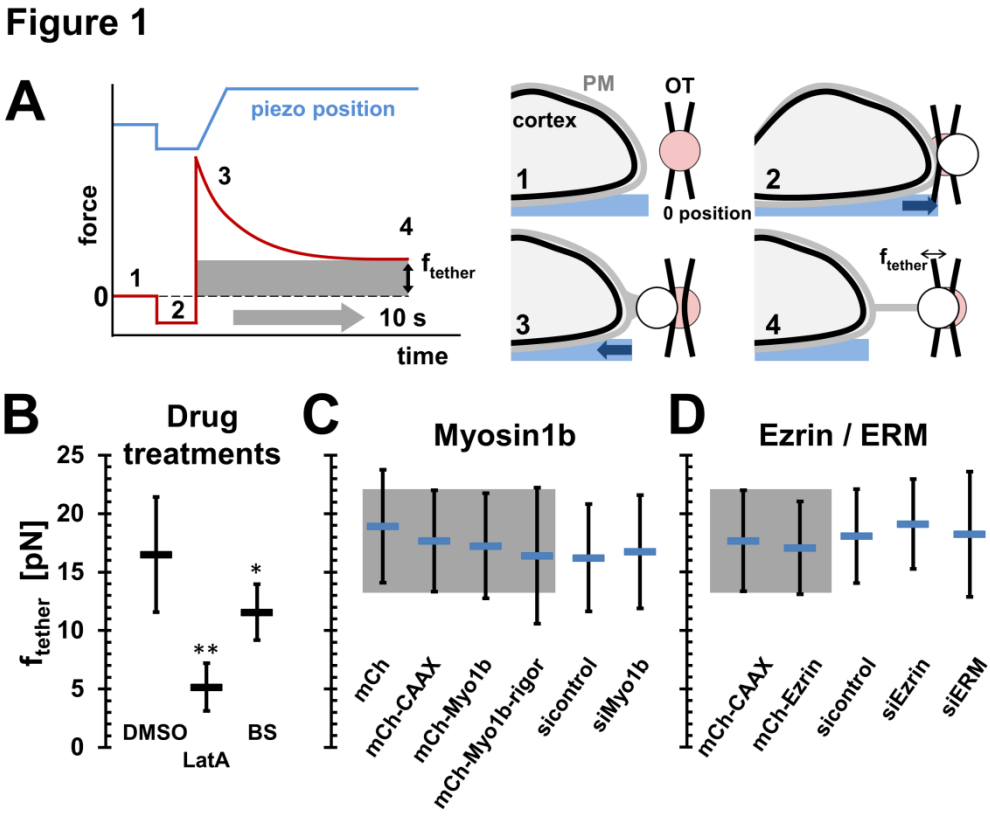

Figure 35 Measuring tether force as a reporter for effective membrane tension.
(A) Force regimes observed during tether pulling from cells corresponding to the steps depicted on the right. A bead at equilibrium position (1) is brought into contact with a cell (2). When the stage is pulled away from the trap, an initial force peak required to detach the membrane from the underlying actin cortex (3) is quickly followed by a stable force ftether (4). | **(B)** Tether forces in EphHEK cells treated with 0.1% DMSO (n=16), 100 nM LatA (n=22), or 20µM BS (n=15). (**p =2.10^{-7}; *p=0.0022) | **(C)** Tether forces in EphHEK cells overexpressing mCherry (mCh, n=36), mCh-CAAX (n=23), mCh-Myo1b (n=44), mCh-Myo1b-rigor (n=40), treated with control siRNA (sicontrol, n=39), or Myo1b siRNA (siMyo1b, n=43). Grey box indicates mean±S.D. for mCh-CAAX | **(D)** Tether forces in EphHEK cells overexpressing mCh-CAAX (n=23), mCh-Ezrin (n=49), treated with control siRNA(sicontrol, n=36), Ezrin siRNA (siEzrin, n=47), or ERM siRNA mix (siERM, n=38). Grey box indicates mean±S.D. for mCh-CAAX | (mean±S.D.)

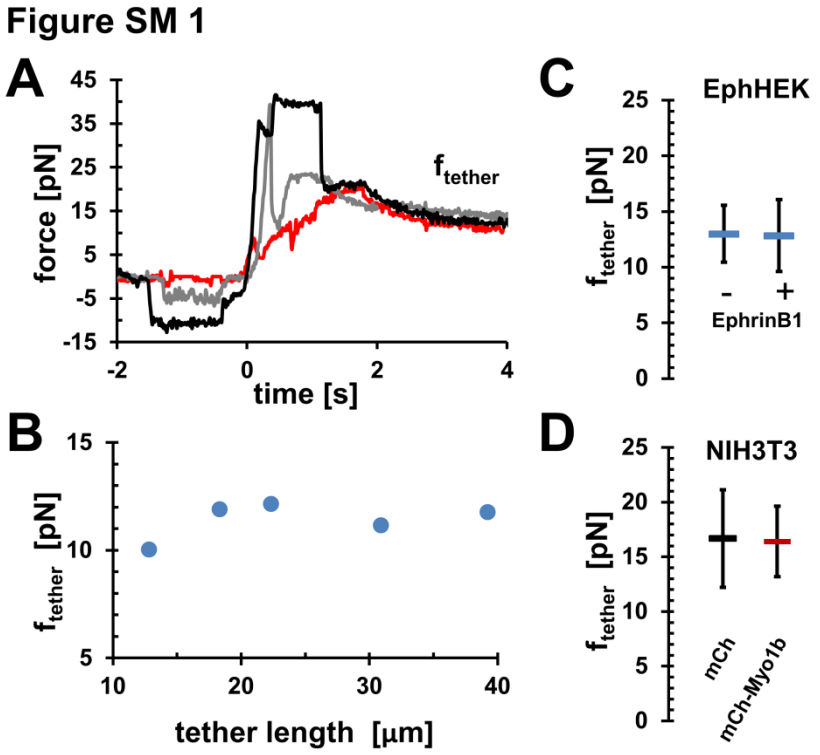

Figure 36 Supplementary figure 1 of MBoC manuscript
(A) Full force profile corresponding to three membrane tethers pulled from different cells during one experiment. While the initial force profile is very different for each of the cells since its depends on the contact area between the bead and the cell membrane, individual tether holding forces converge to similar values within seconds. |**(B)** Tether holding force of an individual membrane tether as a function of tether length. |**(C)** Tether forces measured for untreated EphHEK cells and after stimulation with EphrinB1 (mean± S.D; n=93 untreated; n=52 + EphrinB1). |**(D)** Tether forces measured for NIH3T3 cells expressing mCh or mCh-Myo1b. (mean± S.D; n=24 for both).

We measured a tether force of 16.5±4.9 pN which is at the lower end of values reported for adherent cells[393]. In line with previous findings[401,425] we observed a marked decrease of the tether force when actin was depolymerized by LatrunculinA (LatA) (Figure 35B). Our measurements indicate that around 70% of the effective membrane tension directly depends on actin in EphHEK cells. This value is likely underestimated due to experimental constraints. LatA treatment was done at low concentrations for short periods of time to avoid complete cell detachment from the substrate that precludes tether pulling. When Myosin II activity was blocked using non-cytotoxic Blebbistatin (BS)[457], the tether force decreased to 11.6±2.4 pN, suggesting that contractility influences the static tether force in EphHEK, as reported for other adherent cells[423]. As previous results involve Myo1b in EphB2-driven cell repulsion and given that EphB2 stimulation with ephrin-B1 induces cell contraction[450], we checked if activation of EphB2 and the resulting contraction would alter effective membrane tension, as expected from the effects of BS. For technical reasons, the tether force measurements were performed within a time frame of 10 to 50 minutes after induction

of cell contraction. Under these conditions, we did not observe any difference in tether force (Figure 36C), suggesting that any potential increase in effective membrane tension upon contraction was only transient and undetectable within our experimental approach. Alternatively, the observed effects upon BS treatment might be linked to a global reduction in cortical contractility, yet ephrin-B1-induced contraction might specifically be localized to the ventral surface, not affecting effective membrane tension locally probed by the tether force[431].

Neither Myo1b nor ERM contribute to effective membrane tension in EphHEK cells.

Next we studied the effect of cellular levels of Myo1b and ERM on tether force. Assuming that the membrane bending rigidity is not changed in these conditions, a change in tether force directly reflects a change in effective membrane tension.

Neither overexpression of mCherry-Myo1b nor its rigor mutant, which lacks motor activity[458] and stays bound to actin[1], changed tether force as compared to controls (Figure 35C, Figure 42A&B, Figure 37A&B). Similarly, depletion of Myo1b by siRNA did not affect the measured tether forces (Figure 35C; Figure 37C).

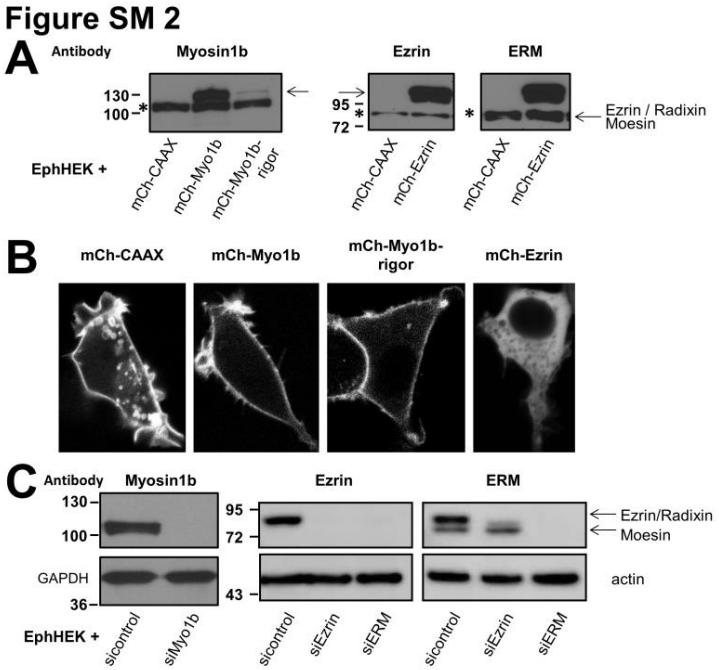

Figure 37 Expression levels of proteins.
(A) Western Blots showing expression levels of proteins after expressing mCherry labeled constructs. The expression of mCherry-Myo1b is of the same order than the endogenous Myo1b (*) while expression of mCherry-Myo1b rigor mutant is quite low (line CAAX_mCH versus with line Myo1b_mCH and Myo1b_rigor_mCH) but this reflects a low transfection efficiency. Expression level of Ezrin_mCh is superior to the endogenous ezrin (*) and ERM. |**(B)** Representative fluorescence images of cells expressing fluorescently-labeled proteins and used for tube experiments. Note that we selected cells with similar expression levels of fluorescent proteins. CAAX and Myo1b constructs are clearly predominantly localized to the plasma membrane, yet Ezrin shows a broad, cytosolic staining. |**(C)** Western Blots showing expression levels of proteins after depletion using siRNA. All siRNA treatments reduce the protein level below detection. GABDH and actin are the loading controls. Note that Ezrin and Radixin are not well separated and correspond to one band (upper band) when detected with anti-ERM antibodies. Thus, this band is only partially reduced in cells treated with Ezrin siRNA. The lower band is unchanged and corresponds to Moesin.

As overexpression of Myo1b had previously been suggested to affect the effective membrane tension in NIH3T3 cells[7], we checked if a difference was detectable in the effective membrane tension as deduced from the static tether force in NIH3T3 cells overexpressing mCherry-Myo1b. Yet, the measured tether forces in NIH3T3 cells were in the same range as in EphHEK cells (Figure 36D). Nambiar and colleagues[7] revealed changes in coalescence dynamics from the analysis of force-time integrals. These integrals contain contributions from static and dynamic forces during elongation, coalescence events of tubes, and the initial energy barrier for tube formation. As such, it seems difficult to extract the contribution of membrane tension from this data.

Concomitantly we tested if manipulation of Ezrin expression affects the effective membrane tension in EphHEK cells. We overexpressed mCherry-Ezrin and depleted Ezrin or ERM using siRNA[459] (Figure 37). Yet, none of these perturbations led to a change in effective membrane tension in EphHEK cells (Figure 35D).

Taken together, this data indicates that neither Myo1b nor ERM contribute significantly to the effective membrane tension in EphHEK cells. The abundance of actin-PM linkers or dominant contribution of adhesion to the substrate may preclude observing a significant effect. Previous papers based on static tether force measurements have reported effects of myosin I isoforms on effective membrane tension in non-adherent cells such as lymphocytes[199], or in cells with high blebbing propensity shortly after plating[6]. Differences between these results and ours might be due to a different regulation of effective membrane tension between adherent and non-adherent cells. Indeed, MLCK alters effective membrane tension in de-adhered smooth muscle cells[441], but does not in adherent keratocytes[442]. Alternatively, considering that our force measurements were performed within 1 and up to 5 days (for depletion) after transfection, changes in tension could be compensated. For example, keratocytes equilibrate membrane tension even after massive increases of the membrane area within ten minutes[433].

Dynamical measurements to probe the PM-actin interface

As shown in [453], another way to probe the effect of PM-actin linkers is dynamic tube pulling. Either the force is measured during tether extension at controlled speed[390,453], or the force relaxation is measured after a fast step elongation[414,460]. Brochard and colleagues had shown from previously published data that PM-actin links – including membrane proteins bound to the cytoskeleton – produce a friction on the lipids when the tether is extended and a tension gradient builds up between the tube and the adjacent membrane[390]. In this regime, force increases with pulling speed and the density of links. Similar effects could also arise from the sorting of membrane constituents out of the tether upon pulling. As tube elongation stops, lipids and

proteins flow into the tether to equilibrate the tension[407,411,460]. Datar and colleagues calculated[414] that this tension gradient, reflected by the tether force, is dissipated with a characteristic relaxation time that depends on membrane-component diffusion, and thus possibly on the density of actin-PM linkers. Here, we performed both types of dynamic tether pulling experiments varying the expression levels of Myo1b and ERM.

Neither Myo1b nor ERM contribute to effective PM-cortex friction in EphHEK cells

We first probed the dependence of tether force on pulling velocity in an intermediate regime (Figure 38A) as proposed in [390]. As expected, the plateau force increases with the pulling velocity $\dot{L}$ (Figure 38B) and scaled as $\dot{L}^{1/3}$(Figure 38C, black line).

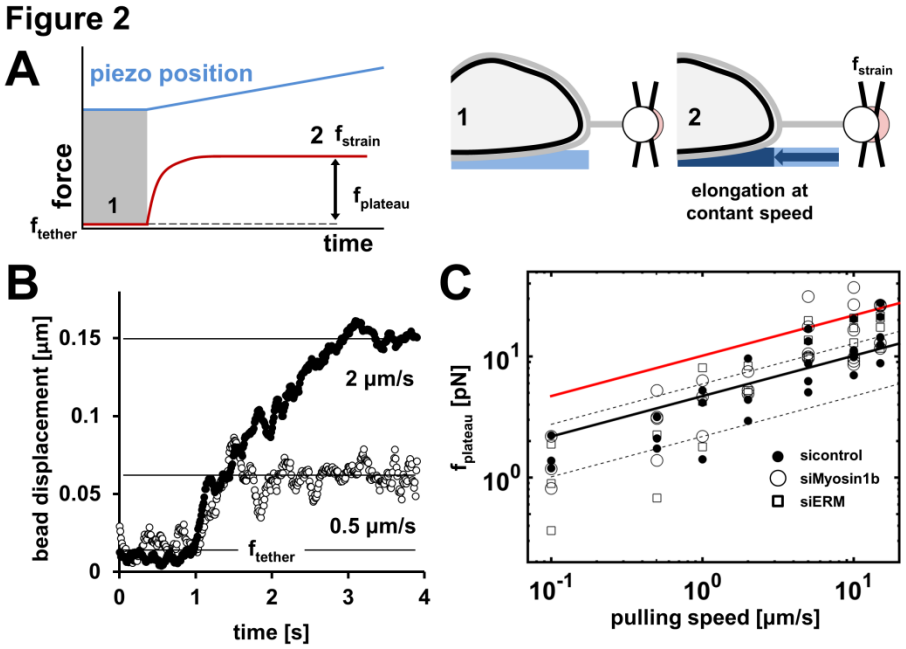

Figure 38 Elongation of membrane tethers at constant speed to assess PM cortex friction.
(A) Elongation of a relaxed membrane tether with holding force f_{tether} (1) at constant speed leads to a force increase that rapidly plateaus at f_{strain} (2). $f_{plateau}$ is defined as the difference between f_{tether} and f_{strain}.|**(B)** Representative data of the bead displacement from trap center measured during tube elongation at 0.5 and 2µm/s. |**(C)** Plot of plateau forces versus pulling speeds. Each data point represents one tether elongation. si_control (●), si_Myo1b (○), si_ERM (□). Fitting with equation 9 as detailed in reference 372, assuming typical values for linker density $v \sim 10^3 \mu m^{-2}$, bending rigidity $\kappa \sim 50 k_BT$, and $\ln(R/r_t) \sim 5$, one finds an effective surface viscosity of $\eta_e \sim 10^{-9}$ Pa.m.s (black line). Imposing an effective viscosity of 10^{-8} Pa.m.s yields the red line, while dashed lines represent a theoretical doubling (upper) or reduction to 10% (lower) of linker density v.

From this data, we extract an effective surface viscosity on the order of 10^{-9} Pa.m.s, supposing a membrane bending rigidity of 50 k_BT and a density of linkers of 103 μm^{-2} as in [390], but we do not detect any difference neither after depletion of Myo1b or ERM (**Figure 38**C), nor overexpression of mCherry-Myo1b-rigor (Figure 41A). The effective surface viscosity is low as compared to other cell types considered in[390], suggesting a low friction between actin and the PM in EphHEK cells. After calculating the force

variation for a higher effective surface viscosity on the order of 10^{-8} Pa.m.s (**Figure 38**C, red line) or a doubling (**Figure 38**C, upper dashed) or reduction by 90% (**Figure 38**C, lower dashed) of the assumed cortex-PM linker density, we conclude that the data obtained with this approach is too spread to detect any difference between PM-cortex interfaces in the same cell type. In contrast, with similar spread in data, significant differences could be detected between different cell types[390].

Myo1b-rigor mutant and ERM affect force relaxation dynamics.

We then asked if any effect of membrane linkers could be detected with step-elongations at high speed. A 5 µm extension at 75 µm/s was applied on a preformed tube with static tether force f_0(Figure 39A). During elongation we observed a rise up to a peak force f_{peak} when elongation is stopped, defined as t=0. We measured the force relaxation over time f(t) at constant tether length. We fitted our data using the expression from[414]. This two-component model was initially developed assuming that during step elongation a minority membrane component accumulates at the neck and behaves as a barrier, eventually passing the neck during the relaxation phase. It accounted well for the force relaxation of axonal tethers. More generally, it should to be valid for any situation where a composition gradient exists between the tether and the cell membrane, and to be sensitive to PM-cortex linker density[414]. Early work on tether pulling from cells generally considered a single exponential relaxation for the force[407,411,461]. Recent work both on vesicles with a reconstituted actin cortex and cellular membranes revealed that the force relaxation cannot be satisfyingly described with a single relaxation time but rather contains both a fast exponential decay (on the order of seconds) independent of actin and a linear slow decay that depends on actin and appears diffusive[460]. We confirmed that a single exponential decay does not account properly for our data (Figure 41A). A double-exponential fits as well as equation 10. However, since the long-time term was phenomenological in [460] and we do not observe a slow relaxation in EphHEK cells (Figure 41C,D), our data is correctly described by a simple model of a composition gradient across the neck. We thus used this model to analyze our experiments and fitted the force relaxation data (Figure 39B) with equation 10, with the relaxation time τ as the only free parameter. τ is expected to depend on the diffusion of the minority component in the cell membrane. Our data set fit well with equation 10 (Figure 39B), giving a relaxation time τ=0.69±0.31 s (Figure 39D).

We first analyzed the impact of actin depolymerization by LatA treatment. We observed a 3-fold decrease of the peak force. As this peak force originates from a variety of processes, we do not further comment on it. Likewise, we found a 3-fold reduction of the characteristic relaxation time (τ=0.22±0.09 s) after LatA treatment (Figure 39D, E).

Similarly, a reduction of peak forces and relaxation times after LatA treatment was previously reported by [414], but the values are different, probably due to cellular differences. This suggests that F-actin affects concentration gradients across tether necks, probably due to actin-PM links reducing diffusion of membrane components.

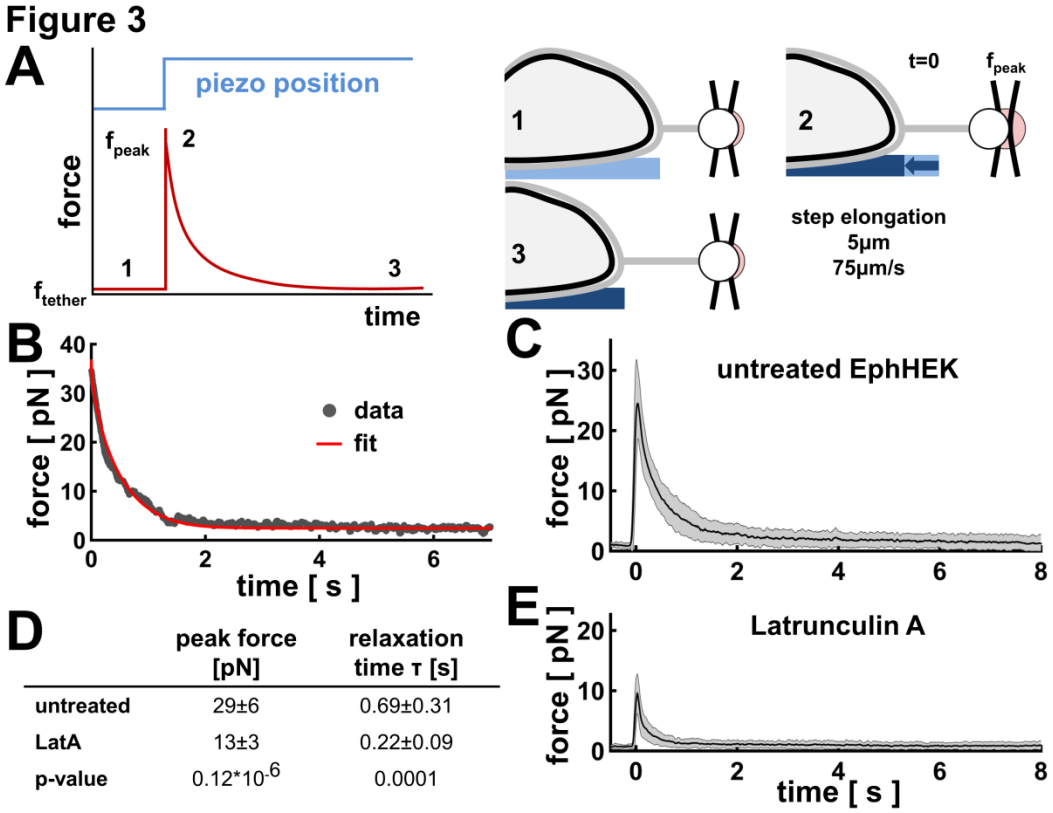

Figure 39 Step elongation of existing membrane tethers to assess tether relaxation.
(A) Three force regimes observed during step elongation of an existing membrane tether (left) corresponding to the sketches on the right. A relaxed membrane tether with holding force f_{tether} (1) is elongated by imposing a fast step displacement of a piezo-controlled stage leading to a peak in force (2). Over time the force relaxes back to the initial value of the tether force (f_{tether}). | **(B)** Individual tube force dataset (grey) and corresponding fit (red) as developed in reference 396 and detailed in the introduction. | **(C)** Plot of forces over time during step-elongation of tethers for EphHEK cells. Mean (black line) ± S.D. (grey area), n=13. | **(D)** Comparison of peak forces and characteristic relaxation times τ as obtained from fits of untreated EphHEK cells and those treated with LatA as shown in panels C & E. | **(E)** Plot of forces over time during step-elongation of tethers for EphHEK cells treated with LatA. Mean (black line) ± S.D. (grey area), n=16. In (C) and (E), for graphic purposes, a rolling average filter was applied to plot the dataset; analysis was performed on full dataset.

Neither depletion of endogenous Myo1b nor overexpression of mCherry-Myo1b changes the relaxation time (Figure 40A, Figure 42C). However, overexpression of the rigor mutant increases it significantly. The rigor mutant is permanently attached to actin, whereas WT Myo1b is bound to actin only during 20% of its ATPase cycle if not under load[165]. This indicates that the force relaxation time is only sensitive to PM-actin linkers when a substantial fraction of them is engaged. Moreover, it suggests that if Myo1b is overexpressed, its catch-bond is not under sufficient load to significantly affect the force relaxation dynamics.

Accordingly, depletion or overexpression of Ezrin did not change the force relaxation time, yet depletion of ERM significantly decreased the force relaxation time (Figure 40B, Figure 42D). This suggests that the potential mechanical effects of ERM in EphHEK cells are either Ezrin-independent, functionally redundant, or individually insufficient to affect force relaxation dynamics due to the high density of other PM-actin linkers[394].

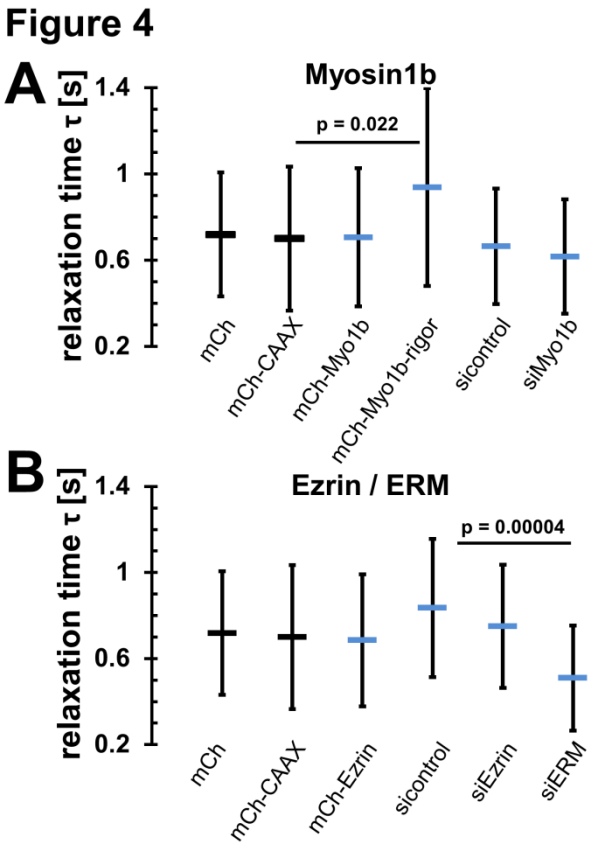

Figure 40 Relaxation times for step-elongated tethers.
(A) Relaxation times obtained from fitting individual data sets for EphHEK cells overexpressing mCh (n=27), mCh-CAAX (n=35), mCh-Myo1b (n=34), mCh-Myo1b-rigor (n=30), treated with control siRNA (sicontrol, n=38) or Myo1b siRNA (siMyo1b, n=34).| **(B)** Relaxation times obtained from fitting individual data sets for EphHEK cells overexpressing mCh (n=27), mCh-CAAX (n=35), mCh-Ezrin (n=33), treated with control siRNA (sicontrol, n=28), Ezrin siRNA (siEzrin, n=34), or ERM siRNA mix (siERM, n=32). (mean±S.D.)

In conclusion, our data shows that manipulation of the expression level of one type of PM-actin linker in EphHEK does not perturb the effective membrane tension nor the friction deduced from tether elongation at constant speed. Although these methods reveal differences between cell types they are not sensitive enough to distinguish between the effects of specific linkers in EphHEK cells. However, we did measure differences in relaxation time after dynamic tether extraction. This suggests that different dynamic tether measurements, at different speeds, probe different properties of the membrane-cytoskeleton interface. Depending on the cell type, the number of expressed linkers of each type (e.g. ERM, Myosin 1, transmembrane, or BAR domain proteins) and their association rate to actin and PM are variable. The sensitivity of the

membrane tether pulling assay to a single type of PM-actin linker might thus strongly vary from one cell type to another, explaining the apparent discrepancy between our results and previous reports. Our work highlights the limitations of the tether pulling approach and the importance to design new assays and to further develop theories describing the impact of PM-actin linkers on membrane mechanics. So far, how linkers contribute to membrane tension remains an open question.

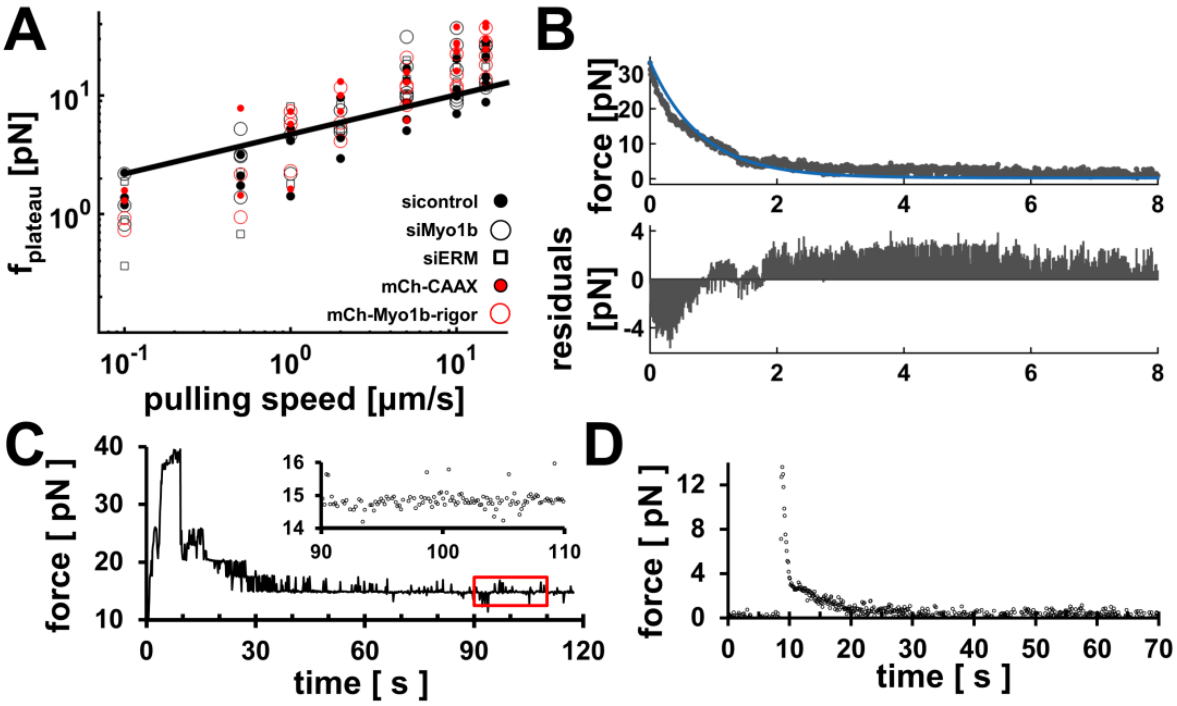

Figure 41 Supplementary Figure 3 of submitted manuscript
(A) Plot of plateau forces versus pulling speeds. Each data point represents one tether elongation at a given pulling speed L . sicontrol (●), siMyo1b (○), siERM (□), mCh-CAAX (●), mCh-Myo1b-rigor (○). Fitting with equation 9 as detailed in reference 372 and assuming typical values for linker density $\nu \sim 10^3 \mu m^{-2}$, bending rigidity $\kappa \sim 50 k_B T$, and $\ln(R/r_t) \sim 5$, one finds an effective surface viscosity of $\eta_e \sim 10^{-9}$ Pa.m.s (black line). |**(B)** Single exponential fit to tether relaxation data after step elongation. Upper panel shows the data set (grey) and corresponding single exponential fit (blue line) imposing fpeak and ftether from data. Lower panel shows the residuals of the fit. |**(C,D)** Long-time force profile for a tether pulled from a cell (C) and for dynamic tether elongation with ftether normalized to 0 (D).

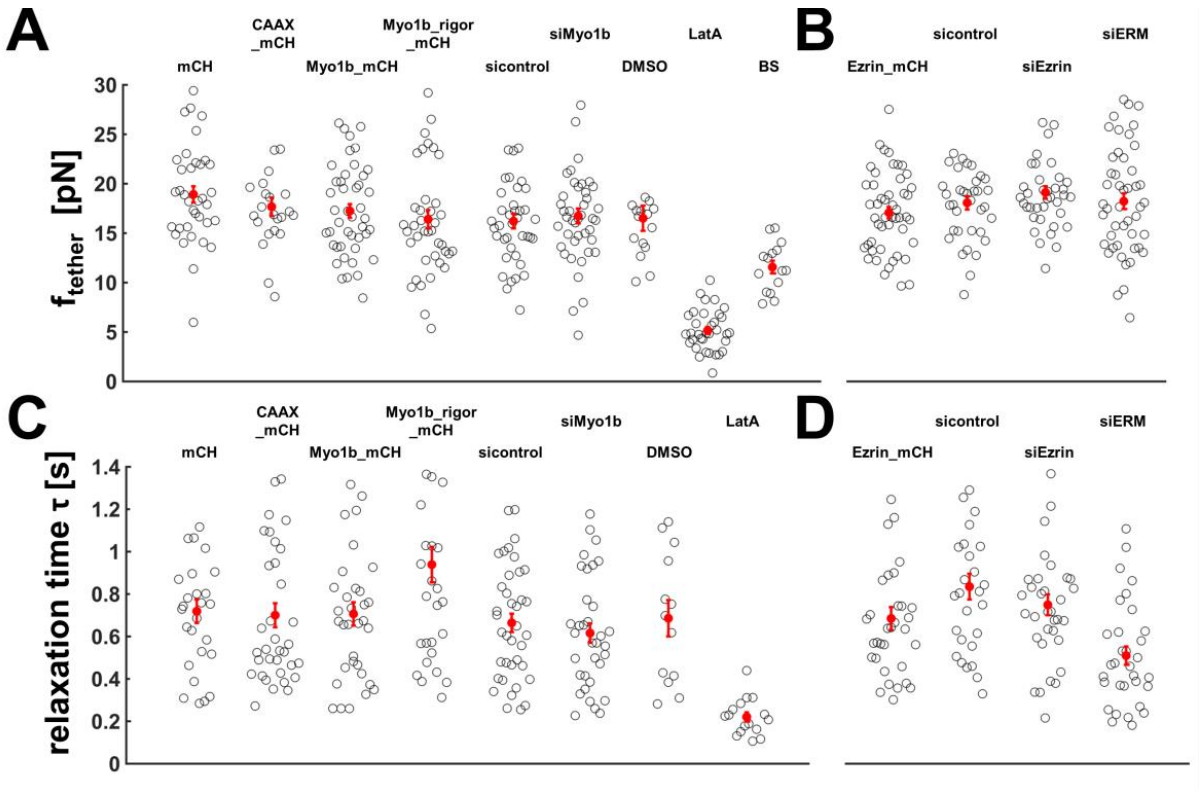

Figure 42 All measurements in the different conditions.
(A/B) All individual ftether measurements as summarized in Figure 1 for all probed conditions.|**(A)** Myosin1b variants and drug treatments|**(B)** Ezrin variants. |**(C/D)** All individual fit results for relaxation time τ as summarized in Figure 4 for all probed conditions.|**(C)** Myosin1b variants and drug treatments.|**(D)** Ezrin variants. The orange error bars correspond to the statistical error (i.e. standard error of the mean)

Discussion

1. Experimental limitations for bead-based EphB2 activation

While we were able to successfully induce a specific response by stimulating EphHEK cells with ligand-covered beads a couple of limitations apply to this particular system that considerably limited further exploitation of this system. Notably, the bead, probably due to its strong adhesion with the plasma membrane through ligand-receptor interactions, strongly adheres to the cell's surface and we were not able to remove the bead from the cell surface with the optical tweezer once contact was made, reminiscent of the reported occurrence *in cellulo* of trans-endocytosis to remove engaged receptor-ligand from the cell surface. As the lab of Evelyne Coudrier evidenced increased filopodia formation around the area of cell to cell contact between ligand and receptor expressing cells we initially thought to potentially be able to quantify, e.g. pushing forces or at least an increase in filopodia density at the contact site between the cell and the bead. Yet, we never observed such an increase, probably because the adhesion area of the bead thus creating a large energy barrier for membrane tube formation. A potential work-around would be to use a ligand-covered GUV instead of a bead, that might be deformable enough to allow for membrane protrusions to form at the interface, yet again only if the adhesion area would stay sufficiently small. Ideally one would want a structure that has an adhesion area that is similar to the tip area of a filopodium, e.g. a thin AFM cantilever, yet highly deformable to allow protrusion generation.

2. Critical blebbing pressure is Myosin 1b independent

We did not observe any striking difference in critical blebbing pressure after depletion of Myosin 1b. Membrane-cortex detachment depends on the density of linkers, on the critical force per linker and on the cortical contractibility. The population of linkers at the plasma membrane is diverse. Considering that this pressure is largely dependent on the density of linkers one might posit that Myosin 1b is simply not abundant enough at the plasma membrane to reveal a fundamental change in blebbing pressure, or that efficient compensatory mechanisms exist (see

hereafter). The relatively low density of Myosin 1b among linkers seems the most likely explanation for the absence of an observable effect. Indeed, at whole cell protein levels[462,463], i.e. not only the plasma membrane bound part, and only considering Myosin 1c and ERM as linkers, i.e. neglecting all other contributions to membrane-cortex adhesion, one finds that full depletion of Myosin 1b with no compensatory effects, would lead to a maximum of ~20 % in linker density reduction assuming comparable binding strengths (Figure 43).

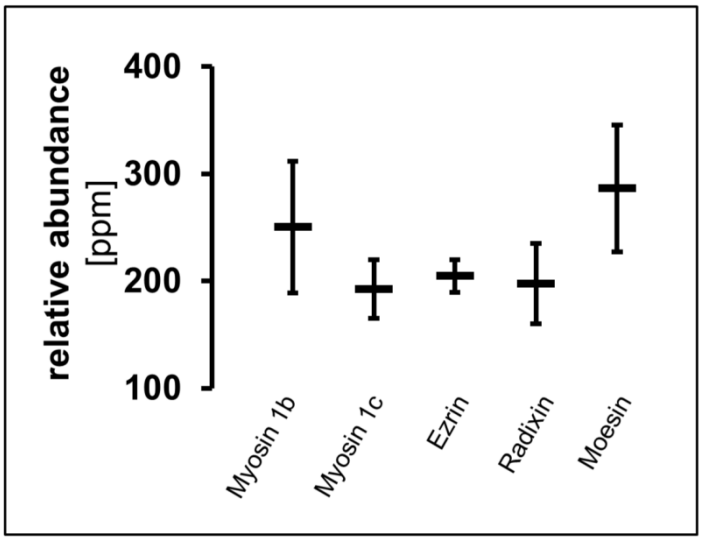

Figure 43 Relative total cellular abundance of Myosin 1b, Myosin 1c and ERM.
Based on published mass spectrometric data of 11 human cell lines the average relative cellular abundance of each protein and its standard deviation is plotted.

3. Tension buffering in cells is generally efficient

In this chapter we have used all available mechanical methods that are usually recognized for measuring the effective plasma membrane tension and probing the mechanics of the cortex-membrane interface. However, we could not detect any influence of Myosin 1b. Considering evidence on other cell types showing efficient cellular processes that buffer membrane tension[415,433] the lack of effect is actually less surprising than the fact that in some cells, e.g. lymphocytes, strong changes in effective membrane tension after depletion or overexpression of proteins can reproducibly be observed. This suggests that cells might react differently to perturbations and show either highly efficient compensation mechanisms, or on the contrary high tolerance towards such changes. While one might posit that every cell type is different and thus propose a continuum distribution of effects and importance of compensation, fundamental biological reasons might underlie the presence of different buffering systems and the vast array of cortex – plasma membrane linkers. Our results and

previous reports[441,442] indicate, that indeed both the relative density at the plasma membrane-actin interface, and a fully established adhesion to the substrate might fundamentally change the measured parameters. Furthermore, a feedback loop between effective membrane tension and adhesion formation has phenomenologically been described[422,464], in which cycles of increasing local membrane tension at the cell edge are critical for the positioning of new adhesion sites. Controlling this process might be the principle role of class 1 myosins and ERM, which disappears once adhesion has been established.

As we do not observe a striking phenotype in absence of Myosin 1b regarding adhesion at steady-state, its effect on the dynamics of cell spreading could be studied using traction-force microscopy and/or reflective interference contrast microscopy. Another set of experiments that remains to be performed is to measure if de-adhered and recently sedimented cells, that have not fully established their adhesion to the substrate, reveal a difference in effective membrane tension in absence of Myosin 1b, as one might expect if the adhesion to the substrate dominates the effective membrane tension throughout the cell. In that case it would mask any potential contribution of Myosin 1s or ERM, or lead to a shift in the cellular control system, thus abrogating the potential roles of Myosin 1 and/or ERM in effective tension that are at play when the cells are rounded. If that is the case, it would be interesting to map effective membrane tension over the cell cycle in cells depleted for Myosin 1s and/or ERMs, as their effect should dynamically become dominant during mitosis, when cells round up to divide. Furthermore, one might suspect a phenotype regarding mitosis in the absence of Myosin 1b, as has been described for Moesin [238,240]. In any case, the phenotypes which have been described in EphHEK cells concerning the role of Myosin 1b as an effector for EphB2[3] are clearly not coupled to a change in effective membrane tension nor membrane cortex friction, at least within the resolution limit of current methods, as these were observed under the same conditions as our mechanical measurements.

In order to better understand these potential compensation mechanisms and circumvent them experimentally, one might use different systems to perform ad-hoc perturbations to the distribution of PM-actin linkers, using e.g. optogenetics or Rapamycin based approaches[465–467]. This would allow the (reversible) removal of a specific protein of interest away from the PM-actin interface within seconds, thus circumventing long-term adaptation occurring after plasmid-based transfections. Secondly, one might employ the Calcium-mediated actin reset as described in[468], during which the entire cortical actin is disassembled and reassembled within minutes as a benchmark for potential changes in static tether force due to cortical dynamics, but independently of adhesion.

4. Tension propagation vs. tension regulation

Recent evidence suggests that membrane tension gradients dissipate very slowly in biological membranes as compared to pure model lipid membranes, which has been attributed to the presence of a dense network of connections between the plasma membrane and the underlying actin cortex[431]. This is in striking contrast to *in silico* results which for bare membranes suggest almost instantaneous tension equilibration[469] as well as theoretical arguments made for cells[470]. This is intriguing, as on the one hand, a slow effective tension relaxation along the plasma membrane would explain the observed tension gradients in migrating cells[432], but it sheds doubt on the conceptual idea that local changes in effective membrane tension by themselves without a need for signaling[470] can be a determining factor in changing cellular behavior on a global level[431].

In light of the obtained results in this work, it would be interesting to assess if instead of tension regulation, the presence and the density of Myosin 1s and ERM might affect relaxation of tension gradients along the membrane. This could experimentally be achieved through overexpression of mechanosensitive channels and Ca^{2+} imaging as performed in [431].

5. Dynamic tether experiments to assess cortex-membrane friction

Both ways of dynamic tether pulling presented in this thesis (i.e. constant speed elongation and step elongation) have been employed to study the mechanical properties of the plasma membrane-actin interface. To our knowledge, this is the first comparative study in which both techniques have been employed on the very same cell type and varying protein expression conditions. Both techniques show different results and suggest that although related, they actually assess different parameters in cells, or at the least have considerable differences in their sensitivity to detect changes. Notably, constant speed elongation is impressively noisy[390,411], and based on parameter sensitivity estimation, this method should only be able to reveal massive changes. While it thus allows to probe a parameter over a vast range of pulling speeds, it seems not to be particularly suited to investigate differences within a given cell type, or to compare closely related cells. In conclusion we find that step elongation is a better suited tool to study changes in cells, at least when studying the effects of PM-actin linkers as done in this work, due to increased signal-to-noise.

6. The biology of friction.

It has to be noted that while the role of tension in biology is well appreciated and multiple demonstrations of its functional relevance exist, the case of friction is more mitigated. In order to reveal changes in friction we employed tether elongations at a speed of 75 μm/s in order to capture the entire relaxation after pulling. While the fact that we only observe differences at high pulling speeds does not preclude an effect of friction at lower speeds, the fast relaxation we observe suggests that only large and steep flows might actually reveal the effect of linkers on cortical friction, whereas at a lower shear level, the cell is able to readily compensate any stress parallel to its surface. The one example in which a steep and large flow can practically occur under real biological conditions would be the transition period for cells in the blood flow that start to adhere to a vessel's endothelium. In that case, one could hypothesize that the density of cortex-linkers plays a role in extravasation efficiency.

7. What is the relevance of a catch-bond *in vivo*?

Actin binding domains experience continuous stresses of around 2 pN in cells originating from persistent cortical actomyosin contractions[471] which means that Myosin 1b should *a priori* be constantly engaged in its catch-bond state. Thus it remains an open question if, why, and how the catch-bond properties are relevant in cells. In order to actually study this question, one would need a Myosin 1b with ideally identical properties, yet with abolished catch-bond behavior. Unfortunately, the structure of Myosin 1b's tail domain is not known at this point and currently precludes the design of such a specific catch-bond mutant. Meanwhile, the three cellular splice isoforms of Myosin 1b have different catch-bond behavior, and thus it would be instructive to study them in detail to distinguish the individual contributions of the different isoforms, assuming that the different catch-bond behavior indeed drives cellular function. This would as well help to better understand the conundrum of Myosin 1b which seems to be functionally involved in seemingly different processes, from PM-related cell functions[3,6] and organelle morphology[1,2], to axon differentiation[5].

Perspectives

It is a nice and generally simple task to come up with ever more complicated experiments once reaching the end of one's own project. I will thus limit my scientific curiosity and fantasy to two main points which I consider of fundamental importance at this step for the field.

Development of new experimental approaches

The goal here is fairly simple yet non-obvious: Instead of pulling local tubes in a reasonably inefficient and tedious way; it would be fantastic to have a tool which allows the observation of effective and/or on plane membrane tension in real-time at the cellular scale. Ideally the reporter would be protein-based and thus allow expression in cells, ultimately even tissues. Obvious candidates to serve as starting points are mechanosensitive channels, which have already almost 20 years ago been suggested as a tool[388]. Interesting eukaryotic candidates which have recently gained considerable attention are the Piezo-family members both as research subjects[427–430] and tools[431]. The fundamental problem in this approach is (at least) two-fold: 1. Mechanosensitive channels tend to have open probability transitions that are affected by higher tensions than what is observed as resting values in the plasma-membrane. Thus, the mechanics of the receptor would need to be fundamentally changed in order to allow a dynamic response range within the biologically relevant tension ranges. This might be achieved through rational design of mutants, as has been performed to optimize fluorescent molecules[472] and transmembrane receptors[473]. 2. Ideally one needs to ensure that the developed system is tension-sensitive but not curvature-sensing.

Alternatively, one might conceive a FRET-based tension sensor (Figure 44), e.g. using DNA origami which could be calibrated in liposomes, resembling the FRET-based sensors developed for adhesion molecules[471]. The principal problem would be that such a sensor critically depends on the lipid-to-lipid distance, which might be changing enough to detect changes if one is in the stretched-tense situation, yet in cells the entropic-tense regime is more likely to be dominant, where lipid-to-lipid distance changes should be negligibly small. Thus, although conceptionally appealing, such an idea is likely not going to work in cells, while it might be useful to characterize, e.g. local changes in tension by protein binding on liposomes.

Thirdly, one might be able to deduce membrane tension from the emission fluctuations of membrane dyes, e.g. laurdan, that are sensitive to hydration, which is a function of tension, packing density, and local curvature[474,475].

Systematic characterization of mechanical properties

In light of the variety in different cell lines both regarding absolute values of effective membrane tension and the different contribution of proteins to it, it would be interesting to systematically measure and compare effective membrane tension in different cell types and correlate it to, e.g. relative abundance of cortex-membrane linkers, adhesion phenotype.

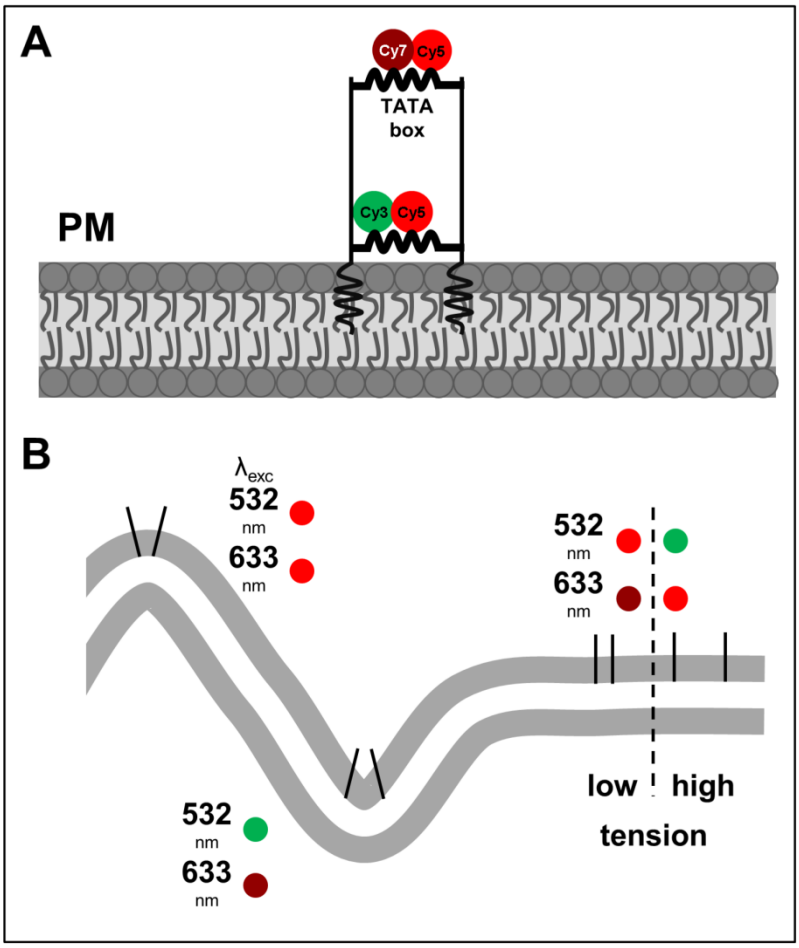

Figure 44 A FRET-based membrane tension sensor
(A) Scheme of the proposed dual FRET-based membrane tension sensor. Lipid anchors allow incorporation of the sensor into cells from the outside. Both FRET pairs are connected by a TATA box allowing low pN force resolution. While one FRET pair is close to the membrane, the other pair is positioned at a distance. | **(B)** Calibration approach to dissect tension and local curvature effects. As both FRET pairs are positioned at a different distance from the membrane the relative change in FRET efficiency is different depending on the local curvature. Whereas positive membrane curvature decreases FRET efficiency in the distal FRET couple, negative membrane curvature decreases FRET efficiency at the proximal FRET couple. Both should in turn respond in a proportional way to in-plane tension. Calibration with liposome would allow characterizing the parameter space of FRET efficiencies that correspond to given combinations of tension and curvature.

Part B – Effects of Myosin 1b on receptor and actin dynamics

Introduction

1. The influence of actin on receptor dynamics in the membrane

Proteins in the cell membrane are mobile and move laterally in the membrane[476], yet consistently exhibit lower diffusion than lipids within the membrane[477,478].

1.1 Definition of a membrane-adjacent mesh that hinders diffusion

Hindered diffusion of the Band 3 transmembrane protein and a regulatory role of membrane-adjacent cytoskeletal structures in restricting its diffusion in the erythrocyte membrane are demonstrated early in the literature and reveal fundamental principles of the interplay between transmembrane proteins and the underlying cytoskeletal network[479–482]. Results from single particle tracking (SPT) and fluorescence recovery after photobleaching (FRAP) of E-cadherin and the transferrin receptor revealed that the membrane is 'felt' by some receptors as a compartmentalized fluid with discrete domains that constitute diffusive barriers, giving rise to four principal modes of motion, i.e. immobilized, Brownian, Brownian with superimposed ballistic motion, and confined Brownian. The dominant mode was confined Brownian motion (64%), whereas ballistic motion was only observed in around 2% of analyzed tracks[483]. The important role of intracellular boundaries, i.e. cortical barriers, was demonstrated by treatment with cytoskeletal drugs[484] and in comparative studies where transmembrane receptors encounter more barriers than GPI-anchored proteins[485]. The measured effective mesh size for the presumed cytoskeletal barriers did not correspond well to assumed sizes of a perfect mesh, suggesting that a dynamic, metabolically active grid was present and encounters with the barrier were probabilistic. This allowed explaining the differences between effective mesh size as probed by barrier-free paths, i.e. the average length a molecule can be dragged along the membrane before encountering a barrier, and ultrastructural information from electron microcopy, and the different temperature-dependent scaling between diffusion coefficients and barrier-free paths[486]. Depending on cell types, and acquisition speeds, effective compartment sizes range from tens to hundreds of nanometers[487], possibly depending on different cytoskeletal elements, e.g. spectrin in red blood cells and actin[488].

In the case of transmembrane receptors, immobilization of the receptor on the actin cytoskeleton can be induced by ligand binding[489]. This is illustrated by the behavior of, e.g. the transferrin receptor. Its local diffusion is unhindered, while its reduced hop frequency leads to a much lower effective diffusion coefficient, due to corralling by the actin cytoskeleton[490]. Furthermore, such corralling and tethering to the underlying actin has been proposed to be responsible for the greatly reduced diffusion coefficients upon clustering[491–494], that is not readily explained by increases in effective radii of oligomers as would be expected from Brownian motion since in 2D, diffusion coefficients change only logarithmically with cluster size[493].

There are two ways how an underlying actin cortex might regulate the diffusion and create boundaries for transmembrane proteins: firstly, through direct interaction and binding to the protein, thus immobilizing it along at the boundary, and secondly simply by spatially inhibiting the passage, thus restricting the available space for diffusion without affecting individual microscopic diffusion[495]. The finding that lipids experience similar compartmentalization in cellular membranes led to the membrane-protein picket model, in which a large population of transmembrane proteins is immobilized in the plasma membrane (up to 30% of total membrane proteins[496]) by its interaction with the underlying actin cytoskeleton, functioning as pickets that maintain the fence, i.e. the actin mesh, in close proximity to the plasma membrane[497,498]. This creates two kinds of diffusion barriers. 'Free' transmembrane proteins can sterically[499] or specifically[500] experience reduced diffusion due to the fence. In addition, the high density of immobilized pickets creates additional diffusion barriers within the plasma membrane as immobilized 'obstacles', thus slowing down macroscopic diffusion of both lipids[501,502] and proteins[503,504]. Beyond these steric effects on thermal fluctuations, active control of nanocluster formation by dynamic actin structures has been demonstrated conceptually in a minimal *in vitro* system[505] and for GPI-anchored proteins[373,506], in which trans-bilayer control is exerted through phosphatidyl-serine mediated coupling[507]. Both active and steric effects on lipid and protein diffusion, and a higher sensitivity of proteins to actin density have been reproduced *in vitro*[508].

1.2 Intra-bilayer obstacles beyond pickets

Beyond the role of immobilized transmembrane pickets and the underlying actin fence, the plasma membrane itself can generate diffusion barriers and lateral segregation of constituents that is independent of actin. The most notable case is the presence of lipid rafts, short-lived, small scale assemblies of specific membrane lipids, specifically cholesterol and sphingomyelin, which are more ordered, i.e. more densely packed, than a standard phospholipid bilayer and can serve as a local hub for enrichment of some proteins and exclusion of others[11,26,27,509]. By the generation of line

tension it can create effective barriers for diffusing proteins and lipids and explains the effects of cholesterol depletion on diffusion[510]. Similarly, the varying length of lipid acyl chains can generate domains of differing membrane thickness thus locally segregating transmembrane proteins based on their transmembrane domain's length and altering their diffusion[511,512]. Figure 45 summarizes the different mechanisms that fundamentally limit/govern the diffusion of both lipids and proteins as highlighted in[513]

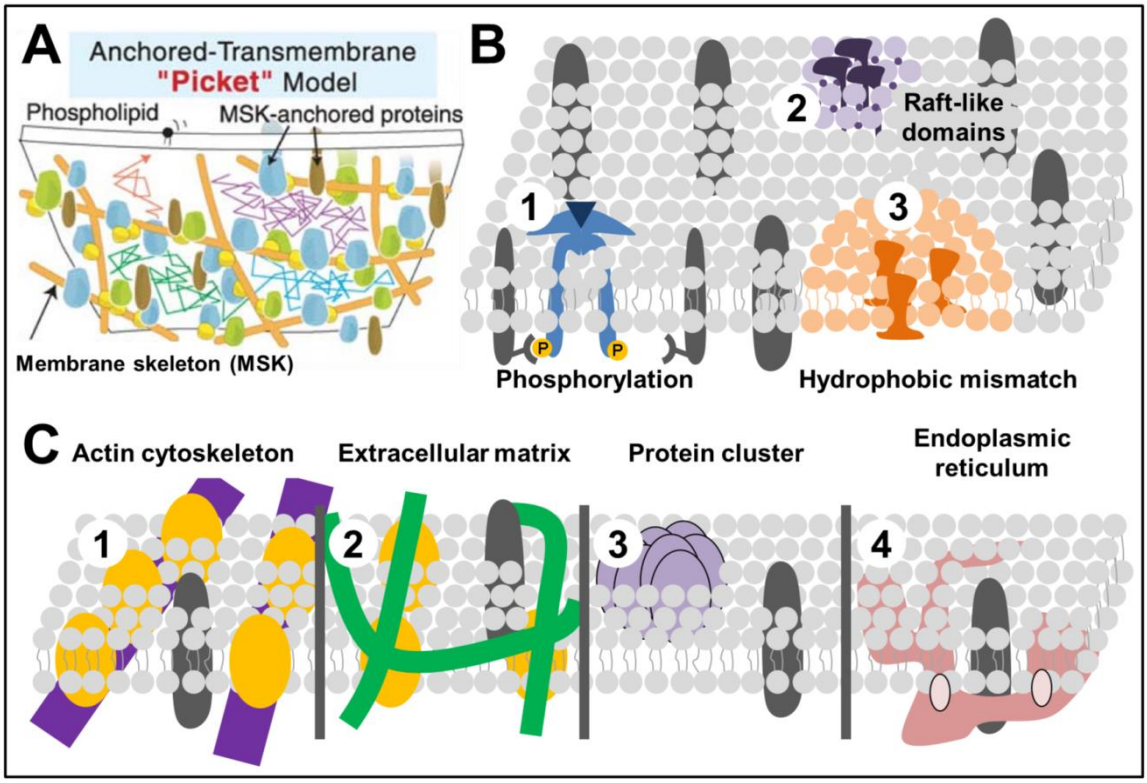

Figure 45 Hindered diffusion in the plasma membrane.
(A) The classical picket-fence model as conceptualized by Kusumi and others. The fence (membrane cytoskeleton) is held in close apposition to the membrane by membrane skeleton bound proteins (pickets). Reference 28 | **(B)** 3 examples of diffusion hindrance in the plasma membrane: 1. Phosphorylation of transmembrane proteins can immobilize other proteins if they interact with the phosphorylated residues. 2. Raft-like nanodomains can partition membrane constituents and limit diffusion by confinement of raft molecules and by hindrance through increased line tension for non-raft molecules. 3. Hydrophobic mismatch can separate and restrict transmembrane proteins based on the length of their transmembrane domains. | **(C)** Changing diffusion through different 'fences': The actin cytoskeleton (1), extracellular matrix proteins (2), large immobile clusters of proteins (3) and endomembrane systems like the endoplasmic reticulum (4) can all limit diffusion and with the exception of case (3) create discrete compartments. Adapted from reference 513.

1.3 State of the art

Through development of new experimental approaches, and notably technical increases in resolution, both in space and time, we nowadays have a rather advanced understanding of the complexity governing diffusive processes in the plasma membrane and how it is affected by both the extra cellular matrix and the underlying actin cortex. Furthermore, using advanced experimental approaches, e.g. high speed single particle tracking[498,514] and advanced fluorescence correlation spectroscopy[515,516], one can characterize compartment sizes and distinguish between specific immobilization and

steric hindrance. HomoFRET measurements[517] and other polarization-sensitive methods[518], super-resolution microscopy, and image correlation spectroscopy methods[519] all give information about the organization of proteins within the membrane, e.g. their relative packing density and cluster-sizes.

1.4 Functional consequences for signaling

Diffusion and cluster formation are of fundamental functional importance for membrane receptors, e.g. to integrate extracellular inputs into effective signaling outputs[520]. Immunoglobulin E receptors (FcεRI) cluster show increased diffusion and delayed immobilization after ligand binding when actin is disrupted[488]. Similar effects were described for CD36, which in macrophages shows a receptor-specific linear diffusive motion that is actin and microtubule dependent but cholesterol independent. Furthermore, cytoskeletal perturbation led to decreased clustering and reduced signaling output after activation[521]. Similar findings were made for the insulin receptor[522]. Integrins show a complex diffusion profile with co-existence of multiple populations of different diffusion and immobilization behavior that depends on actin integrity[523]. It was hypothesized that a small fraction of integrins has to be already immobilized on actin in order to be activated upon mechanical stresses. In this scenario the immobilized molecules serve as a hub that is required as a nucleation point, which is growing through the mobile fraction that can efficiently be recruited[524].

In the case of the antibody-binding Fcγ receptors, diffusion is slowed down upon cholesterol depletion, and controlled by tyrosine kinases, yet independently of receptor phosphorylation. This happens by increase in effective actin mesh size through Syk kinase and promotes increased diffusion and clustering of Fcγ receptors[525]. A similar feedback promoting receptor engagement by means of altered actin structures, here driven by cofilin-mediated severing, has been demonstrated between the toll-like receptor and the B cell receptor[526]. CD1d in antigen presenting cells is equally restricted in motion by interaction with actin that prevents coalescence of nanoclusters, modulating the activation of natural killer T cells[527]. During phagocytosis activation of Fcγ drives the creation of an integrin and actin-based diffusion barrier. This barrier locally excludes CD45, a phosphatase, thus allowing amplification of signaling[514].

In summary, the diffusion of transmembrane receptors in the membrane, its regulation through the actin cytoskeleton, and in some cases the ability to form higher order oligomers after ligand binding are of fundamental importance for successful receptor engagement and signaling output. While the importance of cluster formation in EphB2-driven signaling is well established, how EphB2 diffuses and how it depends on actin has not been studied to our knowledge.

Working hypotheses

1. Diffusion of transmembrane receptors

The influence of the organization and interaction of the actin cortex on transmembrane receptor behavior has been identified and studied, in most detail in the context of the immunological synapse[528,529]. Considering the ability of Myosin 1b to interact with EphB2 we thus decided to study the behavior of EphB2 within the plasma membrane and how it is affected by Myosin 1b. We envisioned three possible scenarios:

Myosin 1b changes the dynamic cortical actin network.

If Myosin 1b is involved in controlling the geometry of the dynamic cortical actin network, its depletion might lead to increased lateral diffusivity of EphB2 receptors and alter clustering efficiency by increasing the likelihood of encounters. Such effects have been described for other receptors depending on actin[521,525,526,530]. As EphB2-driven signaling is known to be sensitive to cluster size[310] this might explain the observed difference in cellular behavior after stimulation. One explanation for a change in effective diffusion coefficient might be a change in the confinement size, thus leading to macroscopically larger effective diffusion rates. In that case one would expect **increased EphB2 diffusion after depletion of Myosin 1b**, an observation that when observed, might be followed up using more advanced methods like high-speed single particle tracking.

Myosin 1b immobilizes EphB2 by linking it to actin.

Myosin 1b could pin a subset of EphB2 receptors to the actin cortex via its interaction with both EphB2 and actin. This immobilized population might serve as a nucleation hub for efficient engagement in signaling, and a loss of it would lead to different outcomes when cells are stimulated. In this case, **depletion of Myosin 1b** would be expected to **increase the mobile fraction** as observed by FRAP, while the diffusivity of EphB2 might stay constant regardless of Myosin 1b.

Myosin 1b changes the steady-state distribution of EphB2 receptor clusters.

Lastly, we postulated that even without affecting immobilization to actin and EphB2's diffusion coefficient, Myosin 1b might be directly involved in the determination of **steady-state cluster size distribution**. We employed fluorescence anisotropy measurements to assess this question.

2. Actin geometry and dynamics

Secondly, beyond an effect of Myosin 1b on EphB2 diffusion or clustering, we also hypothesized that Myosin 1b could be important for the generation of actin flows which are fundamentally linked to cellular contraction. We thus employed TIRF-SIM imaging of the ventral actin cytoskeleton before and after stimulation of EphB2 with its ligand in the presence and absence of Myosin 1b. We quantified and compared the generated flows by performing particle image velocimetry (PIV) on the obtained datasets.

The following scenarios could explain the reduced contractile efficiency:

Myosin 1b controls actomyosin network geometry.

It is well established that actin network structure controls network contractility[97,531]. If Myosin 1b was important for the generation of Myosin II-driven contraction within the ventral side by e.g. changing the actin geometry at the ventral surface or controlling connectivity of the network, its absence could lead to **reduced flow**, thus explaining why cells were contracting less, although signaling was functional and Myosin II was successfully activated.

Myosin 1b acts as a molecular clutch for actin flows.

In contrast, Myosin 1b might as well function like a clutch which is necessary to couple the generated flows to the plasma membrane in order to allow for efficient contraction. Depletion of Myosin 1b could thus lead to **increased flow velocities**. These increased flows and the observed reduction in contractility might be mechanistically linked because the actin generated flows need to be efficiently coupled to the plasma membrane in order to allow the cell to contract.

Myosin 1b changes large scale coherence of the cytoskeleton.

Related to but different from the first hypothesis, Myosin 1b might alter the cytoskeletal coherence of the cells ventral surface rather than its network geometry. Cytoskeletal coherence is the concept that a locally highly dynamic network, as is the case for actin, needs a controlled spatial organization in order to create, e.g. forces across the cell body or well aligned traction forces, as can be observed in cells[63,64]. If Myosin 1b were required in such coherence, one might expect random or chaotic **local variations in flow** that **do not coalesce into spatially well-oriented flows**.

We have used different techniques to test these hypotheses that we present hereafter.

1. EphB2 diffusion

Ventral FRAP reveals no influence of Myosin 1b on EphB2's diffusion coefficient.

Bleaching a circular spot at the ventral surface of EphHEK cells allows the estimation of an effective diffusion coefficient that represents the weighted average of the molecule population's diffusion coefficients (Figure 47A). We treated the cells with mild doses of cytoskeletal drugs which show clear changes in morphology yet maintain a stable adhesion within the experimental time frame. We used LatA to depolymerize actin[532], CK-666 to specifically inhibit the Arp2/3 complex[533] and thus the maintenance of branched actin networks, and SMIFH2[534] to inhibit formins and thus the maintenance of linear actin structures.

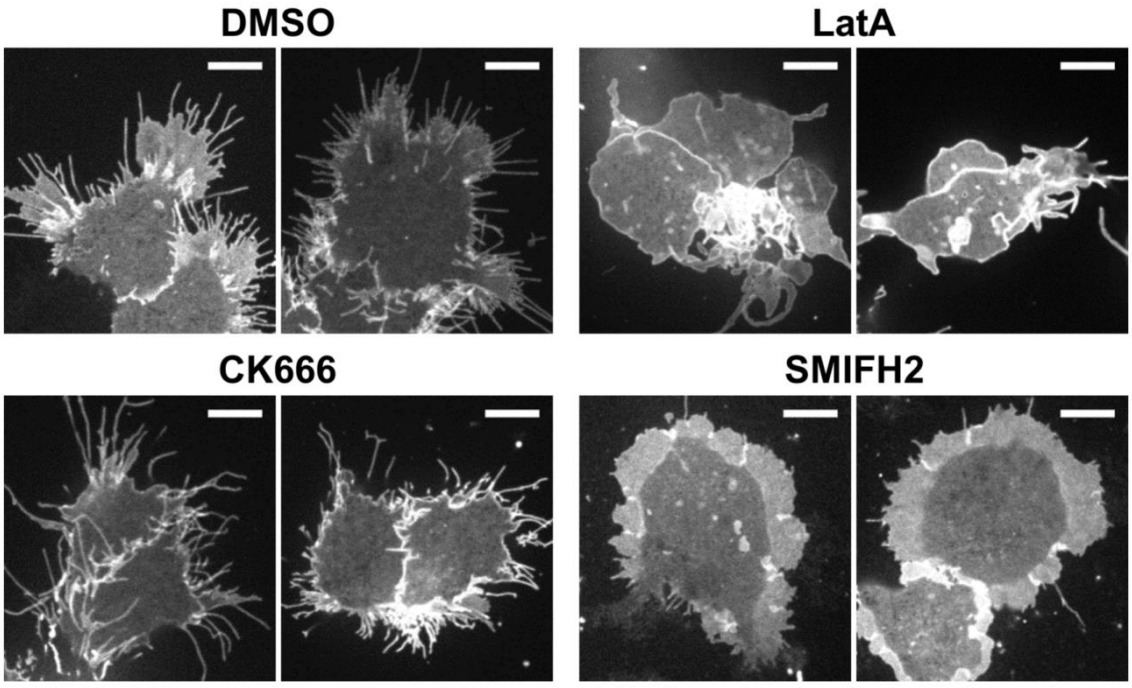

Figure 46 Effect of drug treatments on cell morphology.
Representative fluorescence micrographs of EphHEK cells after treatment with respective drugs. The micrographs show the ventral focal plane of EphB2-YFP that was used as a marker for the plasma membrane due to its homogeneous distribution within the plasma membrane.

Figure 46 shows representative images that reveal clear differences in the cellular morphology corresponding to the drug's expected effects, visualized by imaging the plasma membrane-localized EphB2-YFP receptor. In comparison to DMSO treated

control cells, LatA treated cells were much smaller and lost all well-defined cell protrusions, though some larger diameter, tube-reminiscent structures persisted. CK-666 treatment led to drastically reduced cell size and plenty of long, narrow filopodia-like membrane protrusions, consistent with the expected loss of the branched Arp2/3-dependent actin network. In contrast SMIFH2 treated cells had large lamellipodial sheets emanating around the cells but were devoid of filopodia-like protrusions, again consistent with the expected outcome of blocking linear filament polymerization, thus increasing branched network generation. One can note the increase in signal in the thin lamellipodial sheets in contrast to the cell body, as the lamellipodial thickness is within the focal plane and thus includes contributions from both the ventral and dorsal membrane.

In all of these conditions, although we have affected the cytoskeleton organization as reflected by the change of cell morphology, we did not detect any significant change in the diffusion coefficient of EphB2 in the membrane. Likewise, depletion of either Myosin 1b or ERM did not induce any significant change in diffusion coefficients (Figure 47B).

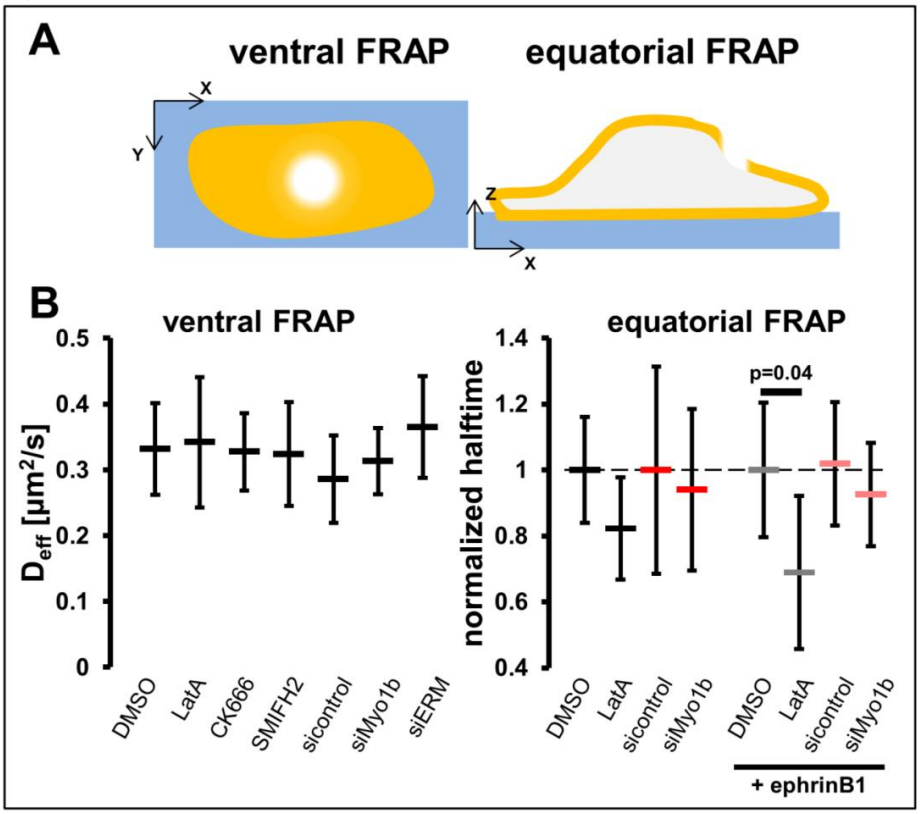

Figure 47 Diffusion assessed by FRAP experiments
(A) Schematic depiciton of the two types of FRAP experiments. The left side represents ventral FRAP, i.e. bleaching of a well-defined area at the ventral side of cells. The right side shows equatorial FRAP, in which bleaching was performed on the side of the cell at roughly 5 µm from the substrate without controlling the exact bleach profile. | **(B)** The left panel shows the effective diffusion coefficient of EphB2-YFP obtained from ventral FRAP for the different conditions as indicated on the bottom. n =12(DMSO), 12(LatA), 11(CK666), 12(SMIFH2), 10(sicontrol), 8(siMyo1b), 7(siERM). The right panel shows the halftimes of equatorial FRAP, normalized to the respective control condition. The left part of this panel shows the data before, and the right after global stimulation of cells with ephrin-B1. n=DMSO(14/9), LatA(16/17), sicontrol(13/11), siMyo1b(14/15).

In order to exclude any specific effect of the ventral surface and the specific nature of adhesion sites that are present at the interface and might thus change the diffusion of EphB2 we performed FRAP analysis at the equatorial plane of cells, both before and after stimulation of EphB2 with ephrin-B1 (Figure 47A). As the geometry of the bleach is not controlled in Z in this approach we plot recovery halftimes normalized by the value of the respective control experiment (either DMSO, or the sicontrol) that allow comparing the different conditions to each other. We observed a large spread in the data, probably due to the aforementioned lack in control of the bleach geometry. While depletion of Myosin 1b did not change the recovery halftimes both before and after activation, mild LatA treatment seemed to reduce recovery halftimes, i.e. increase large scale diffusivity, albeit in a non-significant way before stimulation of EphB2. The same treatment led to significantly reduced recovery halftimes after activation of EphB2 (Figure 47B).

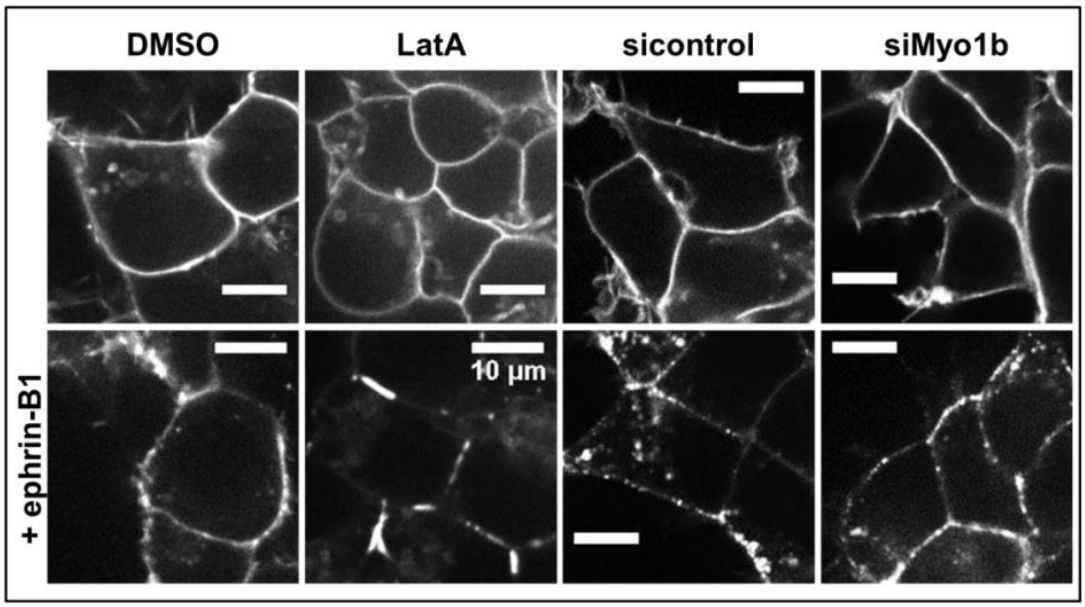

Figure 48 Formation of macroscopic EphB2 clusters upon global stimulation.
Representative fluorescence micrographs of EphB2_YFP at the equatorial plane before and after global stimulation with ephrin-B1 in EphHEK cells, treated as indicated. Scale bar 10 µm

Stimulation led to rapid formation of large, visible clusters of EphB2 that seemed almost completely immobile (Figure 48), thus the normalized halftimes after stimulation with ephrin-B1 represent the contribution of the remaining mobile, probably unclustered, population of EphB2. The mobile fractions were comparable between both experimental approaches (ventral vs. equatorial FRAP) before stimulation (Figure 49). We observed a marked decrease in mobile fraction after stimulation with ephrin-B1 in both control conditions in agreement with a large fraction of the receptors getting engaged in large, quasi-immobile clusters. After LatA treatment the average was

unchanged yet the spread increased markedly. However, we strikingly observed no change of the mobile fraction after stimulation in Myosin 1b depleted cells. A finding in apparent contradiction with the visible clusters after stimulation as shown in Figure 48.

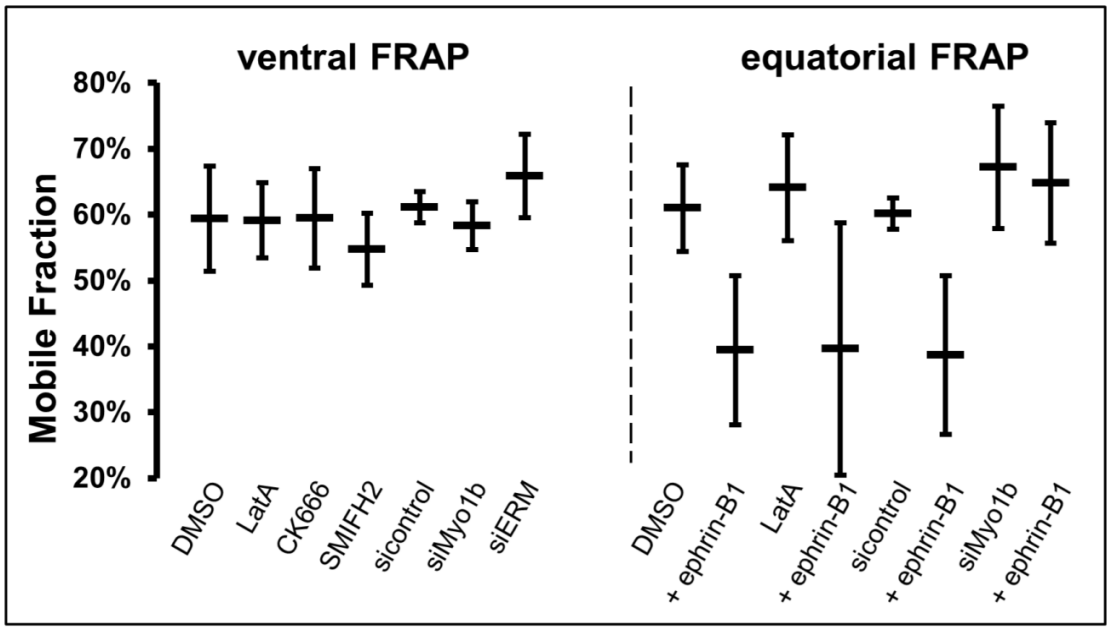

Figure 49 Mobile fractions
The left panel shows the mobile fractions of EphB2-YFP calculated from ventral FRAP for the different conditions as indicated on the bottom. n =DMSO(11), LatA(11), CK666(11), SMIFH2(12), sicontrol(10), siMyo1b(6), siERM(7). The right panel shows the mobile fractions of EphB2-YFP after equatorial FRAP, before and after global stimulation of cells with ephrin-B1. n=DMSO(14/18), LatA(16/16), sicontrol(15/12), siMyo1b(14/14).

FCS shows no change in characteristic diffusion time.

In order to confirm these findings at a different spatial scale we collaborated with the lab of Satyajit Mayor at NCBS in Bangalore and performed confocal FCS experiments on the ventral surface to assess EphB2 diffusion, and how it is affected by Myosin 1b and stimulation with ephrin-B1. These measurements were performed towards the cell center where actin flows were only marginally detectable (see e.g. Figure 54). In agreement with the FRAP results, FCS of EphB2 revealed no difference in the characteristic diffusion time in absence of Myosin 1b and after stimulation at the ventral side. Again, the measurement after stimulation detects only diffusion of the mobile molecules (Figure 50). Representative raw data and fitting results underpinning Figure 50 can be found in the Appendix.

In summary, we did not observe any effect of Myosin 1b on EphB2 diffusion, both before and after receptor stimulation with ephrin-B1. Nevertheless, we saw a stimulation-dependent effect of LatA treatment that was more pronounced after receptor stimulation, yet only observable at the equatorial plane.

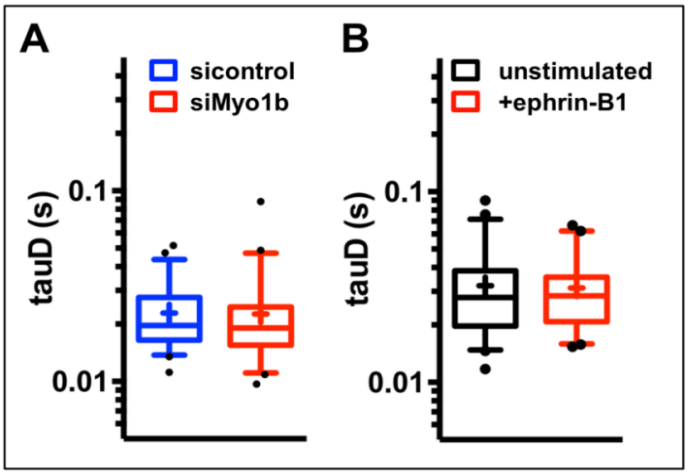

Figure 50 EphB2-YFP diffusion obtained from FCS.
Plot of the characteristic diffusion time tauD in seconds of EphB2-YFP as obtained from FCS curve fitting in sicontrol and siMyo1b-treated EphHEK cells (A), and in non-transfected cells before and after global stimulation with ephrin-B1 (B).

2. EphB2's spatial organization in the PM.

Global stimulation of cells with ephrin-B1 leads to the formation of large EphB2 clusters both at the equatorial plane and the ventral surface, which seem quite heterogeneous in size. These clusters coalesce into large scale aggregates after LatA treatment, yet do not seem fundamentally different in absence of Myosin 1b. Myosin 1b itself is not enriched in these clusters after activation but remains homogeneously distributed in the membrane (Figure 51).

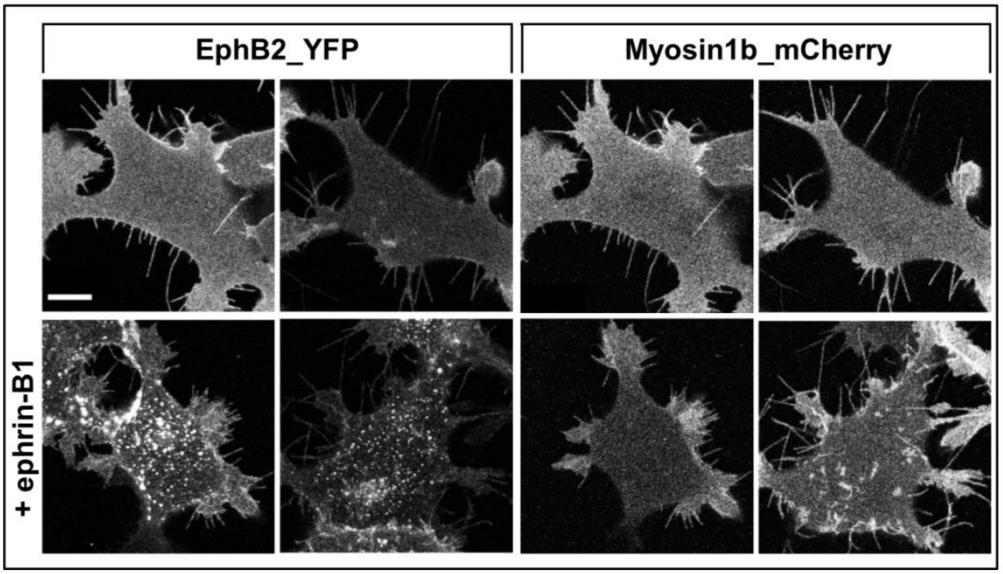

Figure 51 Ventral EphB2 clusters after global stimulation
Representative fluorescence micrographs of EphB2_YFP and Myosin1b_mCherry at the ventral surface of EphHEK cells, after transfection with Myosin 1b_mCherry. Before (top) and after (bottom) global stimulation with ephrin-B1. Scale bar 10 µm

We decided to investigate the cluster size at higher precision and in a more quantitative way in collaboration with Satyajit Mayor's lab at NCBS in Bangalore. We performed fluorescence anisotropy measurements to address homoFRET within the EphB2_YFP population (see M&M section for experimental details) which was homogeneously distributed along the ventral cell surface.

Fluorescence anisotropy is based on homoFRET, i.e. FRET between two identical fluorophores. As such the fluorescence anisotropy depends on the rotational freedom of the fluorophores to each other. In other words, if homoFRET happens between two fluorophores which are close enough to each to undergo FRET, the fluorescence anisotropy is a measure of their rotational freedom. For instance, a tightly packed dimer will show a lower anisotropy than two monomers that are close to each other yet less densely packed. From this statement it becomes clear that in a first approximation, fluorescence anisotropy will be a function of relative packing, i.e. fluorophore density, with a downward facing slope of anisotropy values with increasing fluorophore density, reflected by the intensity per pixel. From the experimental point of view, one is interested in the anisotropy value that carries the information of density-independent, cluster related spatial organization which is obtained from the plateau that is reached, in our case at around 30000 to 45000 arbitrary units. It must be noted that the absolute anisotropy value has no meaning by itself as it largely depends on the experimental set-up and configuration. It does nevertheless allow for a relative comparison in between conditions.

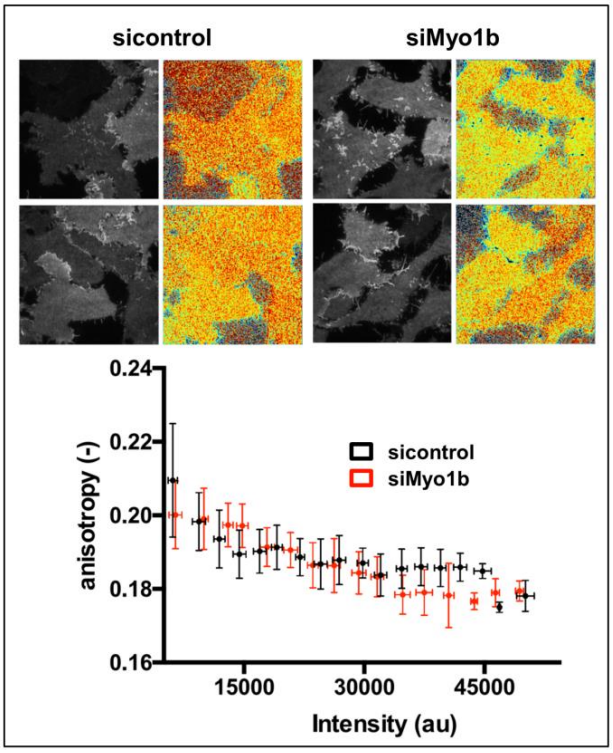

Figure 52 HomoFRET of EphB2_YFP after Myosin 1b depletion
Representative images (top) and fluorescence anisotropy of EphB2_YFP as a function of EphB2_YFP intensity (bottom) for control and siMyosin1b cells.

The spread of anisotropy values for a given intensity bin of EphB2 is relatively large, suggesting a heterogeneous cluster population. Within this widened spread, we did not observe a clear and significant change in anisotropy of EphB2 in absence of Myosin 1b (Figure 52). Likewise, treatment with the drug PClP which inhibits all class 1 Myosins[535] did not lead to a change in anisotropy at a concentration of 1 µM. We did however observe a slight but consistent upshift in anisotropy values at 10 µM, corresponding to reduced clustering of EphB2 at high PClP concentrations (compare with results on PClP in the following section)(Figure 53).

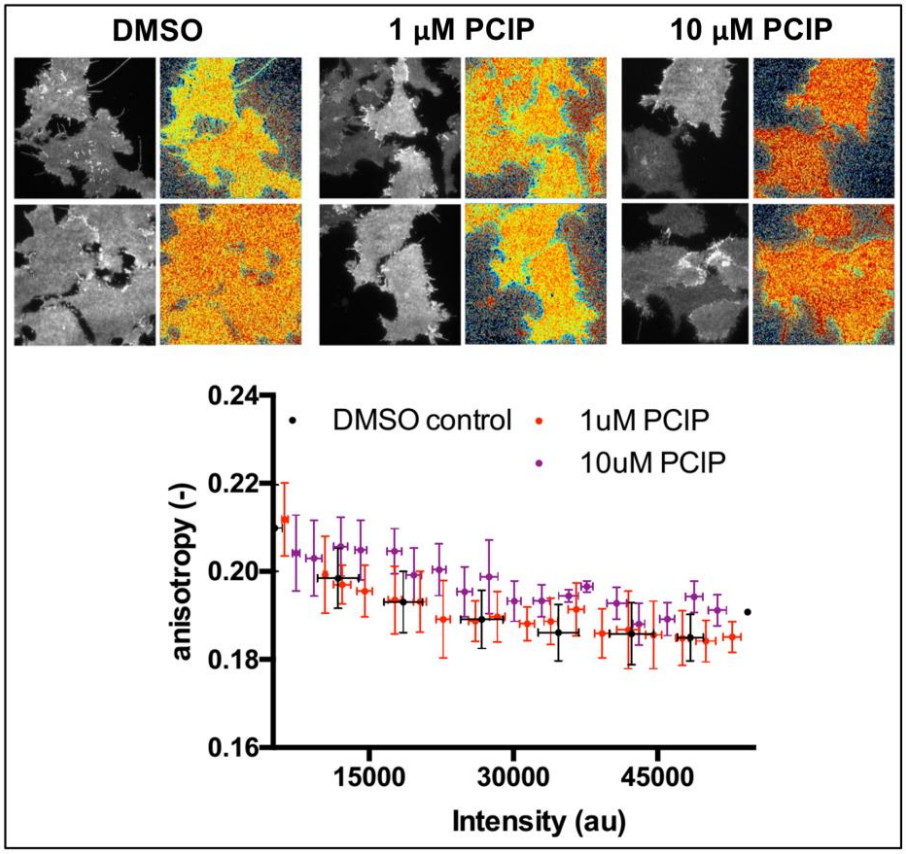

Figure 53 HomoFRET of EphB2_YFP after PCIP treatment
Representative images (top) and fluorescence anisotropy of EphB2_YFP as a function of EphB2_YFP intensity (bottom) for control and PCIP-treated cells.

In summary, our macroscopic results indicate that Myosin1b is likely not directly involved in the clustering of EphB2 (Figure 51), as in that case one would expect a clear local increase of Myosin 1b with the large clusters of EphB2 after stimulation, even if only a subset would be involved in that process. This observation is consistent with our results regarding the fluorescence anisotropy of EphB2 at steady-state where we do not see an effect of Myosin 1b depletion (Figure 52). One major contradiction (see Discussion) is the striking reduction in equatorial immobilization of EphB2 in Myosin 1b depleted cells.

3. TIRF-SIM & PIV analysis of actin flows

In order to study our hypotheses considering a potential effect of Myosin 1b on actin network dynamics and geometry we have, again collaborating with the team of Satyajit Mayor at NCBS Bangalore, used total internal reflection fluorescence - structural illumination microscopy (TIRF-SIM) to study the dynamics of the ventral actin cytoskeleton (see M&M for experimental details).

In a first instance, we have used the obtained datasets to study the flows of the ventral actin cytoskeleton, both at steady-state, and after global stimulation of EphB2 with ephrin-B1. To do this, we have performed particle image velocimetry on image sequences from tractin-mCherry labelled actin filaments.

Iterative PIV and time-averaging recovers coherent flow features in EphHEK cells.

In order to reduce the contribution of SIM reconstruction artifacts and relatively high background noise in the acquired TIRF-SIM datasets, probably due to unbound tractin-mCherry, we performed additional steps of image treatment prior to the PIV analysis. The treatment (detailed in the Methods section) consisted of applying a bandpass filter and performing a ridge detection algorithm. Using the map of ridges as an input, we performed PIV and were able to recover quantitative actin flow profiles in an unbiased way. In order to focus the analysis on flows which have a persisting directionality on the timescale of minutes, as expected from a cell which is, e.g. contracting after stimulation, and to obtain satisfactory signal to noise in the detection of flow vectors we performed time-averaging over 10 frames, leading to an effective time resolution of 75 seconds over a period of around 25 minutes. The time-averaging interval was chosen empirically using the flows in a lamellipodium as a benchmark, where both extensions and retrograde flows are visible qualitatively by eye, and 10-frame time-averages were able to recover these feature in a robust way, giving consistent outputs that match previously reported flow velocities in lamellipodia and full mapping of a given region of interest.

Stimulation of EphHEK cells with ephrin-B1 increases lamellipodial actin flows.

We represent the obtained PIV results in heat maps, in which the local flow velocity is color-coded in a dynamic range where speeds below 1 $nm.s^{-1}$ are blue and flows above 30 $nm.s^{-1}$ are red. The directionality of a given flow vector is indicated with super-imposed black arrows with lengths proportional to the flow velocity. Before stimulation, each cell was imaged over ~2 minutes and then imaged for ~20 minutes after stimulation. The frame-times depended on the exposure time and varied slightly to account for different expression levels of tractin-mCherry. Flow vectors where therefore

calibrated to account for the exact frame intervals. The average of flows during the initial 2 minute period is the 'unstimulated' control. The second column 'peak frame' shows an individual 10-frame average heatmap of flows, corresponding to the qualitatively largest and most expanded flow measured during the experiment. The third column depicts the last 10-frame average, i.e. the last flow heat map obtained for each condition, and can be considered as a proxy for flow duration, in case flows showed prolonged persistence in time. Finally the last column is the heat map of the total average of all flows during the 20 minute time window, i.e. the average of 200 individual heatmaps.

Unstimulated cells showed a heterogeneous flow distribution of labelled F-actin with flow rates in the dynamic lamellipodial areas that are higher than in the cell body. Stimulation of EphB2 with ephrin-B1 led to an increased polarization of the cell and enhancement of flow velocities mainly localized to the lamellipodial regions and only relatively low flow increases in absence of clear lamellipodia at the cell border. Time-averages of flow maps over the entire duration of imaging yields flow maps in which sustained flows are highlighted, whereas random flows cancel each other out. Such maps showed a clear concentration of very coherent flows along the lamellipodial rim and correlated with observed contraction behavior (Figure 54A).

Thus, PIV recovers the fundamental flow profiles in the cells and is able to phenomenologically link the observations upon stimulation of EphB2, i.e. cell contraction, to an increase in actin flow velocities that are concentrated at lamellipodia and directed towards the cell center.

Treatment with PClP freezes actin dynamics.

Treatment with 1 μM PClP abolishes actin dynamics in a cell-wide manner and activation of EphB2 after PClP treatment did not induce any change in the observed flows (Figure 54B). This concentration of PClP is supposed to be low enough to restrict the inhibition effect to all class 1 myosins, and should in principle not affect Myosin II[535]. This very striking observation thus suggests a very important role for class 1 myosins in actin flows parallel to the plasma membrane that was not envisaged before.

Depletion of Myosin 1b affects flow profiles in two distinct ways.

Cells transfected with control siRNA exhibited similar flows as untreated cells and DMSO treated cells. When Myosin 1b was depleted, visual inspection of the heatmaps suggested a slightly increased presence of (disperse) F-actin flows throughout the cell, i.e. a higher number of 'yellow' regions in the cell body (Figure 55). This observation requires further analysis of the data, e.g. binning of flow velocities and comparing the

relative change in bin size between sicontrol and siMyosin 1b cells and quantitative analysis of vector scatter plots limited to central cell regions.

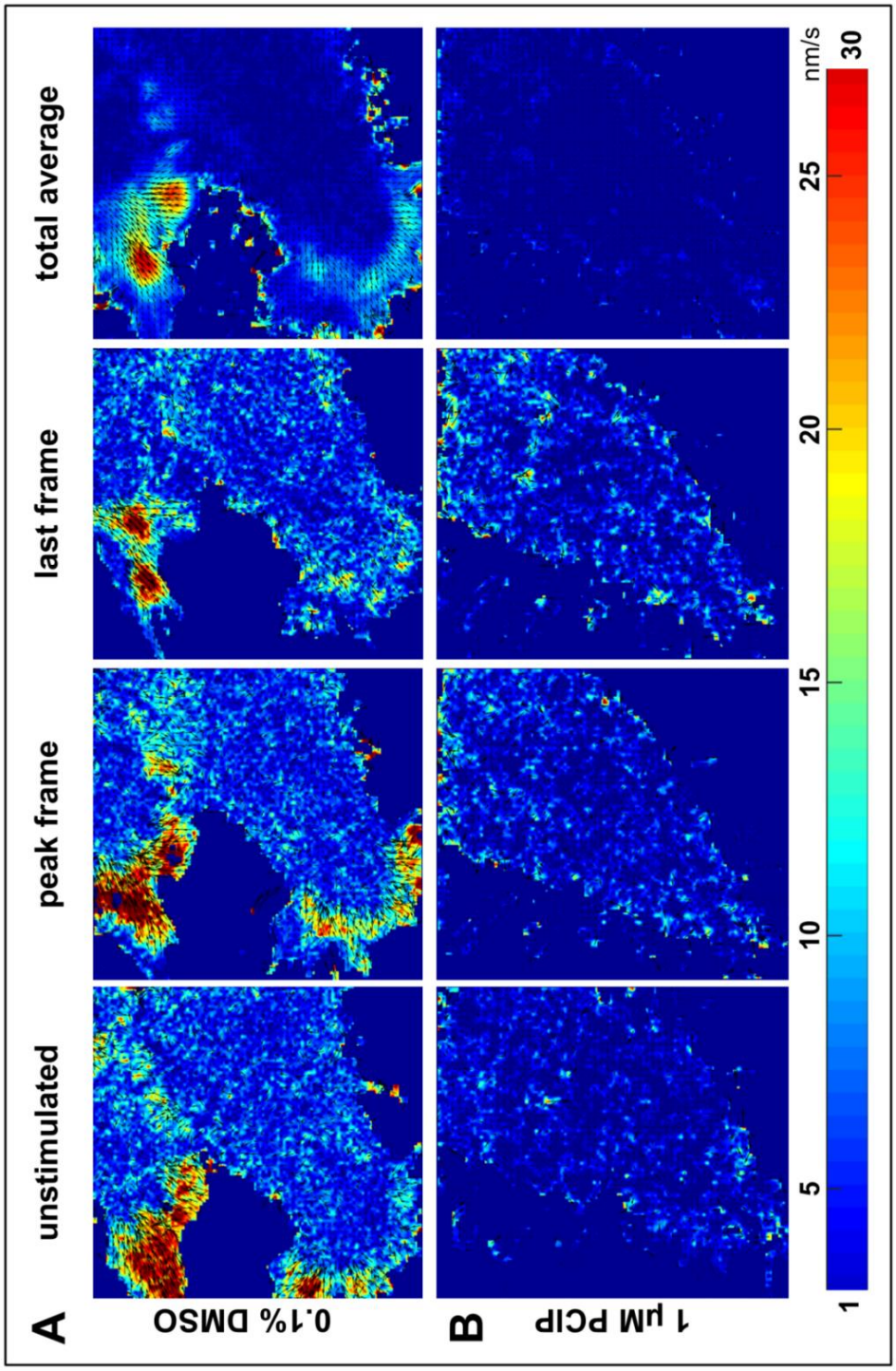

Figure 54 Heatmaps of actin flows
Heatmaps of actin flows for DMSO (A) and PCIP-treated (B) cells. The dynamic range of colors goes from 1 $nm.s^{-1}$ (blue) to 30 $nm.s^{-1}$ (red). The left panel shows the steady state dynamics before activation, averaging over 25 frames (unstimulated). The peak frame is the 10 frame average after activation which shows the highest flows, and the last frame is the last 10 frame average after stimulation. The total average is the average of all frames after stimulation, i.e. 200 frames.

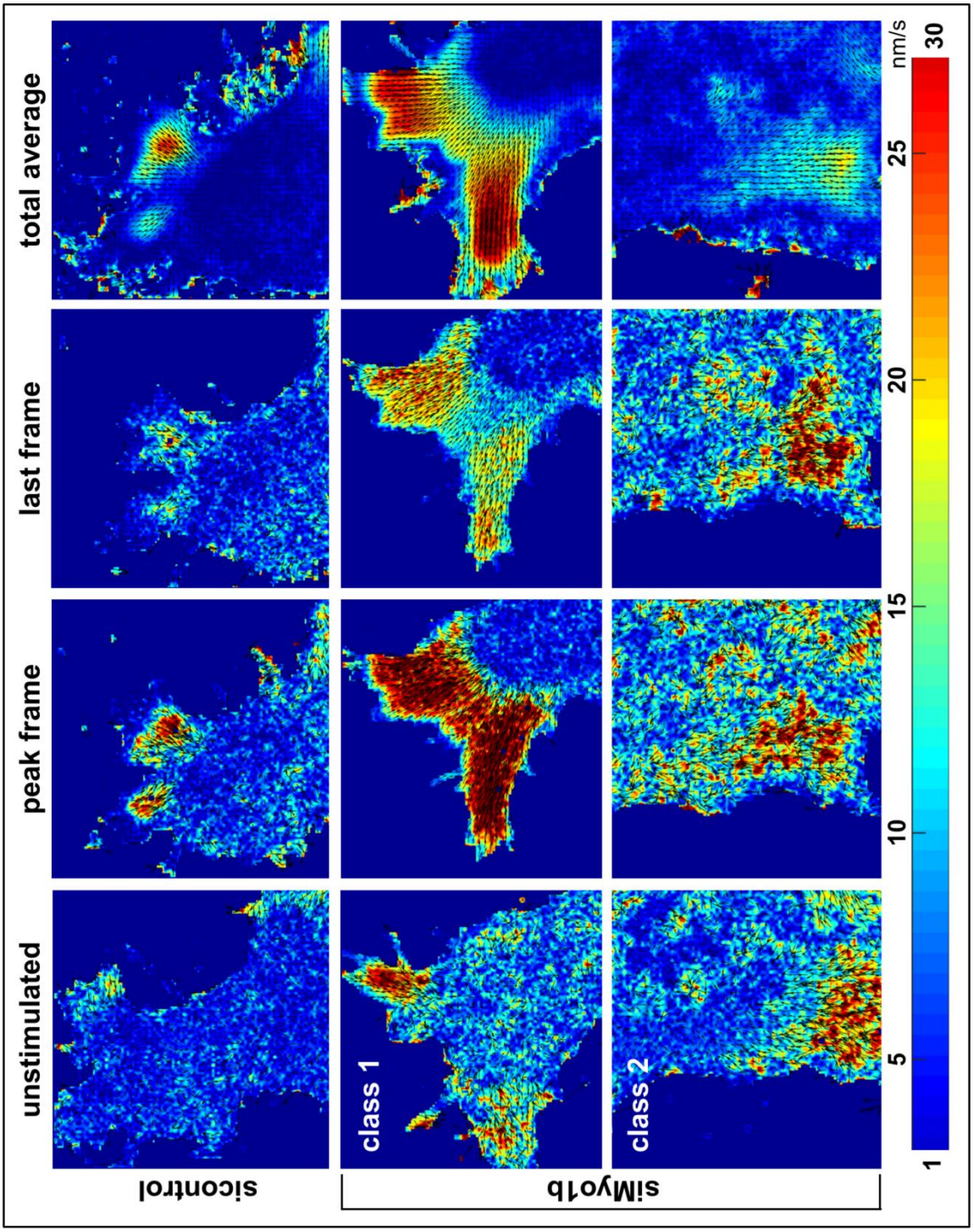

Figure 55 Heatmaps of actin flows: Effect of Myosin 1b depletion
Heatmaps of actin flows for control (top) and siMyosin1b-treated (bottom) cells. The dynamic range of colors goes from 1 $nm.s^{-1}$ (blue) to 30 $nm.s^{-1}$ (red). The left-most panel shows the steady state dynamics before activation, averaging over 25 frames. The peak frame is the 10 frame average after activation which shows the highest flows, and the last frame is the last 10 frame average after stimulation. The total average is the average of all frames after stimulation, i.e. 200 frames.

After activation, the resulting flows in Myosin 1b depleted cells could be classified into two distinct categories that are representatively shown in Figure 55. Cells which had an active lamellipodium before stimulation with ephrin-B1 showed strong increases

in flow rates, with a strong correlation (yet to be quantified). These flows tended to propagate over time and showed clear directionality towards the cell body. In cells initially lacking a clear lamellipodial structure, stimulation of EphB2 led to a different outcome. The flows increased in a dispersed cell-wide manner that did not show a clear spatial coherence over time. This resulted in two fundamentally different total average flow maps, in which the prior case showed extended areas of large flows, whereas the latter one exhibits increased flows, yet with an apparently random localization throughout the cell.

This difference in behavior is epitomized by plotting the individual axial components of flow vectors (Figure 56). Activation in control conditions led to increased flows concentrating around contraction axes (dashed lines). In contrast, in the case of expanded flows after depletion of Myosin 1b, we observed a shift along the axis of increased flows (dashed mask), while the lack in spatial coherence in the latter case resulted in condensed flow vector distribution.

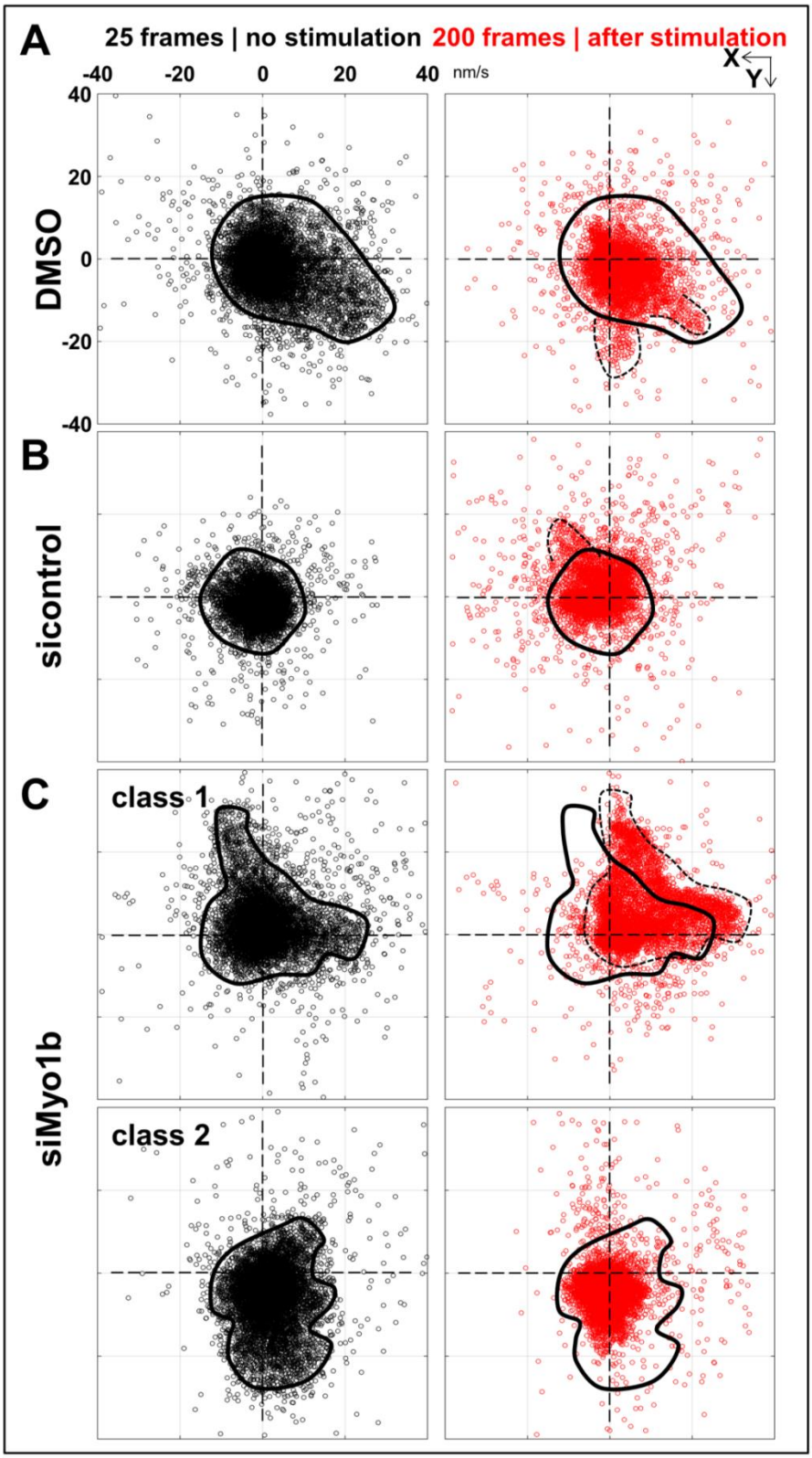

Figure 56 Scatter plots for actin flow vectors

Total amount of flow vectors obtained before activation (left) and over the timecourse after activation (right) for DMSO (A), sicontrol (B), and siMyosin1b (C) treated cells. The plot coordinates represent X and Y components of detected flow vectors ranging from 0 to 40 nm.s^{-1}. Negative flow values represent movement to the left and bottom whereas positive values represent movement to the right/top.

Discussion

The results of this second part of the thesis have been performed over the course of the last 9 months and are thus to be considered preliminary. A number of control experiments are still to be performed and more data needs to be analyzed to conclude on the experimental observations.

1. Diffusion & spatial organization of EphB2

EphB2 shows fast diffusion in the EphHEK plasma membrane.

Our ventral FRAP experiments suggest an effective diffusion coefficient of EphB2 on the order of 0.3 $\mu m^2 \cdot s^{-1}$. This is in line with predictions for proteins with a single trans-membrane domain[536,537], and consistent with previously reported values of transmembrane protein diffusion in HEK293 cells, e.g. the dopamine transporter (0.36 $\mu m^2.s^{-1}$)[538] and the β2-adrenergic receptor (0.4-1.2 $\mu m^2.s^{-1}$)[539]. The diffusion of EphB2 is roughly 3 to 4 times lower than what has been reported for the macroscopic diffusion of lipids in cells[497]. Although the effective bleaching radii had to be estimated and thus D_{eff} in Figure 47 can only feature as a rough estimate, it agrees well with the results obtained from FCS, that give a ventral effective diffusion coefficient for EphB2 on the order of 0.5 $\mu m^2.s^{-1}$

One might consider that EphB2's relatively high diffusion constant is related to its biological function in which efficient spatial exploration of free receptors would allow the efficient formation of functional signaling complexes upon local ligand binding. Such mechanism has been proposed for Rhodopsin which exhibits similarly high diffusion in isolated rods[540]. It would be interesting to compare EphB2 diffusion to that of its deactivating phosphatase PTP1B[314], which is present at the plasma membrane at low concentrations, and model how relative differences in diffusion might create a dynamic regulatory network for receptor signaling.

Myosin 1b has no obvious effect on EphB2 diffusion or spatial organization.

Using both FRAP and FCS we find no evidence for a role of Myosin 1b in the regulation of EphB2 receptor diffusion. Furthermore, our results regarding EphB2's fluorescence anisotropy suggest that the EphB2 receptor distribution is likely unaffected directly by Myosin 1b. Yet, we did not experimentally characterize the dynamics of EphB2 anisotropy just after stimulation with ephrin-B1 but only after 30

minutes of activation at which big cluster formation and contraction have happened. Before activation we did not detect a difference in anisotropy values between control and Myosin 1b depletion, yet the strength of the data was considerably reduced due to the wide spread in anisotropy values we observe at given EphB2 intensities and thus makes it hard to firmly conclude. Still, the fact that Myosin 1b remains homogeneously distributed in the plasma membrane after receptor stimulation makes it unlikely that it would act as a direct effector that drives receptor condensation. A recent publication has shown an elegant approach to studying such problems at high spatial and temporal resolution: Using nano-patterned substrates to locally activate Eph receptors and enhanced number and brightness analysis allowed quantification of the heterogeneous cluster population of EphB at steady state and its change towards higher order oligomers over time after ligand binding[311,312]. In order to study clustering behavior after stimulation in more detail, it thus seems ideal to employ the experimental system used in these publications and characterize both the potential change in steady state distribution (missed in the anisotropy measurements due to the high spread) and its behavior over time after activation with ephrin-B1. As a default, one might as well resort to more classical approaches, e.g. PALM/STORM imaging, something that we had envisioned earlier and for which we already possess the required plasmid, i.e. mEos3.2[472] tagged EphB2, but we did not have the time to proceed during this thesis.

Myosin 1b depletion changes mobile fractions after stimulation

We observe a striking effect of Myosin 1b depletion on the mobile fractions of EphB2 obtained from our equatorial FRAP results after stimulation with ephrin-B1(Figure 49). Whereas in all other conditions, including LatA treatment albeit at higher spread, lead to a reduction in the mobile fraction, corresponding to the expected immobilization of the receptors after clustering, we do not observe such change in mobile fraction after depletion of Myosin 1b. This result is in contradiction with the macroscopic clusters we observed under the same conditions (Figure 48), the homogeneous distribution of Myosin 1b after EphB2 clustering and the absence of an effect of Myosin 1b during fluorescence anisotropy experiments. The obvious consequence at this stage is to redo the FRAP experiments to be able to confirm or discard this observation. If reproducible it would suggest that the EphB2 clusters that form after stimulation remain mobile after depletion of Myosin 1b thus explaining the unchanged mobile fraction. It will be of interest to include ventral FRAP after global stimulation that we have not yet performed in order to be able to compare it directly to the interface that we studied by fluorescence anisotropy and where we did not see any Myosin 1b clustering after EphB2 stimulation. One caveat to consider is that we cannot strictly rule out that

mCherry-labelled Myosin 1b, as imaged in Figure 51, might have a lower affinity to EphB2 than endogenous Myosin 1b and thus not report on local clusters of Myosin 1b.

Effects of cytoskeletal drugs.

The coalescence of EphB2 clusters into large scale structures after LatA treatment suggests that EphB2 clusters are spatially separated to a certain extent by the underlying actin cytoskeleton which precludes large scale coalescence after stimulation, either through binding or because it acts as a diffusion barrier for large clusters.

In the light of this it seems puzzling that only LatA treatment after activation shows a significant effect on effective receptor diffusion. Considering the non-significant decrease in recovery halftime at the equatorial plane after LatA treatment before stimulation of EphB2 it is tempting and reasonable to speculate that with higher precision methods one might expect a generalized effect of LatA. Previous reports suggest that upon LatA treatment confinement areas (as probed for lipids) increase roughly by a factor of 2[497]. In light of this and the fact that the confinement size in HEK293 cells is on the order of 70 nm[28], only methods offering high spatial and temporal precision, e.g. high-speed single particle tracking of EphB2 or advanced FCS, would allow a detailed characterization of confinement zone size and microscopic diffusion coefficients. In that case, one might additionally be able to distinguish between mere confinement, i.e. the actin mesh being a passive boundary for EphB2, or local immobilization of receptors to the actin mesh via either direct or mediated binding[487].

Different effects of LatA at the ventral and equatorial plane.

Considering the absence of any effect of LatA treatment on EphB2 diffusion and mobile fraction at the ventral side, one might speculate that this is related to the ventral's side specific function and composition, i.e. integrin-mediated adhesion and presence of stress fibers. It might thus be less sensitive to the drug treatments. As we did observe a clear change in morphology upon drug treatment, this would imply that a specifically stable subset of actin structures withstands these treatments better than, e.g. the cortex, and is sufficient to restrict the diffusion of EphB2. Indeed, at the concentrations used in our experiments, cells maintained attached to the substrate during the course of the experiments, yet do detach at higher concentrations of LatA (250 nM).

2. TIRF-SIM

PIV treatment of TIRF-SIM datasets successfully recovers actin flow speeds.

With the analysis described in this thesis we find F-actin flow speeds (dynamic range between 1 and 40 nm/s) that are in excellent agreement with reported values throughout the literature, and compatible with results obtained from methods ranging from speckle microscopy to spatio-temporal image correlation spectrosocopy[541–544].

PClP blocks actin flows at low concentrations.

We find that PClP treatment, a drug that at this concentration should be specific for class 1 myosins[535], completely stops actin flows in HEK293T cells. The same effect is observed as well in U2OS cells and is found in PClP from different chemical syntheses (personal communication Satyajit Mayor's lab). While one explanation might lay in the blockage of all class 1 myosins, it is a remarkably strong phenotype and should be studied in detail. The finding is particularly surprising as the flow of actin, especially in the lamellipodium is considered to arise from two main contributors, i.e. Myosin II-driven contractility and the retrograde flow of polymerizing actin barbed ends. The fact that we see a cell-wide loss in dynamics suggests that both processes are affected by the PClP treatment. Two experiments are particularly interesting to be done as a consequence: First, characterization of specific inhibition of Myosin-2 by Blebbistatin, and second, control of actin polymerization at the leading edge of cells after PClP treatment. This could be done by overexpressing photo-convertible actin dyes, e.g. tractin_mEos.

The availability and lack of alternatives makes PClP a particularly attractive compound for cell biological studies in which depletion is inefficient or not possible, e.g. in primary cells[5,190,545]. Yet, considering its massive effects on actin flows, an off-target effect that goes beyond blockage of class 1 myosins should be at least considered in the interpretation of experimental results. For now no conclusive evidence is present, yet our and other's observations regarding the effect on actin flows pose an urgent issue, that is of fundamental importance to the biological community working on class 1 myosins. If PClP treatment were to be specific beyond doubt, this would mean that class 1 Myosins would be a newly identified essential factor for in-plane actin flows. In this case, it would be of fundamental interest to quantify the relative abundance of all different isoforms, e.g. using quantitative mass spectrometry, and secondly start systematic knock-down experiments to identify the isoforms that are relevant for in-plane actin flows.

Myosin 1b depletion changes actin flow dynamics.

We observe an intriguing yet non-trivial effect of Myosin 1b depletion on actin flows. At steady-state we see a slightly increased magnitude of flows around the cell. After activation, cells exhibit two distinct behaviors. One subpopulation shows increased coordinated flow velocities that tend to expand over large areas and start locally (class 1), while others show a generalized and disorganized, yet less pronounced, increase in flows around the cell's ventral surface (class 2). There is a correlation between the presence of a lamellipodial structure at steady-state (already being quite dynamic) and class 1 behavior, suggesting that pre-existing lamellipodial actin flows are sufficient to polarize the system sufficiently to create large directional flows in response to EphB2 stimulation. Yet, non-intuitively but in agreement with our data on contractile deficiency in absence of Myosin 1b, this increased actin flow does not correlate well with efficient contraction of the cells in response to EphB2 stimulation. Taken together, the observed results are in good agreement with a role of Myosin 1b acting as a clutch during cellular contraction or altering actin network geometry. As we do not have an *in situ* control of siRNA treatment efficiency per cell (of a generally very efficient depletion), the observation of two different phenotypes in actin flows after Myosin 1b depletion might in principal be related to differences in cellular depletion efficiency. The correlation between pre-existing lamellipodial flows and the distinction of class 1 and class 2 flow behavior after activation might be further investigated employing cells on micro-patterns, thus allowing for a more controlled cell shape and stereotypic cell organization.

Clutch hypothesis

In a clutch model, one would expect that the absence of Myosin 1b would combine both increased actin flows and reduced contractility. As the flows would be sufficiently generated by activated Myosin II but experience less counteracting force by membrane attachment they should increase in magnitude. Yet, in absence of Myosin 1b, these flows would less efficiently be transmitted to the membrane thus explaining the decrease in contractility. This hypothesis is supported by recent evidence showing that Myosin 1c puts E-cadherins under tension by linking them to actin[546]. In the case of Myosin 1b a similar mechanism could potentially couple EphB2 to underlying actin dynamics. Interestingly, due to its catch-bond behavior and the spatial restriction of physiological EphB2 activation at cell contact sites through ligand binding might additionally serve as a geometrical cue defining an axis of contraction *in cellulo.*

Altered network geometry

Another alternative is that Myosin 1b might simply change the local architecture of the actin network and thus lead to reduced contractility. *In vitro* studies have shown that contractility is a function of the actin network geometry (ordered bundles, disordered network, disordered bundles) and their connectivity, governed by crosslinkers and notably Arp2/3[531,547]. This scenario, which is in agreement with recent *in vitro* results in the lab (unpublished, Julien Pernier), does however not offer an obvious mechanistic link between flow speed increases and reduced contractility that we observe.

Nevertheless, it would be consistent with reported phase diagrams of the percolation dynamics in active gels, in which at intermediate motor activity levels subtle changes in network connectivity would *a priori* be sufficient to switch the systems behavior from global contractility to local contractility and non-contractile active solutions[548]. In such a scenario the cells would be predicted to be close to the transition point in the phase diagram but consistently in the global contraction phase. Myosin 1b depletion could lead to a small loss in network connectivity that might be sufficient to shift the system towards either local contractions or, at a slightly higher loss in connectivity, to active solutions without large scale order.

Perspectives

The obtained results strongly suggest that actin dynamics are changed after depletion of Myosin 1b, which is specifically striking after induction of EphB2-driven cell contraction.

In order to understand this phenotype and get down to a mechanistic understanding two main hypotheses are promising:

Clutch hypothesis of Myosin 1b

To evidence the role of Myosin 1b as a clutch, potentially specific for EphB2, one might go back to our initially developed system of bead-based receptor activation which allows spatial control of receptor engagement. In line with the findings for Myosin 1c, an ideal experiment would include a FRET-based axial tension sensor, which would allow detection of Myosin 1b-dependent tension build-up at local activation sites. It is not trivial to generate such a reporter without changing the molecular properties and at the same time get specific results. One idea might be the low level expression of a membrane-linked FRET tension sensor that has the Myosin 1b binding-domain of EphB2 (which still is not fully characterized and needs to be specific). Such an approach would evade any pitfalls of reduced receptor activation after inclusion of a tension sensor within EphB2, while still conserving specificity for Myosin 1b. Yet, it is puzzling that such a clutch-like behavior of Myosin 1b would not translate into any change regarding the plasma membrane's mechanical properties. Yet, as we highlighted in the first part of this thesis, we do not and cannot exclude a local and short-lived effect of Myosin 1b during EphB2 activation and contraction that might be detected if the right experimental tools were available (see Perspective Part A).

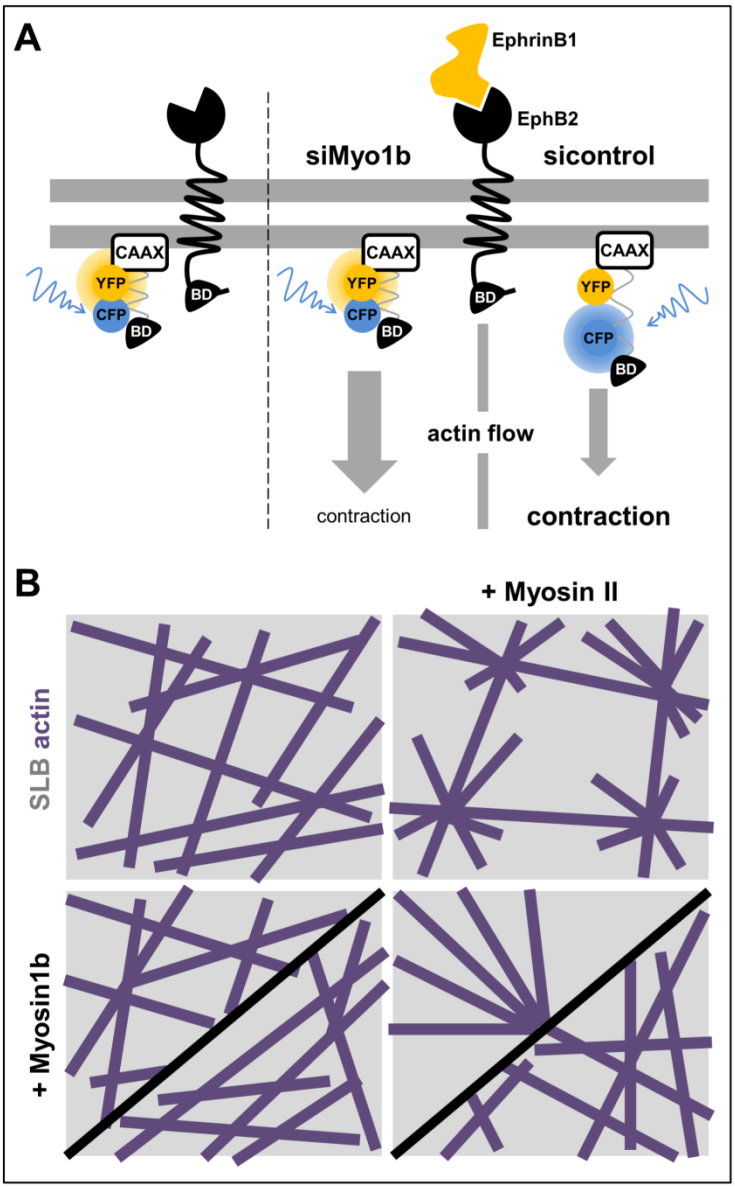

Figure 57 Molecular FRET sensor for Myosin1b generated axial tension
(A) Schematic representation of the described axial stress sensor for Myosin1b –dependent stresses on EphB2. A CAAX domain localizes the sensor to the PM and is coupled to EphB2's binding domain for Myosin 1b with an interspersed FRET sensor. Such design prevents potential loss in receptor function due to addition of the stress sensor. Upon local stimulation the FRET efficiency is a readout of Myosin 1b-specific local stresses in response to EphB2 activation. | **(B)** Overview of the proposed SLB-based experiments to study the control of actin geometry by Myosin 1b. The top row depicts the well characterized addition of Myosin II to a pre-assembled actin network leading to contraction and coalescence. The lower row depicts some potential outcomes of addition of Myosin 1b, e.g. a change of filament orientation before addition of Myosin II (left), or hindered/enhanced network compaction (right bottom/top triangle respectively)

Myosin 1b changes network geometry/connectivity

The hypothesis of altered actin network geometry/connectivity might on the one hand be studied *in vitro* by creating composite actin – membrane systems[505] and characterizing the density dependent effect of Myosin 1b on steady state network geometry and the dynamic contractile modes after addition of Myosin II. On the other hand, we already have high resolution datasets of actin from our TIRF-SIM

experiments, thus geometrical information is stored within this data, that might readily reveal differences if analyzed in the proper way. Currently we have not been able to do so, but in principle advanced image analysis, e.g. principal component analysis, should be adaptable to this particular problem.

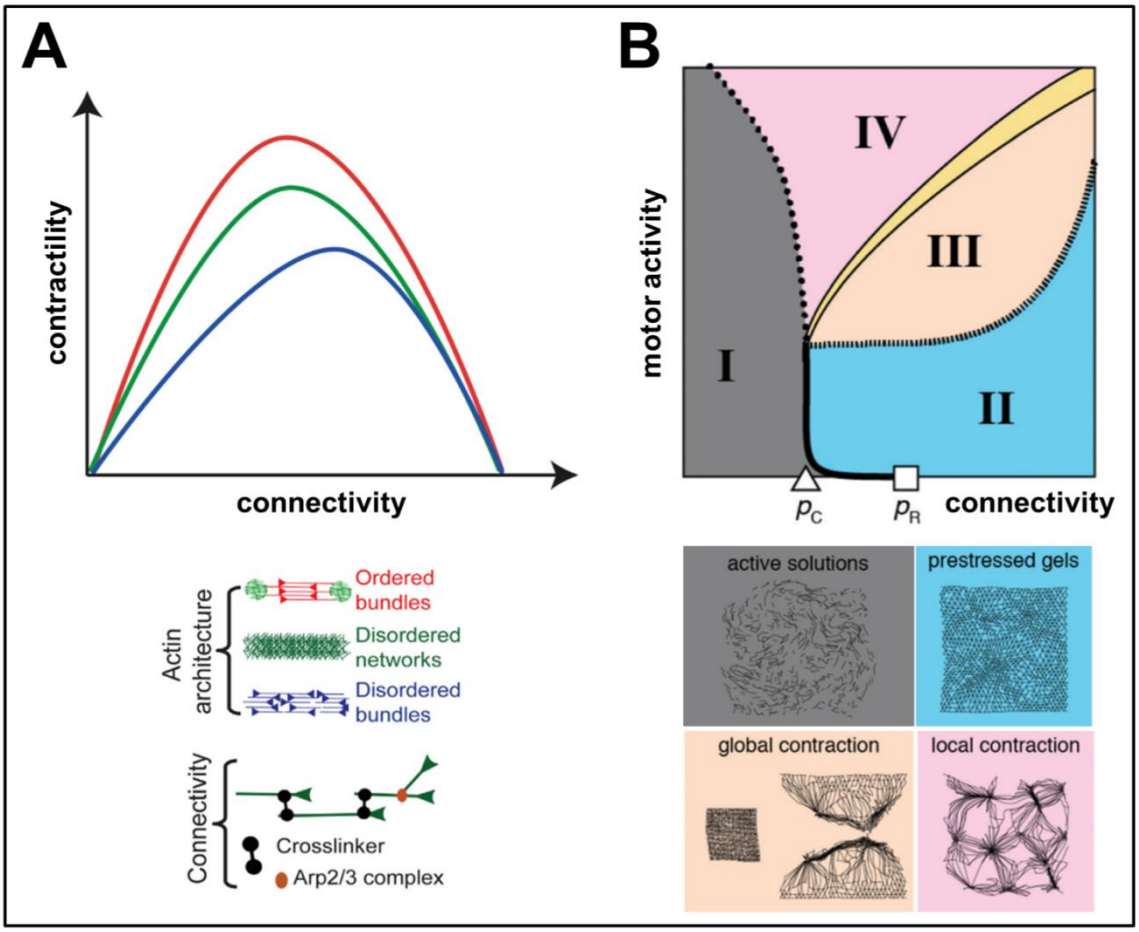

Figure 58 Active gel contraction
(A) Actin network contractility is a function of actin architecture (ordered bundles (red), disordered networks (green), disordered bundles (blue)) and network connectivity. Adapted from Ref.531 | **(B)** Active gel phase diagram depending on contractility and motor activity. Four main phases can be distinguished: Active solutions that are not contractile at low connectivity (grey), pre-stressed, non-contractile gels at medium to high connectivity and low motor activity (turquoise), a global contractile regime at medium connectivity and medium motor activity (salmon), and local contractility at medium connectivity and high motor activity (rosé) Adapted from Ref. 548.

General conclusion

Based on the initial observation that Myosin 1b reduces the efficiency of the cellular response to EphB2 stimulation, yet does not affect its signaling, I have pursued two hypotheses during this thesis work:

I have studied the effect of Myosin 1b, and ERM proteins as a benchmark, and shown that in adherent HEK293T cells (and NIH3T3 fibroblasts for Myosin 1b) both types of linkers do not change the effective membrane tension. From the point of view of tether pulling techniques I have furthermore shown that step elongations of membrane tethers can reveal differences in tether relaxation behavior as a function of relative linker density, which is not resolvable in the more established regime of constant speed elongations.

Considering the role of class 1myosins on plasma membrane mechanics, we strongly refute the interpretation of reference [7] that class 1 myosins GENERALLY control effective membrane tension, as this view does not withstand thorough experimental verification in at least two different cell lines.

I interpret the differences with other experimental results regarding effective membrane tension as an indication that cells have dynamic and efficient ways to compensate changes in membrane tension, as elegantly demonstrated in keratocytes[433] as well as by compensatory endocytosis that rapidly equilibrates effective membrane tension increases after cell stretching (personal communication J. Thottacherry, Satyajit Mayor's lab). Moreover, strong differences might exist between adherent cells and cells in suspension/3D, and between cells favoring amoeboid over lamellipodial motion. In conclusion, the data presented in this thesis together with published reports in the literature suggest that effective membrane tension can be efficiently equilibrated in cells and might depend on relative adhesion to the substrate. Furthermore I provide conclusive data showing that the effect of Myosin 1b on EphB2-driven segregation and notably the reduced contractility after Myosin 1b depletion is not linked to globally altered membrane mechanics, while some local, transient effects might be of relevance.

In the second part of the thesis (which is still of preliminary nature), I have considered whether Myosin 1b could have an influence on the clustering of EphB2 receptors, and thus potentially on the downstream signaling after activation, by investing the dynamics of these receptors and their clustering state. I have found that the diffusion of mobile EphB2 receptors and their clustering seem rather independent

of Myosin 1b and actin before activation. After activation I observe large scale coalescence of receptors in actin-perturbed cells, suggesting that actin limits the formation of such large clusters that form upon stimulation by locally confining them. Furthermore, we see a striking effect of Myosin 1b depletion on the mobile fraction after stimulation that needs to be reproduced in a new round of experiments. In summary, most of the data suggests that Myosin 1b does not change receptor dynamics. If the striking loss in changes of mobile fraction after Myosin 1b depletion is reproducible, and thus relevant, remains to be seen.

The last hypothesis that I pursued was that Myosin 1b could have a direct influence on the organization of the cellular actin fluxes and thus on the efficiency of cell contractility after EphB2 activation. I used TIRF-SIM imaging followed by quantification of the actin flows and identified an intriguing yet non-intuitive effect of Myosin 1b at the ventral surface of EphHEK cells. This effect is the only obvious manifestation of Myosin 1b that I could detect in my thesis. I have not been able to go beyond a phenomenological description of this effect but propose two fundamental experimental approaches that would help to differentiate between the two most likely mechanisms, i.e. a clutch-like function of Myosin 1b that couples actin-flows to the plasma membrane, potentially through specific interactions with receptors, or a more general effect on actin network architecture.

In conclusion, even if the mechanism by which Myosin 1b changes cellular response to EphB2 stimulation is still not fully elucidated, I have finally been able to pinpoint its function to a reasonably well-defined and quantifiable observation, i.e. changed actin flow dynamics. Future experiments will hopefully be able to dissect the mechanism that causes this observation, and follow it up considering other reported phenotypes of Myosin 1b depletion. This will allow concluding on whether Myosin 1b has a common underlying mechanism shared between all those biological processes.

References

1. Almeida, C. G. *et al.* Myosin 1b promotes the formation of post-Golgi carriers by regulating actin assembly and membrane remodelling at the trans-Golgi network. *Nat. Cell Biol.* **13,** 779–789 (2011).
2. Salas-Cortes, L. Myosin Ib modulates the morphology and the protein transport within multi-vesicular sorting endosomes. *J. Cell Sci.* **118,** 4823–4832 (2005).
3. Prospéri, M. T. *et al.* Myosin 1b functions as an effector of EphB signaling to control cell repulsion. *J. Cell Biol.* **210,** 347–361 (2015).
4. Yamada, A. *et al.* Catch-bond behaviour facilitates membrane tubulation by non-processive myosin 1b. *Nat. Commun.* **5,** 3624 (2014).
5. Iuliano, O. *et al.* Myosin 1b promotes axon formation by regulating actin wave propagation and growth cone dynamics. *J. Cell Biol.* jcb.201703205 (2018). doi:10.1083/jcb.201703205
6. Diz-Muñoz, A. *et al.* Control of directed cell migration in vivo by membrane-to-cortex attachment. *PLoS Biol.* **8,** (2010).
7. Nambiar, R., McConnell, R. E. & Tyska, M. J. Control of cell membrane tension by myosin-I. *Proc. Natl. Acad. Sci.* **106,** 11972–11977 (2009).
8. Honigmann, A. & Pralle, A. Compartmentalization of the Cell Membrane. *Journal of Molecular Biology* **428,** 4739–4748 (2016).
9. Singer, S. J. & Nicolson, G. L. The Fluid Mosaic Model of the Structure of Cell Membranes. *Science (80-.).* **175,** 720–731 (1972).
10. Van Meer, G., Voelker, D. R. & Feigenson, G. W. Membrane lipids: Where they are and how they behave. *Nature Reviews Molecular Cell Biology* **9,** 112–124 (2008).
11. Lingwood, D. & Simons, K. Lipid rafts as a membrane-organize principle. *Science (80-.).* **327,** 46–50 (2010).
12. Engelman, D. M. Membranes are more mosaic than fluid. *Nature* **438,** 578–580 (2005).
13. Suzuki, K. G. N. *New Insights into the Organization of Plasma Membrane and Its Role in Signal Transduction. International Review of Cell and Molecular Biology* **317,** (Elsevier, 2015).
14. Ikonen, E. & Simons, K. Protein and lipid sorting from the trans-Golgi network to the plasma membrane in polarized cells. *Semin. Cell Dev. Biol.* **9,** 503–509 (1998).
15. Roux, A. *et al.* Role of curvature and phase transition in lipid sorting and fission of membrane tubules. *EMBO J.* **24,** 1537–1545 (2005).
16. Harayama, T. & Riezman, H. Understanding the diversity of membrane lipid composition. *Nat. Rev. Mol. Cell Biol.* **19,** 281–296 (2018).
17. Huang, C. Empirical Estimation of the Gel to Liquid-Crystalline Phase Transition Temperatures for Fully Hydrated Saturated Phosphatidylcholines. *Biochemistry* **30,** 26–30 (1991).
18. Cooper, B. S., Hammad, L. A. & Montooth, K. L. Thermal adaptation of cellular membranes in natural populations of *Drosophila melanogaster*. *Funct. Ecol.* **28,** 886–894 (2014).
19. Muir, A. P., Nunes, F. L. D., Dubois, S. F. & Pernet, F. Lipid remodelling in the reef-building honeycomb worm, Sabellaria alveolata, reflects acclimation and local adaptation to temperature. *Sci. Rep.* **6,** 1–10 (2016).
20. Fadok, V. A. *et al.* Exposure of phosphatidylserine on the surface of apoptotic lymphocytes triggers specific recognition and removal by macrophages. *J. Immunol.* **148,** 2207–16 (1992).
21. Panatala, R., Hennrich, H. & Holthuis, J. C. M. Inner workings and biological impact of phospholipid flippases. *J. Cell Sci.* **128,** 2021–2032 (2015).
22. Marsh, D. Lateral pressure profile, spontaneous curvature frustration, and the incorporation and conformation of proteins in membranes. *Biophys. J.* **93,** 3884–3899 (2007).
23. Van Den Brink-Van Der Laan, E., Antoinette Killian, J. & De Kruijff, B. Nonbilayer lipids affect peripheral and integral membrane proteins via changes in the lateral pressure profile. *Biochim. Biophys. Acta - Biomembr.* **1666,** 275–288 (2004).
24. Di Paolo, G. & De Camilli, P. Phosphoinositides in cell regulation and membrane dynamics. *Nature* **443,** 651–657 (2006).
25. De Craene, J. O., Bertazzi, D. L., Bär, S. & Friant, S. Phosphoinositides, major actors in membrane trafficking and lipid signaling pathways. *Int. J. Mol. Sci.* **18,** (2017).
26. Simons, K. & Ikonen, E. Functional rafts in cell membranes. *Nature* **387,** 569–572 (1997).
27. Sezgin, E., Levental, I., Mayor, S. & Eggeling, C. The mystery of membrane organization: Composition, regulation and roles of lipid rafts. *Nat. Rev. Mol. Cell Biol.* **18,** 361–374 (2017).
28. Kusumi, A. *et al.* Paradigm shift of the plasma membrane concept from the two-dimensional

continuum fluid to the partitioned fluid: high-speed single-molecule tracking of membrane molecules. *Annu. Rev. Biophys. Biomol. Struct.* **34,** 351–78 (2005).

29. Mostowy, S. & Cossart, P. Septins: The fourth component of the cytoskeleton. *Nature Reviews Molecular Cell Biology* **13,** 183–194 (2012).
30. Moseley, J. B. An expanded view of the eukaryotic cytoskeleton. *Mol. Biol. Cell* **24,** 1615–8 (2013).
31. Pollard, T. D. Actin and Actin-Binding Proteins. *Cold Spring Harb. Perspect. Biol.* **8,** 381–5 (2016).
32. Otterbein, L. R., Graceffa, P. & Dominguez, R. The crystal structure of uncomplexed actin in the ADP state. *Science (80-.).* **293,** 708–11 (2001).
33. Szent-Györgyi, A. G. The Early History of the Biochemistry of Muscle Contraction. *J. Gen. Physiol.* **123,** 631–641 (2004).
34. Banga, I. *et al.* Myosin and Muscular Contraction. *Studies from the Institute of Medical Chemistry University Szeged1* 1–68 (1942).
35. Balenovic, K. & Straub, F. Ueber das Actomyosin des Kaninchenmuskels. *Stud. Inst. Med. Chem. Szeged* (1942).
36. Finck, H. On the Discovery of Actin. *Science (80-.).* **160,** 332 (1968).
37. Halliburton, W. D. On muscle-plasma. *J. Physiol.* **8,** 133–202 (1887).
38. Herman, I. M. Actin isoforms. *Curr. Opin. Cell Biol.* **5,** 48–55 (1993).
39. Perrin, B. J. & Ervasti, J. M. The actin gene family: Function follows isoform. *Cytoskeleton* **67,** 630–634 (2010).
40. Skruber, K., Read, T.-A. & Vitriol, E. A. Reconsidering an active role for G-actin in cytoskeletal regulation. *J. Cell Sci.* **131,** jcs203760 (2018).
41. Abraham, V. C., Krishnamurthi, V., Lansing Taylor, D. & Lanni, F. The actin-based nanomachine at the leading edge of migrating cells. *Biophys. J.* **77,** 1721–1732 (1999).
42. Suarez, C. & Kovar, D. R. Internetwork competition for monomers governs actin cytoskeleton organization. *Nature Reviews Molecular Cell Biology* **17,** 799–810 (2016).
43. Suarez, C. *et al.* Profilin regulates F-Actin network homeostasis by favoring formin over Arp2/3 complex. *Dev. Cell* **32,** 43–53 (2015).
44. Burke, T. A. *et al.* Homeostatic actin cytoskeleton networks are regulated by assembly factor competition for monomers. *Curr. Biol.* **24,** 579–585 (2014).
45. Chesarone, M. A., Dupage, A. G. & Goode, B. L. Unleashing formins to remodel the actin and microtubule cytoskeletons. *Nature Reviews Molecular Cell Biology* **11,** 62–74 (2010).
46. Svitkina, T. M. Ultrastructure of the actin cytoskeleton. *Curr. Opin. Cell Biol.* **54,** 1–8 (2018).
47. Rotty, J. D., Wu, C. & Bear, J. E. New insights into the regulation and cellular functions of the ARP2/3 complex. *Nat. Rev. Mol. Cell Biol.* **14,** 7–12 (2013).
48. Stevenson, R. P., Veltman, D. & Machesky, L. M. Actin-bundling proteins in cancer progression at a glance. *J. Cell Sci.* **125,** 1073–1079 (2012).
49. Kanellos, G. & Frame, M. C. Cellular functions of the ADF/cofilin family at a glance. *J. Cell Sci.* **129,** 3211–3218 (2016).
50. Michelot, A. & Drubin, D. G. Building distinct actin filament networks in a common cytoplasm. *Curr. Biol.* **21,** 560–569 (2011).
51. Goehring, N. W. & Hyman, A. A. Organelle growth control through limiting pools of cytoplasmic components. *Current Biology* **22,** R330–R339 (2012).
52. Mohapatra, L., Lagny, T. J., Harbage, D., Jelenkovic, P. R. & Kondev, J. The Limiting-Pool Mechanism Fails to Control the Size of Multiple Organelles. *Cell Syst.* **4,** 559–567.e14 (2017).
53. Etienne-Manneville, S. & Hall, A. Rho GTPases in cell biology. *Nature* **420,** 629–635 (2002).
54. Ridley, A. J. Rho GTPase signalling in cell migration. *Curr. Opin. Cell Biol.* **36,** 103–112 (2015).
55. Carlier, M. F. & Shekhar, S. Global treadmilling coordinates actin turnover and controls the size of actin networks. *Nature Reviews Molecular Cell Biology* **18,** 389–401 (2017).
56. Hotulainen, P. & Lappalainen, P. Stress fibers are generated by two distinct actin assembly mechanisms in motile cells. *J. Cell Biol.* **173,** 383–394 (2006).
57. Endlich, N., Otey, C. A., Kriz, W. & Endlich, K. Movement of stress fibers away from focal adhesions identifies focal adhesions as sites of stress fiber assembly in stationary cells. *Cell Motil. Cytoskeleton* **64,** 966–976 (2007).
58. Rossier, O. M. *et al.* Force generated by actomyosin contraction builds bridges between adhesive contacts. *EMBO J.* **29,** 1055–1068 (2010).
59. Dugina, V., Zwaenepoel, I., Gabbiani, G., Clement, S. & Chaponnier, C. beta- and gamma-cytoplasmic actins display distinct distribution and functional diversity. *J. Cell Sci.* **122,** 2980–2988 (2009).
60. Burton, K., Park, J. H. & Taylor, D. L. Keratocytes generate traction forces in two phases. *Mol. Biol. Cell* **10,** 3745–3769 (1999).
61. Cai, Y. *et al.* Nonmuscle myosin IIA-dependent force inhibits cell spreading and drives F-actin flow. *Biophys. J.* **91,** 3907–3920 (2006).

62. Balaban, N. Q. *et al.* Force and focal adhesion assembly: a close relationship studied using elastic micropatterened substrates. *Nat. Cell Biol.* **3,** 466–472 (2001).

63. Cai, Y. & Sheetz, M. P. Force propagation across cells: mechanical coherence of dynamic cytoskeletons. *Current Opinion in Cell Biology* **21,** 47–50 (2009).

64. Cai, Y. *et al.* Cytoskeletal coherence requires myosin-IIA contractility. *J. Cell Sci.* **123,** 413–423 (2010).

65. Khurana, S. & George, S. P. The role of actin bundling proteins in the assembly of filopodia in epithelial cells. *Cell Adh. Migr.* **5,** 409–420 (2011).

66. Mattila, P. K. & Lappalainen, P. Filopodia: Molecular architecture and cellular functions. *Nat. Rev. Mol. Cell Biol.* **9,** 446–454 (2008).

67. Svitkina, T. M. *et al.* Mechanism of filopodia initiation by reorganization of a dendritic network. *J. Cell Biol.* **0240913,** 21–9525 (2003).

68. Steffen, A. *et al.* Filopodia formation in the absence of functional WAVE- and Arp2/3-complexes. *Mol. Biol. Cell* **17,** 2581–91 (2006).

69. Yang, C. *et al.* Novel roles of formin mDia2 in lamellipodia and filopodia formation in motile cells. *PLoS Biol.* **5,** 2624–2645 (2007).

70. Tokuo, H., Mabuchi, K. & Ikebe, M. The motor activity of myosin-X promotes actin fiber convergence at the cell periphery to initiate filopodia formation. *J. Cell Biol.* **179,** 229–238 (2007).

71. Almagro, S. *et al.* The motor protein myosin-X transports VE-cadherin along filopodia to allow the formation of early endothelial cell-cell contacts. *Mol. Cell. Biol.* **30,** 1703–1717 (2010).

72. Mattila, P. K. *et al.* Missing-in-metastasis and IRSp53 deform PI(4,5)P2-rich membranes by an inverse BAR domain-like mechanism. *J. Cell Biol.* **176,** 953–964 (2007).

73. Prévost, C. *et al.* IRSp53 senses negative membrane curvature and phase separates along membrane tubules. *Nat. Commun.* **6,** (2015).

74. Small, J. V., Winkler, C., Vinzenz, M. & Schmeiser, C. Reply: Visualizing branched actin filaments in lamellipodia by electron tomography. *Nature Cell Biology* **13,** 1013–1014 (2011).

75. Urban, E., Jacob, S., Nemethova, M., Resch, G. P. & Small, J. V. Electron tomography reveals unbranched networks of actin filaments in lamellipodia. *Nat. Cell Biol.* **12,** 429–435 (2010).

76. Small, J. V *et al.* Unravelling the structure of the lamellipodium. *J. Microsc.* **231,** 479–85 (2008).

77. Svitkina, T. The Actin Cytoskeleton and Actin-Based Motility. *Cold Spring Harb. Perspect. Biol.* **10,** 1–22 (2018).

78. Svitkina, T. M. Ultrastructure of protrusive actin filament arrays. *Curr. Opin. Cell Biol.* **25,** 574–581 (2013).

79. Xu, K., Babcock, H. P. & Zhuang, X. Dual-objective STORM reveals three-dimensional filament organization in the actin cytoskeleton. *Nat. Methods* **9,** 185–188 (2012).

80. Giannone, G. *et al.* Periodic lamellipodial contractions correlate with rearward actin waves. *Cell* **116,** 431–443 (2004).

81. Ponti, A., Machacek, M., Gupton, S. L., Waterman-Storer, C. M. & Danuser, G. Two distinct actin networks drive the protrusion of migrating cells. *Science (80-.).* **305,** 1782–1786 (2004).

82. Burnette, D. T. *et al.* A role for actin arcs in the leading-edge advance of migrating cells. *Nat. Cell Biol.* **13,** 371–382 (2011).

83. Keren, K. *et al.* Mechanism of shape determination in motile cells. *Nature* **453,** 475–480 (2008).

84. Lacayo, C. I. *et al.* Emergence of large-scale cell morphology and movement from local actin filament growth dynamics. *PLoS Biol.* **5,** 2035–2052 (2007).

85. Yam, P. T. *et al.* Actin-myosin network reorganization breaks symmetry at the cell rear to spontaneously initiate polarized cell motility. *J. Cell Biol.* **178,** 1207–1221 (2007).

86. Wilson, C. A. *et al.* Myosin II contributes to cell-scale actin network treadmilling through network disassembly. *Nature* **465,** 373–377 (2010).

87. Ofer, N., Mogilner, A. & Keren, K. Actin disassembly clock determines shape and speed of lamellipodial fragments. *Proc. Natl. Acad. Sci.* **108,** 20394–20399 (2011).

88. Mogilner, A. & Rubinstein, B. Actin disassembly 'clock' and membrane tension determine cell shape and turning: A mathematical model. *J. Phys. Condens. Matter* **22,** 194118 (2010).

89. Medeiros, N. A., Burnette, D. T. & Forscher, P. Myosin II functions in actin-bundle turnover in neuronal growth cones. *Nat. Cell Biol.* **8,** 215–226 (2006).

90. Yang, Q., Zhang, X. F., Pollard, T. D. & Forscher, P. Arp2/3 complex-dependent actin networks constrain myosin II function in driving retrograde actin flow. *J. Cell Biol.* (2012). doi:10.1083/jcb.201111052

91. Vicente-Manzanares, M., Zareno, J., Whitmore, L., Choi, C. K. & Horwitz, A. F. Regulation of protrusion, adhesion dynamics, and polarity by myosins IIA and IIB in migrating cells. *J. Cell Biol.* **176,** 573–580 (2007).

92. Lombardi, M. L., Knecht, D. A., Dembo, M. & Lee, J. Traction force microscopy in Dictyostelium reveals distinct roles for myosin II motor and actin-crosslinking activity in polarized cell movement. *J. Cell Sci.* **120,** 1624–1634 (2007).

93. Smith, L. A., Aranda-Espinoza, H., Haun, J. B., Dembo, M. & Hammer, D. A. Neutrophil traction stresses are concentrated in the uropod during migration. *Biophys. J.* **92,** L58–L60 (2007).

94. Lämmermann, T. & Sixt, M. Mechanical modes of 'amoeboid' cell migration. *Curr. Opin. Cell Biol.* **21,** 636–644 (2009).

95. Bergert, M., Chandradoss, S. D., Desai, R. A. & Paluch, E. Cell mechanics control rapid transitions between blebs and lamellipodia during migration. *Proc. Natl. Acad. Sci.* **109,** 14434–14439 (2012).

96. Soares e Silva, M. *et al.* Active multistage coarsening of actin networks driven by myosin motors. *Proc. Natl. Acad. Sci.* **108,** 9408–9413 (2011).

97. Reymann, A. C. *et al.* Actin network architecture can determine myosin motor activity. *Science (80-.).* **336,** 1310–1314 (2012).

98. Lenz, M., Thoresen, T., Gardel, M. L. & Dinner, A. R. Contractile units in disordered actomyosin bundles arise from f-actin buckling. *Phys. Rev. Lett.* **108,** (2012).

99. Lenz, M., Gardel, M. L. & Dinner, A. R. Requirements for contractility in disordered cytoskeletal bundles. *New J. Phys.* **14,** (2012).

100. Dasanayake, N. L., Michalski, P. J. & Carlsson, A. E. General mechanism of actomyosin contractility. *Phys. Rev. Lett.* **107,** 1–4 (2011).

101. Murrell, M. P. & Gardel, M. L. F-actin buckling coordinates contractility and severing in a biomimetic actomyosin cortex. *Proc. Natl. Acad. Sci.* **109,** 20820–20825 (2012).

102. Murrell, M., Oakes, P. W., Lenz, M. & Gardel, M. L. Forcing cells into shape: The mechanics of actomyosin contractility. *Nature Reviews Molecular Cell Biology* **16,** 486–498 (2015).

103. Lenz, M. Extensile actomyosin? *ArXive* (2017).

104. Luo, W. *et al.* Analysis of the local organization and dynamics of cellular actin networks. *J. Cell Biol.* **202,** 1057–1073 (2013).

105. Baird, M. A. *et al.* Local pulsatile contractions are an intrinsic property of the myosin 2A motor in the cortical cytoskeleton of adherent cells. *Mol. Biol. Cell* **28,** 240–251 (2017).

106. Lewis, W. H. Contorted Mitosis and the Superficial Plasmagel Layer. *Am. J. Cancer* **35,** 408–415 (1939).

107. Lewis, W. H. The role of a superficial plasmagel layer in changes of form, locomotion and division of cells in tissue cultures. *Arch. exper. Zellforsch.* 3–7 (1939).

108. Geiger, B. Membrane-cytoskeleton interaction. *BBA - Reviews on Biomembranes* (1983). doi:10.1016/0304-4157(83)90005-9

109. Hartwig, J. H., Niederman, R. & Lind, S. E. Cortical actin structures and their relationship to mammalian cell movements. *Subcell Biochem* **11,** 1–49 (1985).

110. Morone, N. *et al.* Three-dimensional reconstruction of the membrane skeleton at the plasma membrane interface by electron tomography. *J. Cell Biol.* **174,** 851–862 (2006).

111. Eghiaian, F., Rigato, A. & Scheuring, S. Structural, mechanical, and dynamical variability of the actin cortex in living cells. *Biophys. J.* **108,** 1330–1340 (2015).

112. Salbreux, G., Charras, G. & Paluch, E. Actin cortex mechanics and cellular morphogenesis. *Trends in Cell Biology* **22,** 536–545 (2012).

113. Bray, D. & White, J. G. Cortical flow in animal cells. *Science (80-.).* **239,** 883–8 (1988).

114. Stewart, M. P. *et al.* Hydrostatic pressure and the actomyosin cortex drive mitotic cell rounding. *Nature* **469,** (2011).

115. Yoneda, M. & Dan, K. Tension at the surface of the dividing sea-urchin egg. *J. Exp. Biol.* **57,** 575–587 (1972).

116. Mukhina, S., Wang, Y. li & Murata-Hori, M. α-Actinin Is Required for Tightly Regulated Remodeling of the Actin Cortical Network during Cytokinesis. *Dev. Cell* **13,** 554–565 (2007).

117. Humphrey, D., Duggan, C., Saha, D., Smith, D. & Käs, J. Active fluidization of polymer networks through molecular motors. *Nature* (2002). doi:10.1038/416413

118. Waugh, R. & Evans, E. A. Thermoelasticity of red blood cell membrane. *Biophys. J.* **26,** 115–131 (1979).

119. Evans, E. & Yeung, A. Apparent viscosity and cortical tension of blood granulocytes determined by micropipet aspiration. *Biophys. J.* **56,** 151–160 (1989).

120. Wang, N. Mechanical interactions among cytoskeletal filaments. *Hypertension* **32,** 162–165 (1998).

121. Harris, A. R. & Charras, G. T. Experimental validation of atomic force microscopy-based cell elasticity measurements. *Nanotechnology* **22,** 345102 (2011).

122. Sato, M., Theret, D. P., Wheeler, L. T., Ohshima, N. & Nerem, R. M. Application of the micropipette technique to the measurement of cultured porcine aortic endothelial cell viscoelastic properties. *J. Biomech. Eng.* **112,** 263–268 (1990).

123. Cartagena-Rivera, A. X., Logue, J. S., Waterman, C. M. & Chadwick, R. S. Actomyosin Cortical Mechanical Properties in Nonadherent Cells Determined by Atomic Force Microscopy. *Biophys. J.* **110,** 2528–2539 (2016).

124. Brenner, S. L. & Korn, E. D. The effects of cytochalasins on actin polymerization and actin ATPase provide insights into the mechanism of polymerization. *J. Biol. Chem.* **255,** 841–844 (1980).

125. Haga, H. *et al.* Elasticity mapping of living fibroblasts by AFM and immunofluorescence observation of the cytoskeleton. *Ultramicroscopy* **82,** 253–258 (2000).

126. Rotsch, C. & Radmacher, M. Drug-induced changes of cytoskeletal structure and mechanics in fibroblasts: An atomic force microscopy study. *Biophys. J.* **78,** 520–535 (2000).

127. Ananthakrishnan, R. *et al.* Quantifying the contribution of actin networks to the elastic strength of fibroblasts. *J. Theor. Biol.* **242,** 502–516 (2006).

128. Elson, E. L. Cellular mechanics as an indicator of cytoskeletal structure and function. *Annu. Rev. Biophys. Biophys. Chem.* **17,** 397–430 (1988).

129. Mayer, M., Depken, M., Bois, J. S., Jülicher, F. & Grill, S. W. Anisotropies in cortical tension reveal the physical basis of polarizing cortical flows. *Nature* **467,** (2010).

130. Nishikawa, M., Naganathan, S. R., Jülicher, F. & Grill, S. W. Controlling contractile instabilities in the actomyosin cortex. *Elife* **6,** (2017).

131. Streichan, S. J., Lefebvre, M. F., Noll, N., Wieschaus, E. F. & Shraiman, B. I. Global morphogenetic flow is accurately predicted by the spatial distribution of myosin motors. *Elife* **7,** (2018).

132. Köster, D. V. & Mayor, S. Cortical actin and the plasma membrane: Inextricably intertwined. *Current Opinion in Cell Biology* **38,** 81–89 (2016).

133. Roh-Johnson, M. *et al.* Triggering a cell shape change by exploiting preexisting actomyosin contractions. *Science (80-.).* **335,** 1232–1235 (2012).

134. Kapus, A. & Janmey, P. Plasma membrane--cortical cytoskeleton interactions: a cell biology approach with biophysical considerations. *Compr. Physiol.* **3,** 1231–81 (2013).

135. Doherty, G. J. & McMahon, H. T. Mediation, Modulation, and Consequences of Membrane-Cytoskeleton Interactions. *Annu. Rev. Biophys.* **37,** 65–95 (2008).

136. Raucher, D. *et al.* Phosphatidylinositol 4,5-Bisphosphate Functions as a Second Messenger that Regulates Cytoskeleton–Plasma Membrane Adhesion. *Cell* **100,** 221–228 (2000).

137. Sheetz, M. P., Sable, J. E., Döbereiner, H.-G. & Obereiner, H.-U. Continuous membrane-cytoskeleton adhesion requires continuous accommodation to lipid and cytoskeleton dynamics. *Annu. Rev. Biophys. Biomol. Struct.* **35,** 417–34 (2006).

138. Kwik, J. *et al.* Membrane cholesterol, lateral mobility, and the phosphatidylinositol 4,5-bisphosphate-dependent organization of cell actin. *Proc. Natl. Acad. Sci.* **100,** 13964–13969 (2003).

139. Mooseker, M. S. Brush border motility: Microvillar contraction in triton-treated brush borders isolated from intestinal epithelium. *J. Cell Biol.* **71,** 417–433 (1976).

140. Collins, J. H. & Borysenko, C. W. The 110,000-dalton actin- and calmodulin-binding protein from intestinal brush border is a myosin-like ATPase. *J. Biol. Chem.* **259,** 14128–35 (1984).

141. Coluccio, L. M. & Bretscher, A. Reassociation of microvillar core proteins: Making a microvillar core in vitro. *J. Cell Biol.* **108,** 495–502 (1989).

142. Collins, K., Sellers, J. R. & Matsudaira, P. Calmodulin dissociation regulates brush border myosin I (110-kD-calmodulin) mechanochemical activity in vitro. *J. Cell Biol.* **110,** 1137–47 (1990).

143. Garcia, A. *et al.* Partial deduced sequence of the 110-kD-calmodulin complex of the avian intestinal microvillus shows that this mechanoenzyme is a member of the myosin I family. *J. Cell Biol.* **109,** 2895–2903 (1989).

144. McConnell, R. E. & Tyska, M. J. Leveraging the membrane - cytoskeleton interface with myosin-1. *Trends in Cell Biology* **20,** 418–426 (2010).

145. McIntosh, B. B. & Ostap, E. M. Myosin-I molecular motors at a glance. *J. Cell Sci.* **129,** 2689–2695 (2016).

146. Adams, R. J. & Pollard, T. D. Binding of myosin I to membrane lipids. *Nature* **340,** 565–568 (1989).

147. Bowers, B. & Korn, E. D. Plasma Membrane Association of Acanthamoeba Myosin I to Plasma Membranes. *J. Cell Biol.* **109,** 1519–1528 (1989).

148. Hayden, S. M., Wolenski, J. S. & Mooseker, M. S. Binding of brush border myosin I to phospholipid vesicles. *J. Cell Biol.* **111,** 443–451 (1990).

149. Cheney, R. E., Riley, M. A. & Mooseker, M. S. Phylogenetic analysis of the myosin superfamily. *Cell Motility and the Cytoskeleton* **24,** 215–223 (1993).

150. De La Cruz, E. M. & Ostap, E. M. Relating biochemistry and function in the myosin superfamily. *Current Opinion in Cell Biology* **16,** 61–67 (2004).

151. Kollmar, M., Dürrwang, U., Kliche, W., Manstein, D. J. & Kull, F. J. Crystal structure of the motor domain of a class-I myosin. *EMBO J.* **21,** 2517–25 (2002).

152. Swanljung-Collins, H. & Collins, J. H. Ca2+ stimulates the Mg2+-ATPase activity of brush border myosin I with three or four calmodulin light chains but inhibits with less than two bound. *J. Biol. Chem.* **266,** 1312–1319 (1991).

153. Collins, K. & Matsudaira, P. Differential regulation of vertebrate myosins I and II. *J. Cell Sci.* **98 Suppl.,** 11–16 (1991).

154. Wolenski, J. S., Hayden, S. M., Forscher, P. & Mooseker, M. S. Calcium-calmodulin and regulation of brush border myosin-I MgATPase and mechanochemistry. *J. Cell Biol.* **122,** 613–21 (1993).

155. Zhu, T., Sata, M. & Ikebe, M. Functional expression of mammalian myosin I beta: analysis of its motor activity. *Biochemistry* **35,** 513–522 (1996).

156. Houdusse, A., Silver, M. & Cohen, C. A model of Ca2+-free calmodulin binding to unconventional myosins reveals how calmodulin acts as a regulatory switch. *Structure* **4,** 1475–1490 (1996).

157. Zhu, T., Beckingham, K. & Ikebe, M. High affinity Ca2+ binding sites of calmodulin are critical for the regulation of myosin Ibeta motor function. *J. Biol. Chem.* **273,** 20481–6 (1998).

158. Gillespie, P. G. & Cyr, J. L. Calmodulin binding to recombinant myosin-1c and myosin-1c IQ peptides. *BMC Biochem.* **3,** (2002).

159. Bähler, M. & Rhoads, A. Calmodulin signaling via the IQ motif. *FEBS Lett.* **513,** 107–113 (2002).

160. Ruppert, C., Kroschewski, R. & Bahler, M. Identification, characterization and cloning of myr-1, a mammalian myosin-I. *J. Cell Biol.* **120,** 1393–1403 (1993).

161. Coluccio, L. M. & Geeves, M. A. Transient Kinetic Analysis of the 130-kDa Myosin I (MYR-1 Gene Product) from Rat Liver A MYOSIN I DESIGNED FOR MAINTENANCE OF TENSION?*. *J. Biol. Chem.* **274,** 21575–80 (1999).

162. Jontes, J. D., Milligan, R. A., Pollard, T. D. & Ostap, E. M. Kinetic characterization of brush border myosin-I ATPase. *Proc. Natl. Acad. Sci.* **94,** 14332–14337 (1997).

163. Veigel, C. *et al.* The motor protein myosin-I produces its working stroke in two steps. *Nature* **398,** 530–533 (1999).

164. Lewis, J. H., Lin, T., Hokanson, D. E. & Ostap, E. M. Temperature dependence of nucleotide association and kinetic characterization of Myo1b. *Biochemistry* **45,** 11589–11597 (2006).

165. Laakso, J. M., Lewis, J. H., Shuman, H. & Ostap, E. M. Myosin I can act as a molecular force sensor. *Science (80-.).* **321,** 133–136 (2008).

166. Laakso, J. M., Lewis, J. H., Shuman, H. & Ostap, E. M. Control of myosin-I force sensing by alternative splicing. *Proc. Natl. Acad. Sci.* **107,** 698–702 (2010).

167. Lewis, J. H., Greenberg, M. J., Laakso, J. M., Shuman, H. & Ostap, E. M. Calcium regulation of Myosin-I tension sensing. *Biophys. J.* **102,** 2799–2807 (2012).

168. Lin, T., Tang, N. & Ostap, E. M. Biochemical and motile properties of Myo1b splice isoform. *J. Biol. Chem.* **280,** 41562–41567 (2005).

169. Mentes, A. *et al.* High-resolution cryo-EM structures of actin-bound myosin states reveal the mechanism of myosin force sensing. *Proc. Natl. Acad. Sci.* **115,** 1292–1297 (2018).

170. Manceva, S. *et al.* Calcium regulation of calmodulin binding to and dissociation from the Myo1c regulatory domain. *Biochemistry* **46,** 11718–11726 (2007).

171. Greenberg, M. J., Lin, T., Goldman, Y. E., Shuman, H. & Ostap, E. M. Myosin IC generates power over a range of loads via a new tension-sensing mechanism. *Proc. Natl. Acad. Sci.* **109,** E2433–E2440 (2012).

172. Greenberg, M. J. & Ostap, E. M. Regulation and control of myosin-I by the motor and light chain-binding domains. *Trends in Cell Biology* **23,** 81–89 (2013).

173. Greenberg, M. J., Lin, T., Shuman, H. & Ostap, E. M. Mechanochemical tuning of myosin-I by the N-terminal region. *Proc. Natl. Acad. Sci.* **112,** E3337–E3344 (2015).

174. Shuman, H. *et al.* A vertebrate myosin-I structure reveals unique insights into myosin mechanochemical tuning. *Proc. Natl. Acad. Sci.* **111,** 2116–2121 (2014).

175. Bähler, M., Kroschewski, R., Stöffler, H. E. & Behrmann, T. Rat myr 4 defines a novel subclass of myosin I: Identification, distribution, localization, and mapping of calmodulin-binding sites with differential calcium sensitivity. *J. Cell Biol.* **126,** 375–389 (1994).

176. Goodson, H. V & Spudich, J. A. Molecular evolution of the myosin family: relationships derived from comparisons of amino acid sequences. *Proc. Natl. Acad. Sci.* **90,** 659–663 (1993).

177. Komaba, S. & Coluccio, L. M. Localization of myosin 1b to actin protrusions requires phosphoinositide binding. *J. Biol. Chem.* **285,** 27686–27693 (2010).

178. Hokanson, D. E., Laakso, J. M., Lin, T., Sept, D. & Ostap, E. M. Myo1c binds phosphoinositides through a putative pleckstrin homology domain. *Mol. Biol. Cell* **17,** 4856–65 (2006).

179. Lemmon, M. a & Ferguson, K. M. Molecular determinants in pleckstrin homology domains that allow specific recognition of phosphoinositides. *Biochem. Soc. Trans.* **29,** 377–384 (2001).

180. Lemmon, M. A., Ferguson, K. M. & Abrams, C. S. Pleckstrin homology domains and the cytoskeleton. *FEBS Lett.* **513,** 71–76 (2002).

181. Hokanson, D. E. & Ostap, E. M. Myo1c binds tightly and specifically to phosphatidylinositol 4,5-bisphosphate and inositol 1,4,5-trisphosphate. *Proc. Natl. Acad. Sci.* **103,** 3118–23 (2006).

182. McKenna, J. M. D. & Ostap, E. M. Kinetics of the Interaction of myo1c with Phosphoinositides. *J. Biol. Chem.* **284,** 28650–28659 (2009).

183. Feeser, E. A., Ignacio, C. M. G., Krendel, M. & Ostap, E. M. Myo1e binds anionic phospholipids with high affinity. *Biochemistry* **49,** 9353–9360 (2010).

184. Pyrpassopoulos, S., Shuman, H. & Michael Ostap, E. Single-molecule adhesion forces and attachment lifetimes of Myosin-I phosphoinositide interactions. *Biophys. J.* **99,** 3916–3922 (2010).

185. Evans, E. & Ludwig, F. Dynamic strengths of molecular anchoring and material cohesion in fluid biomembranes. *J. Phys. Condens. Matter* **12,** A315–A320 (2000).

186. Tang, N. & Ostap, E. M. Motor domain-dependent localization of myo1b (myr-1). *Curr. Biol.* **11,** 1131–1135 (2001).

187. Ruppert, C. *et al.* Localization of the rat myosin I molecules myr 1 and myr 2 and in vivo targeting of their tail domains. *J. Cell Sci.* **108 (Pt 1,** 3775–86 (1995).

188. Yu, Y., Xiong, Y., Montani, J.-P., Yang, Z. & Ming, X.-F. Arginase-II activates mTORC1 through myosin-1b in vascular cell senescence and apoptosis. *Cell Death Dis.* **9,** (2018).

189. Delestre-Delacour, C. *et al.* Myosin 1b and F-actin are involved in the control of secretory granule biogenesis. *Sci. Rep.* **7,** (2017).

190. Kittelberger, N., Breunig, M., Martin, R., Knölker, H.-J. & Miklavc, P. The role of myosin 1c and myosin 1b in surfactant exocytosis. *J. Cell Sci.* **129,** 1685–1696 (2016).

191. Chapman, B. V *et al.* MicroRNA-363 targets myosin 1B to reduce cellular migration in head and neck cancer. *BMC Cancer* **15,** (2015).

192. Ohmura, G. *et al.* Aberrant Myosin 1b Expression Promotes Cell Migration and Lymph Node Metastasis of HNSCC. *Mol. Cancer Res.* **13,** 721–731 (2015).

193. Maravillas-Montero, J. L., Gillespie, P. G., Patino-Lopez, G., Shaw, S. & Santos-Argumedo, L. Myosin 1c Participates in B Cell Cytoskeleton Rearrangements, Is Recruited to the Immunologic Synapse, and Contributes to Antigen Presentation. *J. Immunol.* **187,** 3053–3063 (2011).

194. Fan, Y., Eswarappa, S. M., Hitomi, M. & Fox, P. L. Myo1c facilitates G-actin transport to the leading edge of migrating endothelial cells. *J. Cell Biol.* **198,** 47–55 (2012).

195. Yip, M. F. *et al.* CaMKII-Mediated Phosphorylation of the Myosin Motor Myo1c Is Required for Insulin-Stimulated GLUT4 Translocation in Adipocytes. *Cell Metab.* **8,** 384–398 (2008).

196. Benesh, A. E. *et al.* Differential Localization and Dynamics of Class I Myosins in the Enterocyte Microvillus. *Mol. Biol. Cell* **21,** 970–978 (2010).

197. McConnell, R. E. & Tyska, M. J. Myosin-1a powers the sliding of apical membrane along microvillar actin bundles. *J. Cell Biol.* (2007). doi:10.1083/jcb.200701144

198. Patino-Lopez, G. *et al.* Myosin 1G is an abundant class I myosin in lymphocytes whose localization at the plasma membrane depends on its ancient divergent pleckstrin homology (PH) domain (Myo1PH). *J. Biol. Chem.* **285,** 8675–8686 (2010).

199. Gérard, A. *et al.* Detection of rare antigen-presenting cells through T cell-intrinsic meandering motility, mediated by Myo1g. *Cell* **158,** 492–505 (2014).

200. López-Ortega, O. & Santos-Argumedo, L. Myosin 1g Contributes to CD44 Adhesion Protein and Lipid Rafts Recycling and Controls CD44 Capping and Cell Migration in B Lymphocytes. *Front. Immunol.* **8,** (2017).

201. Benesh, A. E., Fleming, J. T., Chiang, C., Carter, B. D. & Tyska, M. J. Expression and localization of myosin-1d in the developing nervous system. *Brain Res.* **1440,** 9–22 (2012).

202. Tingler, M. *et al.* A Conserved Role of the Unconventional Myosin 1d in Laterality Determination. *Curr. Biol.* **28,** 810–816.e3 (2018).

203. Gupta, P. *et al.* Myosin 1E localizes to actin polymerization sites in lamellipodia, affecting actin dynamics and adhesion formation. *Biol. Open* **2,** 1288–1299 (2013).

204. Yu, H.-Y. E. & Bement, W. M. Multiple Myosins Are Required to Coordinate Actin Assembly with Coat Compression during Compensatory Endocytosis □ D. *Mol. Biol. Cell* **18,** 4096–4105 (2007).

205. Schietroma, C. *et al.* A role for myosin 1e in cortical granule exocytosis in Xenopus oocytes. *J. Biol. Chem.* **282,** 29504–29513 (2007).

206. Krendel, M., Osterweil, E. K. & Mooseker, M. S. Myosin 1E interacts with synaptojanin-1 and dynamin and is involved in endocytosis. *FEBS Lett.* **581,** 644–650 (2007).

207. Kim, S. V *et al.* Modulation of cell adhesion and motility in the immune system by Myo1f. *Science (80-.).* **314,** 136–139 (2006).

208. Idrissi, F. Z. *et al.* Distinct acto/myosin-I structures associate with endocytic profiles at the plasma membrane. *J. Cell Biol.* (2008). doi:10.1083/jcb.200708060

209. Geli, M.-I. & Riezman, H. Role of type I myosins in receptor-mediated endocytosis in yeast. *Science (80-.).* **272,** 533–535 (1996).

210. Pyrpassopoulos, S. *et al.* Force generation by membrane-associated myosin-I. *Sci. Rep.* **6,** (2016).

211. Olety, B., Wälte, M., Honnert, U., Schillers, H. & Bähler, M. Myosin 1G (Myo1G) is a haematopoietic specific myosin that localises to the plasma membrane and regulates cell elasticity. *FEBS Lett.* **584,** 493–499 (2010).

212. López-Ortega, O. *et al.* Myo1g is an active player in maintaining cell stiffness in B-lymphocytes. *Cytoskeleton* **73,** 258–268 (2016).

213. Dai, J., Ting-Beall, H. P., Hochmuth, R. M., Sheetz, M. P. & Titus, M. A. Myosin I contributes to the generation of resting cortical tension. *Biophys. J.* **77,** 1168–1176 (1999).

214. Sato, N. *et al.* A gene family consisting of ezrin, radixin and moesin. Its specific localization at actin filament/plasma membrane association sites. *J. Cell Sci.* **103 (Pt 1,** 131–143 (1992).

215. Bretscher, A. Purification of an 80,000-dalton protein that is a component of the isolated microvillus cytoskeleton, and its localization in nonmuscle cells. *J. Cell Biol.* **97,** 425–432 (1983).

216. Pakkanen, R., Hedman, K., Turunen, O., Wahlstrom, 1drsten & Vaheri, A. Microvillus-specific Mr 75,000 Plasma Membrane Protein of Human Choriocarcinoma Cells1. *J. Histochem. Cytochem.* **35,** 809–816 (1987).

217. Saotome, I., Curto, M. & McClatchey, A. I. Ezrin is essential for epithelial organization and villus morphogenesis in the developing intestine. *Dev. Cell* **6,** 855–864 (2004).

218. Göbel, V., Barrett, P. L., Hall, D. H. & Fleming, J. T. Lumen morphogenesis in C. elegans requires the membrane-cytoskeleton linker erm-1. *Dev. Cell* **6,** 865–873 (2004).

219. Van Fürden, D., Johnson, K., Segbert, C. & Bossinger, O. The C. elegans ezrin-radixin-moesin protein ERM-1 is necessary for apical junction remodelling and tubulogenesis in the intestine. *Dev. Biol.* **272,** 262–276 (2004).

220. Gautreau, A., Louvard, D. & Arpin, M. Morphogenic effects of ezrin require a phosphorylation-induced transition from oligomers to monomers at the plasma membrane. *J. Cell Biol.* **150,** 193–203 (2000).

221. Zwaenepoel, I. *et al.* Ezrin regulates microvillus morphogenesis by promoting distinct activities of Eps8 proteins. *Mol. Biol. Cell* **23,** 1080–1095 (2012).

222. Bretscher, A., Edwards, K. & Fehon, R. G. ERM proteins and merlin: Integrators at the cell cortex. *Nature Reviews Molecular Cell Biology* (2002). doi:10.1038/nrm882

223. Doi, Y. *et al.* Normal development of mice and unimpaired cell adhesion/cell motility/actin-based cytoskeleton without compensatory up-regulation of ezrin or radixin in moesin gene knockout. *J. Biol. Chem.* **274,** 2315–21 (1999).

224. Kikuchi, S. *et al.* Radixin deficiency causes conjugated hyperbilirubinemia with loss of Mrp2 from bile canalicular membranes. *Nat. Genet.* **31,** 320–325 (2002).

225. Fehon, R. G., McClatchey, A. I. & Bretscher, A. Organizing the cell cortex: the role of ERM proteins. *Nat. Rev. Mol. Cell Biol.* **11,** 276–87 (2010).

226. Turunen, O., Wahlström, T. & Vaheri, A. Ezrin has a COOH-terminal actin-binding site that is conserved in the ezrin protein family. *J. Cell Biol.* **126,** 1445–1453 (1994).

227. Gary, R. & Bretscher, A. Ezrin self-association involves binding of an N-terminal domain to a normally masked C-terminal domain that includes the F-actin binding site. *Mol. Biol. Cell* **6,** 1061–75 (1995).

228. Li, Q. *et al.* Self-masking in an Intact ERM-merlin Protein: An Active Role for the Central α-Helical Domain. *J. Mol. Biol.* **365,** 1446–1459 (2007).

229. Pearson, M. A., Reczek, D., Bretscher, A. & Karplus, P. A. Structure of the ERM protein moesin reveals the FERM domain fold masked by an extended actin binding tail domain. *Cell* **101,** 259–270 (2000).

230. Hamada, K., Shimizu, T., Matsui, T., Tsukita, S. & Hakoshima, T. Structural basis of the membrane-targeting and unmasking mechanisms of the radixin FERM domain. *EMBO J.* **19,** 4449–62 (2000).

231. Edwards, S. D. & Keep, N. H. The 2.7 A crystal structure of the activated FERM domain of moesin: an analysis of structural changes on activation. *Biochemistry* **40,** 7061–8 (2001).

232. Matsui, T. *et al.* Rho-kinase phosphorylates COOH-terminal threonines of ezrin/radixin/moesin (ERM) proteins and regulates their head-to-tail association. *J. Cell Biol.* **140,** 647–657 (1998).

233. Herrig, A. *et al.* Cooperative adsorption of ezrin on PIP2-containing membranes. *Biochemistry* **45,** 13025–13034 (2006).

234. Braunger, J. A. *et al.* Phosphatidylinositol 4,5-bisphosphate alters the number of attachment sites between ezrin and actin filaments: A colloidal probe study. *J. Biol. Chem.* **289,** 9833–9843 (2014).

235. Yonemura, S., Matsui, T., Tsukita, S. & Tsukita, S. Rho-dependent and -independent activation mechanisms of ezrin/radixin/moesin proteins: an essential role for polyphosphoinositides in vivo. *J. Cell Sci.* **115,** 2569–2580 (2002).

236. Fievet, B. T. *et al.* Phosphoinositide binding and phosphorylation act sequentially in the activation mechanism of ezrin. *J. Cell Biol.* **164,** 653–659 (2004).

237. Bosk, S., Braunger, J. A., Gerke, V. & Steinem, C. Activation of F-actin binding capacity of ezrin: Synergism of PIP2 interaction and phosphorylation. *Biophys. J.* **100,** 1708–1717 (2011).

238. Carreno, S. *et al.* Moesin and its activating kinase Slik are required for cortical stability and microtubule organization in mitotic cells. *J. Cell Biol.* **180,** 739–746 (2008).

239. Kunda, P., Pelling, A. E., Liu, T. & Baum, B. Moesin Controls Cortical Rigidity, Cell Rounding, and Spindle Morphogenesis during Mitosis. *Curr. Biol.* **18,** 91–101 (2008).

240. Roubinet, C. *et al.* Molecular networks linked by Moesin drive remodeling of the cell cortex during mitosis. *J. Cell Biol.* **195,** 99–112 (2011).

241. Charras, G. T., Hu, C. K., Coughlin, M. & Mitchison, T. J. Reassembly of contractile actin cortex in cell blebs. *J. Cell Biol.* **175,** 477–490 (2006).

242. Rouven Brückner, B., Pietuch, A., Nehls, S., Rother, J. & Janshoff, A. Ezrin is a Major Regulator of Membrane Tension in Epithelial Cells. *Sci. Rep.* **5,** 14700 (2015).

243. Liu, Y. *et al.* Constitutively active ezrin increases membrane tension, slows migration, and impedes endothelial transmigration of lymphocytes in vivo in mice. *Blood* **119,** 445–453 (2012).

244. McClatchey, A. I. & Fehon, R. G. Merlin and the ERM proteins - regulators of receptor distribution and signaling at the cell cortex. *Trends in Cell Biology* **19,** 198–206 (2009).

245. Tsukita, S. *et al.* ERM family members as molecular linkers between the cell surface glycoprotein CD44 and actin-based cytoskeletons. *J. Cell Biol.* **126,** 391–401 (1994).

246. Mori, T. *et al.* Structural basis for CD44 recognition by ERM proteins. *J. Biol. Chem.* **283,** 29602–29612 (2008).

247. Kondo, T. *et al.* ERM (Ezrin/Radixin/Moesin)-based Molecular Mechanism of Microvillar Breakdown at an Early Stage of Apoptosis. *J. Cell Biol.* **139,** 749–758 (1997).

248. Yonemura, S., Tsukita, S. & Tsukita, S. Direct Involvement of Ezrin/Radixin/Moesin (ERM)-binding Membrane Proteins in the Organization of Microvilli in Collaboration with Activated ERM Proteins. *J. Cell Biol.* **145,** 1497–1509 (1999).

249. Orian-Rousseau, V. *et al.* Hepatocyte growth factor-induced Ras activation requires ERM proteins linked to both CD44v6 and F-actin. *Mol. Biol. Cell* **18,** 76–83 (2007).

250. Parameswaran, N., Matsui, K. & Gupta, N. Conformational Switching in Ezrin Regulates Morphological and Cytoskeletal Changes Required for B Cell Chemotaxis. *J. Immunol.* **186,** 4088–4097 (2011).

251. Lee, J.-H. *et al.* Roles of p-ERM and Rho–ROCK signaling in lymphocyte polarity and uropod formation. *J. Cell Biol.* **167,** 327–337 (2004).

252. Coffey, G. P. *et al.* Engagement of CD81 induces ezrin tyrosine phosphorylation and its cellular redistribution with filamentous actin. *J. Cell Sci.* **122,** 3137–3144 (2009).

253. Allenspach, E. J. *et al.* ERM-dependent movement of CD43 defines a novel protein complex distal to the immunological synapse. *Immunity* **15,** 739–750 (2001).

254. Roumier, A. *et al.* The membrane-microfilament linker ezrin is involved in the formation of the immunological synapse and in T cell activation. *Immunity* **15,** 715–728 (2001).

255. Delon, J., Kaibuchi, K. & Germain, R. N. Exclusion of CD43 from the immunological synapce is mediated by phosphorylation-regulated relocation of the cytoskeletal adaptor Moesin. *Immunity* **15,** 691–701 (2001).

256. Faure, S. *et al.* ERM proteins regulate cytoskeleton relaxation promoting T cell-APC conjugation. *Nat. Immunol.* **5,** 272–279 (2004).

257. Shaffer, M. H. *et al.* Ezrin and Moesin Function Together to Promote T Cell Activation. *J. Immunol.* **182,** 1021–1032 (2009).

258. Ilani, T., Khanna, C., Zhou, M., Veenstra, T. D. & Bretscher, A. Immune synapse formation requires ZAP-70 recruitment by ezrin and CD43 removal by moesin. *J. Cell Biol.* **179,** 733–746 (2007).

259. Pore, D. *et al.* Ezrin Tunes the Magnitude of Humoral Immunity. *J. Immunol.* **191,** 4048–4058 (2013).

260. Treanor, B. *et al.* The Membrane Skeleton Controls Diffusion Dynamics and Signaling through the B Cell Receptor. *Immunity* **32,** 187–199 (2010).

261. Treanor, B., Depoil, D., Bruckbauer, A. & Batista, F. D. Dynamic cortical actin remodeling by ERM proteins controls BCR microcluster organization and integrity. *J. Exp. Med.* **208,** 1055–1068 (2011).

262. Parameswaran, N., Enyindah-Asonye, G., Bagheri, N., Shah, N. B. & Gupta, N. Spatial coupling of JNK activation to the B cell antigen receptor by tyrosine-phosphorylated ezrin. *J. Immunol.* **190,** 2017–26 (2013).

263. Hogue, M. J. The Effect of Hypotonic and Hypertonic Solutions on Fibroblasts of the Embryonic Chick Heart in Vitro. *J. Exp. Med.* **xxx,** 617–649 (1919).

264. Robertson, A. M. G., Bird, C. C., Waddell, A. W. & Currie, A. R. Morphological aspects of glucocorticoid-induced cell death in human lymphoblastoid cells. *J. Pathol.* **126,** 181–187 (1978).

265. MacKenzie, A. *et al.* Rapid secretion of interleukin-1β by microvesicle shedding. *Immunity* **15,** 825–835 (2001).

266. Trinkaus, J. P. Activity and Locomotion Blastula of Funduhs Stages Deep Cells During and Gastrula The Fun-. *Dev. Biol.* **103,** 68–103 (1973).

267. Charras, G. & Paluch, E. Blebs lead the way: How to migrate without lamellipodia. *Nature Reviews Molecular Cell Biology* **9,** 730–736 (2008).

268. Blaser, H. *et al.* Migration of Zebrafish Primordial Germ Cells: A Role for Myosin Contraction and Cytoplasmic Flow. *Dev. Cell* **11,** 613–627 (2006).

269. Yoshida, K. & Soldati, T. Dissection of amoeboid movement into two mechanically distinct modes. *J. Cell Sci.* **119,** 3833–3844 (2006).

270. Fishkind, D. J., Cao, L.-G. & Wang, Y.-L. Microinjection of the Catalytic Fragment of Myosin Light Chain Kinase into Dividing Cells : Effects on Mitosis and Cytokinesis. *J. Cell Biol.* **114,** (1991).

271. Tinevez, J.-Y. *et al.* Role of cortical tension in bleb growth. *Proc. Natl. Acad. Sci.* **106,** 18581–18586 (2009).

272. Cunningham, C. *et al.* Actin-binding protein requirement for cortical stability and efficient locomotion. *Science (80-.).* **255,** 325–327 (1992).

273. Coleman, M. L. *et al.* Membrane blebbing during apoptosis results from caspase-mediated activation of ROCK I. *Nat. Cell Biol.* **3,** 339–45 (2001).

274. Sahai, E. & Marshall, C. J. Differing modes for tumour cell invasion have distinct requirements for Rho/ROCK signalling and extracellular proteolysis. *Nat. Cell Biol.* **5,** 711–719 (2003).

275. Stastna, J. *et al.* Differing and isoform-specific roles for the formin DIAPH3 in plasma membrane blebbing and filopodia formation. *Cell Res.* **22,** 728–745 (2012).

276. Hannemann, S. *et al.* The diaphanous-related formin FHOD1 associates with ROCK1 and promotes

Src-dependent plasma membrane blebbing. *J. Biol. Chem.* **283,** 27891–27903 (2008).

277. Eisenmann, K. M. *et al.* Dia-Interacting Protein Modulates Formin-Mediated Actin Assembly at the Cell Cortex. *Curr. Biol.* **17,** 579–591 (2007).

278. Kitzing, T. M. *et al.* Positive feedback between Dia1, LARG, and RhoA regulates cell morphology and invasion. *Genes Dev.* **21,** 1478–1483 (2007).

279. Kitzing, T. M., Wang, Y., Pertz, O., Copeland, J. W. & Grosse, R. Formin-like 2 drives amoeboid invasive cell motility downstream of RhoC. *Oncogene* **29,** 2441–2448 (2010).

280. Charras, G. T., Coughlin, M., Mitchison, T. J. & Mahadevan, L. Life and times of a cellular bleb. *Biophys. J.* **94,** 1836–1853 (2008).

281. Cunningham, C. C. Actin polymerization and intracellular solvent flow in cell surface blebbing. *J. Cell Biol.* **129,** 1589–1599 (1995).

282. Biro, M. *et al.* Cell cortex composition and homeostasis resolved by integrating proteomics and quantitative imaging. *Cytoskeleton* **70,** 741–754 (2013).

283. Bovellan, M. *et al.* Cellular control of cortical actin nucleation. *Curr. Biol.* **24,** 1628–1635 (2014).

284. Hirai, H., Maru, Y., Hagiwara, K., Nishida, J. & Takaku, F. A novel putative tyrosine kinase receptor encoded by the eph gene. *Science (80-.).* **238,** 1717–20 (1987).

285. Anderson, D. J. *et al.* Unified Nomenclature for Eph Family Receptors and Their Ligands, the Ephrins. *Cell* **90,** 403–404 (1997).

286. Letwin, K., Yee, S. P. & Pawson, T. Novel protein-tyrosine kinase cDNAs related to fps/fes and eph cloned using anti-phosphotyrosine antibody. *Oncogene* **3,** 621–627 (1988).

287. Lindberg, R. A. & Hunter, T. cDNA cloning and characterization of eck, an epithelial cell receptor protein-tyrosine kinase in the eph/elk family of protein kinases. *Mol. Cell. Biol.* **10,** 6316–6324 (1990).

288. Tischer, S., Reineck, M., Söding, J., Münder, S. & Böttger, A. Eph receptors and ephrin class B ligands are expressed at tissue boundaries in Hydra vulgaris. *Int. J. Dev. Biol.* **57,** 759–765 (2013).

289. Nikolov, D., Li, C., Lackmann, M., Jeffrey, P. & Himanen, J. Crystal structure of the human ephrin-A5 ectodomain. *Protein Sci.* **16,** 996–1000 (2007).

290. Himanen, J. P. *et al.* Ligand recognition by A-class Eph receptors: crystal structures of the EphA2 ligand-binding domain and the EphA2/ephrin-A1 complex. *EMBO Rep.* **10,** 722–728 (2009).

291. Himanen, J.-P., Henkemeyer, M. & Nikolov, D. B. Crystal structure of the ligand-binding domain of the receptor tyrosine kinase EphB2. *Nature* **396,** 486–491 (1998).

292. Nikolov, D., Li, C., Lackmann, M., Jeffrey, P. & Himanen, J. Crystal structure of the human ephrin-A5 ectodomain. *Protein Sci.* **16,** 996–1000 (2007).

293. Himanen, J. P. *et al.* Repelling class discrimination: Ephrin-A5 binds to and activates EphB2 receptor signaling. *Nat. Neurosci.* **7,** 501–509 (2004).

294. Bartley, T. D. *et al.* B61 is a ligand for the ECK receptor protein-tyrosine kinase. *Nature* **368,** 558–560 (1994).

295. Davis, S. *et al.* Ligands for EPH-related receptor tyrosine kinases that require membrane attachment or clustering for activity. *Science (80-.).* **266,** 816–819 (1994).

296. Holland, S. J. *et al.* Bidirectional signalling through the EPH-family receptor Nuk and its transmembrane ligands. *Nature* **383,** 722–725 (1996).

297. Brückner, K., Pasquale, E. B. & Klein, R. Tyrosine phosphorylation of transmembrane ligands for Eph receptors. *Science (80-.).* **275,** 1640–1643 (1997).

298. Davy, A., Aubin, J. & Soriano, P. Ephrin-B1 forward and reverse signaling are required during mouse development. *Genes Dev.* **18,** 572–583 (2004).

299. Pasquale, E. B. Eph receptors and ephrins in cancer: bidirectional signalling and beyond. *Nat. Rev. Cancer* **10,** 165–180 (2010).

300. Lisabeth, E. M., Falivelli, G. & Pasquale, E. B. Eph receptor signaling and ephrins. *Cold Spring Harb. Perspect. Biol.* **5,** (2013).

301. Himanen, J. P. *et al.* Crystal structure of an Eph receptor-ephrin complex. *Nature* (2001). doi:10.1038/414933a

302. Stein, E. *et al.* Eph receptors discriminate specific ligand oligomers to determine alternative signaling complexes, attachment, and assembly responses. *Genes Dev.* **12,** 667–678 (1998).

303. Lawrenson, I. D. *et al.* Ephrin-A5 induces rounding, blebbing and de-adhesion of EphA3-expressing 293T and melanoma cells by CrkII and Rho-mediated signalling. *J. Cell Sci.* **115,** 1059–72 (2002).

304. Huynh-Do, U. Surface densities of ephrin-B1 determine EphB1-coupled activation of cell attachment through alpha vbeta 3 and alpha 5beta 1 integrins. *EMBO J.* **18,** 2165–2173 (1999).

305. Mann, F., Miranda, E., Weinl, C., Harmer, E. & Holt, C. E. B-Type Eph Receptors and Ephrins Induce Growth Cone Collapse through Distinct Intracellular Pathways. *J. Neurobiol.* **57,** 323–336 (2003).

306. Wimmer-Kleikamp, S. H., Janes, P. W., Squire, A., Bastiaens, P. I. H. & Lakmann, M. Recruitment of Eph receptors into signaling clusters does not require ephrin contact. *J. Cell Biol.* **164,** 661–666 (2004).

307. Himanen, J. P. *et al.* Architecture of Eph receptor clusters. *Proc. Natl. Acad. Sci.* **107,** 10860–10865

(2010).

308. Seiradake, E., Harlos, K., Sutton, G., Aricescu, A. R. & Jones, E. Y. An extracellular steric seeding mechanism for Eph-ephrin signaling platform assembly. *Nat. Struct. Mol. Biol.* **17,** 398–402 (2010).

309. Seiradake, E. *et al.* Structurally encoded intraclass differences in EphA clusters drive distinct cell responses. *Nat. Struct. Mol. Biol.* **20,** 958–964 (2013).

310. Schaupp, A. *et al.* The composition of EphB2 clusters determines the strength in the cellular repulsion response. *J. Cell Biol.* **204,** 409–422 (2014).

311. Hortigüela, V. *et al.* Nanopatterns of Surface-Bound EphrinB1 Produce Multivalent Ligand-Receptor Interactions That Tune EphB2 Receptor Clustering. *Nano Lett.* **18,** 629–637 (2018).

312. Ojosnegros, S. *et al.* Eph-ephrin signaling modulated by polymerization and condensation of receptors. *Proc. Natl. Acad. Sci.* **114,** 13188–13193 (2017).

313. Sabet, O. *et al.* Ubiquitination switches EphA2 vesicular traffic from a continuous safeguard to a finite signalling mode. *Nat. Commun.* **6,** 1–13 (2015).

314. Nievergall, E. *et al.* PTP1B regulates Eph receptor function and trafficking. *J. Cell Biol.* **191,** 1189–1203 (2010).

315. Stallaert, W., Sabet, O., Bruggemann, Y., Baak, L. & Bastiaens, P. Contact inhibitory Eph signalling decouples EGFR activity from vesicular recycling to generate contextual plasticity. *bioRxiv* 202705 (2017). doi:10.1101/202705

316. Kania, A. & Klein, R. Mechanisms of ephrin-Eph signalling in development, physiology and disease. *Nature Reviews Molecular Cell Biology* **17,** 240–256 (2016).

317. Rohani, N., Canty, L., Luu, O., Fagotto, F. & Winklbauer, R. EphrinB/EphB Signaling Controls Embryonic Germ Layer Separation by Contact-Induced Cell Detachment. *PLoS Biol* **9,** (2011).

318. Fagotto, F. O., Rohani, N., Touret, A.-S. & Li, R. A Molecular Base for Cell Sorting at Embryonic Boundaries: Contact Inhibition of Cadherin Adhesion by Ephrin/Eph-Dependent Contractility. *Dev. Cell* **27,** 72–87 (2013).

319. Batlle, E. *et al.* Beta-catenin and TCF mediate cell positioning in the intestinal epithelium by controlling the expression of EphB/ephrinB. *Cell* **111,** 251–63 (2002).

320. Genander, M. *et al.* Dissociation of EphB2 Signaling Pathways Mediating Progenitor Cell Proliferation and Tumor Suppression. *Cell* **139,** 679–692 (2009).

321. Holmberg, J. *et al.* EphB Receptors Coordinate Migration and Proliferation in the Intestinal Stem Cell Niche. *Cell* **125,** 1151–1163 (2006).

322. Bush, J. O. & Soriano, P. Ephrin-B1 forward signaling regulates craniofacial morphogenesis by controlling cell proliferation across Eph-ephrin boundaries. *Genes Dev.* **24,** 2068–80 (2010).

323. Batlle, E. *et al.* EphB receptor activity suppresses colorectal cancer progression. *Nature* **435,** 1126–1130 (2005).

324. Cortina, C. *et al.* EphB-ephrin-B interactions suppress colorectal cancer progression by compartmentalizing tumor cells. *Nat. Genet.* **39,** 1376–1383 (2007).

325. Lodola, A., Giorgio, C., Incerti, M., Zanotti, I. & Tognolini, M. Targeting Eph/ephrin system in cancer therapy. *European Journal of Medicinal Chemistry* **142,** 152–162 (2017).

326. Charmsaz, S., Scott, A. M. & Boyd, A. W. Targeted therapies in hematological malignancies using therapeutic monoclonal antibodies against Eph family receptors. *Experimental Hematology* **54,** 31–39 (2017).

327. Astin, J. W. *et al.* Competition amongst Eph receptors regulates contact inhibition of locomotion and invasiveness in prostate cancer cells. *Nat. Cell Biol.* **12,** 1194–1204 (2010).

328. Mclaughlin, T., Lim, Y.-S., Santiago, A. & O 'leary, D. D. M. Multiple EphB receptors mediate dorsal–ventral retinotopic mapping via similar bi-functional responses to ephrin-B1. *Mol. Cell. Neurosci.* **63,** 24–30 (2014).

329. Cheng, H. J., Nakamoto, M., Bergemann, A. D. & Flanagan, J. G. Complementary gradients in expression and binding of ELF-1 and Mek4 in development of the topographic retinotectal projection map. *Cell* **82,** 371–381 (1995).

330. Holash, J. A. & Pasquale, E. B. Polarized expression of the receptor protein-tyrosine kinase CEK% in the developing avian visual-system. *Dev. Biol.* **172,** 683–693 (1995).

331. Kenny, D., Bronner-Fraser, M. A., DasGupta, R., Charnay, P. & Wilkinson, D. G. The receptor tyrosine kinase QEK5 messenger-RNA is expressed in a gradient within the neural retina and the tectum. *Dev. Biol.* **172,** 708–716 (1995).

332. Birgbauer, E., Cowan, C. A., Sretavan, D. W. & Henkemeyer, M. Kinase independent function of EphB receptors in retinal axon pathfinding to the optic disc from dorsal but not ventral retina. *Development* **127,** 1231–41 (2000).

333. Marcus, R. C., Gale, N. W., Morrison, M. E., Mason, C. A. & Yancopoulos, G. D. Eph family receptors and their ligands distribute in opposing gradients in the developing mouse retina. *Dev. Biol.* **180,** 786–789 (1996).

334. Nunan, R. *et al.* Ephrin-Bs Drive Junctional Downregulation and Actin Stress Fiber Disassembly to Enable Wound Re-epithelialization. *Cell Rep.* **13,** 1380–1395 (2015).

335. Santiago, A. & Erickson, C. A. Ephrin-B ligands play a dual role in the control of neural crest cell

migration. *Development* **129,** 3621–3632 (2002).

336. O'Neill, A. K. *et al.* Unidirectional Eph/ephrin signaling creates a cortical actomyosin differential to drive cell segregation. *J. Cell Biol.* **215,** 217–229 (2016).

337. Kayser, M. S., Nolt, M. J. & Dalva, M. B. EphB Receptors Couple Dendritic Filopodia Motility to Synapse Formation. *Neuron* **59,** 56–69 (2008).

338. Cissé, M. *et al.* Reversing EphB2 depletion rescues cognitive functions in Alzheimer model. *Nature* **469,** (2011).

339. Locke, C., Machida, K., Wu, Y. & Yu, J. Optogenetic activation of EphB2 receptor in dendrites induced actin polymerization by activating Arg kinase. *Biol. Open* **6,** 1820–1830 (2017).

340. Holmberg, J., Clarke, D. L. & Frisen, J. Regulation of repulsion versus adhesion by different splice forms of an Eph receptor. *Nature* **408,** 203–206 (2000).

341. Grunwald, I. C. *et al.* Kinase-Independent Requirement of EphB2 Receptors in Hippocampal Synaptic Plasticity. *Neuron* **32,** 1027–1040 (2001).

342. Soskis, M. J. *et al.* A chemical genetic approach reveals distinct EphB signaling mechanisms during brain development. *Nat. Neurosci.* (2012). doi:10.1038/nn.3249

343. Drescher, U. *et al.* In vitro guidance of retinal ganglion cell axons by RAGS, a 25 kDa tectal protein related to ligands for Eph receptor tyrosine kinases. *Cell* **82,** 359–370 (1995).

344. Bonanomi, D. *et al.* Ret Is a Multifunctional Coreceptor that Integrates Diffusible- and Contact-Axon Guidance Signals. *Cell* **148,** 568–582 (2012).

345. Villar-Cerviñ, V. *et al.* Contact Repulsion Controls the Dispersion and Final Distribution of Cajal-Retzius Cells. *Neuron* **77,** 457–471 (2013).

346. Bush, J. O. & Soriano, P. Ephrin-B1 regulates axon guidance by reverse signaling through a PDZ-dependent mechanism. *Genes Dev.* **23,** 1586–1599 (2009).

347. Durbin, L. *et al.* Eph signaling is required for segmentation and differentiation of the somites. *Genes Dev.* **12,** 3096–3109 (1998).

348. Barrios, A. *et al.* Eph/Ephrin Signaling Regulates the Mesenchymal- to-Epithelial Transition of the Paraxial Mesoderm during Somite Morphogenesis. *Curr. Biol.* **13,** 1571–1582 (2003).

349. Compagni, A., Logan, M., Klein, R. D. & Adams, R. H. Control of Skeletal Patterning by EphrinB1-EphB Interactions. *Dev. Cell* **5,** 217–230 (2003).

350. Xu, Q., Mellitzer, G., Robinson, V. & Wilkinson, D. G. In vivo cell sorting in complementary segmental domains mediated by Eph receptors and ephrins. *Nature* **399,** 267–71 (1999).

351. Mellitzer, G., Xu, Q. & Wilkinson, D. G. Eph receptors and ephrins restrict cell intermingling and communication. *Nature* **400,** 77–81 (1999).

352. Canty, L., Zarour, E., Kashkooli, L., François, P. & Fagotto, F. Sorting at embryonic boundaries requires high heterotypic interfacial tension. *Nat. Commun.* **8,** (2017).

353. Taylor, H. B. *et al.* Cell segregation and border sharpening by Eph receptor–ephrin-mediated heterotypic repulsion. *J. R. Soc. Interface* **14,** 20170338 (2017).

354. Rodriguez-Franco, P. *et al.* Long-lived force patterns and deformation waves at repulsive epithelial boundaries. *Nat. Mater.* **16,** 1029–1036 (2017).

355. Stramer, B. & Mayor, R. Mechanisms and in vivo functions of contact inhibition of locomotion. *Nat. Rev. Mol. Cell Biol.* **18,** (2016).

356. Evergren, E., Cobbe, N. & McMahon, H. T. Eps15R and clathrin regulate EphB2-mediated cell repulsion. *Traffic* **19,** 44–57 (2018).

357. Marston, D. J., Dickinson, S. & Nobes, C. D. Rac-dependent trans-endocytosis of ephrinBs regulates Eph–ephrin contact repulsion. *Nat. Cell Biol.* **5,** (2003).

358. Zimmer, M., Palmer, A., Köhler, J. & Klein, R. EphB-ephrinB bi-directional endocytosis terminates adhesion allowing contact mediated repulsion. *Nat. Cell Biol.* **5,** 869–878 (2003).

359. Gaitanos, T. N., Koerner, J. & Klein, R. Tiam-Rac signaling mediates trans-endocytosis of ephrin receptor EphB2 and is important for cell repulsion. *Journal of Cell Biology* **215,** 431–431 (2016).

360. Hattori, M., Osterfield, M. & Flanagan, J. G. Regulated cleavage of a contact-mediated axon repellent. *Science (80-.).* **289,** 1360–1365 (2000).

361. Janes, P. W. *et al.* Adam meets Eph: An ADAM substrate recognition module acts as a molecular switch for ephrin cleavage in trans. *Cell* **123,** 291–304 (2005).

362. Lin, K. T., Sloniowski, S., Ethell, D. W. & Ethell, I. M. Ephrin-B2-induced cleavage of EphB2 receptor is mediated by matrix metalloproteinases to trigger cell repulsion. *J. Biol. Chem.* **283,** 28969–28979 (2008).

363. Solanas, G., Cortina, C., Sevillano, M. & Batlle, E. Cleavage of E-cadherin by ADAM10 mediates epithelial cell sorting downstream of EphB signalling. *Nat. Cell Biol.* **13,** 1100–1109 (2011).

364. Carter, N., Nakamoto, T., Hirai, H. & Hunter, T. EphrinA1-induced cytoskeletal re-organization requires FAK and p130cas. *Nat. Cell Biol.* **4,** 565–573 (2002).

365. Shi, Y., Pontrello, C. G., DeFea, K. A., Reichardt, L. F. & Ethell, I. M. Focal Adhesion Kinase Acts Downstream of EphB Receptors to Maintain Mature Dendritic Spines by Regulating Cofilin Activity. *J. Neurosci.* **29,** 8129–8142 (2009).

366. Salaita, K. *et al.* Restriction of receptor movement alters cellular response: Physical force sensing by EphA2. *Science (80-.).* **327,** 1380–1385 (2010).

367. Xu, Q., Lin, W. C., Petit, R. S. & Groves, J. T. EphA2 receptor activation by monomeric ephrin-A1 on supported membranes. *Biophys. J.* **101,** 2731–2739 (2011).

368. Lohmüller, T., Xu, Q. & Groves, J. T. Nanoscale obstacle arrays frustrate transport of EphA2-ephrin-A1 clusters in cancer cell lines. *Nano Lett.* **13,** 3059–3064 (2013).

369. Groeger, G. & Nobes, C. D. Co-operative Cdc42 and Rho signalling mediates ephrinB-triggered endothelial cell retraction. *Biochem. J.* **404,** 23–29 (2007).

370. Neuman, K. C. & Block, S. M. Optical trapping. *Review of Scientific Instruments* **75,** 2787–2809 (2004).

371. Soumpasis, D. M. Theoretical analysis of fluorescence photobleaching recovery experiments. *Biophys. J.* **41,** 95–97 (1983).

372. Petrášek, Z. & Schwille, P. Precise measurement of diffusion coefficients using scanning fluorescence correlation spectroscopy. *Biophys. J.* **94,** 1437–1448 (2008).

373. Gowrishankar, K. *et al.* Active Remodeling of Cortical Actin Regulates Spatiotemporal Organization of Cell Surface Molecules. *Cell* **149,** 1353–1367 (2012).

374. Chan, F. T. S., Kaminski, C. F. & Kaminski Schierle, G. S. HomoFRET Fluorescence Anisotropy Imaging as a Tool to Study Molecular Self-Assembly in Live Cells. *ChemPhysChem* **12,** 500–509 (2011).

375. Gustafsson, M. G. L. Surpassing the lateral resolution limit by a factor of two using structured illumination microscopy. *J. Microsc.* **198,** 82–7 (2000).

376. Gustafsson, M. G. L. Nonlinear structured-illumination microscopy: Wide-field fluorescence imaging with theoretically unlimited resolution. *Proc. Natl. Acad. Sci.* **102,** 13081–13086 (2005).

377. Müller, M., Mönkemöller, V., Hennig, S., Hübner, W. & Huser, T. Open-source image reconstruction of super-resolution structured illumination microscopy data in ImageJ. *Nat. Commun.* **7,** 1–6 (2016).

378. Steger, C. An unbiased detector of curvilinear structures. *IEEE Trans. Pattern Anal. Mach. Intell.* **20,** 113–125 (1998).

379. Thielicke, W. & Stamhuis, E. J. PIVlab - Time-Resolved Digital Particle Image Velocimetry Tool for MATLAB (version: 1.42). (2014). doi:http://dx.doi.org/10.6084/m9.figshare.1092508

380. Thielicke, W. & Stamhuis, E. J. PIVlab – Towards User-friendly, Affordable and Accurate Digital Particle Image Velocimetry in MATLAB. *J. Open Res. Softw.* **2,** (2014).

381. W. Helfrich. Elastic Properties of Lipid Bilayers—Theory and Possible Experiments. *Zeitschrift fur Naturforsch. Tl. C Biochem. Biophys. Biol. Virol.* **28,** 693–703 (1973).

382. Canham, P. B. The minimum energy of bending as a possible explanation of the biconcave shape of the human red blood cell. *J. Theor. Biol.* **26,** 61–81 (1970).

383. Fournier, J. B., Ajdari, A. & Peliti, L. Effective-area elasticity and tension of micromanipulated membranes. *Phys. Rev. Lett.* **86,** 4970–4973 (2001).

384. Evans, E. A. & Hochmuth, R. M. Mechanochemical Properties of Membranes. in *Current Topics in Membranes and Transport* 1–64 (1978). doi:10.1016/S0070-2161(08)60833-3

385. Rawicz, W., Olbrich, K. C., McIntosh, T., Needham, D. & Evans, E. A. Effect of chain length and unsaturation on elasticity of lipid bilayers. *Biophys. J.* **79,** 328–339 (2000).

386. Deuling, H. J. & Helfrich, W. Red blood cell shapes as explained on the basis of curvature elasticity. *Biophys. J.* **16,** 861–868 (1976).

387. Evans & Rawicz. Entropy-driven tension and bending elasticity in condensed-fluid membranes. *Phys. Rev. Lett.* **64,** 2094–2097 (1990).

388. Sukharev, S. Mechanosensitive channels in bacteria as membrane tension reporters. *FASEB J.* **13 Suppl,** S55–S61 (1999).

389. Berk, D. A. & Hochmuth, R. M. Lateral mobility of integral proteins in red blood cell tethers. *Biophys. J.* **61,** 9–18 (1992).

390. Brochard-Wyart, F., Borghi, N., Cuvelier, D. & Nassoy, P. Hydrodynamic narrowing of tubes extruded from cells. *Proc. Natl. Acad. Sci.* **103,** 7660–7663 (2006).

391. Hochmuth, R. M., Wiles, H. C., Evans, E. A. & McCown, J. T. Extensional flow of erythrocyte membrane from cell body to elastic tether. II. Experiment. *Biophys. J.* **39,** 83–89 (1982).

392. Dai, J. & Sheetz, M. P. Mechanical properties of neuronal growth cone membranes studied by tether formation with laser optical tweezers. *Biophys. J.* **68,** 988–996 (1995).

393. Pontes, B., Monzo, P. & Gauthier, N. C. Membrane tension: A challenging but universal physical parameter in cell biology. *Semin. Cell Dev. Biol.* **71,** 30–41 (2017).

394. Sheetz, M. P. Cell control by membrane-cytoskeleton adhesion. *Nature Reviews Molecular Cell Biology* (2001). doi:10.1038/35073095

395. Raucher, D. & Sheetz, M. P. Characteristics of a membrane reservoir buffering membrane tension. *Biophys. J.* **77,** 1992–2002 (1999).

396. Titushkin, I. & Cho, M. Distinct membrane mechanical properties of human mesenchymal stem cells determined using laser optical tweezers. *Biophys. J.* **90,** 2582–2591 (2006).

397. Sheetz, M. P. & Dai, J. Modulation of membrane dynamics and cell motility by membrane tension. *Trends in Cell Biology* (1996). doi:10.1016/0962-8924(96)80993-7

398. Dai, J. & Sheetz, M. P. Membrane tether formation from blebbing cells. *Biophys. J.* **77,** 3363–3370 (1999).

399. Popescu, G. *et al.* Optical measurement of cell membrane tension. *Phys. Rev. Lett.* **97,** (2006).

400. Gov, N., Zilman, A. G. & Safran, S. Cytoskeleton Confinement and Tension of Red Blood Cell Membranes. *Phys. Rev. Lett.* **90,** 4 (2003).

401. Kanda, H. & Gu, J. G. Membrane Mechanics of Primary Afferent Neurons in the Dorsal Root Ganglia of Rats. *Biophys. J.* **112,** 1654–1662 (2017).

402. Alert, R., Casademunt, J., Brugués, J. & Sens, P. Model for probing membrane-cortex adhesion by micropipette aspiration and fluctuation spectroscopy. *Biophys. J.* **108,** 1878–1886 (2015).

403. Merkel, R. *et al.* A micromechanic study of cell polarity and plasma membrane cell body coupling in Dictyostelium. *Biophys. J.* **79,** 707–719 (2000).

404. Shao, J. Y. & Hochmuth, R. M. Micropipette suction for measuring piconewton forces of adhesion and tether formation from neutrophil membranes. *Biophys. J.* **71,** 2892–2901 (1996).

405. Derényi, I., Jülicher, F. & Prost, J. Formation and interaction of membrane tubes. *Phys. Rev. Lett.* **88,** 238101 (2002).

406. Koster, G., Cacciuto, A., Derényi, I., Frenkel, D. & Dogterom, M. Force barriers for membrane tube formation. *Phys. Rev. Lett.* **94,** 068101 (2005).

407. Hwang, W. C. & Waugh, R. E. Energy of dissociation of lipid bilayer from the membrane skeleton of red blood cells. *Biophys. J.* **72,** 2669–2678 (1997).

408. Waugh, R. E. & Bauserman, R. G. Physical measurements of bilayer-skeletal separation forces. *Ann. Biomed. Eng.* **23,** 308–321 (1995).

409. Cuvelier, D., Derényi, I., Bassereau, P. & Nassoy, P. Coalescence of membrane tethers: Experiments, theory, and applications. *Biophys. J.* **88,** 2714–2726 (2005).

410. Hochmuth, R. M., Shao, J.-Y., Dai, J. & Sheetzt, M. P. Deformation and Flow of Membrane into Tethers Extracted from Neuronal Growth Cones. *Biophys. J.* **70,** 358–369 (1996).

411. Li, Z. *et al.* Membrane tether formation from outer hair cells with optical tweezers. *Biophys. J.* **82,** 1386–1395 (2002).

412. Hochmuth, R. M. & Evans, E. A. Extensional flow of erythrocyte membrane from cell body to elastic tether. I. Analysis. *Biophys. J.* **39,** 71–81 (1982).

413. Evans, E. & Yeung, A. Hidden dynamics in rapid changes of bilayer shape. *Chem. Phys. Lipids* **73,** 39–56 (1994).

414. Datar, A., Bornschlögl, T., Bassereau, P., Prost, J. & Pullarkat, P. A. Dynamics of membrane tethers reveal novel aspects of cytoskeleton-membrane interactions in axons. *Biophys. J.* **108,** 489–497 (2015).

415. Sinha, B. *et al.* Cells Respond to Mechanical Stress by Rapid Disassembly of Caveolae. *Cell* **144,** 402–413 (2011).

416. Sens, P. & Turner, M. S. Budded membrane microdomains as tension regulators. *Phys. Rev. E - Stat. Nonlinear, Soft Matter Phys.* **73,** 1–4 (2006).

417. Pietuch, A., Brückner, B. R. & Janshoff, A. Membrane tension homeostasis of epithelial cells through surface area regulation in response to osmotic stress. *BBA - Mol. Cell Res.* **1833,** 712–722 (2013).

418. Figard, L. & Sokac, A. M. A membrane reservoir at the cell surface. *Bioarchitecture* **4,** 39–46 (2014).

419. Figard, L. *et al.* Membrane Supply and Demand Regulates F-Actin in a Cell Surface Reservoir. *Dev. Cell* **37,** 267–278 (2016).

420. Staykova, M., Holmes, D. P., Read, C. & Stone, H. A. Mechanics of surface area regulation in cells examined with confined lipid membranes. *Proc. Natl. Acad. Sci.* **108,** 9084–9088 (2011).

421. Gauthier, N. C., Rossier, O. M., Mathur, A., Hone, J. C. & Sheetz, M. P. Plasma Membrane Area Increases with Spread Area by Exocytosis of a GPI-anchored Protein Compartment. *Mol. Biol. Cell* **20,** 3261–3272 (2009).

422. Gauthier, N. C., Fardin, M. A., Roca-Cusachs, P. & Sheetz, M. P. Temporary increase in plasma membrane tension coordinates the activation of exocytosis and contraction during cell spreading. *Proc. Natl. Acad. Sci.* **108,** 14467–14472 (2011).

423. Bretou, M. *et al.* Cdc42 controls the dilation of the exocytotic fusion pore by regulating membrane tension. *Mol. Biol. Cell* **25,** 3195–3209 (2014).

424. Bucher, D. *et al.* Clathrin-adaptor ratio and membrane tension regulate the flat-to-curved transition of the clathrin coat during endocytosis. *Nat. Commun.* **9,** 1109 (2018).

425. Masters, T. A., Pontes, B., Viasnoff, V., Li, Y. & Gauthier, N. C. Plasma membrane tension orchestrates membrane trafficking, cytoskeletal remodeling, and biochemical signaling during phagocytosis. *Proc. Natl. Acad. Sci.* **110,** 11875–11880 (2013).

426. Norman, L. L., Bruges, J., Sengupta, K., Sens, P. & Aranda-Espinoza, H. Cell blebbing and membrane area homeostasis in spreading and retracting cells. *Biophys. J.* **99,** 1726–1733 (2010).

427. Syeda, R. *et al.* Piezo1 Channels Are Inherently Mechanosensitive. *Cell Rep.* **17,** 1739–1746 (2016).

428. Lewis, A. H. & Grandl, J. Mechanical sensitivity of Piezo1 ion channels can be tuned by cellular membrane tension. *Elife* **4,** (2015).

429. Guo, Y. R. & MacKinnon, R. Structure-based membrane dome mechanism for Piezo mechanosensitivity. *Elife* **6,** (2017).

430. Jia, Z., Ikeda, R., Ling, J., Viatchenko-Karpinski, V. & Gu, J. G. Regulation of Piezo2 mechanotransduction by static plasma membrane tension in primary afferent neurons. *J. Biol. Chem.* **291,** 9087–9104 (2016).

431. Shi, Z., Graber, Z. T., Baumgart, T., Stone, H. A. & Cohen, A. E. Cell membranes resist flow. *bioRXiv* (2018). doi:https://doi.org/10.1101/290643

432. Lieber, A. D., Schweitzer, Y., Kozlov, M. M. & Keren, K. Front-to-rear membrane tension gradient in rapidly moving cells. *Biophys. J.* **108,** 1599–1603 (2015).

433. Lieber, A. D., Yehudai-Resheff, S., Barnhart, E. L., Theriot, J. A. & Keren, K. Membrane Tension in Rapidly Moving Cells Is Determined by Cytoskeletal Forces. *Curr. Biol.* **23,** 1409–1417 (2013).

434. Khatibzadeh, N., Gupta, S., Farrell, B., Brownell, W. E. & Anvari, B. Effects of cholesterol on nano-mechanical properties of the living cell plasma membrane. *Soft Matter* **8,** 8350 (2012).

435. Hissa, B. *et al.* Membrane cholesterol removal changes mechanical properties of cells and induces secretion of a specific pool of lysosomes. *PLoS One* **8,** e82988 (2013).

436. Biswas, A., Kashyap, P., Datta, S., Sengupta, T. & Sinha, B. Cholesterol depletion by MβCD enhances membrane tension, its heterogeneity and affects cellular integrity. *ArXive* 1–28 (2018).

437. Schweitzer, Y., Lieber, A. D., Keren, K. & Kozlov, M. M. Theoretical analysis of membrane tension in moving cells. *Biophys. J.* **106,** 84–92 (2014).

438. Fogelson, B. & Mogilner, A. Computational Estimates of Membrane Flow and Tension Gradient in Motile Cells. *PLoS One* **9,** (2014).

439. Raucher, D. & Sheetz, M. P. Cell Spreading and Lamellipodial Extension Rate Is Regulated by Membrane Tension. *J. Cell Biol.* **148,** 127–136 (2000).

440. Batchelder, E. L. *et al.* Membrane tension regulates motility by controlling lamellipodium organization. *Proc. Natl. Acad. Sci.* **108,** 11429–11434 (2011).

441. Chen, C. *et al.* Myosin Light Chain Kinase (MLCK) Regulates Cell Migration in a Myosin Regulatory Light Chain Phosphorylation-independent Mechanism. *J. Biol. Chem.* **289,** 28478–28488 (2014).

442. Lou, S. S., Diz-Muñoz, A., Weiner, O. D., Fletcher, D. A. & Theriot, J. A. Myosin light chain kinase regulates cell polarization independently of membrane tension or Rho kinase. *J. Cell Biol.* (2015). doi:10.1083/jcb.201409001

443. Houk, A. R. *et al.* Membrane Tension Maintains Cell Polarity by Confining Signals to the Leading Edge during Neutrophil Migration. *Cell* **148,** 175–188 (2012).

444. Wang, W. *et al.* Exploring the inhibitory effect of membrane tension on cell polarization. *PLoS Comput. Biol.* **13,** (2017).

445. Raucher, D. & Sheetz, M. P. Membrane expansion increases endocytosis rate during mitosis. *J. Cell Biol.* **144,** 497–506 (1999).

446. Simunovic, M. & Voth, G. A. Membrane tension controls the assembly of curvature-generating proteins. *Nat. Commun.* **6,** (2015).

447. Tsujita, K., Takenawa, T. & Itoh, T. Feedback regulation between plasma membrane tension and membrane-bending proteins organizes cell polarity during leading edge formation. *Nat. Cell Biol.* **17,** 749–758 (2015).

448. Gov, N. S. Guided by curvature: shaping cells by coupling curved membrane proteins and cytoskeletal forces. *Philos. Trans. R. Soc. Lond. B. Biol. Sci.* **373,** 20170115 (2018).

449. Kirchner, J., Kam, Z., Tzur, G., Bershadsky, A. D. & Geiger, B. Live-cell monitoring of tyrosine phosphorylation in focal adhesions following microtubule disruption. *J. Cell Sci.* **116,** 975–986 (2003).

450. Riedl, J. A. *et al.* Down-regulation of Rap1 activity is involved in ephrinB1-induced cell contraction. *Biochem. J.* **389,** 465–9 (2005).

451. Rentsch, P. S. & Keller, H. Suction pressure can induce uncoupling of the plasma membrane from cortical actin. *Eur. J. Cell Biol.* **79,** 975–981 (2000).

452. Niggli, V., Andréoli, C., Roy, C. & Mangeat, P. Identification of a phosphatidylinositol-4,5-bisphosphate-binding domain in the N-terminal region of ezrin. *FEBS Lett.* **376,** 172–176 (1995).

453. Hochmuth, F. M., Shao, J. Y., Dai, J. & Sheetz, M. P. Deformation and flow of membrane into tethers extracted from neuronal growth cones. *Biophys. J.* **70,** 358–69 (1996).

454. Diz-Muñoz, A., Fletcher, D. A. & Weiner, O. D. Use the force: Membrane tension as an organizer of cell shape and motility. *Trends in Cell Biology* **23,** 47–53 (2013).

455. Sens, P. & Plastino, J. Membrane tension and cytoskeleton organization in cell motility. *Journal of Physics Condensed Matter* **27,** 273103 (2015).

456. Nussenzveig, H. M. Cell membrane biophysics with optical tweezers. *Eur. Biophys. J.* 249–17 (2017). doi:10.1007/s00249-017-1268-9

457. Képiró, M. *et al.* Para-nitroblebbistatin, the non-cytotoxic and photostable myosin II inhibitor. *Angew. Chemie - Int. Ed.* **53,** 8211–8215 (2014).

458. Friedman, A. L., Geeves, M. A., Manstein, D. J. & Spudich, J. A. Kinetic characterization of myosin head fragments with long-lived myosin.ATP states. *Biochemistry* **37,** 9679–87 (1998).

459. Chirivino, D. *et al.* The ERM proteins interact with the HOPS complex to regulate the maturation of endosomes. *Mol. Biol. Cell* **22,** 375–385 (2011).

460. Campillo, C. *et al.* Unexpected membrane dynamics unveiled by membrane nanotube extrusion. *Biophys. J.* **104,** 1248–1256 (2013).

461. Jauffred, L., Callisen, T. H. & Oddershede, L. B. Visco-elastic membrane tethers extracted from Escherichia coli by optical tweezers. *Biophys. J.* **93,** 4068–4075 (2007).

462. Wang, M. *et al.* PaxDb, a Database of Protein Abundance Averages Across All Three Domains of Life. *Mol. Cell. Proteomics* **11,** 492–500 (2012).

463. Geiger, T., Wehner, A., Schaab, C., Cox, J. & Mann, M. Comparative Proteomic Analysis of Eleven Common Cell Lines Reveals Ubiquitous but Varying Expression of Most Proteins. *Mol. Cell. Proteomics* **11,** M111.014050 (2012).

464. Pontes, B. *et al.* Membrane tension controls adhesion positioning at the leading edge of cells. *J. Cell Biol.* **216,** 2959–2977 (2017).

465. Putyrski, M. & Schultz, C. Protein translocation as a tool: The current rapamycin story. *FEBS Lett.* **586,** 2097–2105 (2012).

466. Buckley, C. E. *et al.* Reversible Optogenetic Control of Subcellular Protein Localization in a Live Vertebrate Embryo. *Dev. Cell* **36,** 117–126 (2016).

467. Duan, L. *et al.* Optogenetic control of molecular motors and organelle distributions in cells. *Chem. Biol.* **22,** 671–682 (2015).

468. Wales, P. *et al.* Calcium-mediated actin reset (CaAR) mediates acute cell adaptations. *Elife* **5,** 1–31 (2016).

469. Aponte-Santamaría, C., Brunken, J. & Gräter, F. Stress propagation through biological lipid bilayers in silico. *J. Am. Chem. Soc.* **139,** 13588–13591 (2017).

470. Kozlov, M. M. & Mogilner, A. Model of polarization and bistability of cell fragments. *Biophys. J.* **93,** 3811–3819 (2007).

471. Borghi, N. *et al.* E-cadherin is under constitutive actomyosin-generated tension that is increased at cell-cell contacts upon externally applied stretch. *Proc. Natl. Acad. Sci.* **109,** 12568–12573 (2012).

472. Zhang, M. *et al.* Rational design of true monomeric and bright photoactivatable fluorescent proteins. *Nat. Methods* **9,** 727–729 (2012).

473. Hochbaum, D. R. *et al.* All-optical electrophysiology in mammalian neurons using engineered microbial rhodopsins. *Nat. Methods* **11,** 825–833 (2014).

474. Zhang, Y. L., Frangos, J. A. & Chachisvilis, M. Laurdan fluorescence senses mechanical strain in the lipid bilayer membrane. *Biochem. Biophys. Res. Commun.* **347,** 838–841 (2006).

475. Kim, H. M. *et al.* A two-photon fluorescent probe for lipid raft imaging: C-laurdan. *ChemBioChem* **8,** 553–559 (2007).

476. Frye, L. D. & Edidin, M. The Rapid Intermixing of Cell Surface Antigens After Formation of Mouse-Human Heterokaryons. *J. Cell Sci.* **7,** 319–335 (1970).

477. Schlessinger, J. *et al.* Lateral transport on cell membranes: mobility of concanavalin A receptors on myoblasts. *Proc. Natl. Acad. Sci. U. S. A.* **73,** 2409–13 (1976).

478. Lajoie, P., Goetz, J. G., Dennis, J. W. & Nabi, I. R. Lattices, rafts, and scaffolds: domain regulation of receptor signaling at the plasma membrane. *J. Cell Biol.* **185,** 381–5 (2009).

479. Peters, R., Peters, J., Tews, K. H. & Bähr, W. A microfluorimetric study of translational diffusion in erythrocyte membranes. *BBA - Biomembr.* **367,** 282–294 (1974).

480. Koppel, D. E., Sheetz, M. P. & Schindler, M. Matrix control of protein diffusion in biological membranes. *Proc. Natl. Acad. Sci.* **78,** 3576–3580 (1981).

481. Sheetz, M. P., Schindler, M. & Koppel, D. E. Lateral mobility of integral membrane proteins is increased in spherocytic erythrocytes. *Nature* **285,** 510–512 (1980).

482. Tomishige, M., Sako, Y. & Kusumi, A. Regulation mechanism of the lateral diffusion of band 3 in erythrocyte membranes by the membrane skeleton. *J. Cell Biol.* **142,** 989–1000 (1998).

483. Kusumi, A., Sako, Y. & Yamamoto, M. Confined lateral diffusion of membrane receptors as studied by single particle tracking (nanovid microscopy). Effects of calcium-induced differentiation in cultured epithelial cells. *Biophys. J.* **65,** 2021–2040 (1993).

484. Sako, Y. & Kusumi, A. Barriers for lateral diffusion of transferrin receptor in the plasma membrane as characterized by receptor dragging by laser tweezers: Fence versus tether. *J. Cell Biol.* **129,** 1559–1574 (1995).

485. Edidin, M. & Stroynowski, I. Differences between the lateral organization of conventional and inositol phospholipid-anchored membrane proteins. A further definition of micrometer scale membrane domains. *J. Cell Biol.* **112,** 1143–1150 (1991).

486. Edidin, M., Kuo, S. C. & Sheetz, M. P. Lateral movements of membrane glycoproteins restricted by dynamic cytoplasmic barriers. *Science (80-.).* **254,** 1379–82 (1991).

487. Ritchie, K. *et al.* Detection of non-Brownian diffusion in the cell membrane in single molecule tracking. *Biophys. J.* **88,** 2266–2277 (2005).

488. Andrews, N. L. *et al.* Actin restricts FceRI diffusion and facilitates antigen-induced receptor immobilization. *Nat. Cell Biol.* **10,** 955–963 (2008).

489. Felsenfeld, D. P., Choquet, D. & Sheetz, M. P. Ligand binding regulates the directed movement of β1 integrins on fibroblasts. *Nature* **383,** 438–440 (1996).

490. Sako, Y. & Kusumi, A. Compartmentalized structure of the plasma membrane for receptor movements as revealed by a nanometer-level motion analysis. *J. Cell Biol.* **125,** 1251–1264 (1994).

491. Iino, R., Koyama, I. & Kusumi, A. Single molecule imaging of green fluorescent proteins in living cells: E-cadherin forms oligomers on the free cell surface. *Biophys. J.* **80,** 2667–2677 (2001).

492. Holowka, D. & Baird, B. Antigen-Mediated IGE Receptor Aggregation and Signaling: A Window on Cell Surface Structure and Dynamics. *Annu. Rev. Biophys. Biomol. Struct.* **25,** 79–112 (1996).

493. Saffman, P. & Delbrück, M. Brownian motion in biological membranes. *Proc. Natl. Acad. Sci.* **72,** 3111–3113 (1975).

494. Menon, A. K., Holowska, D., Webb, W. W. & Baird, B. Cross-linking of receptor-bound IgE to aggregates larger than dimers leads to rapid immobilization. *J. Cell Biol.* **102,** 541–550 (1986).

495. Sako, Y., Nagafuchi, A., Tsukita, S., Takeichi, M. & Kusumi, A. Cytoplasmic Regulation of the Movement of E-Cadherin on the Free Cell Surface as Studied by Optical Tweezers and Single Particle Tracking: Corralling and Tethering by the Membrane Skeleton. *J. Cell Biol.* **140,** 1227–1240 (1998).

496. Ryan, T. a, Myers, J., Holowka, D., Baird, B. & Webb, W. W. Molecular crowding on the cell surface. *Science (80-.).* **239,** 61–64 (1988).

497. Fujiwara, T., Ritchie, K., Murakoshi, H., Jacobson, K. & Kusumi, A. Phospholipids undergo hop diffusion in compartmentalized cell membrane. *J. Cell Biol.* **157,** 1071–1081 (2002).

498. Fujiwara, T. K. *et al.* Confined diffusion of transmembrane proteins and lipids induced by the same actin meshwork lining the plasma membrane. *Mol. Biol. Cell* **27,** 1101–1119 (2016).

499. Saxton, M. J. Anomalous diffusion due to obstacles: a Monte Carlo study. *Biophys. J.* **66,** 394–401 (1994).

500. Saxton, M. J. Anomalous diffusion due to binding: A Monte Carlo study. *Biophys. J.* **70,** 1250–1262 (1996).

501. Sperotto, M. M. & Mouritsen, O. G. Monte Carlo simulation studies of lipid order parameter profiles near integral membrane proteins. *Biophys. J.* **59,** 261–270 (1991).

502. Almeida, P. F. F., Thompson, T. E. & Vaz, W. L. C. Lateral Diffusion and Percolation in Two-Phase, Two-Component Lipid Bilayers. Topology of the Solid-Phase Domains In-Plane and Across the Lipid Bilayer. *Biochemistry* **31,** 7198–7210 (1992).

503. Bussell, S. J., Koch, D. L. & Hammer, D. A. Effect of hydrodynamic interactions on the diffusion of integral membrane proteins: diffusion in plasma membranes. *Biophys. J.* **68,** 1836–1849 (1995).

504. Dodd, T. L., Hammer, D. A., Koch, D. L. & Sangani, A. S. Numerical Simulations of the Effect of Hydrodynamic Interactions on Diffusivities of Integral Membrane Proteins. *J. Fluid Mech.* **293,** 147–180 (1995).

505. Köster, D. V. *et al.* Actomyosin dynamics drive local membrane component organization in an in vitro active composite layer. *Proc. Natl. Acad. Sci.* **113,** E1645–E1654 (2016).

506. Saha, S. *et al.* Diffusion of GPI-anchored proteins is influenced by the activity of dynamic cortical actin. *Mol. Biol. Cell* (2015). doi:10.1091/mbc.E15-06-0397

507. Raghupathy, R. *et al.* Transbilayer lipid interactions mediate nanoclustering of lipid-anchored proteins. *Cell* **161,** 581–594 (2015).

508. Heinemann, F., Vogel, S. K. & Schwille, P. Lateral membrane diffusion modulated by a minimal actin cortex. *Biophys. J.* **104,** 1465–1475 (2013).

509. Simons, K. Cell membranes: A subjective perspective. *Biochim. Biophys. Acta - Biomembr.* **1858,** 2569–2572 (2016).

510. Triantafilou, M. Lateral diffusion of Toll-like receptors reveals that they are transiently confined within lipid rafts on the plasma membrane. *J. Cell Sci.* **117,** 4007–4014 (2004).

511. Ramadurai, S. *et al.* Influence of hydrophobic mismatch and amino acid composition on the lateral diffusion of transmembrane peptides. *Biophys. J.* **99,** 1447–1454 (2010).

512. Ramadurai, S., Duurkens, R., Krasnikov, V. V. & Poolman, B. Lateral diffusion of membrane proteins: Consequences of hydrophobic mismatch and lipid composition. *Biophys. J.* **99,** 1482–1489 (2010).

513. Trimble, W. S. & Grinstein, S. Barriers to the free diffusion of proteins and lipids in the plasma membrane. *Journal of Cell Biology* **208,** 259–271 (2015).

514. Freeman, S. A. *et al.* Integrins Form an Expanding Diffusional Barrier that Coordinates Phagocytosis. *Cell* **164,** 128–140 (2016).

515. Maraspini, R., Beutel, O. & Honigmann, A. Circle scanning STED fluorescence correlation spectroscopy to quantify membrane dynamics and compartmentalization. *Methods* (2017). doi:10.1016/j.ymeth.2017.12.005

516. Billaudeau, C. *et al.* Probing the plasma membrane organization in living cells by spot variation fluorescence correlation spectroscopy. *Methods Enzymol.* **519,** 277–302 (2013).

517. van Zanten, T. S. & Mayor, S. Current approaches to studying membrane organization.

F1000Research (2015). doi:10.12688/f1000research.6868.1

518. Kress, A. *et al.* Mapping the local organization of cell membranes using excitation- polarization-resolved confocal fluorescence microscopy. *Biophys. J.* **105,** 127–136 (2013).

519. Kolin, D. L. & Wiseman, P. W. Advances in image correlation spectroscopy: measuring number densities, aggregation states, and dynamics of fluorescently labeled macromolecules in cells. *Cell Biochem. Biophys.* **49,** 141–64 (2007).

520. Taylor, M. J., Husain, K., Gartner, Z. J., Mayor, S. & Vale, R. D. A DNA-Based T Cell Receptor Reveals a Role for Receptor Clustering in Ligand Discrimination. *Cell* **169,** 108–119 (2017).

521. Jaqaman, K. *et al.* Cytoskeletal Control of CD36 Diffusion Promotes Its Receptor and Signaling Function. *Cell* **146,** 593–606 (2011).

522. Winter, P. W., Van Orden, A. K., Roess, D. A. & Barisas, B. G. Actin-dependent clustering of insulin receptors in membrane microdomains. *BBA - Biomembr.* **1818,** 467–473 (2012).

523. Bakker, G. J. *et al.* Lateral mobility of individual integrin nanoclusters orchestrates the onset for leukocyte adhesion. *Proc. Natl. Acad. Sci.* **109,** 4869–4874 (2012).

524. Alon, R. & Dustin, M. L. Force as a Facilitator of Integrin Conformational Changes during Leukocyte Arrest on Blood Vessels and Antigen-Presenting Cells. *Immunity* **26,** 17–27 (2007).

525. Jaumouillé, V. *et al.* Actin Cytoskeleton Reorganization by Syk Regulates Fcγ Receptor Responsiveness by Increasing Its Lateral Mobility and Clustering. *Dev. Cell* **29,** 534–546 (2014).

526. Freeman, S. A. *et al.* Toll-like receptor ligands sensitize B-cell receptor signalling by reducing actin-dependent spatial confinement of the receptor. *Nat. Commun.* **6,** 6168 (2015).

527. Torreno-Pina, J. A. *et al.* The actin cytoskeleton modulates the activation of iNKT cells by segregating CD1d nanoclusters on antigen-presenting cells. *Proc. Natl. Acad. Sci.* **113,** E772–E781 (2016).

528. Kaizuka, Y., Douglass, A. D., Varma, R., Dustin, M. L. & Vale, R. D. Mechanisms for segregating T cell receptor and adhesion molecules during immunological synapse formation in Jurkat T cells. *Proc. Natl. Acad. Sci.* **104,** 20296–20301 (2007).

529. Dustin, M. L. & Cooper, J. A. The immunolgical synapse and the actin cyroskeleton: monecular hardware for T cell signaling. *Nat. Immunol.* **1,** 23–29 (2000).

530. Freeman, S. A. *et al.* Transmembrane Pickets Connect Cyto- and Pericellular Skeletons Forming Barriers to Receptor Engagement. *Cell* **172,** 305–317.e10 (2018).

531. Ennomani, H. *et al.* Architecture and Connectivity Govern Actin Network Contractility. *Curr. Biol.* **26,** 616–626 (2016).

532. Coué, M., Brenner, S. L., Spector, I. & Korn, E. D. Inhibition of actin polymerization by latrunculin A. *FEBS Lett.* **213,** 316–8 (1987).

533. Nolen, B. J. *et al.* Characterization of two classes of small molecule inhibitors of Arp2/3 complex. *Nature* **460,** 1031–1034 (2009).

534. Rizvi, S. A. *et al.* Identification and Characterization of a Small Molecule Inhibitor of Formin-Mediated Actin Assembly. *Chem. Biol.* **16,** 1158–1168 (2009).

535. Chinthalapudi, K. *et al.* Mechanism and specificity of pentachloropseudilin-mediated inhibition of myosin motor activity. *J. Biol. Chem.* **286,** 29700–29708 (2011).

536. Worch, R., Petrášek, Z., Schwille, P. & Weidemann, T. Diffusion of Single-Pass Transmembrane Receptors: From the Plasma Membrane into Giant Liposomes. *J. Membr. Biol.* **250,** 393–406 (2017).

537. Javanainen, M., Martinez-Seara, H., Metzler, R. & Vattulainen, I. Diffusion of Integral Membrane Proteins in Protein-Rich Membranes. *J. Phys. Chem. Lett.* **8,** 4308–4313 (2017).

538. Adkins, E. M. *et al.* Membrane mobility and microdomain association of the dopamine transporter studied with fluorescence correlation spectroscopy and fluorescence recovery after photobleaching. *Biochemistry* **46,** 10484–10497 (2007).

539. Barak, L. S. *et al.* Internal trafficking and surface mobility of a functionally intact beta2-adrenergic receptor-green fluorescent protein conjugate. *Mol. Pharmacol.* **51,** 177–184 (1997).

540. Poo, M. M. & Cone, R. A. Lateral diffusion of rhodopsin in the photoreceptor membrane. *Nature* **247,** 438–441 (1974).

541. Meddens, M. B. M. *et al.* Actomyosin-dependent dynamic spatial patterns of cytoskeletal components drive mesoscale podosome organization. *Nat. Commun.* **7,** 1–17 (2016).

542. Ashdown, G. W., Cope, A., Wiseman, P. W. & Owen, D. M. Molecular flow quantified beyond the diffraction limit by spatiotemporal image correlation of structured illumination microscopy data. *Biophys. J.* **107,** L21–L23 (2014).

543. Gardel, M. L. *et al.* Traction stress in focal adhesions correlates biphasically with actin retrograde fl ow speed. *J. Cell Biol.* **183,** 999–1005 (2008).

544. Vallotton, P., Gupton, S. L., Waterman-Storer, C. M. & Danuser, G. Simultaneous mapping of filamentous actin flow and turnover in migrating cells by quantitative fluorescent speckle microscopy. *Proc. Natl. Acad. Sci.* **101,** 9660–9665 (2004).

545. Gupta, P., Martin, R., Knölker, H. J., Nihalani, D. & Sinha, D. K. Myosin-1 inhibition by PClP affects membrane shape, cortical actin distribution and lipid droplet dynamics in early Zebrafish embryos. *PLoS One* **12,** 1–21 (2017).

546. Kannan, N. & Tang, V. W. Myosin-1c promotes E-cadherin tension and force-dependent recruitment

of □- actinin-4 to the epithelial cell junction. (2018).

547. Koenderink, G. H. & Paluch, E. K. Architecture shapes contractility in actomyosin networks. *Curr. Opin. Cell Biol.* **50,** 79–85 (2018).

548. Alvarado, J., Sheinman, M., Sharma, A., MacKintosh, F. C. & Koenderink, G. H. Force percolation of contractile active gels. *Soft Matter* **13,** 5624–5644 (2017).

549. Lamb, R. F. *et al.* Essential functions of ezrin in maintenance of cell shape and lamellipodial extension in normal and transformed fibroblasts. *Curr. Biol.* **7,** 682–688 (1997).

550. Wollman, R. & Meyer, T. Coordinated oscillations in cortical actin and Ca2+ correlate with cycles of vesicle secretion. *Nat. Cell Biol.* **14,** 1261–1269 (2012).

Appendix

1. Bead-tracking routine

```
range=length(folder)-4;    %total amount of individual images in the acquired movie
for k=0:range
    filename=['folder\img_00000',sprintf('%04d',k),'_Sequence_000.tif'];
    obj=imread(filename);         %load the image
    max_value=max(obj(:));        %find the max gray value
    min_value=min(obj(:));        %find the min gray value
    J=imadjust(obj,[(double(min_value)/65535) (double(max_value)/65535)],[0 1]);
                          %creates an image allowing visualization on screen
    if ~isempty(imfindcircles(J,[10 30],'Method','TwoStage','ObjectPolarity','dark'))
       [centers(k+1,:),radii(k+1)]=imfindcircles(J,[10 20],'Method','TwoStage','Object
       Polarity','dark');
    end
    %fits a circle to the image by finding the transition of bright to dark regions at
    the bead edge, storing the fitting results (center positions and radius)
end
```

2. List of plasmids

mCherry	pmCherry-C1, Clontech
mCherry-CAAX	Fatima El Marjou, Institut Curie, Paris
mCherry-Myo1b	as described in[1]
mCherry-Myo1b-rigor	cDNA encoding Myo1b-rigor corresponding to FlagHA-Myo1b-5MR in 1 were subcloned into pcDNA5/FRT/FA-Cherry
mCherry-EzrinWT	subcloning of Ezrin WT cDNA[549] (Stephanie Miserey-Lenkei, Institut Curie)
dSH2_mCherry	generous gift from Philippe Bastiaens as described in[310]
mCherry-tractin	used in Satyajit Mayor's lab, obtained from Addgene, based on[550]

3. List of siRNA

sicontrol	Dharmacon ON-TARGETplus Non-targeting Control siRNA	
siMyosin1b	GCTTACCTGGAAATCAACAAG	custom, as described in[1]
siEzrin	GCGCGGAGCUGUCUAGUGAUU	Dharmacon J-017370-08
siRadixin	GGCAUUAAGUUCAGAAUUA	Dharmacon J-011762-07
siMoesin	UCGCAAGCCUGAUACCAUU	Dharmacon J-011732-08

4. FCS raw data & fits

Representative FCS results and corresponding fits (see Materials & Methods for details) for EphB2_YFP in control conditions, after Myosin 1b depletion and after stimulation of EphB2 with its ligand ephrinB1.

4.1 siControl

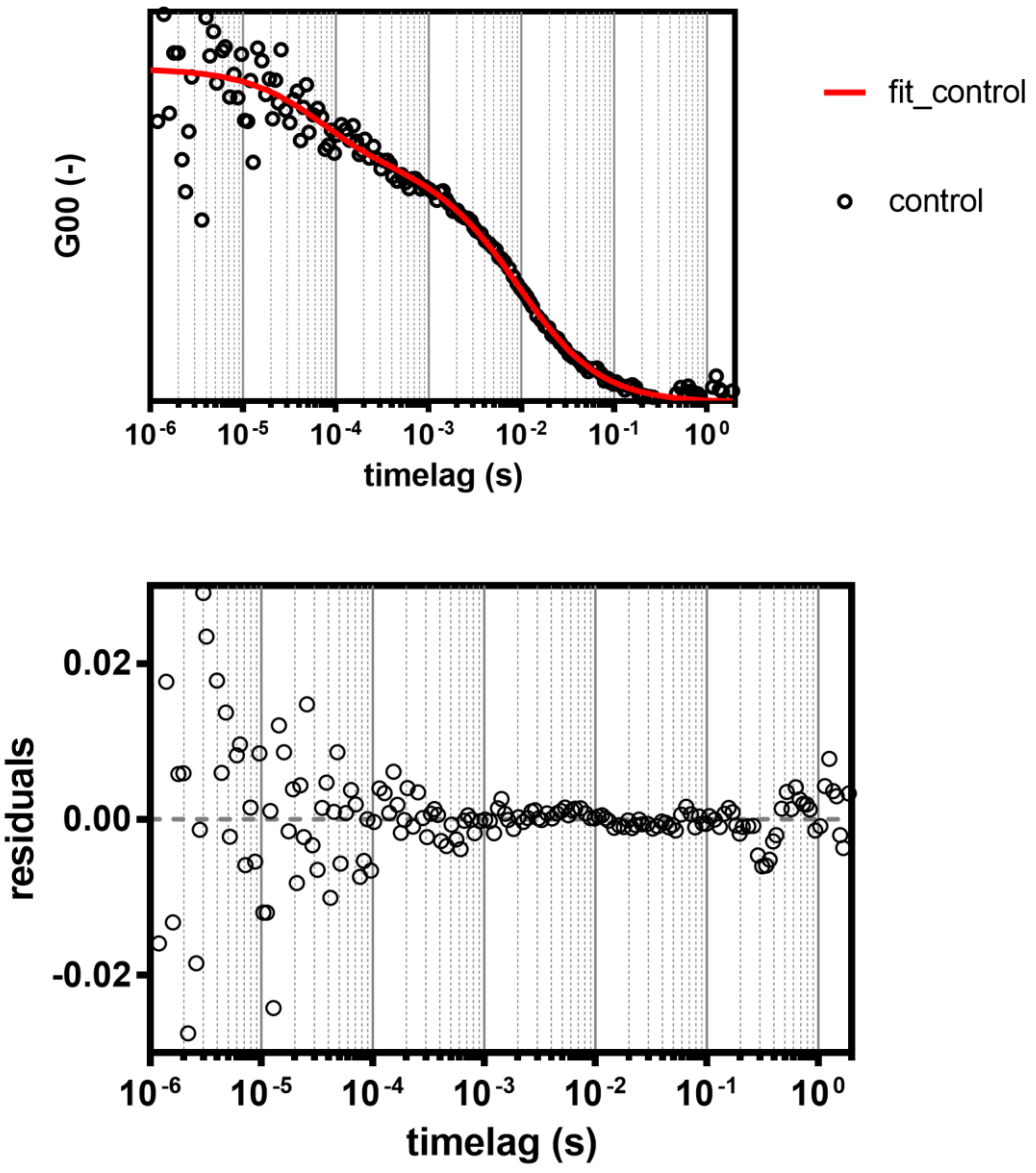

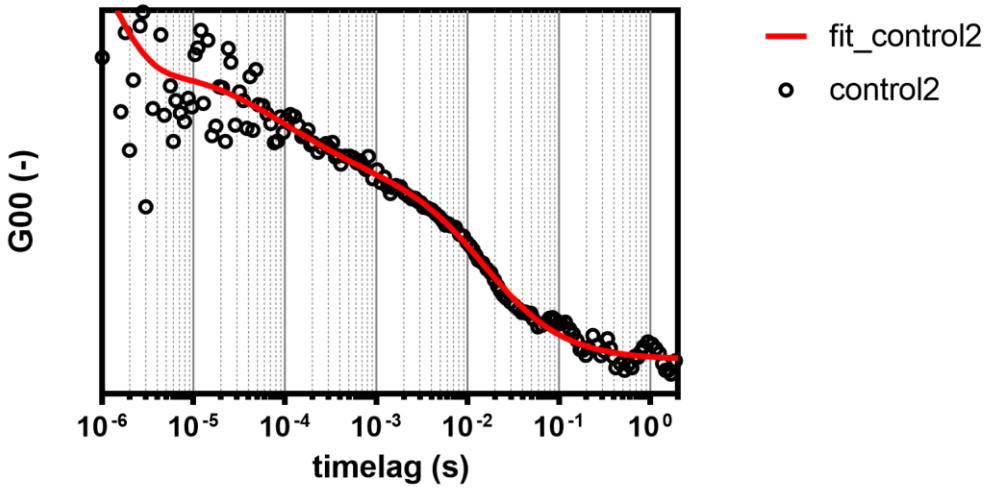
fit_control2
control2
G00 (-)
10-6
10-5
10-4
10-3
10-2
10-1
100
timelag (s)

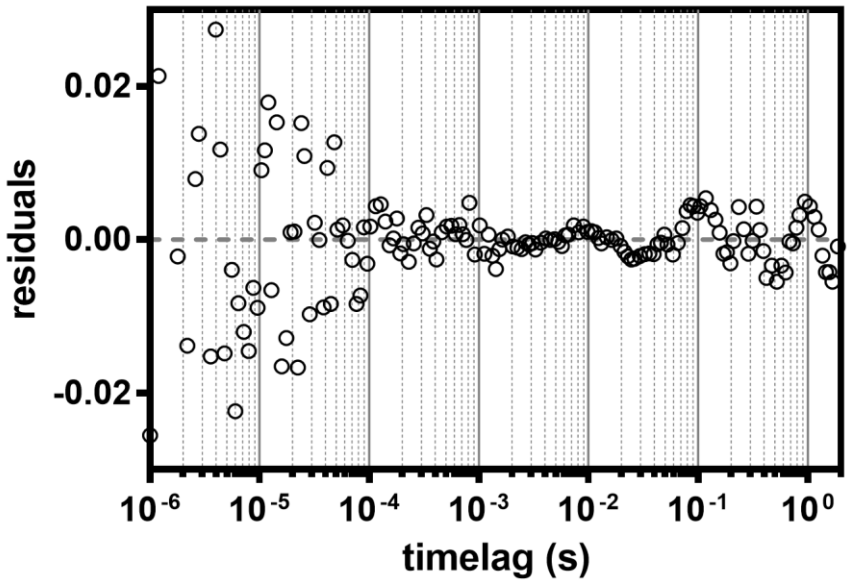
residuals
0.02
0.00
-0.02
10-6
10-5
10-4
10-3
10-2
10-1
100
timelag (s)

4.2 siMyosin1b

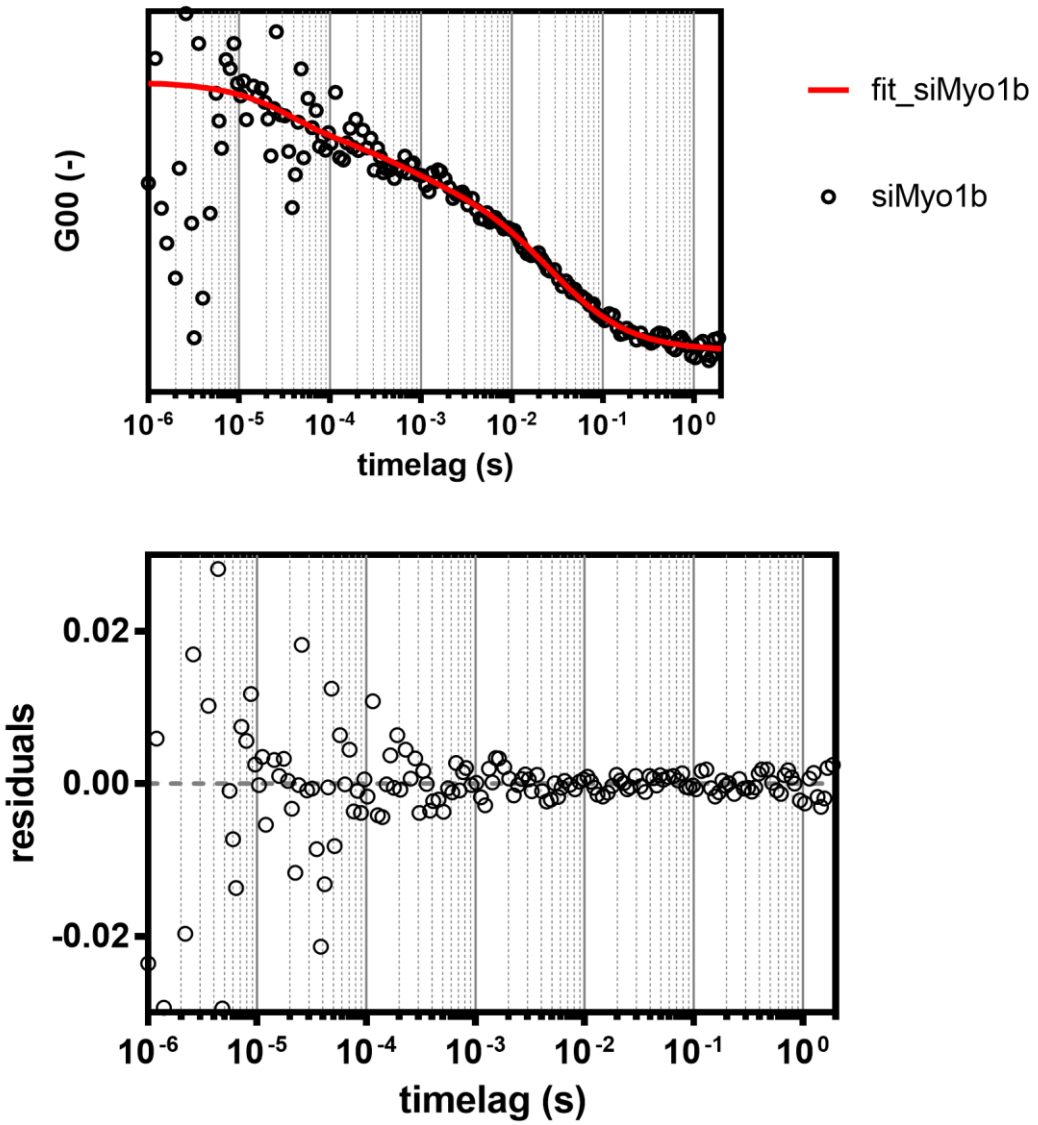

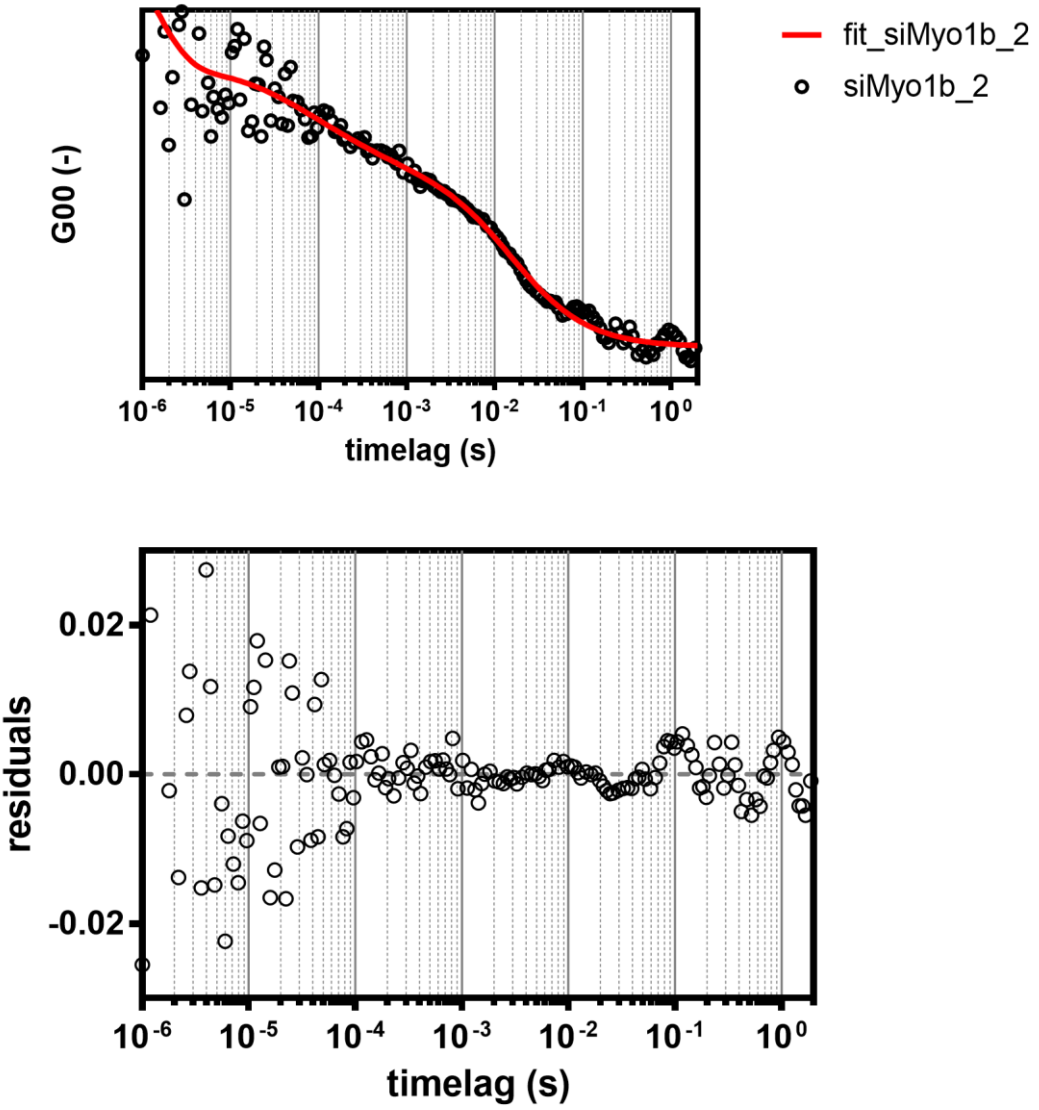
fit_siMyo1b_2
siMyo1b_2
G00 (-)
timelag (s)
residuals
0.02
0.00
-0.02
timelag (s)

4.3 EphB2 stimulation with ephrinB1

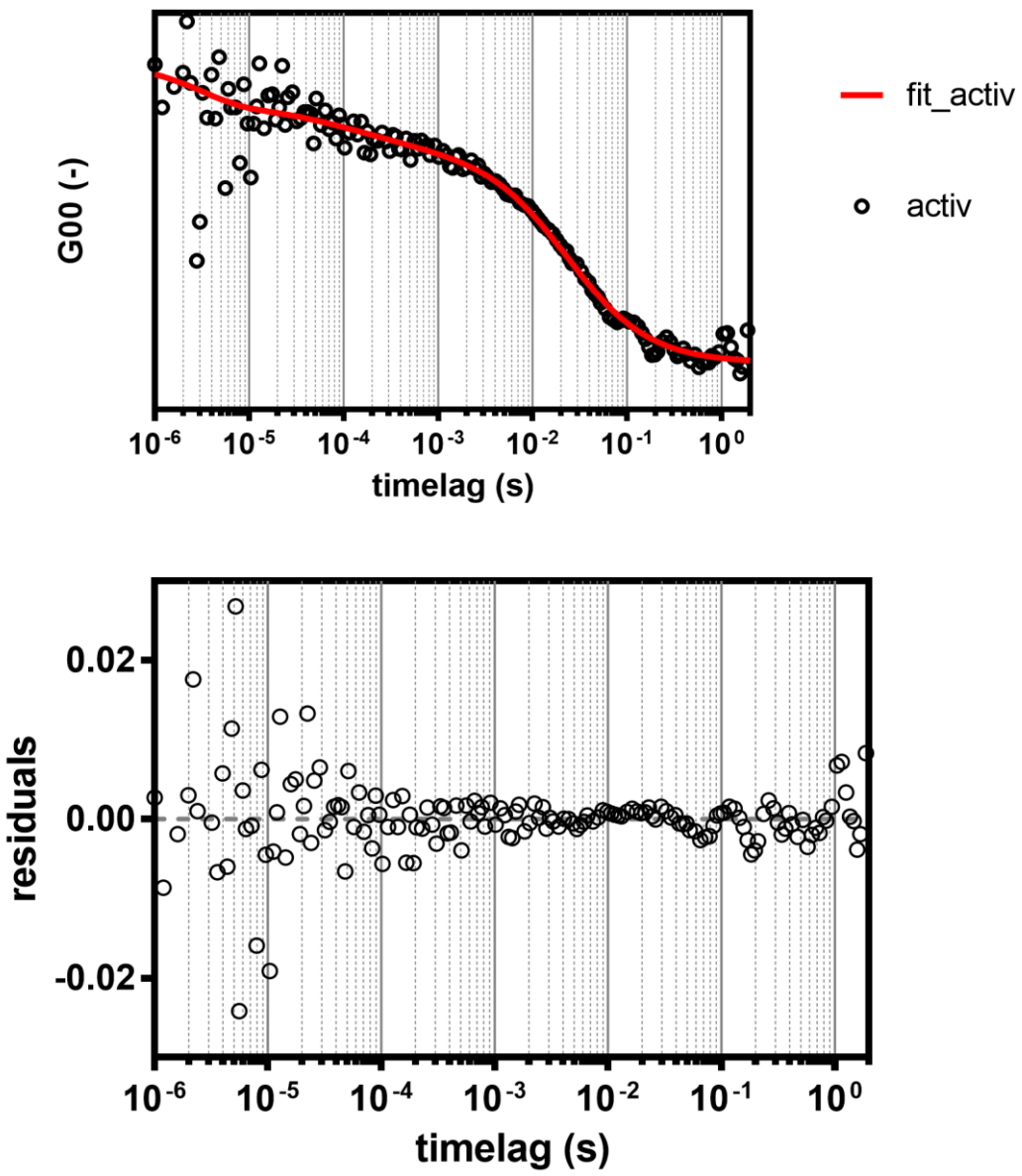

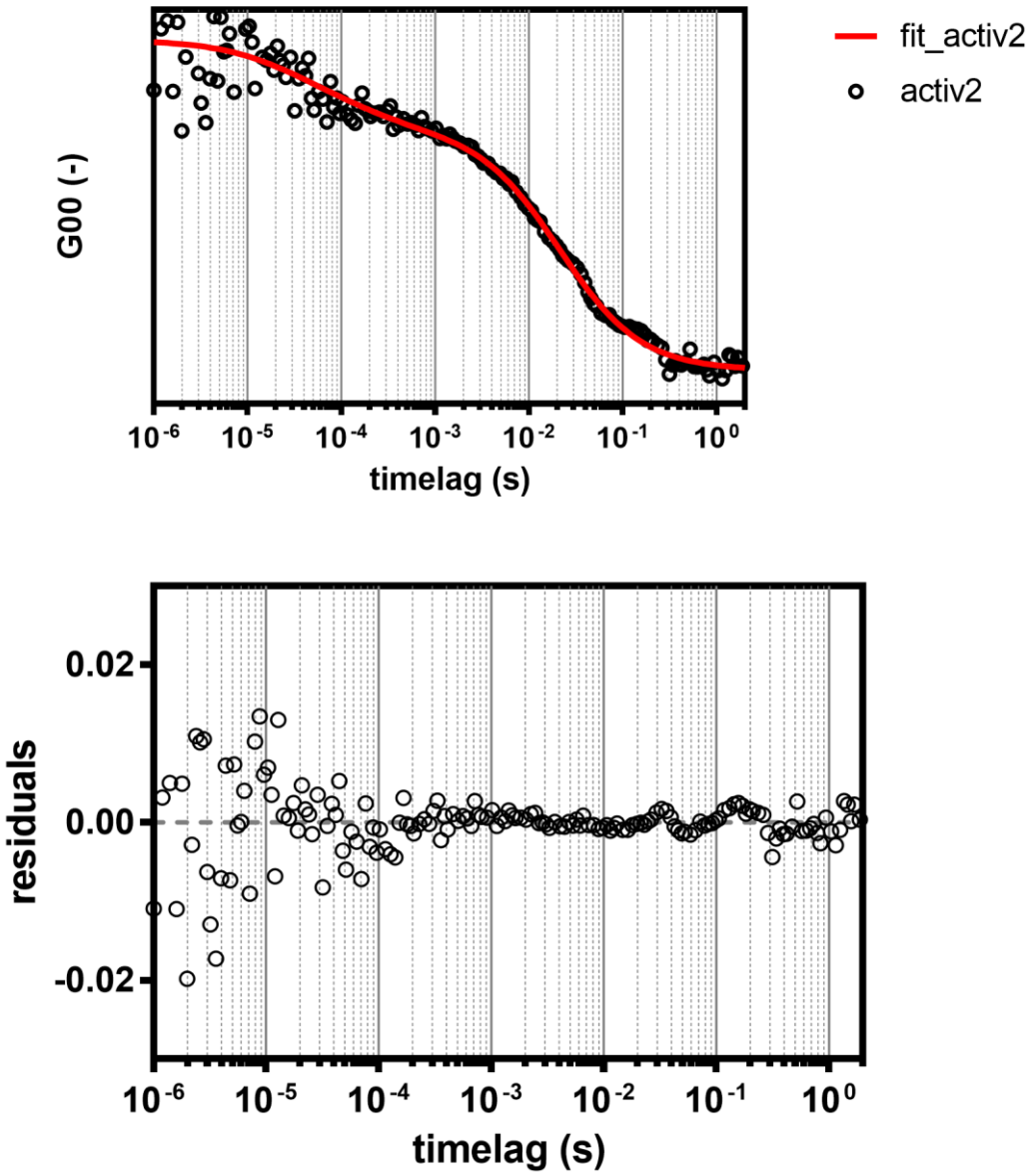
fit_activ2
activ2
G00 (-)
timelag (s)
residuals
0.02
0.00
-0.02
timelag (s)

Résumé

La myosine 1b, un moteur moléculaire non-conventionnel, est impliquée dans une variété de processus cellulaires, contrôlant, par exemple la morphologie endomembranaire, le développement des axones et la ségrégation cellulaire. Le mécanisme par lequel la myosine 1b est capable de remplir ses fonctions dans une variété de régions cellulaires reste inconnu à ce jour, mais les phénotypes décrits suggèrent un rôle de la myosine 1b à l'interface entre les membranes et l'actine. Notamment, elle est nécessaire pour une ségrégation cellulaire efficace après l'activation du récepteur EphB2 qui induit la contraction cellulaire. Cette thèse présente une caractérisation détaillée des effets de la myosine 1b sur (1) les propriétés mécaniques de la membrane cellulaire, étudiées par tirage de tubes membranaires à l'aide d'une pince optique, et (2) la dynamique du cytosquelette d'actine et des protéines transmembranaires, étudiées à l'aide d'une variété de méthodes basées sur l'imagerie microscopique. Dans cette thèse nous montrons que les myosines de classe 1 ne changent pas généralement la tension membranaire effective dans les cellules adhérentes, probablement en raison de mécanismes de compensation efficaces. De plus, nous montrons que la friction entre le cortex d'actine et la membrane plasmique dépend de la densité totale des liens entre membrane et cortex et de la fraction relative des protéines liées. L'inefficacité de la contraction cellulaire observée en absence de la myosine 1b est donc indépendante d'un changement global et persistant de la tension membranaire effective. Dans la deuxième partie de cette thèse, nous montrons que la myosine 1b ne modifie pas la dynamique du récepteur EphB2, c'est-à-dire son comportement de diffusion et de clustering, dans la membrane plasmique. Enfin, en utilisant la microscopie TIRF-SIM et une description quantitative des flux d'actine, nous révélons que la myosine 1b a un effet intrigant mais non-intuitif sur la dynamique de l'actine à la surface ventrale des cellules. En conclusion, même si le mécanisme par lequel la myosine 1b change la réponse cellulaire après stimulation des récepteurs EphB2 reste encore inconnu, nous avons finalement été en mesure de lier sa fonction à une observation bien définie et quantifiable, à savoir la modification de la dynamique des flux d'actine. Les expériences futures seront en mesure de répondre à cette observation et de disséquer son mécanisme sous-jacent. Cela permettra de conclure si la myosine 1b a un effet commun qui régit tous ses rôles biologiques décrits.

Mots Clés

Myosine 1b, EphB2, mécanique membranaire, pince optique, nanotubes membranaires, diffusion de récepteurs transmembranaires, flux d'actine, TIRF-SIM

Abstract

The unconventional motor protein myosin 1b is involved in a variety of cellular processes, controlling, e.g. endomembrane shape, axon development, and cell segregation. The mechanism by which myosin 1b is able to fulfil its functions in a variety of cellular locations remains unknown to date, yet the described phenotypes suggest a role of myosin 1b at the interface between membranes and actin. Notably, it is required for efficient cell segregation after activation of the EphB2 receptor which induces cell contraction. This thesis presents a detailed characterization of the effects of myosin 1b on (1) the mechanical properties of the cell membrane, studied by membrane tether pulling with an optical tweezer, and (2) the dynamics of the actin cytoskeleton and transmembrane proteins, studied by a variety of microscopy-based methods. Here we show that class 1 myosins do not generally change effective membrane tension in adherent cells, likely due to efficient compensation mechanisms. Furthermore, we show that friction between the actin cortex and the plasma membrane depends on the total density of membrane-cortex linkers and the relative fraction of bound proteins. The observed deficiency in cell contraction in absence of myosin 1b is thus independent of a persistent, global change in effective membrane tension. In the second part of this thesis, we show that myosin 1b likely does not change EphB2's receptor dynamics in the plasma membrane, i.e. its diffusion and clustering behavior. Finally, using TIRF-SIM imaging and quantitative description of actin flows, we reveal that myosin 1b has an intriguing yet non-intuitive effect on actin dynamics at the cellular ventral surface. In conclusion, even if the mechanism by which myosin 1b changes cellular response to EphB2 stimulation still remains unknown, we have finally been able to pinpoint its function to a well-defined and quantifiable observation, i.e. changed actin flow dynamics. Future experiments will be able to address this observation and dissect its underlying mechanism. This will allow concluding on whether myosin 1b has a common effect that governs all its described biological roles.

Keywords

Myosin 1b, EphB2, membrane mechanics, optical tweezer, membrane nanotubes, transmembrane receptor diffusion, actin flows, TIRF-SIM